Springer Proceedings in Physics 140

Thorsten M. Buzug
Jörn Borgert *Editors*

Magnetic Particle Imaging

A Novel SPIO Nanoparticle Imaging Technique

1st Edition

Springer

Springer Proceedings in Physics 140

Springer Proceedings in Physics

Please view available titles in *Springer Proceedings in Physics* on series homepage
http://www.springer.com/series/361/

Editors

Thorsten M. Buzug · Jörn Borgert

Magnetic Particle Imaging

A Novel SPIO Nanoparticle Imaging Technique

Springer

Editors
Thorsten M. Buzug
University of Luebeck
Institute of Medical Engineering
Luebeck
Germany

Jörn Borgert
Philips Technologie GmbH
Forschungslaboratorien
Hamburg
Germany

ISSN 0930-8989
e-ISSN 1867-4941
ISBN: 978-3-642-24132-1
e-ISBN: 978-3-642-24133-8
DOI 10.1007/ 978-3-642-24133-8
Springer Heidelberg New York Dordrecht London

Library of Congress Control Number: 2012930496

Printed on acid-free paper

Springer is part of Springer Science+Business Media (www.springer.com)

Preface and Acknowledgements

Magnetic particle imaging is a novel imaging modality which uses various static and oscillating magnetic fields, as well as tracer materials made from iron oxide nanoparticles to perform background-free measurements of the particles' local concentration. The method exploits the non-linear re-magnetization behavior of the particles and has the potential to surpass current methods for the detection of iron oxide in sensitivity and spatio-temporal resolution.

This volume is a collection of the accepted contributions of the Second International Workshop on Magnetic Particle Imaging (IWMPI 2012) held at the University of Lübeck, Germany on March 15-16, 2012. The workshop has been organized locally by Medisert, the technology transfer platform of the University of Lübeck, and the Institute of Medical Engineering.

The workshop proceedings cover the status and recent developments in theory and both, instrumentation and tracer materials, as each of them is equally important in designing a well performing MPI. Furthermore, the book aims at presenting first results from phantom and pre-clinical studies.

As workshop chairs we would like to thank the members of the program committee for the selection of the works included in this proceedings: C. Alexiou, University Erlangen; J. Barkhausen, University Clinics Schleswig-Holstein, Campus Lübeck; J. Bulte, Johns Hopkins University, School of Medicine, Baltimore; S. Conolly, UC Berkeley; O. Dössel, University of Karlsruhe; S. Dutz, IPHT Jena; D. Finas, University Clinics Schleswig-Holstein, Campus Lübeck; B. Gleich, Philips Research Hamburg; U. Häfeli, The University of British Columbia, Vancouver; J. Haueisen, Technical University Ilmenau; M. Heidenreich, Bruker BioSpin; U. Heinen, Bruker BioSpin; F. Kießling, University of Aachen (RWTH); T. Knopp, Bruker BioSpin; K. Krishnan, University of Washington; M. Kuhn, Philips Healthcare Hamburg; M. Magnani, Università degli Studi di Urbino; Q. Pankhurst, Davy-Faraday Research Laboratory, London; U.Pison, TOPASS GmbH, Berlin; J. Rahmer, Philips Research Europe – Hamburg; M. Schilling, TU Braunschweig; G. Schütz, Bayer Schering Pharma Berlin; M. Taupitz, Charité Berlin; B. ten Haken, University of Twente; L. Trahms, PTB Berlin; J. B. Weaver, Dartmouth Medical School; J. Weizenecker, University of Applied Sciences Karlsruhe; B. Wollenberg, University Clinics Schleswig-Holstein, Campus Lübeck; Y. Ishihara, Meiji University.

For supporting the workshop we would like to thank the Chamber of Industry and Commerce Lübeck (IHK), Bruker BioSpin, Ettlingen, the cluster agency NORGENTA, Hamburg/Schleswig-Holstein, Philips, Hamburg,

LANXESS Deutschland GmbH, Leverkusen und TOPASS GmbH, Berlin, and nanoPET, Berlin, Fork Labs, Lübeck, as well as the German Society for Biomedical Engineering within VDE (DGBMT), the Arbeitsgemeinschaft Medizintechnik (AGMT e.V.), and the EMB section of the IEEE.

Finally, the workshop would not be possible without the work of the local organization team at the University of Lübeck and, especially, Kanina Botterweck. Thank you so much.

March 2012 Thorsten M. Buzug
Lübeck Jörn Borgert

Contents

Modelling and Simulation Theory

Spectroscopy

Magnetic Particle Separation

Magnetic Nanoparticles

Magnetic Particle Imaging Theory

Medical Applications

Magnetic Particle Imaging

Magnetic Particle Theory

Magneto-Relaxometry

Imaging Technology and Safety Aspects

Short Contributions

Modelling and Simulation Theory

Characterization of Resovist® Nanoparticles for Magnetic Particle Imaging

Takashi Yoshida[1], Keiji Enpuku[1], Frank Ludwig[2], Jan Dieckhoff[2], Thilo Wawrzik[2], Aidin Lak[2], and Meinhard Schilling[2]

[1] Department of Electrical Engineering, Kyushu University, 744 Motooka, Nishi-ku Fukuoka, 819-0395, Japan
t_yoshi@ees.kyushu-u.ac.jp
[2] Institut für Elektrische Messtechnik und Grundlagen der Elektrotechnik, TU Braunschweig, Hans-Sommer-Str. 66, 38106 Braunschweig, Germany
f.ludwig@tu-bs.de

Abstract. This study investigates the dynamic magnetic properties of Resovist® for magnetic particle imaging (MPI) utilizing static M-H, ac susceptibility (ACS) and magnetic particle spectroscopy (MPS) measurements on a Resovist® suspension and an immobilized sample. Investigating the magnetic moment and anisotropy energy barrier distributions in the sample as well as the relationship between them, we clarified that the MNPs with large magnetic moment (10^{-24}~10^{-23} Wb·m) and small anisotropy energy barrier play an important role in MPI.

1 Introduction

Resovist® (Bayer Schering Pharma) is the mostly used magnetic nanoparticles (MNP) in MPI since it produces numerous harmonics even for high frequencies of the drive field. It is well recognized that MNPs with large magnetic moment and short relaxation time are suitable for MPI. In previous studies, magnetic properties of Resovist® for MPI were studied, however, without taking account of the relaxation times [1]. Therefore, it is important to quantitatively clarify the dynamic properties of Resovist®. In this study, we first estimate the magnetic moment and anisotropy energy barrier distributions in Resovist® sample as well as the relationship between them. Next, performing a MPS measurement and a numerical simulation on an immobilized sample, we show that MNPs with large magnetic moment and small anisotropy energy barrier in Resovist® particles play an important role in MPI.

T.M. Buzug and J. Borgert (Eds.): Magnetic Particle Imaging, SPPHY 140, pp. 3–7.
springerlink.com

2 Material and Method

Resovist® is a hydrophilic colloidal solution of γ-Fe_2O_3 coated with carboxydextran. Resovist® consists of clusters of single-domain particles as shown in Fig. 1. In this case, the magnetic properties of the MNPs are determined by the magnetic moment, relaxation time, and the dipolar interactions between the single-domain particles in the multi-core particle. Since it becomes, however, very complicated to characterize the magnetic properties taking account of the interactions, we introduce a simple model for multi-core particles as shown in Fig. 1. Briefly, we assume that a multi-core particle has an equivalent magnetic moment m and an equivalent anisotropy energy barrier E_B, which is related to the Néel relaxation time, and behaves like a single-domain particle. In order to estimate the m and E_B distribution which exist in a real sample, we prepared a suspension and an immobilized sample. Both samples contained the same amount of MNPs (418 μg Fe) in the same volume (150 μl). Gypsum was used to immobilize the sample.

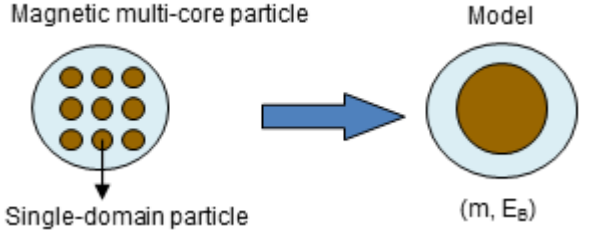

Fig. 1. Analysis model for multi-core particle

3 Estimation of the Anisotropy Energy Barrier and Magnetic Moment Distributions

First, we estimated the E_B distribution from ACS measurement on the immobilized sample. As shown in Fig. 2, the real part of the susceptibility χ'_N of the immobilized sample decreases linearly with ln(f), while its imaginary part χ''_N was almost constant independent of frequency. It can be shown that these dependences occur when the normalized anisotropy energy $\sigma=E_B/k_BT$ of the particles uniformly distributes in the sample. In this case, the complex susceptibility χ_N is given by

$$\chi_N = g_\sigma m^2 \int_{\sigma_1}^{\sigma_2} (1+j\omega\tau_N)^{-1} d\sigma = \chi_{Ndc} (\sigma_2 - \sigma_1)^{-1} \int_{\sigma_1}^{\sigma_2} (1+j\omega\tau_N)^{-1} d\sigma, \quad (1)$$

with a Néel relaxation time of

$$\tau_N = \tau_{0N} \exp(\sigma) = 10^{-9} \exp(\sigma), \quad (2)$$

where g_σ and χ_{Ndc} is the number density and dc susceptibility of the immobilized sample, respectively. Analyzing χ_N under a constraint that χ_{Ndc} agrees with the dc susceptibility of the suspension sample under small external field [2], the lower and upper values of σ as σ_1=0.26 and σ_2=27 as shown in Fig. 2(b) were obtained.

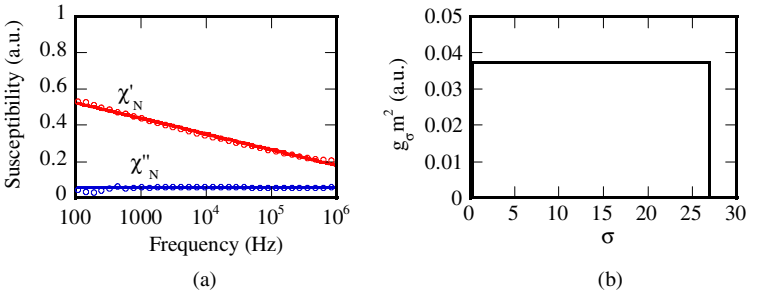

Fig. 2. (a) Frequency dependence of the real χ'_N and imaginary χ''_N parts of the ACS measured on immobilized sample when excitation field amplitude of 95μT was applied. Symbols represent the experimental results, while solid lines represent the calculated ACS for immobilized sample using the obtained anisotropy energy barrier distribution shown in (b).

Next, we estimated the m distribution from a M-H curve measurement on the suspension sample (Fig. 3(a)) using a SVD method [3] . In Fig. 3 (b), the estimated magnetic moment distribution is shown. As can be seen, there are three peaks in $g_m \cdot m^2$, where g_m is the number density. The peak with the highest value of m corresponds to the magnetic moment of multicore particles, and the other two peaks with small values of m correspond to single-domain particles.

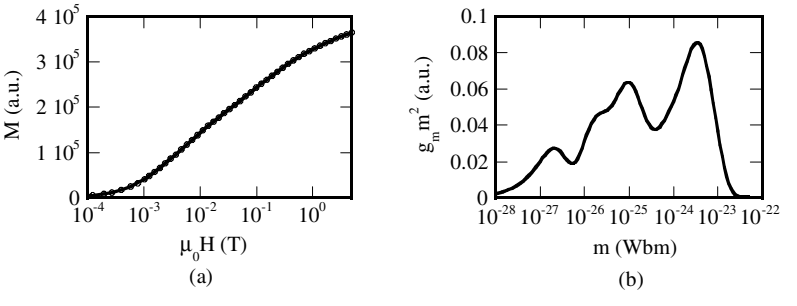

Fig. 3. (a) M-H Curve. Circles represent experimental results, while solid line shows calculated results using the estimated magnetic moment distribution depicted in (b).

Finally, combining the two estimated distributions, i.e., $g_\sigma m^2$-σ and $g_m m^2$-m, the relationship between σ and m was estimated. As shown in Fig. 4, there are three types of MNPs in Resovist®: Type-I MNPs with small m and small σ. Type-II MNPs with large m and small σ. Type-III MNPs with large m and large σ. The fraction of type-II MNPs with large m (10^{-24}~10^{-23} Wb·m) and small σ (τ_N=10^{-8}~1 s) was 34% in terms of g_mm.

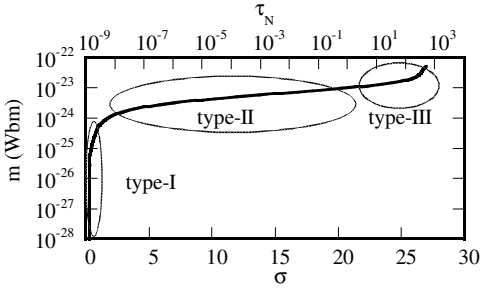

Fig. 4. Relationship between magnetic moment and anisotropy energy barrier.

4 Harmonics Spectrum

When the MNPs are used to bind to a target of interest inside the body in MPI application, MNPs are physically immobilized. In this case, relaxation and magnetization occur via the Néel mechanism. Therefore, one of the important characteristics of MNPs in MPI is the harmonics spectrum on immobilized sample. In Fig. 5, the harmonics spectra of the immobilized Resovist® sample are shown, when a field amplitude of 20 mT_{rms} with 1 kHz or 10 kHz was applied. As can be seen, the harmonics spectrum has a frequency-dependence due to the Néel relaxation.

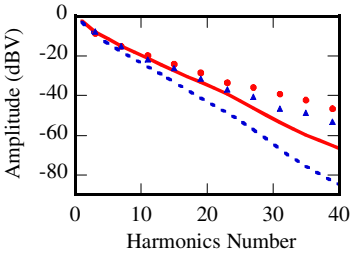

Fig. 5. Harmonics spectra of immobilized Resovist® sample when field amplitude of 20mT_{rms} was applied. Circles and triangles represent the experimental results with drive frequency of 1 kHz and 10 kHz, respectively. Solid and dashed lines represent the simulation results with drive frequency of 1 kHz and 10 kHz, respectively.

In order to make a comparison between the experimental and theoretical harmonics spectra, we performed MPS simulations for the immobilized sample using the estimated distributions as shown in Fig. 2(b) and 3(b) as well as the relationship between m and σ as shown in Fig. 4. In this MPS simulation, we solved the following Fokker-Planck equation:

$$2\tau_N \sin\theta \frac{\partial W}{\partial t} = \frac{\partial}{\partial \vartheta}\left\{ \sin\theta \left(\frac{1}{k_B T} \frac{\partial E}{\partial \theta} W + \frac{\partial W}{\partial \theta} \right) \right\} + \frac{\partial}{\partial \vartheta}\left(\frac{1}{\sin\theta} \frac{\partial W}{\partial \phi} \right), \tag{3}$$

with

$$E = -mH\cos(\omega t)\cos\theta. \tag{4}$$

This equation is applicable for Néel particles when σ is small [4]. In order to take into account of the σ-dependent Néel relaxation time, we used the σ-dependent Néel relaxation time τ_N given by eq. (2). As shown in Fig. 5, the simulated harmonic spectrum reasonably agreed with the measured results for lower harmonics, though the simulated results became smaller than the experimental ones for higher harmonics. From the numerical simulation, we found that roughly 90% of the 3rd harmonic signal was generated from type-II MNPs with large m (10^{-24}~10^{-23} Wb·m) and small σ (τ_N=10^{-8}~1 s).

5 Conclusion

Investigating the magnetic moment and anisotropy energy barrier distributions in Resovist® particles as well as the relationship between them, we clarified that the harmonics spectrum is mainly generated by the MNPs with large magnetic moment (10^{-24}~10^{-23} Wb·m) and small anisotropy energy barrier (τ_N=10^{-8}~1 s), whose relative portion is roughly 30% in terms of number times magnetic moment.

We thank Dr. D. Eberbeck of PTB for measuring the M-H curve. Financial supports from the DFG via SFB 578, the European Commission Framework Programme 7 under the NAMDIATREAM project (No. NMP-2010-246479), the JSPS Institutional Program for Young Researcher Overseas Visits, and the JSPS via Grant-in-Aid for Young Scientists (B) (23760369) are acknowledged.

References

1. Biederer, S., et al.: Magnetization response spectroscopy of superparamagnetic nanoparticles for magnetic particle imaging. J. Phys. D: Appl. Phys. 42, 205007 (2009)
2. García-Palacios, J.L., Lázaro, F.J.: Langevin-dynamics study of the dynamical properties of small magnetic particles. Phys. Rev. B 58, 14937–14958 (1998)
3. Berkov, D.V., et al.: New method for the determination of the particle magnetic moment distribution in a ferrofluid. J. Phys. D 33, 331–337 (2000)
4. Coffey, W.T., Cregg, P.J., Kalmykov, Y.P.: In: Prigogine, I., Rice, S.A. (eds.) Advances in Chemical Physics, vol. 83, p. 263. Wiley, New York (1993)

Nonlinear Behavior of Magnetic Fluid in Brownian Relaxation: Numerical Simulation and Derivation of Empirical Model

Takashi Yoshida and Keiji Enpuku

Department of Electrical Engineering, Kyushu University, University Name,
744 Motooka, Nishi-ku Fukuoka, 819-0395, Japan
t_yoshi@ees.kyushu-u.ac.jp

Abstract. Nonlinear Brownian relaxation of magnetic fluids for the case of large excitation field was studied in relation to its biomedical applications. The Fokker-Planck equation, which describes the nonlinear behavior of magnetic fluids, was solved by numerical simulation when ac field was applied. Frequency-dependences of the harmonics were investigated in terms of the effective Brownian relaxation time τ_{eff}, which was empirically obtained from the ac susceptibility of the fundamental component. It was shown that higher harmonics become small even at $\omega\tau_{eff}=1$ compared to each quasi-static harmonics amplitudes.

1 Introduction

Magnetic nanoparticles (MNPs) have been widely studied for biomedical applications. In many cases, MNPs are used in a suspension, i.e., magnetic fluids. One important property of magnetic fluids is Brownian relaxation. It is well-known that this property can be represented by Debye model in linear regime, i.e., for small excitation field. On the other hand, nonlinear properties of the Brownian relaxation appear under large excitation field, such as the decrease in ac susceptibility and the occurrence of the higher harmonics [1]. Recently, these nonlinear properties have been used for magnetic particle imaging [2] and immunoassay [3]. Therefore, it is important to quantitatively characterize the nonlinear Brownian properties for biomedical applications.

2 Numerical Simulation

We studied nonlinear behavior of the magnetic fluid in Brownian relaxation when ac field was applied. For the case of spherical single-domain particles,

T.M. Buzug and J. Borgert (Eds.): Magnetic Particle Imaging, SPPHY 140, pp. 9–13.
springerlink.com

the behavior of magnetic fluids can be described by the Fokker-Planck equation [1]:

$$2\tau_B \frac{\partial W(\theta,t)}{\partial t} = \frac{1}{\sin\theta}\frac{\partial}{\partial\theta}\left\{\sin\theta\left[\xi\cos(\omega t)\sin\theta\cdot W(\theta,t)+\frac{\partial W(\theta,t)}{\partial\theta}\right]\right\}, \quad (1)$$

where θ is the angle of the magnetic moment m with respect to the applied field of $H_{ac}=H\cos(\omega t)$, $W(\theta,t)$ is the distribution function of m, $\xi = mH/k_BT$ is the ratio of external field energy to the thermal energy k_BT. τ_B is the Brownian relaxation time given by $\tau_B=3\eta V/k_BT$, where η is the viscosity of the fluid, V is the volume of the particle. We obtain the distribution function $W(\theta,t)$ solving eq. (1) with numerical simulation. Then, we can calculate the mean magnetic moment $\langle m\rangle$ in the direction of the applied field by

$$\langle m\rangle / m = \int_0^{\pi} W(\theta,t)\sin\theta\cos\theta d\theta\,. \quad (2)$$

3 Simulation Results and Discussion

Harmonic signals from the magnetic fluids are detected to reconstruct the space distribution of the magnetic fluids in MPI application [2]. Harmonic spectrum in ac field is also used to characterize the magnetic properties [4]. Therefore, it is important to quantitatively clarify the frequency-dependence of the harmonic spectrum. In Fig. 1, numerical simulation results of the harmonic amplitudes in quasi-static case, i.e., when the frequency approaches zero, are shown. The values of $m_k(0)$ (k=1 - 11) are shown for various field amplitudes of ξ=2, 5, and 20. Here k is the harmonics number. As shown, harmonic spectrum has strong dependence on the field amplitude.

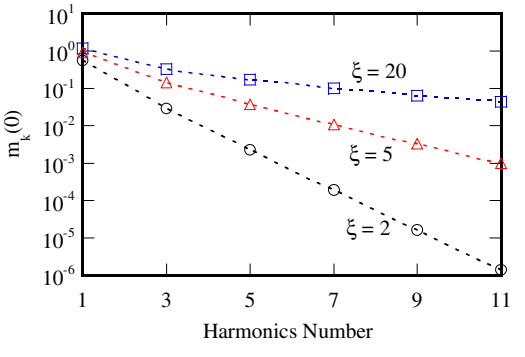

Fig. 1. Harmonic spectra for quasi-static case when various field amplitude of ξ = 2, 5, and 20 are applied. Symbols represent the numerical simulation results, while dashed lines represent the theoretical spectra, which are obtained by the Fourier expansion of the Langevin function.

In Fig. 2, frequency dependences of the harmonic amplitudes normalized by each quasi-static amplitude, i.e., $|m_k(\omega)|/m_k(0)$, are shown. As shown, frequency dependences of the normalized harmonic amplitudes are not the same, but strongly depend on the harmonic number k.

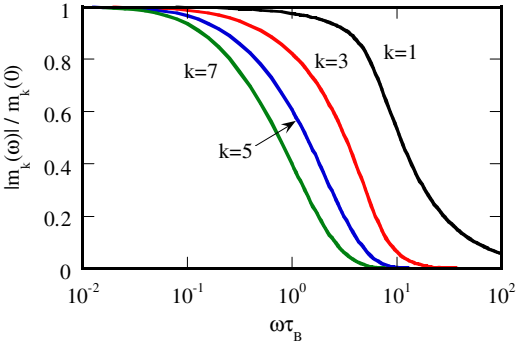

Fig. 2. Frequency-dependences of the harmonic amplitudes normalized by each quasi-static amplitude.

Next, we study the ac susceptibility of the fundamental component in order to explore the field-dependence and frequency-dependence of the nonlinear properties of the magnetic fluids. In Fig. 3, the frequency dependences of the real (χ'_1) and imaginary (χ''_1) parts of the susceptibility are shown. As shown in Fig. 3(b), ac susceptibility becomes different from the Debye equation when the field becomes large, i.e., for the case of ξ=10. For example, the frequency f_p at which χ''_1 has a peak value becomes higher when ξ =10.

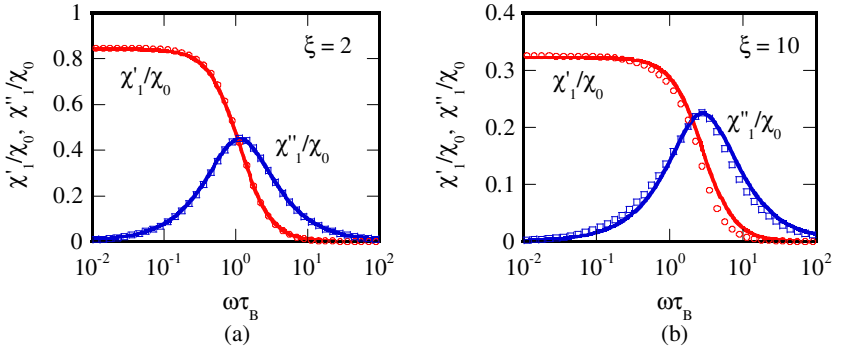

Fig. 3. Frequency dependences of the real (χ'_1) and imaginary (χ''_1) parts of the susceptibility of the fundamental component for ac excitation fields. (a) ξ=2 and (b) ξ=10. Symbols represent simulation results, while solid lines are obtained from eqs. (3) and (4).

In order to obtain empirical equations that can explain the simulation results, we modified the Debye equation as:

$$\chi'_1(\omega)/\chi_1(0) = 1/\left[1+(\omega\tau_{\text{eff}})^2\right], \tag{3}$$

$$\chi''_1(\omega)/\chi_1(0) = k''(\xi)\omega\tau_{\text{eff}}/\left[1+(\omega\tau_{\text{eff}})^2\right], \tag{4}$$

with

$$\chi_1(0)/\chi_0 = 1-\xi^3/\left(10+9\xi+3.81\xi^2+\xi^3\right), \tag{5}$$

$$\omega_{\text{p}} = 2\pi f_{\text{p}} = 1/\tau_{\text{eff}} = \sqrt{1+0.07\xi^2}/\tau_{\text{B}}, \tag{6}$$

$$k''(\xi) = 1+0.024\xi^2/\left(1+0.18\xi+0.033\xi^2\right). \tag{7}$$

Here, $\chi_1(0)$ is the susceptibility in the quasi-static case, $\chi_0 = \mu_0 M_s^2 V/(3k_B T)$ is the dc susceptibility for small fields, M_s is the saturation magnetization. Simulation results of $\chi_1(0)/\chi_0$ and the effective relaxation time τ_{eff}, given by $\tau_{\text{eff}}=1/\omega_p$, are shown in Fig. 4. As shown in Fig. 4(a), $\chi_1(0)/\chi_0$ decreased with ξ, which indicates a decrease in the susceptibility at large fields. Effective relaxation time τ_{eff} also decreased with ξ as shown in Fig. 4(b). Dependences of $\chi_1(0)$ and τ_{eff} on ξ can be well expressed with eqs. (5) and (6).

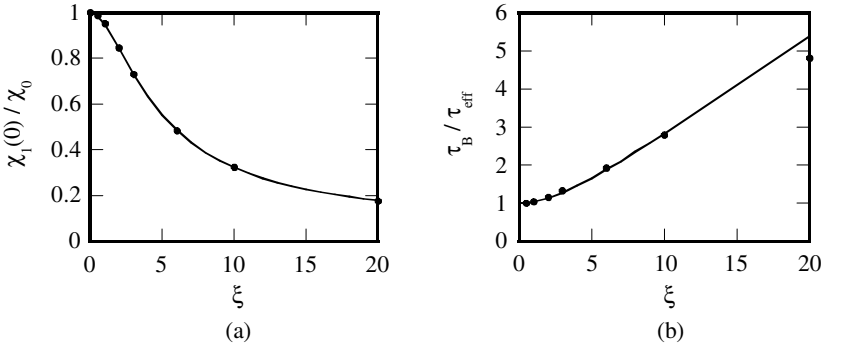

Fig. 4. (a) Dependence of $\chi_1(0)$ on ξ. Circles are simulation results, while the solid line is obtained from eq. (5). (b) Effective Brownian relaxation time τ_{eff} for ac fields. τ_{eff} is determined from the frequency f_p at which χ''_1 shown in Fig. 3 has a peak value. Circles are simulation results, while the solid line is obtained from eq. (6).

Finally, we explore the frequency dependences of $|m_k(\omega)|/m_k(0)$ by taking into account the effective relaxation time τ_{eff} given by eq. (6). In Fig. 5, frequency dependences of $|m_k(\omega\tau_{\text{eff}})|/m_k(0)$ are shown when ξ=20. Note that the horizontal axis depicts the angular frequency normalize by $1/\tau_{\text{eff}}$,

i.e., $\omega\tau_{eff}$. As can be seen, frequency dependence becomes stronger for larger harmonic number k. For example, at the frequency of $\omega\tau_{eff}=1$, the value of $|m_k(\omega\tau_{eff})|/m_k(0)$ becomes 0.8, 0.27, 0.06, and 0.0094 for the harmonic number of k=1, 3, 5 and 7, respectively. On the other hand, if we obtain the same amplitude of $|m_k(\omega\tau_{eff})|/m_k(0)=0.8$, the frequency should be $\omega\tau_{eff}=1$, 1/4.9, 1/12, and 1/21 for k=1, 3, 5 and 7, respectively. This result indicates the rapid decrease of the harmonic signals at high frequencies. Therefore, these frequency dependences of the higher harmonics should be taken into account when they are used.

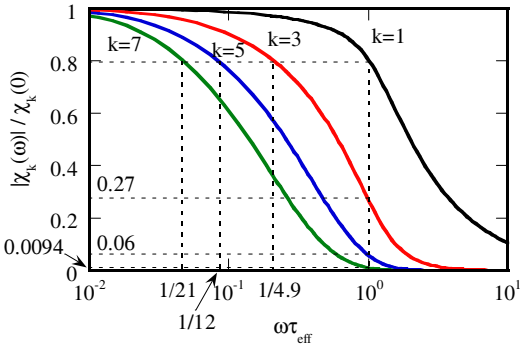

Fig. 5. Comparison of the frequency-dependences of the harmonic amplitudes.

4 Conclusion

The nonlinear Brownian relaxation of magnetic fluids was studied by numerically solving the Fokker-Planck equation. Nonlinear properties such as field-dependent effective relaxation time τ_{eff} and susceptibilities were clarified quantitatively. It was shown that the frequency dependence of the harmonic signal became stronger for larger harmonic number, resulting in the significant decrease in the signal even at $\omega\tau_{eff}=1$. These frequency dependences of the higher harmonics should be taken into account when they are used.

References

1. Yoshida, T., Enpuku, K.: Simulation and Quantitative Clarification of AC Susceptibility of Magnetic Fluid in Nonlinear Brownian Relaxation Region. Jpn. J. Appl. Phys. 48, 127002 (2009)
2. Gleich, B., Weizenecker, J.: Tomographic imaging using the nonlinear response of magnetic particles. Nature 435, 1214–1217 (2005)
3. Nikitina, P.I., Vetoshko, P.M., Ksenevich, T.I.: New type of biosensor based on magnetic nanoparticle detection. J. Magn. Magn. Mater. 311, 445–449 (2007)
4. Biederer, S., et al.: Magnetization response spectroscopy of superparamagnetic na-noparticles for magnetic particle imaging. J. Phys. D: Appl. Phys. 42, 205007 (2009)

Magnetic Particle Imaging Using Ferromagnetic Magnetization

Stephan Euting[1], Fernando M. Araújo-Moreira[2], and Waldemar Zylka[1]

[1] Department of Physical Engineering, Westfälische Hochschule
Neidenburger Str. 43, Gelsenkirchen, 45877, Germany
euting@medicalengineer.de, waldemar.zylka@fh-gelsenkirchen.de
[2] Department of Physics, Federal University of São Carlos (UFSCar)
Via Washington Luis, km 235, Caxia postal 676, São Carlos, 13565-905, Brazil
faraujo@df.ufscar.br

Abstract. Nanofluids, defined as fluids containing suspended solid nanoparticles, are potential systems for utilization in biomedical applications. Magnetic Particle Imaging (MPI) uses superparamagnetic nanofluids, e.g. a colloidal suspension of iron oxide particles. In this work a new biocompatible nanofluid based on pure and stable ferromagnetic carbon is investigated. Although this material has a relatively small value of coercive magnetic field, it does exhibit a true ferromagnetic behavior up to 300 K. We present results obtained from numerical investigations performed to calculate the impact of a ferromagnetic magnetization to the MPI signal chain. Moreover, by modeling ferromagnetic magnetization we prove here the general suitability of ferromagnetic materials for MPI. Due to the low saturation magnetization, however, MPI for ferromagnetic carbon will be possible only in the near future when realistic concentrations of the nanofluid ferromagnetic carbon will be experimentally obtainable.

1 Introduction

The members of the class of materials called magnetic can be classified by their magnetization and/or their magnetic susceptibility to an applied magnetic field into *diamagnetic*, *paramagnetic*, and *ferromagnetic* materials. *Superparamagnetism* is a form of magnetism which appears in ferromagnetic nanoparticles, among other types of magnetic materials. If those nanoparticles are sufficiently small, the magnetization can randomly flip its direction under the influence of temperature. The magnetization curve of the assembly as a function of the applied magnetic field is a reversible S-shaped curve.

Potential nano-systems for uses in biological and medical applications are the so-called nanofluids defined as fluids containing suspended solid nanoparticles with different sizes. A most recognizable class of magnetically

T.M. Buzug and J. Borgert (Eds.): Magnetic Particle Imaging, SPPHY 140, pp. 15–20.
springerlink.com

controllable nanofluid simultaneously exhibiting both fluid and magnetic properties is the ferrofluid, a suspended colloidal fluid of nanosized iron oxide (Fe3O4 or g-Fe2O3) particles frequently called SPIO. When used in MPI the nanoparticles are sufficiently small and the ferrofluid suspension became superparamagnetic [1].

Instead of ferrofluids, a new nanofluid based on pure ferromagnetic carbon is investigated as contrast material for MPI in this paper. Carbon materials, especially nanocarbons, constitute one of the most fascinating classes of structures, exhibiting a wide variety of forms and properties. The possibility of achieving striking properties in macroscopic carbon - such as room-temperature magnetic properties and even superconductivity – is attracting the scientific community and open up a plethora of possible applications of this material in engineering, as well as in medicine and biology, as a biocompatible magnetic material.

While the basic research of the ferromagnetic carbon is in progress, a model describing ferromagnetic magnetization is already available [5]. This allows studying the suitability of ferromagnetic materials, e.g. nanofluid ferromagnetic carbon, in MPI.

2 Material and Methods

2.1 Ferromagnetic Graphite and Nanofluid Magnetic Carbon

Ferromagnetic carbon can be produced by a vapor phase redox reaction in closed nitrogen atmosphere with copper oxide (CuO) [2,3]. Recent theoretical and experimental reports confirm that magnetic carbon is originated from defects [6-9]. In the present case, those defects are introduced into the carbon structure by the vapor phase redox reaction. Atomic and magnetic force microscopy (AFM/MFM) can be used to study the presence of magnetic regions which are approximately 1µm.

The chemical route for synthesizing nanofluid magnetic carbon (NFMG) is described in [4]. The structural characterization can be performed by transmission electron microscopy (TEM) leading results shown in Fig. 1, revealing a flake-like morphology. Relating the size of the scale in Fig. 1 (left) with the size of the particle in the nanofluid, the latter is estimated to be of the order of 10nm.

Besides, according to Fig. 1 (right), which shows M-H curves at 2 and 300K, the hysteresis does not disappear with increasing temperature and manifests itself in nonzero values of remnant magnetization and coercive magnetic field. Consequently, we can conclude that, even though the NFMG nanofluid has a relatively small value of coercive magnetic field (quasi-superparamagnetic state), it does exhibit a true ferromagnetic behavior up to 300K.

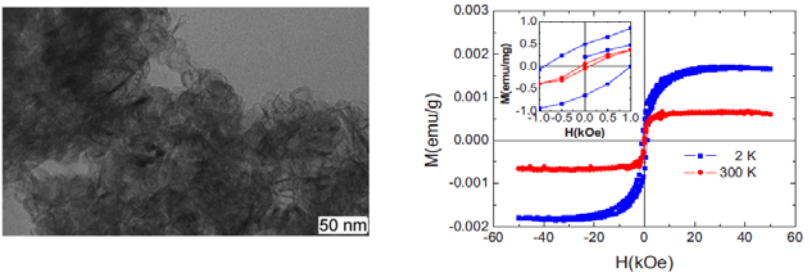

Fig. 1. Left: TEM image of NFMG sample showing a flake-like structure with an average size of the particle of the order of 10 nm. Right: The hysteresis curves for NFMG sample for two temperatures 2 and 300 K showing a ferromagnetic like behavior of the sample. Inset: low-field M-H curves.

The stability of NFMG can be verified by Zeta potential measurements of the nanoparticles under suspension. The Zeta potential indicates the level of the repulsion between particles similarly charged in dispersion. This means that the higher the Zeta potential, the more the dispersion will resist to aggregation, resulting in a longer period of stability. The stability of the dispersed solution of NFMG associated to its magnetic features, confirms its potential to be used in biological and medical applications, like imaging specifically MPI.

2.2 MPI Using Ferromagnetic Magnetization

Numerical investigations of a MPI systems using superparamagnetic nanofluid demonstrated, among others, good resolution and high sensitivity [10], field free line feasibility for signal encoding [11] even for different trajectories and trajectory densities [12]. To compare simulation results of a superparamagnetic versus a ferromagnetic nanofluid a two dimensional MPI setup similar to [12] is implemented. Two perpendicular Maxwell coil pairs, diameter of $D=500mm$, are generating the selection and driven field. The distance between the coil and its opponent is $1000mm$. The size central field of view is $30mm$ x $15mm$. The Biot-Savart law is solved for the sensitivity profile using elliptic integrals [13] and a current strength of $I=1A$. In turn, the sensitivity profile is used to calculate induced voltages. The gradient strengths are $dH_z/dz=2.5T/\mu_0 m$ and $dH_x/dx=1.25T/\mu_0 m$.

Frequently the well-known Langevin function for the anhysteretic S-shaped magnetization M_{an} is used to model a superparamagnetic magnetization [10]. In contrast, the ferromagnetic behavior can be expressed by the differential equation [5]:

$$\frac{dM_{hyst}}{dH} = \frac{1}{(1+c)} \frac{1}{\delta k/\mu_0 - \alpha\,(M_{an} - M_{hyst})} (M_{an} - M_{hyst}) + \frac{c}{(1+c)} \frac{dM_{an}}{dH}.$$

Here H is the magnetic field while H_e (occurring in the Langevin function) is the effective magnetic field given by $H_e = H + \alpha M_{hyst}$, where α denotes a mean field parameter representing inter-domain coupling. The coefficient c describes the ratio of the initial differential susceptibilities of the normal and the anhysteretic magnetization curves, $c = \chi'_{0norm} / \chi'_{0anhy}$ which can be measured experimentally. The parameter k is called shape forming parameter; μ_0 is the permeability in free space and δ takes the value $+1$ if H increases, $dH/dt > 0$ and -1 if H decreases, $dH/dt < 0$. Implicit parameters of the magnetization M_{an} are: M_s the saturation magnetization, $a = (k_B T)/(\mu_0 m)$ with k_B the Boltzmann constant, T the temperature in Kelvin, and m the magnetic moment of a particle. We solved the differential equation implementing a standard 4th order Runge-Kutta method [14].

The image reconstruction, i.e. solution of the equation $\hat{\mathbf{G}}\mathbf{c} = \hat{\mathbf{u}}$, for $\mathbf{c}$, where $\hat{\mathbf{G}}$ is the one dimensional discrete Fourier transformed system matrix, $\mathbf{c}$ the unknown concentration and $\hat{\mathbf{u}}$ the Fourier transformed induced voltage, is obtained by a combination of singular value decomposition and Tikhonov regularization. The regularization parameter suggested in [10] is used.

To compare MPI results for superparamagnetic versus ferromagnetic nanofluids, parameters from [12] are adopted: For the superparamagnetic nanofluid, the saturation magnetization is $M_s = 477 \times 10^3 A/m$ and $a = 505.06\ A/m$. Those values are used for the ferromagnetic nanofluid too and, in addition, the following values to form an adequate hysteresis curve: $k = 1.6 \times 10^3 Vs/m^2$, $\alpha = 1.6 \times 10^{-3}$, $c = 0.01$.

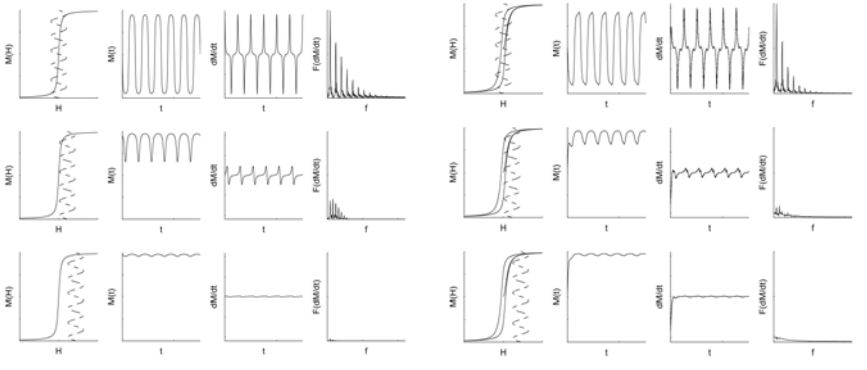

Fig. 2. Comparison of MPI signals chain for three different offset fields using superparamagnetic (left) and ferromagnetic nanofluid (right).

3 Results

Figure 2 shows the MPI signal chain for superparamagnetic and ferromagnetic particles for various values of the offset field: Magnetization, induced voltage, and frequency spectrum. In both magnetization classes, higher

modulation offset causes saturation of the oscillating magnetization which determines the local MPI resolution. Comparing the spectra for the same values of the offset field, differences of the amplitude of frequency peaks between the superparamagnetic and the ferromagnetic magnetization can be observed.

Figure 3 presents reconstruction results for both particle models. The two dimensional object is reconstructed with a resolution of 64x64 pixel and 50 time points per sinus wave of the trajectory current. The trajectory density is $\kappa=30$, see [12]. In general, image quality will increase with higher concentrations while the smoothness of the reconstructed image increases with the regularization parameter. A comparison of MPI results from superparamagnetic to those from ferromagnetic magnetization reveals the later to produce less blurred and more edged images.

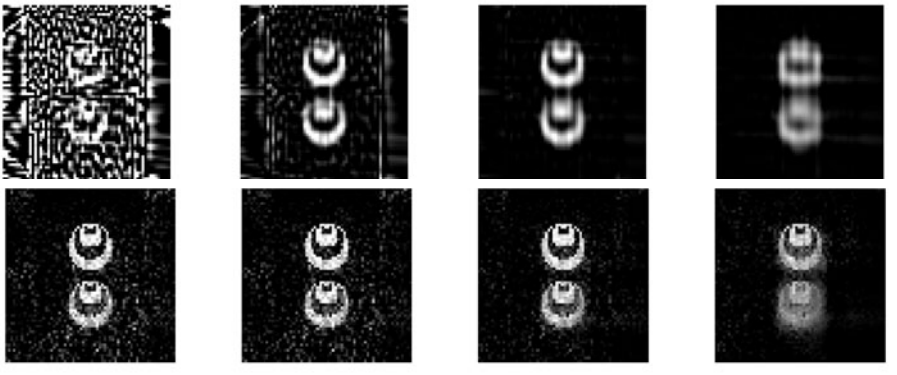

Fig. 3. Results of 2D reconstruction for different regularization parameters λ_k (rows) increasing from left to right and different particle models (lines): ferromagnetic model, bottom, superparamagnetic model, top. The concentration is $c = 74.4\ \mu mol$.

4 Discussion and Conclusions

In this study we investigated materials synthesized into a nanofluidic ferromagnetic solution as a new class of contrast agent in MPI. The class of ferromagnetic nanofluids - possessing a non-reversible magnetization curve - extends the originally used superparamagnetic ferrofluid suspensions.

We proved the feasibility of using ferromagnetic materials in MPI. The reconstruction problem requires – as in the superparamagnetic class – a solution of an ill-posed linear system of equations. The image quality using the ferromagnetic nanofluid is comparable or better than for superparamagnetic nanofluids. In particular, it shows more edged and less blurred results. This may be attributed to the existence of a remanence magnetization of the ferromagnetic particles. Whereas by a decreasing magnetic field the Langevin function generates a decreasing magnetization, the ferromagnetic model includes a magnetization even if the magnetic field reaches zero.

Due to the currently low saturation magnetization of the nanofluid ferromagnetic carbon the generation of a strong MPI signal will only be possible in the future when high concentrations will be obtainable.

References

1. Gleich, B., Weizenecker, J.: Tomographic imaging using the nonlinear response of magnetic particles. Nature 435, 1214–1217 (2005)
2. Mombrú, A.W., Pardo, H., Faccio, R., de Lima, O.F., Leite, E.R., Zanelatto, G., Lanfredi, A.J.C., Cardoso, C.A., Araújo-Moreira, F.M.: Physical Review B 71, 100404 (2005)
3. Pardo, H., Faccio, R., Araújo-Moreira, F.M., de Lima, O.F., Mombrú, A.W.: Carbon 44, 565 (2006)
4. Souza, N.S., Sergeenkov, S., Speglich, C., Rivera, V.A.G., Cardoso, C.A., Pardo, H., Mombrú, A.W., Rodrigues, A.D., de Lima, O.F., Araújo-Moreira, F.M.: Applied Physics Letters 95, 233120 (2009)
5. Jiles, D.C., Atherton, D.L.: Theory of ferromagnetic hysteresis. Journal of Magnetism and Magnetic Materials 61, 48–60 (1986)
6. Faccio, R., Pardo, H., Denis, P.A., Yoshikawa Oeiras, R., Araújo-Moreira, F.M., Veríssimo-Alves, M., Mombrú, A.W.: Physical Review B 77, 035416 (2008)
7. Cervenka, J., Katsnelson, M.I., Flipse, C.F.J.: Nature Physics 5, 840 (2009)
8. Ugeda, M.M., Brihuega, I., Guinea, F., Gómez-Rodríguez, J.M.: Phys. Rev. Lett. 104, 096804 (2010)
9. Chen, J.-H., Li, L., Cullen, W.G., Williams, E.D., Fuhrer, M.S.: Nature Physics 7, 535–538 (2011)
10. Weizenecker, J., Borgert, J., Gleich, B.: Phys. Med. Biol. 52, 6363–6374 (2007)
11. Weizenecker, J., Gleich, B., Borgert, J.: J. Phys. D 41, 105009 (2008)
12. Knopp, T., Biederer, S., Sattel, T., Weizenecker, J., Gleich, B., Borgert, J., Buzug, T.M.: Phys. Med. Biol. 54, 385–397 (2009)
13. Bladel, J.V.: Electromagnetic Fields, vol. 2. IEEE (2007)
14. Press, W.H., Teukolsky, S.A., Vetterling, W.T., Flannery, B.P.: Numerical Recipes in C, 2nd edn. Cambridge University Press (1992)

Magnetic Particle Imaging: Exploring Particle Mobility

Thilo Wawrzik, Frank Ludwig, and Meinhard Schilling

Institut für Elektrische Messtechnik und Grundlagen der Elektrotechnik,
TU Braunschweig, Hans-Sommer-Str. 66, 38106 Braunschweig, Germany
t.wawrzik@tu-braunschweig.de

Abstract. Magnetic Particle Imaging (MPI) is a promising new imaging modality, providing 3-dimensional imaging of magnetic nanoparticle tracers with high spatial and temporal resolution. Some recently developed experimental scanners have proven MPI to be feasible for small animal imaging. So far, one assumes that all particles contributing to the MPI signal share the same size distribution. An interesting extension of MPI would be to measure the mobility (or binding affinity) of the particles in the imaging volume. In this scenario, particles in certain regions may be partly immobilized by chemical binding, resulting in a transition from a Brownian to a Néel-dominated magnetization behavior – which is generally assumed for MNP tracers in blood. We propose that using two distinct frequencies, one below and one above the Brownian-Néel transition frequency, the binding state of the particles can be determined and utilized in MPI imaging. In this paper, we describe our MPI system and present simulations of 2-dimensional "Mobility MPI".

1 Introduction

Magnetic Particle Imaging (MPI) – since its invention in 2005 [1] – has been recognized as a promising modality for medical imaging with high spatial and temporal resolution. It was demonstrated that MPI is applicable for in-vivo imaging with a clinically approved dose of Resovist – a magnetic nanoparticle tracer [2]. Although the development of MPI scanners has just begun and, at this point, does not reveal the full potential of MPI for real-world applications, it is already apparent that MPI might play a role in molecular imaging scenarios.

The tracer nanoparticles used in MPI, although stable in water, are expected to aggregate in complex media or blood. For some use cases, such as lung ventilation imaging, or research applications aside from the medical aspects of MPI, one would like to measure the mobility of the particles in the volume of interest. Particle mobility goes along with Néel-dominated

T.M. Buzug and J. Borgert (Eds.): Magnetic Particle Imaging, SPPHY 140, pp. 21–25.
springerlink.com

magnetization behavior for immobile particles and Brownian rotational motion for free ones.

2 Magnetic Particle Imaging

Recently, we developed at our institution a 3-dimensional scanner for Magnetic Particle Imaging. The water-cooled coil assembly of the scanner setup is depicted in Fig. 1.

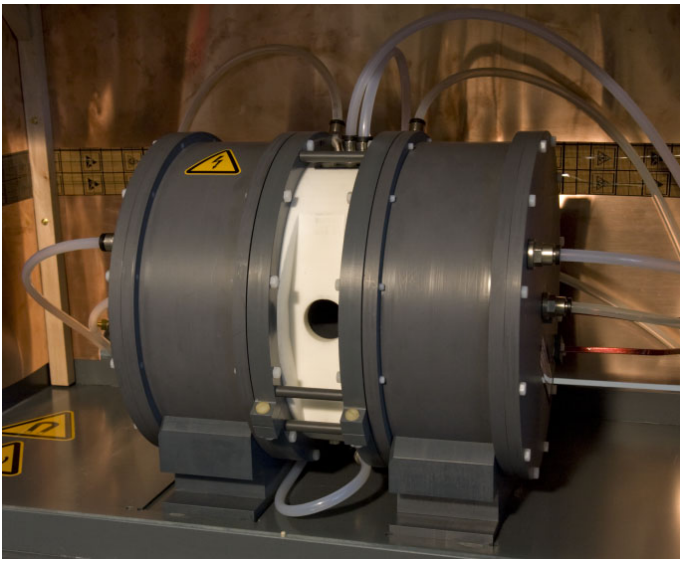

Fig. 1. Photo of 3-dimensional Magnetic Particle Imaging Scanner.

The scanner is constructed around a 30 mm bore – suitable to fit a mouse. The adjustable encoding gradient is created by a combination of NeFeB permanent magnets (3 T/m) and a pair of Maxwell coils (max. 4 T/m) resulting in a maximum field gradient of about 7 T/m. For generating the three orthogonal drive fields, required for 3-dimensional spatial encoding, coils in Helmholtz-type configuration are used on the y- and z- axes, while the x-axis is designed with a single solenoid.

The entire coil system is enclosed in a PVC housing to enable water-cooling of the coils. Along the main axis of the gradient field a maximum field of 60 mT can be generated. On the orthogonal axes 30 mT fields are possible. However, for normal operation of the system a lower drive field amplitude is used, and the maximum field can be composed of an ac field and a dc field offset. All ac signals are generated by a D/A

converter card (NI PCI-6733, 3x 16-bit @ 1 MS/s), amplified by three audio power amplifiers (img StageLine STA-3000, 2x 1.5 kW @ 4 Ohms) and fed into a hybrid series-parallel resonating circuit, which acts as a band-pass filter for the drive field frequencies around 10 kHz. The current revision of the system achieves a spectral purity with THD < 0.002% (> 94 dB_C). Temperature drift of the analog power circuits are monitored with an A/D converter (NI PCIe-6320, 3x 16-bit @ 250 kS/s) correcting current amplitude and phase of each drive field axis separately by adjusting the D/A generated signals appropriately. For detection, three pairs of detection coils close to the surface of the bore are used. The induction signals are passed through a passive, resonating band-stop filter, amplified by a custom build low noise amplifier ($e_n \approx 1.2$ nV/√Hz, bandwidth 1 MHz) and finally digitized by a high-speed A/D converter card (NI PCI-6133, 3x 14-bit @ 2.5 MS/s).

For imaging three orthogonal sinusoidal drive fields are superimposed, forming a Lissajous pattern in the 3-dimensional field of view. Drive field frequencies are selected to be $f_x = 10.4$ kHz, $f_y = 10.0$ kHz and $f_z = 9.6$ kHz. The resulting Lissajous trajectory repeats about every $t_r = 31.2$ ms ($f_r \approx 32$ Hz).

3 Simulation Study

Besides imaging of 2-/3-dimensional distributions of magnetic nanoparticles [1, 2], MPI also has the potential to distinguish between mobile and immobile particles. To investigate the effect of different excitation frequencies on the resulting image, we created a simulation environment of an artificial 2-dimensional MPI system based on the effective field method [3]. We solved the differential equation inserting the Langevin function for equilibrium magnetization and using an effective time constant, composed of the field-dependent Brownian and the Néel relaxation times [4]. Mobile particles are assumed to have a hydrodynamic diameter of 40 nm, increasing to about 90 nm when bound or immobilized. The simulation was performed twice with different drive field frequencies, 1 kHz and 10 kHz. For all simulations, the core diameter of the particles was fixed to $d_c = 25$ nm (without distribution). Figure 3 shows the magnitude of the detection signal dropping for large hydrodynamic diameters. The transition diameter, where the particles switch from Brownian-dominated magnetization behavior (for small/free particles) to Néel relaxation (for large/immobile clusters), strongly depends on the drive field frequency. Driving the system with a higher frequency concludes a shift of the curve towards lower particle sizes.

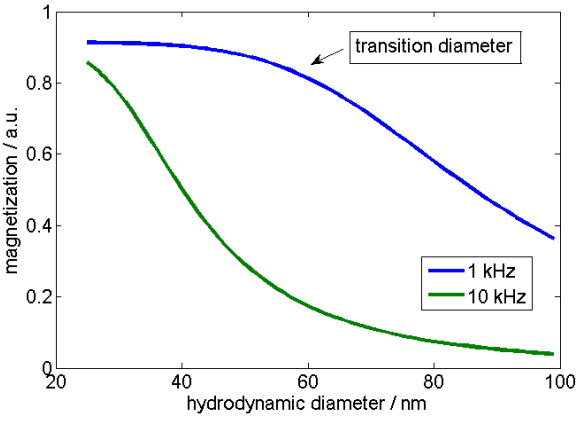

Fig. 3. Magnetization magnitude versus hydrodynamic diameter of the particles for excitation frequencies of 1 kHz (blue) and 10 kHz (green). Transition diameter marks transition from Brownian- to Néel-dominated relaxation.

For high enough excitation frequencies, the particles always respond via Néel relaxation and the hydrodynamic diameter does not play any role. Performing a MPI scan at such frequencies results in an image which directly reflects the particle concentration (Fig. 4(a)). Ideally, the particles are not subject to any Brownian relaxation and the phase is constant over a large frequency range. However, in the phase image (Fig. 4(b)) a strong influence of the particle size is visible because – as can be seen from Fig. 3 – Brownian relaxation is still observed for the smaller particles at 10 kHz.

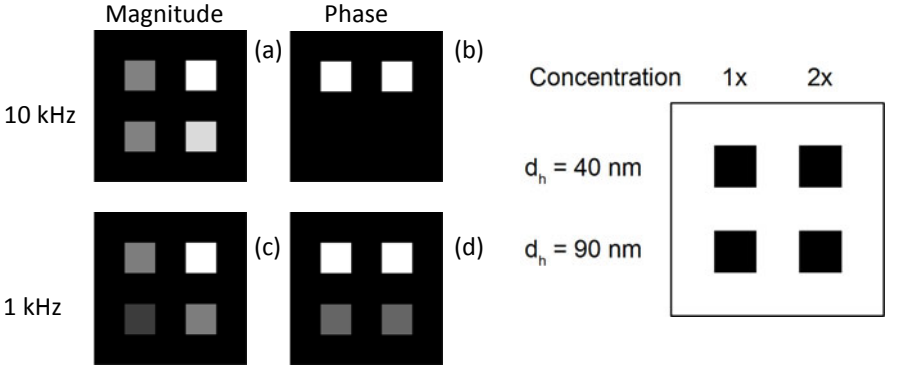

Fig. 4. Simulated images of mobile (40 nm) and immobile (90 nm) particles in a 2-dimensional MPI system for mean drive field frequencies of 1 kHz and 10 kHz

At a second, lower excitation frequency the magnitude image is weighted by particle concentration and particle mobility at the same time (Fig. 4(c)), while the phase image (Fig. 4(d)) is sensitive to the hydrodynamic diameter only.

4 Conclusion

We described the design of our 3-dimensional MPI scanner. The system is constructed to fit a mouse and operates at 10 kHz excitation frequency. To extend the applications of MPI beyond imaging of 2-/3-dimensional nanoparticle distributions, we proposed a 2-step imaging process, where a second drive field frequency is used to explore the mobility of particles in the imaging volume. The additional degree of freedom in the imaging process, introduced by a second imaging frequency, opens the potential for selective contrasts, similar to T1/T2 weighting in MRI. Since optimal contrast is directly connected to the particles time constants, ideally, at least one frequency should be tunable. The high required spectral purity of the excitation signal for imaging remains, however, challenging and the feasibility of this method in a real MPI system has to be investigated.

This work was financially supported by the DFG via SFB 578.

References

1. Gleich, B., Weizenecker, J.: Tomographic imaging using the nonlinear response of magnetic particles. Nature 435, 1214–1217 (2005)
2. Weizenecker, J., Gleich, B., Rahmer, J., Dahnke, H., Borgert, J.: Three-dimensional real-time in vivo magnetic particle imaging. Phys. Med. Biol. 54, L1–L10 (2009)
3. Raikher, Y.L., Shliomis, M.I.: The effective field method in the orientational kinetics of magnetic fluids and liquid crystals. Adv. Chem. Phys. 87, 595–751 (1994)
4. Yoshida, T., Enpuku, K.: Simulation and Quantitative Clarification of AC Susceptibility of Magnetic Fluid in Nonlinear Brownian Relaxation Region. Japan. J. Appl. Phys. 48, 127002 (2009)

System Calibration Unit for Magnetic Particle Imaging: Focus Field Based System Function

Aleksi Halkola[1], Thorsten Buzug[1], Jürgen Rahmer[2], Bernhard Gleich[2], and Claas Bontus[2]

[1] Institute of Medical Engineering, University of Lübeck, Ratzeburger Allee 160, 23562 Lübeck, Germany
halkola@imt.uni-luebeck.de
[2] Philips Technologie GmbH Innovative Technologies, Research Laboratories, Röntgenstraße 24-26, 22335 Hamburg, Germany

Abstract. Magnetic particle imaging usually requires image reconstruction in order to obtain the distribution of the superparamagnetic iron oxide particle concentration from the measured signal. An integral part of the reconstruction is the system function, which relates the superparamagnetic iron oxide distribution to the signal it generates in the MPI scanner. Traditionally, the system function is obtained by measuring the signal generated by a known point-like concentration throughout the imaging volume. This however, requires a robot and is very time consuming. In this contribution we demonstrate a method for estimating the system function using focus fields, which avoids the need for a robot.

1 Introduction

Obtaining an image of the measured magnetic particle imaging (MPI) [2] signal generally requires image reconstruction. This is normally done using a so-called system function (e.g. [3]) that contains the expected signal for a point source for a set of positions within the imaging volume. The image signal can be reconstructed as a weighted linear combination of these system function signals [4]. The system function depends on the magnetic fields used to generate the signal, the properties of the SPIO particles, the characteristics of the receive coils and the receive chain used to process the signal before recording. The system function can be acquired using a small tracer voxel, which is moved with a robot to the positions of interest where the signal can then be measured. This is, however, very time consuming and suffers from low signal to noise ratio. Simulations on the other hand have difficulties to account for particle properties accurately [3].

T.M. Buzug and J. Borgert (Eds.): Magnetic Particle Imaging, SPPHY 140, pp. 27–31.
springerlink.com

2 System Calibration Unit

The idea of a system calibration unit (SCU) is to reproduce the fields seen by the SPIO sample at the positions used for the system function at one fixed position, much like a spectrometer [1]. In an SCU, homogeneous focus fields are used to emulate positional changes. Whereas in an MPI scanner the sample size is limited by the gradient field used to spatially encode the signal, an SCU will have no such limitation. Additionally, highly sensitive receive coils can be used to measure the signal from the stationary sample. The SPIO particle properties will be explicitly accounted for. Thus, an SCU combines the benefits of both a robot based system function and a simulated one.

Alternatively to a dedicated SCU, any MPI scanner with focus fields can be used as an SCU. When using an SCU to estimate the system function for another MPI scanner, it is necessary to account for all aspects of the MPI scanner: all the magnetic fields, receive chain characteristics, etc. In this contribution we demonstrate the use of focus fields for the acquisition of a system function without robot, using the scanner itself as an SCU.

3 Measurements

We will use the preclinical demonstrator (PCD) at Philips Research Laboratory in Hamburg to perform the measurements. The PCD has the disadvantage that the selection field is generated by permanent magnets, which limits the usable sample size and therefore the achievable signal to noise ratio. For this work the gradient field is of no consequence since we only want demonstrate the use of focus fields in the system function measurement while keeping everything else constant for easier comparison.

In the current configuration, the PCD has drive field amplitudes of 13 mT for each x-, y-, and z-axes. With magnetic field gradients of G_x=1.25 T/m/μ_0, G_y=1.25 T/m/μ_0, G_z=2.50 T/m/μ_0, the volume covered by the field free point measures ±8.8 mm, ±8.8 mm, ±4.4 mm. The drive fields are driven at frequencies 24038 Hz, 26041 Hz and 25252 Hz, respectively. This combination of frequencies defines a closed Lissajous path for the field free point with a period of 21.5424 ms. The SPIO sample is a cylinder 2 mm in length, with a diameter of 1 mm, filled with pure Resovist [5].

We first measure a reference system function using a robot. The robot is moved on a regular grid about the field free point between ±16.2 mm in the x- and y-directions in 14 steps and ±9.5 mm in the z-direction in 10 steps. The system function covers a larger volume than the Lissajous path in order to include any signal from SPIO particles close to the Lissajous path that can contribute significantly to the lower harmonics. In order to later subtract the background signal from the measurements we also measure the signal without the sample after every 10 robot positions. Together with the background measurements we have a total of 2945 measurement

positions. At each position we measure the average signal from 20 Lissajous periods. For the background positions we measure 100 periods. The total time of the measurement was 1 hour.

For the focus field based system function we first measure the selection field within the bore of the PCD using a Hall sensor. This is necessary in order to know the selection field strengths at the positions of the robot-based system function. The sample is placed at the centre of the scanner. Since the sample stays in the same place during the measurements, it is necessary to know the focus fields only there. The focus fields as functions of focus coil currents at the centre of the scanner are also measured using a Hall sensor. The system function measurement with the focus fields is performed analogously to the robot-based measurement with the exception that instead of moving the sample, we move the field free point by setting the focus field currents appropriately. The measurement took less than 40 minutes to complete.

4 Results

In Fig. 1 we show the norms of the spectra measured for the x channel for the robot-based (top) and focus field-based (bottom) system matrices. The spectra show the norm over all system function positions after background subtraction.

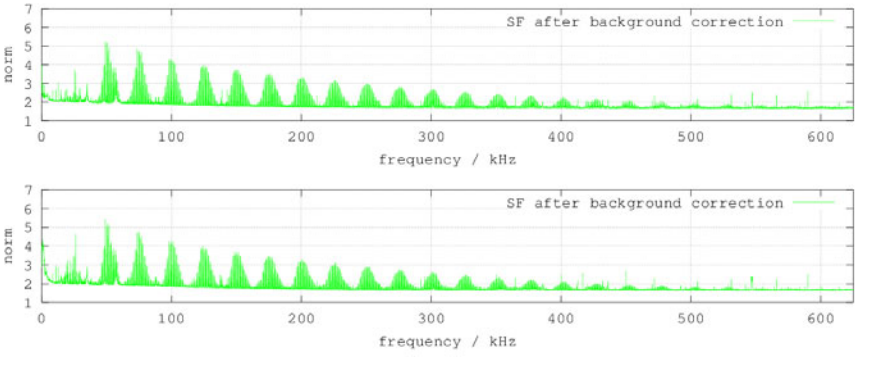

Fig. 1. The signal spectra for robot (top) and focus field (bottom) based system matrices for the x channel. The panels show the spectra after background subtraction.

In order to compare the spatial similarities between the two system matrices we show the real part of one spectral component of the system function in 3 slices in x-, y-, and z-planes in Fig. 2. The slight offset between the two system functions is due to an offset in the field free point position. Both system matrices show the same patterns.

Fig. 3 shows the reconstruction of a phantom for the two system matrices. The simple images show good resemblance.

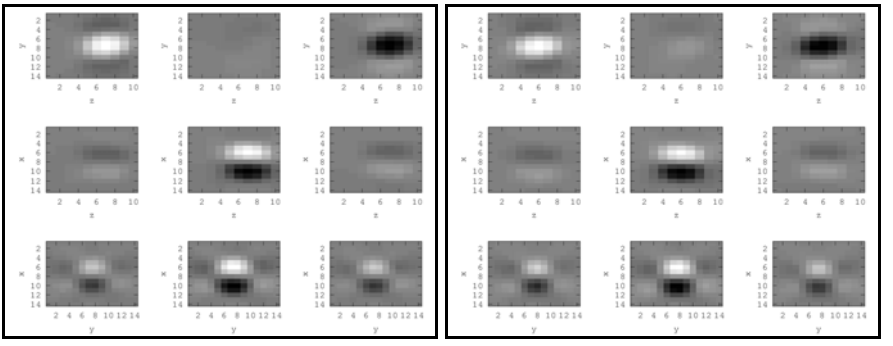

Fig. 2. The spatial pattern of one spectral component for the robot (left) and focus field (right) based system matrices for the x channel. The axis units are positions with in the measurement volume. The grey scale levels used for all the panels are the same.

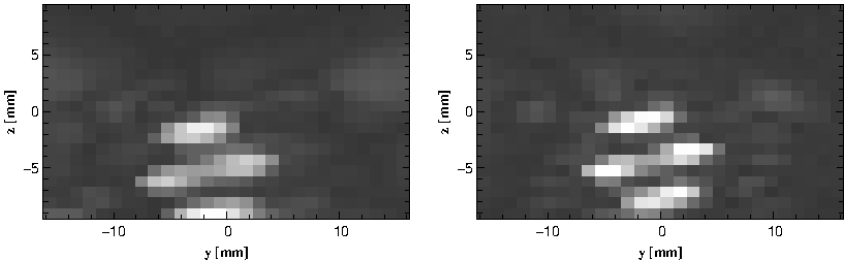

Fig. 3. The reconstructed images for robot (left) and focus field (right) based system matrices. The grey scale levels used for the two panels are the same.

5 Discussion

As Figs. 1, 2, and 3 show, the system function can be accurately estimated using a static sample while applying appropriate focus fields instead of moving the sample with a robot. The system function here is measured only within a relatively small volume at the centre of the bore where the magnetic fields are homogeneous. At the edges of the imaging volume where field inhomogeneities become significant the focus field based approach might not work as well. In the setup used in this contribution, the use of focus fields provides a factor of 1.5 timesaving over the robot-based system function. In a dedicated SCU with a larger sample and optimised receive coils we expect to gain at least an order of magnitude in signal to noise which will enable further time savings.

6 Conclusion

We have shown that a focus field based system function can be successfully used for the image reconstruction of an MPI scanner signal. This is the first step in our effort to realise an SCU that can be used for a fast acquisition of a high signal to noise system function for any MPI scanner.

Acknowledgement. The authors acknowledge funding by the German Federal Ministry of Education and Research (BMBF) under the grant numbers FKZ 13N9079 and FKZ 13N11086.

References

1. Biederer, S., Sattel, T.F., Knopp, T., Lüdtke-Buzug, K., Gleich, B., Weizenecker, J., Borgert, J., Buzug, T.M.: A Spectrometer for Magnetic Particle Imaging. In: Vander Sloten, J., Verdonck, P., Nyssen, M., Haueisen, J. (eds.) ECIFMBE 2008. IFMBE, vol. 22, pp. 2313–2316. Springer, Heidelberg (2008)
2. Gleich, B., Weizenecker, J.: Tomographic imaging using the nonlinear response of magnetic particles. Nature 435, 1214–1217 (2005)
3. Knopp, T., Sattel, T., Biederer, S., Rahmer, J., Weizenecker, J., Gleich, B., Borgert, J., Buzug, T.M.: Model-Based Reconstruction for Magnetic Particle Imaging. IEEE Trans. Med. Imag. 29(1), 12–28 (2010)
4. Knopp, T., Rahmer, J., Sattel, T.F., Biederer, S., Weizenecker, J., Gleich, B., Borgert, J., Buzug, T.M.: Weighted iterative reconstruction for magnetic particle imaging. Physics in Medicine and Biology 55, 1577–1589 (2010)
5. Lawaczeck, R., Bauer, H., Frenzel, T., Hasegawa, M., Ito, Y., Kito, K., Miwa, N., Tsutsui, H., Vogler, H., Weinmann, H.: Magnetic iron oxide particles coated with carboxydextran for parenteral administration and liver contrasting. Pre-clinical profile of SH U555A. Acta Radiologica 38(4) Pt. 1, 584–597 (1997)
6. Rahmer, J., Weizenecker, J., Gleich, B., Borgert, J.: Signal encoding in magnetic particle imaging: properties of the system function. BMC Medical Imaging 9, 4 (2009)

Spectroscopy

Characterization of Magnetic Nanoparticles for Magnetic Particle Imaging by Magnetorelaxometry, AC Susceptibility, Magnetic Particle Spectroscopy and Static Magnetization Measurements

Frank Ludwig, Thilo Wawrzik, and Meinhard Schilling

Institut für Elektrische Messtechnik und Grundlagen der Elektrotechnik,
TU Braunschweig, Hans-Sommer-Str. 66, 38106 Braunschweig, Germany
f.ludwig@tu-bs.de

Abstract. To investigate various magnetic nanoparticle samples for their suitability as markers for Magnetic Particle Imaging (MPI), various magnetic techniques can be applied. Whereas Magnetic Particle Spectroscopy (MPS) directly provides the harmonic spectrum for a given excitation frequency and ac field amplitude, for the design of optimal markers, it is important to relate the measured harmonic spectra to specific nanoparticle properties. We have applied fluxgate magnetorelaxometry (MRX), ac susceptibility (ACS) up to 1 MHz, multivariate MPS - varying the excitation field amplitude and frequency as well as the magnitude of a superimposed dc field - and static magnetization measurements for the comprehensive characterization of representative magnetic nanoparticle samples. To distinguish between core and hydrodynamic properties, aqueous suspensions as well as immobilized samples were investigated.

1 Introduction

The wide-spread application of magnetic particle imaging (MPI) is tightly connected with the availability of optimum magnetic markers. A direct method to study the harmonic response of magnetic nanoparticles (MNP) to a sinusoidal excitation field is magnetic particle spectroscopy (MPS). In the basic version of a MPS measurement, a sinusoidal magnetic field of sufficiently large amplitude and frequency f_{exc} is exposed to the MNP sample and the harmonic spectrum is measured reflecting the nonlinear properties of the magnetization curve [1]. Naively, one would thus expect that MNP with core diameters of > 25 nm are most suitable since not too high magnetic fields of the order of 20 mT are sufficient to drive them into

T.M. Buzug and J. Borgert (Eds.): Magnetic Particle Imaging, SPPHY 140, pp. 35–40.
springerlink.com

saturation and thus to produce harmonics. Figure 1 depicts MPS spectra of single-core MNP suspensions from Ocean Nanotech with 15 nm and 25 nm core diameter. As expected, sample SHP-25 shows considerably more harmonics. Also displayed is the harmonic spectrum of Resovist. Although the individual iron oxide particles of Resovist are known to have diameters of the order of 5-6 nm, a rich harmonic spectrum is measured.

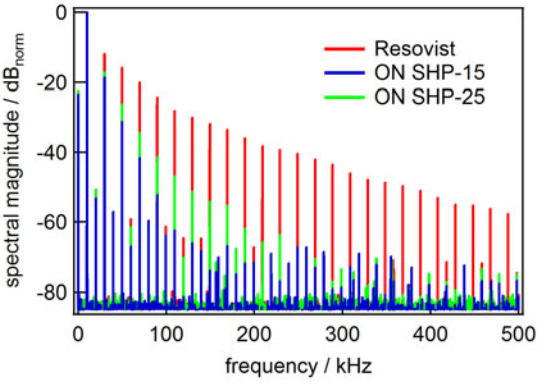

Fig. 1. MPS spectra measured on Resovist as well as on suspensions of SHP-15 and SHP-25 from Ocean Nanotech. All spectra are normalized to their 3f magnitudes.

Another important point that has to be taken into account for the realization of MPI is the MNP dynamics. With regard to a high detection signal and a high spatial and temporal resolution, a high excitation frequency would be desirable. On the other hand, the MNP must be able to follow the excitation field. However, the larger the particle core, the higher is the characteristic time constant of the particles (the Brownian time constant τ_B is proportional to the hydrodynamic volume V_h and the Néel time constants τ_N scales with $\exp(K \cdot V_c/(k_B \cdot T)$ where V_c is the core volume and K the anisotropy constant). Consequently, the requirements of large magnetic cores/magnetic moments and small relaxation times apparently contradict each other. Thus, to understand why Resovist exhibits such a rich harmonic spectrum despite the comparably small magnetic cores and to finally optimize MNP for MPI, various magnetic techniques have to be combined to get a self-consistent picture.

Another important issue in this context is whether the MNP are mobile or immobilized (e.g, bound to cells). In the former case, the Brownian relaxation dynamics have to be considered whereas in the latter one the Néel relaxation must be accounted for.

2 Magnetic Methods

Magnetic Particle Spectroscopy

The most direct technique for the characterization of MNP for MPI is magnetic particle spectroscopy (MPS) [1,2]. The detection signal is preferably recorded using a gradiometric detection coil. Since the ac field amplitude is large enough to cover the nonlinear magnetization range of the MNP, the detection signal contains higher harmonics which are characteristic for the specific magnetization curve. Most MPS systems operate at a fixed excitation frequency and amplitude. It is, however, important that the MNP dynamics are taken into account. To account for the particle dynamics of a MNP suspension, the Langevin function and the Debye model can simply be combined [3] using an effective, excitation field amplitude dependent Brownian time constant τ_{Beff} which was derived by Yoshida and Enpuku [4]. So far, no adequate solution has been proposed for the Néel mechanism. This frequency dependence of the harmonics spectrum has, however, so far been experimentally studied only by Wawrzik et al. [2]. In addition to finding the optimum excitation frequency for a given MNP sample, the variation of the excitation frequency in MPS allows one to determine both the core and the hydrodynamics size distributions of the MNP [2].

For MPI applications where the MNP are immobilized, MPS measurements have to be performed on immobilized samples. MNPs which were optimized for liquid-phases MPI applications are not necessarily optimal for applications where they are immobilized [5].

For an absolute comparison of the MPI performance of various MNP samples it is not sufficient to just compare the number of harmonics but the harmonic spectra should be normalized to the same iron content.

Static Magnetization Measurements

A standard technique for the characterization of MNP is the measurement of static *M-H* curves, e.g., using a SQUID Magnetic Property Measurement System (MPMS). This system allows one to study the sample's magnetic moment in fields up to a few Tesla. The magnetization of a suspension of magnetic nanoparticles is generally described by the Langevin function. If a distribution of magnetic moments (or core sizes) is present, one has to integrate over their distribution f(m) which is generally assumed to be log-normal. Importantly, all MNP contribute to the signal proposed that the maximum magnetic field is sufficiently large. Consequently the analysis of static *M-H* curves measured on MNP suspensions allows one to determine the distribution of magnetic moments f(m). The *M-H* curve can be analyzed either by assuming a certain function for f(m) (e.g., a bimodal distribution [6]) or by applying the SVD technique [7,8].

Quite often, *M-H* measurements are also performed on reference samples with immobilized nanoparticles. In contrast to a suspension, immobilized particles can only align with the external field by a rotation of the

internal magnetization vector. Thus, in addition to the magnetic $m \cdot B$ and the thermal energy $k_B T$, the anisotropy energy $K \cdot V_c$ comes into play causing that the *M-H* curves of mobile and immobilized MNP samples generally differ. Although the anisotropy energy barrier is of importance when considering the relaxation time constants of immobile MNP, the analysis of *M-H* curves of immobilized MNP samples is quite complicated since it includes the saturation magnetization M_s, anisotropy constant K as well as the core size and shape of each individual nanoparticle. The situation considerably simplifies if fixed values for M_s and K as well as spherical particle core shape are assumed.

AC Susceptibility

Another widely used magnetic technique for the characterization of magnetic nanoparticles is the measurement of the complex (ac) susceptibility (ACS). In an ACS measurement, a sinusoidal field of constant amplitude is applied and the frequency is swept. In contrast to MPS, excitation amplitudes are in the linear range. From the in-phase and out-of-phase signal of two antiserially connected detection coils – one being filled with the sample -, real and imaginary parts of the susceptibility can be determined. The basic model for the analysis is the Debye model [9] providing equations for real χ' and imaginary part χ'' of the susceptibility. For monodisperse nanoparticles samples, the imaginary part is maximum for $\omega \cdot \tau_{eff} = 1$ where τ_{eff} is the effective time constant given by $\tau_{eff} = \tau_B \tau_N / (\tau_B + \tau_N)$.

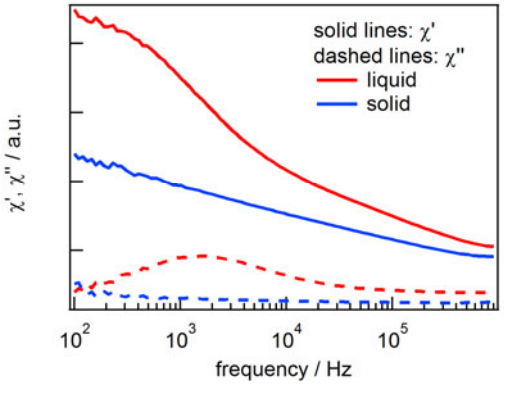

Fig. 2. ACS spectra measured on Resovist suspension and immobilized reference sample.

If multidispersity is taken into account, the Debye model generalizes correspondingly [10]. Figure 2 depicts the susceptibility spectra measured on a Resovist suspension and on an immobilized reference sample. As can be seen the imaginary part of the suspension exhibits a pronounced maximum at 1.6 kHz which is caused by the Brownian relaxation of particles having a

mean hydrodynamic diameter of 58 nm. In contrast, the imaginary part of the immobilized sample is close to zero and flat for frequencies up to 1 MHz. At an excitation frequency of 25 kHz, the real part amounts to less than 50% compared to the dc value.

For MPI applications where the MNP are immobilized e.g., or by binding to cells, only the Néel relaxation is of importance. As the blue curves in Fig. 2 show, real and imaginary parts of the immobilized Resovist sample are considerably lower than those of the suspension. Both the constant, but non-zero imaginary and the real part which decays proportionally to ln(f) indicate a uniform distribution of Néel time constants and thus anisotropy energies $\Delta E = K \cdot V_c$ [8]. The lower limit of the uniform distribution is given by the maximum excitation frequency (1 MHz in this case) whereas the upper limit can be estimated from an extrapolation to the χ_0 value of the suspension (all particle moments can follow the excitation field).

Magnetorelaxometry

In magnetorelaxometry (MRX) the magnetic moments of the MNP are aligned by an external magnetic field pulse with an amplitude of a few mT and a duration of 1-2 s. After abruptly switching off the magnetizing magnetic field, the decay of the magnetic signal is measured with highly sensitive magnetic field sensors (either SQUIDs or fluxgates). The decay is determined by the characteristic time constants τ_{eff} of the MNP analogously to ac susceptibility measurements. For the analysis of the MRX signal of multidisperse MNP, the so called moment superposition model can be applied [11,12]. For immobilized samples, the characteristic time constant is given by the Néel time constant, reflecting the anisotropy barrier. Whereas an ACS measurement on an immobilized sample can be used to reconstruct the $f(\Delta E) \cdot m^2$ distribution versus energy barriers ΔE (f is the number distribution) [8], from MRX the $f(\Delta E) \cdot m$ distribution can be obtained. A main advantage of MRX is that MNP with rather long relaxation times are accessible whereas the ACS measurement is more suited in the high-frequency range.

3 Discussion and Conclusion

The various magnetic methods applied to either MNP suspensions or immobilized MNP provide different information on MNP properties. Whereas the distribution of magnetic moments can be obtained from static M-H measurements, information on the dynamic properties is provided by ACS or MRX measurements. Whereas measurements on immobilized samples allow the determination of the anisotropy barrier distribution which is of importance for applications where the markers are immobile, e.g., bound to cells, measurements on suspensions provide the distribution of hydrodynamic sizes. Since the harmonic spectra of mobile and immobilized MNP are deter-

mined by the Néel and Brownian mechanism, respectively, optimum markers must not necessarily be the same for all MPI applications [5]. The main challenge that remains to be solved is to relate the obtained distribution of magnetic moments or particle sizes to the distribution of time constants and thus to identify optimum markers for MPI. The self-consistency of the obtained picture can be proven by MPS measurements performed for different excitation frequencies and their theoretical modeling using the distributions obtained from other magnetic measurements.

This work was financially supported by the DFG via SFB 578.

References

1. Biederer, S., et al.: Magnetization response spectroscopy of superparamagnetic nanoparticles for magnetic particle imaging. J. Phys. D: Appl. Phys. 42, 205007 (2009)
2. Wawrzik, T., et al.: Multivariate magnetic particle spectroscopy for magnetic nanoparticle characterization. In: Proc. of AIP Conf., vol. 1311, pp. 267–270 (2010)
3. Ferguson, R.M., et al.: Optimization of nanoparticle core size for magnetic particle imaging. J. Magn.Magn. Mater. 321, 1548–1551 (2009)
4. Yoshida, T., Enpuku, K.: Simulation and quantitative clarification of ac susceptibility of magnetic fluid in nonlinear Brownian relaxation region. Japan. J. Appl. Phys. 48, 127002 (2009)
5. Gehrke, N., Briel, A., Ludwig, F., Remmer, H., Wawrzik, T., Wellert, S.: New Perspectives for MPI: A Toolbox for Tracer Research. In: Buzug, T.M., Borgert, J. (eds.) Magnetic Particle Imaging. SPPHY, vol. 140, pp. 99–103. Springer, Heidelberg (2012)
6. Eberbeck, D., et al.: How the size distribution of magnetic nanoparticles determines their magnetic particle imaging performance. Appl. Phys. Lett. 98, 182502 (2010)
7. Berkov, D.V., et al.: New method for the determination of the particle magnetic moment distribution in a ferrofluid. J. Phys. D 33, 331–337 (2000)
8. Yoshida, T., Enpuku, K., Ludwig, F., Dieckhoff, J., Wawrzik, T., Lak, A., Schilling, M.: Characterization of Resovist® Nanoparticles for Magnetic Particle Imaging. In: Buzug, T.M., Borgert, J. (eds.) Magnetic Particle Imaging. SPPHY, vol. 140, pp. 3–7. Springer, Heidelberg (2012)
9. Debye, P.: Polar Molecules. Chemical Catalog Company, New York (1929)
10. Ludwig, F.: Characterization of magnetic core-shell nanoparticle suspensions using ac susceptibility for frequencies up to 1 MHz. In: Proc. of AIP Conf., vol. 1311, p. 249 (2010)
11. Eberbeck, D., et al.: Aggregation behaviour of magnetic nanoparticlesuspensions investigated by magnetorelaxometry. J. Phys. Condens. Matter 18, S2829 (2006)
12. Ludwig, F., et al.: Characterization of superparamagnetic Fe_3O_4 nanoparticles by fluxgate magnetorelaxometry for use in biomedical applications. J. Appl. Phys. 103, 07A314 (2008)

Perspectives of Magnetic Particle Spectroscopy for Magnetic Nanoparticle Characterization

Thilo Wawrzik, Meinhard Schilling, and Frank Ludwig

Institut für Elektrische Messtechnik und Grundlagen der Elektrotechnik,
TU Braunschweig, Hans-Sommer-Str. 66, 38106 Braunschweig, Germany
t.wawrzik@tu-braunschweig.de

Abstract. Magnetic Particle Spectroscopy (MPS) has been used to estimate the performance of magnetic nanoparticles for Magnetic Particle Imaging. It was demonstrated that one can reconstruct the particles core size distribution from the measured MPS spectrum. However, using MPS as an analytical instrument for the characterization of magnetic nanoparticle samples includes systematic errors. First, previous reports on MPS-based core size estimation only take the Néel process of the relaxation into account. However, other methods, e.g. ac susceptometry, show that for excitation frequencies in the lower kilohertz regime the Brownian magnetization process also plays an important role. We developed an extended MPS setup that enables parameter measurements of the harmonics, depending on the amplitude and frequency of the excitation signal and the amplitude of a static offset field. Based on a dynamic magnetization model, we utilize a multi-variate fitting routine to describe the sample's core size and hydrodynamic size distribution. Second, existing implementations assume mono-modal log-normal distributions of core sizes, which cannot be guaranteed to match the actual size distribution of the sample. For that reason, we also use a regularized singular value decomposition (SVD) based method for reconstructing arbitrary core size distributions from the harmonic spectrum.

1 Introduction

Magnetic Particle Spectroscopy (MPS) has been developed as a supporting method for evaluating the properties of magnetic nanoparticle (MNP) tracers for Magnetic Particle Imaging (MPI) [1]. It was demonstrated that one can reconstruct the core size distribution of such tracers from the measured harmonic spectrum [2]. For that purpose, the sample is generally exposed to an oscillating excitation field of sufficiently high field strength to drive the particles into saturation or at least into the non-linear range of

T.M. Buzug and J. Borgert (Eds.): Magnetic Particle Imaging, SPPHY 140, pp. 41–45.
springerlink.com

the magnetization curve. The magnetization response is then picked up by an induction coil and transformed into frequency space to get the harmonic spectrum. For estimating the core size distribution, a least-squares method, such as Levenberg-Marquardt, is used with a particle model based on the Langevin function of superparamagnetism and assuming a log-normal distribution of core sizes. Such assumption creates a systematic error since neither the measurement accounts for deviations from the log-normal distribution nor does it include the Brownian rotational motion of the MNP. For that reason, we extended our MPS measuring system and the algorithms for evaluation.

2 Multivariate MPS

Our extended Magnetic Particle Spectrometer enables parametric measurement of the harmonic spectrum depending on the amplitude and frequency of the excitation field and an additionally applied static offset field. In the current setup the excitation signal, generated by an arbitrary waveform generator (Tektronics AFG-310), is amplified with an standard audio power amplifier and fed into a resonating circuit which is tuned to the excitation frequency to reduce the harmonic distortion. The excitation coil is constructed as an elongated solenoid and the pair of gradiometric detection coils is aligned on its center line. Due to the anti-serial configuration of the coils, it avoids the direct coupling of the excitation signal into the detection chain and therefore removes the need for a band-stop filter before the signal is amplified and digitized (NI PCI-6133). The excitation field can be varied from 0-25 mT in amplitude and the frequency can be selected from a discrete set of six different frequencies (496 Hz, 1.30 kHz, 2.11 kHz, 3.85 kHz, 6.43 kHz, 9.96 kHz). A dc offset field can be applied serially or perpendicularly to the excitation field at a flux density between 0 and 30 mT.

From a measured multi-dimensional dataset, which enfolds the dependence of the harmonic spectrum on the three parameters (excitation field amplitude and frequency, dc field amplitude), a multi-variate fitting algorithm based on standard least-squares approximation can be utilized for reconstructing the core and hydrodynamic size distribution of the magnetic nanoparticle sample.

The forward model includes the Néel and Brownian magnetization response as well as the field-dependence of the corresponding relaxation time constants. Figure 1 shows the first three odd harmonics from the spectra measured for four different excitation frequencies on a suspension of SHP-25 MNP from Ocean Nanotech.

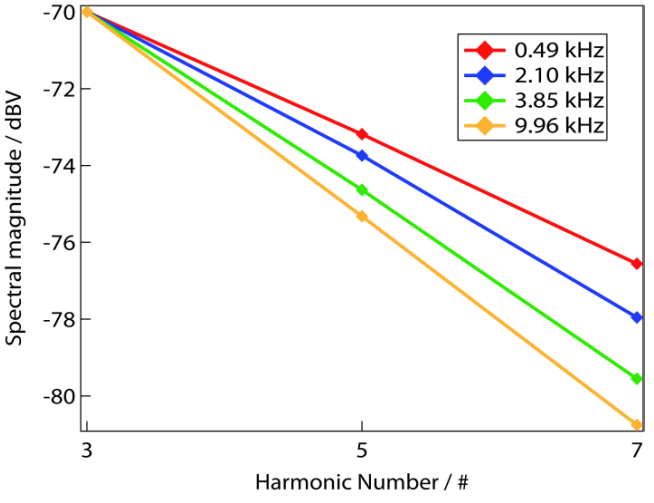

Fig. 1. Spectral magnitude vs. harmonic number measured on SHP-25 suspension from Ocean Nanotech for four different excitation frequencies.

Apparently, the slope of the harmonic decay differs for the different applied frequencies. This can be explained by the different "portion" of particles from the size distribution contributing to the signal. For small excitation frequencies – below the characteristic frequency or inverse of the relaxation time constant – all particles in the sample contribute to the spectrum. For higher frequencies, only the smaller particles in the sample relax fast enough to follow the excitation signal, which leads to a phase shift in the spectrum and a faster decay of the harmonics, since small particles require a higher field to reach saturation.

For the other parameters, i.e., the amplitude of the excitation signal and the field strength of the offset field, one can find similar dependencies. The dc field modulates the harmonic response – reflecting the most non-linear field range of the magnetization curve – and it allows one to simulate positions of the sample along the encoding gradient in a Magnetic Particle Imaging system, resulting in a system matrix of a 1-dimensional MPI scanner [3].

3 SVD-Based Reconstruction

One limitation of previously reported least-squares methods is the fact that they always assume a log-normal distribution of particle sizes. For making the transition from a pre-defined distribution function to an arbitrary shaped distribution, which also includes bi- or multi-model size distributions, we utilize a SVD-based algorithm for reconstruction. SVD (singular value decomposition) allows us to estimate the contribution of N discrete particle sizes to the measured spectrum. For a good estimation, the number of size bins N to be extracted is limited by the number of harmonics M, which

are observed in the harmonic spectrum, and the variance and noise of the measurement. Typically, we observe more than 50 harmonics for a concentrated sample so that a discrete size distribution with about 40 sizes can be found.

To proof the concept of a SVD-based reconstruction of the particle size distribution, Fig. 2 shows a comparison of standard Levenberg-Marquardt (LM) estimation – as described in the previous section – with a discrete distribution obtained from SVD. As can be seen, the bimodality of the original size distribution is not visible from the LM fit, whereas it is most evident in the SVD reconstruction. However, for poor data, with less harmonics visible or high data variance or noise, a LM fit gives more stable results. Here, the absolute deviation of the SVD fitted spectrum and the model-given harmonics is mostly determined by the bigger particles leading to a over-representation of the right peak in SVD reconstruction.

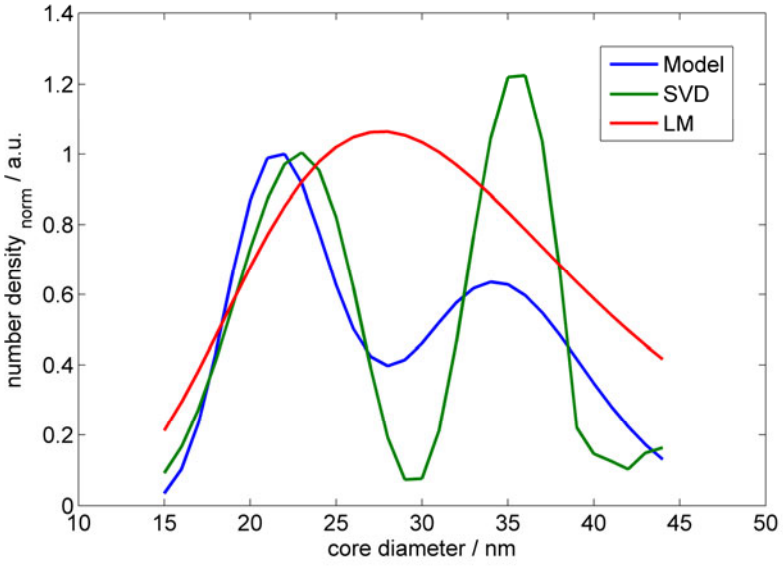

Fig. 2. Comparison of modeled core size distribution (blue) fitted by standard Levenberg-Marquardt algorithm (red) and from SVD-based reconstruction (green).

4 Conclusion

In this paper, two major extensions to previous reports on Magnetic Particle Spectroscopy were presented. With a multi-variate dataset, obtained by measuring the harmonic spectrum in dependence of the excitation field amplitude and frequency and a dc offset field, it is possible to estimate not only the core size distribution but also the hydrodynamic size distribution of the measured nanoparticle sample. For multi-modal size distributions,

as observed especially for multi-core particles, such as Resovist [4], it is also advantageous to use a SVD-based algorithm for reconstruction, since it does not require any prior-knowledge, i.e., assuming a log-normal distribution of core sizes, to be inserted into the algorithms.

This work was financially supported by the DFG via SFB 578.

References

1. Gleich, B., Weizenecker, J.: Tomographic imaging using the nonlinear response of magnetic particles. Nature 435, 1214–1217 (2005)
2. Biederer, S., Knopp, T., Sattel, T.F., Lüdtke-Buzug, K., Gleich, B., Weizenecker, J., Borgert, J., Buzug, T.M.: Magnetization response spectroscopy of superparamagnetic nanoparticles for magnetic particle imaging. J. Phys. D: Appl. Phys. 42, 205007 (2009)
3. Wawrzik, T., Hahn, J., Ludwig, F., Schilling, M.: Magnetic particle spectroscopy for the evaluation of field-dependent harmonics generation. In: Magnetic Nanoparticles: Particle Science, Imaging Technology, and Clinical Applications, pp. 86–91. World Scientific Publishing Company (2010)
4. Yoshida, T., Enpuku, K., Ludwig, F., Dieckhoff, J., Wawrzik, T., Lak, A., Schilling, M.: Characterization of Resovist® Nanoparticles for Magnetic Particle Imaging. In: Buzug, T.M., Borgert, J. (eds.) Magnetic Particle Imaging. SPPHY, vol. 140, pp. 3–7. Springer, Heidelberg (2012)

Initial MPS Response of Adsorptively-Coated Fluorescent Iron Oxide Nanoparticles

Jabadurai Jayapaul[1], Daniel Truhn[1], Fabian Kiessling[1], Kerstin Lüdtke-Buzug[2], and Thorsten M. Buzug[2]

[1] Institute of Experimental Molecular Imaging, RWTH Aachen University
Pauwelsstrasse 30, Aachen, 52074, Germany
fkiessling@ukaachen.de
[2] Institute of Medical Engineering, University of Luebeck
Ratzeburger Allee 160, Luebeck, 23562, Germany
luedtke-buzug@imt.uni-luebeck.de

Abstract. The search for optimal nanoparticles for magnetic particle imaging (MPI) has been receiving much attention. Currently, Resovist® an iron oxide nanoparticle-based MR contrast agent is considered as the gold standard for MPS and MPI measurements. In this paper, we evaluate the initial MPS response of iron oxide-based nanoparticle systems with variation in core size and coating. In this context, we synthesized iron oxide nanoparticles with different core sizes (5 and 10 nm) by employing co-preciptiation method. Further, these iron cores were adsorptively coated with endogenous fluorophores (flavin analogues: FMN, FAD) to increase their stability and to enhance MR contrast. We have performed initial experiments on these particles in a magnetic particle spectrometer. Their spectrum of higher harmonics was obtained and found to fall off more rapidly than Resovist®. No difference in magnetic behavior was seen between particles with different coatings.

1 Introduction

We have recently developed adsorptively coated fluorescent iron oxide nanoparticles (FLUSPIO) using endogenous flavin analogues (flavin mononucleotide - FMN) and have demonstrated their potential as versatile molecular MR probes for targeting the riboflavin carrier protein (RCP) [1]. These FMN decorated nanoparticles displayed high MR relaxivity (r2) congruent to Resovist®.

MPI was developed as a sensitive method for detecting superparamagnetic iron oxide (SPIO) nanoparticles in vivo [2]. In comparison to MRI, the sensitivity for iron oxide nanoparticle detection in MPI is hoped to be

T.M. Buzug and J. Borgert (Eds.): Magnetic Particle Imaging, SPPHY 140, pp. 47–52.
springerlink.com

higher by a factor of 100 or more. In order to gain more insights about the behavior of FLUSPIO with different core size in MPI, we performed initial experiments with a magnetic particle spectrometer (MPS). Additionally, we evaluated flavin adenine dinucleotide (FAD) adsorptively coated fluorescent nanoparticles (FAD USPIO) with different core sizes in order to check the influence of size and coating molecules on the magnetic response of the particles in MPS.

2 Material and Methods

2.1 Synthesis of USPIO

Ultrasmall Superparamagnetic Iron Oxide nanoparticles (USPIO) were synthesized by co-precipitation of ferrous (Fe^{2+}) and ferric (Fe^{3+}) salts in aqueous alkaline conditions. A modified one-pot synthesis protocol was followed [3]. We used a stoichiometric ratio of $2Fe^{3+}$:Fe^{2+}, 16 mmol (2.66 g) of $FeCl_3$ and 8 mmol (1.63 g) of $FeCl_2.4H_2O$ which was dissolved in 190 mL de-ionized water at room temperature by magnetic stirring. Further, 10 mL of 25% NH_3 was poured down the vortex of the iron solution to form a black precipitate. After stirring for 20 min, the particles were retrieved with a magnet and washed thrice with water and twice with 0.1 M HCl solution. Magnetic fluids were dispersed in 100 mL (0.1 M HCl). The USPIO were further sonicated and centrifuged in order to remove aggregates. The total iron concentration of USPIO (5 nm) determined by titrimetry [4] and colorimetry (tiron method) [5] was 161 mM. USPIO (10 nm) were generated by short reaction time (10 min stirring) and by following analogous synthetic steps to that of 5 nm USPIO.

2.2 Synthesis of Fluorescent Nanoparticles

Fluorescent Ultrasmall Superparamagnetic Iron Oxide nanoparticles (FLUSPIO) were synthesized by coating iron oxide cores with simple organic molecules (non-polymeric coating) [6]. To achieve the coating, 35 mM of flavin mononucleotide (FMN) was sonicated (Ultrasonic cleaner, 30 W, VWR GmbH, Germany) with 143 mM USPIO for 1 h at ambient temperature. Excess FMN was removed by high-gradient magnetophoresis. Further, FMN modified particles were further sonicated with 50 mM guanosine monophosphate (GMP) similar to the FMN coating. The particles were purified further by employing high gradient magnetophoresis to yield FLUSPIO. Flavin adenine dinucleotide (FAD)-coated USPIO were synthesized analogous to FLUSPIO generation respectively.

2.3 Characterization of Fluorescent Nanoparticles

The core diameter and surface morphology of the FLUSPIO were evaluated using TEM techniques. The relaxivity and MR-contrast enhancement

properties of FLUSPIO were determined using MRI. The fluorescence intensity of FLUSPIO was studied using fluorescence spectroscopy.

2.4 In Vitro Evaluation of Fluorescent Nanoparticles

The biocompatibility of FLUSPIO was evaluated using different cell viability assays (Trypan blue staining and TUNEL assay). In vitro labeling of cancer cells (PC-3, DU-145, LnCap) and activated endothelial cells (HUVEC) by FLUSPIO was evaluated using MRI and fluorescence microscopy. The specific uptake of FLUSPIO mediated by RCP was investigated using MRI.

2.5 Magnetic Particle Spectroscopy of Fluorescent Nanoparticles

The suitability of the particles for magnetic particle imaging was investigated using a magnetic particle spectrometer (MPS) [7]. The MPS was built at the Institute of Medical Engineering, University of Lübeck. The MPS consists of two equivalent coil systems. To generate an almost homogenous magnetic field, two circular transmit coils are mounted in Helmholtz configuration with a distance of 9 mm. Their outer diameter is 58 mm, their inner diameter is 19 mm and their height is 6 mm. The signal is received by a solenoid coil; its self-resonance is above 2.5 MHz and its dimensions are specified by the inner diameter of 10 mm and its length of 7 mm. The generated field strengths oscillate with a frequency of 25 kHz and a maximum field strength of 40 mT / μ_0.

3 Results

USPIO nanoparticles prepared by co-precipitation were coated with FMN, which strongly binds to the iron oxide cores via phosphate groups. The fluorescent coating was achieved in aqueous solutions of USPIO and FMN (at pH 4) under sonication at ambient temperature. The coating of USPIO with FMN alone did not lead to an efficient and stable coverage of the entire nanoparticle surface, which might be due to steric hindrance caused by the isoalloxazine ring of FMN. Additionally, the nanoparticle surface should not be covered entirely with FMN due to the quenching of green fluorescence that occurs at high concentrations. GMP is less bulky and contains a phosphate group (similar to that of FMN), which strongly chemisorbs to the iron oxide surface during the non-polymeric coating. Both, FMN and GMP are negatively charged molecules and their binding to USPIO results in a negative surface charge of FLUSPIO at pH 7.0, thus providing colloidal stabilization.

TEM indicated FLUSPIO`s spherical surface morphology with an average core diameter of 5 ± 1 nm. FLUSPIO showed high relaxivity with contrast equal to that of clinically used MR contrast agent (Resovist®).

FLUSPIO displayed intense fluorescence with moderate decrease in its intensity after exposure to daylight for 3 days.

The viability assays indicated that there is no decrease in cell viability at relevant FLUSPIO cell labeling concentration (0.3 µmol Fe/mL). High uptake of FLUSPIO by prostate cancer and endothelial cells was confirmed by MRI and fluorescence microscopy. Further, the RCP-mediated uptake of FLUSPIO by PC-3 cells and HUVEC was proved (using MRI) by competitively blocking its uptake with a 10- and 100-fold excess of free FMN.

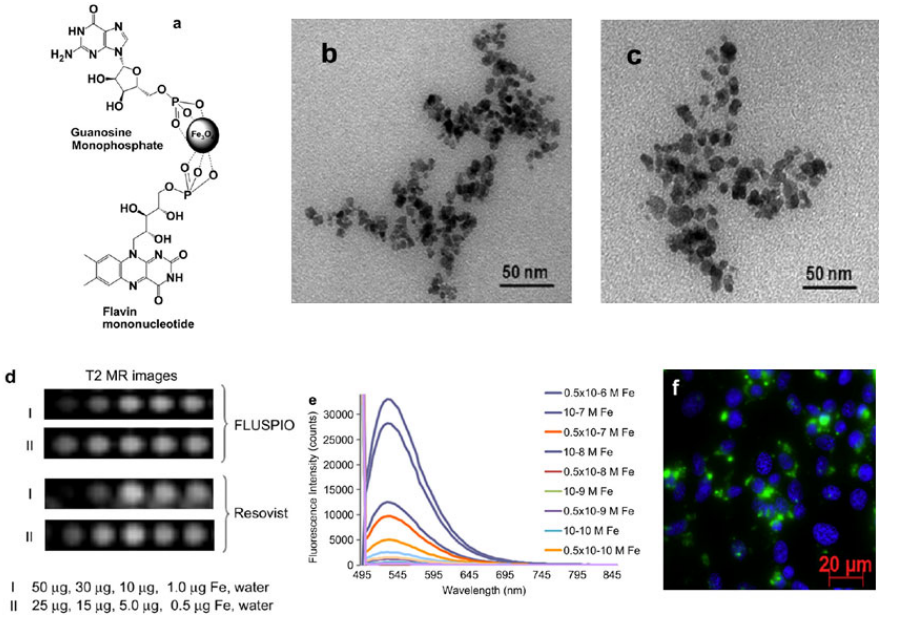

Fig. 1. FLUSPIO characateristics. a: Schematic diagram showing the mode of binding of FMN and GMP to the iron oxide cores in FLUSPIO. b-c: TEM images of USPIO (b) and FLUSPIO (c). Quantitative analysis of the images reveals that both types of nanoparticles have a core diameter of 5 ± 1 nm and a narrow size distribution. d: T_2-weighted MR images of FLUSPIO (50 – 0.005 µg) in comparison to Resovist in water. e: Fluorescence emission spectrum of FLUSPIO at different concentration in water. f: FLUSPIO uptake analyzed by means of fluorescence microscopy (FLUSPIO plus DAPI). The images clearly show the vesicular localizaiton of the FLUSPIO respectively.

In MPS, the higher harmonics of the measured particles of 5 nm and 10 nm iron core size fall off more rapidly than the current standard Resovist®, see figure 1. No difference was seen in the response of the particles coated with FMN as compared to those coated with FAD.

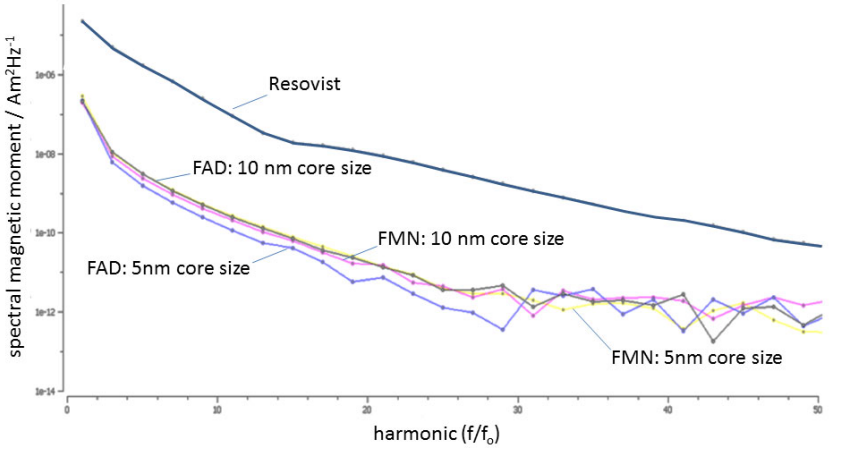

Fig. 2. MPS measurements of USPIO, coated with FMN (5 nm core size, 10 nm core size) and FAD (5 nm core size, 10 nm core size) as compared to Resovist (grey curve). The iron concentration in each of the samples was 5 µmol/ml.

4 Discussion

All particles performed well *in vitro* and *in vivo* with respect to biotolerability and target specificity. As expected due to their comparatively small iron core sizes (5 and 10 nm) the higher harmonics in the MPI signal fall off more rapidly than in the current standard Resovist®. As no difference in the magnetic behavior of differently coated nanoparticles was seen, it can be assumed that it is mainly the magnetic core, which influences the MPI performance. The 5 nm and 10 nm USPIOs do not show a magnetic behavior which is advantageous for MPI. However, now having particles with excellent surface properties at hand may allow us to tailor particle size and their physical and chemical properties to optimize their suitability for MPI.

5 Conclusion

The behavior of the tested particles with respect to MPI is not yet optimal. Having a potential as a versatile molecular probe for targeting the RCP, their small iron core sizes limits the signal strength in MPI. Further work is needed to optimize the particles' magnetic properties.

Acknowledgement. This work was supported by the DFG grant KI 1072/1-3 "Dual modal contrast agents for MRI and Optical Imaging techniques" and by the InnoMET grant z0909im008a "Entwicklung und Bildgebung patientenoptimierter Implantate".

References

1. Jayapaul, J., Hodenius, M., Arns, S., Lederle, W., Lammers, T., Comba, P., Kiessling, F., Gaetjens, J.: FMN-coated fluorescent iron oxide nanoparticles for RCP-mediated targeting and labeling of metabolically active cancer and endothelial cells. Biomaterials 32, 5863–5871 (2011)
2. Gleich, B., Weizenecker, J.: Tomographic imaging using the nonlinear response of magnetic particles. Nature 435, 1214–1217 (2005)
3. Bumb, A., Brechbiel, M.W., Choyke, P.L., Fugger, L., Eggeman, A., Prabhakaran, D., Hutchinson, J., Dobson, P.J.: Synthesis and characterization of ultrasmall superpara magnetic iron oxidenanoparticles thinly coated with silica. Nanotechnology 19, 335601 (2008)
4. Jander, G., Jahr, K.: Massanalyse, 17th edn., pp. 219–221 (2009)
5. Bashir, W.A.: Photometric determination of iron (III). Microchem. J. 26, 477–480 (1981)
6. Portet, D., Denizot, B., Rump, E., Lejeune, J.J., Jallet, P.: Nonpolymeric coatings of iron oxide colloids for biological use as magnetic resonance imaging contrast agents. J. Colloid Interface Sci. 238, 37–42 (2001)
7. Biederer, S., Knopp, T., Sattel, T.F., Lüdtke-Buzug, K., Gleich, B., Weizenecker, J., Borgert, J., Buzug, T.M.: Magnetization Response Spectroscopy of Superparamagnetic Nanoparticles for Magnetic Particle Imaging. Journal of Physics D: Applied Physics 42, 205007 (2009)

Evaluation of Different Magnetic Particle Systems with Respect to Its MPI Performance

Dietmar Eberbeck[1], Lutz Trahms[1], and Harald Kratz[2]

[1] Physikalisch-Technische Bundesanstalt
Abbestraße 2-12, Berlin, 10587, Germany
dietmar.eberbeck@ptb.de
[2] Department of Radiology, Charité - Universitätsmedizin Berlin,
Charitéplatz 1, 10117 Berlin, Germany
Harald.Kratz@charite.de

Abstract. The Magnetic Particle Spectroscopy (MPS)-amplitudes were measured on 7 suspensions of magnetite based magnetic particles (MNP) differing in core size and magnetic anisotropy. The distributions of the effective domain sizes, estimated by means of quasistatic M(H) measurements and Magnetorelaxometry (MRX), matches well the core size distribution for the single core MNP-systems estimated by electron microscopy. Two systems, namely Resovist and M4E clearly exhibit a bimodal domain size distribution. It was shown, that the MPS amplitudes strongly increase with increasing domain size up to 21 nm, the mean value of the larger fraction of Resovist. For M4E with a mean size of the larger fraction of 33 nm the measured MPS-amplitudes became much smaller than those of Resovist, in particular for the higher harmonics. That behaviour was attributed to the mean anisotropy energy of these MNPs, estimated by MRX, exceeding that of Resovist by one order of magnitude. The effect of the MNP's magnetic anisotropy is also supported by comparison of measured MPS-amplitudes with those which were calculated on the base of M(H)-data.

1 Introduction

For a good MPI-performance magnetite/maghemite based MNP should have a narrow core size distribution with a mean diameter between 30 nm and 60 nm [1] and the magnetic anisotropy should be small ensuring that the moments can follow the ac-field easily. Modelling the spectra from MPS (magnetic particle spectroscopy) using M(H)-data, it was found that the reasonable good MPI-performance of Resovist is caused by the MNP aggregates (30% of magnetic volume) which have a mean effective

T.M. Buzug and J. Borgert (Eds.): Magnetic Particle Imaging, SPPHY 140, pp. 53–57.
springerlink.com

magnetic domain size of 22 nm whereas the single core (mean 5 nm) fraction practically do not contribute to the signal [2].

In present study, we investigated MNP suspensions with very different core size distribution in order to show, how also the *measured* MP-spectra support the previous finding. The influence of the particle magnetic anisotropy will be enlightened comparing these spectra with those calculated from quasistatic magnetisation data M(H) and by Magnetorelaxometry (MRX) measurements.

2 Materials and Methods

Beside Resovist, we investigated (i) a set of commercial available magnetite based single core MNP suspensions, SHP-10, SHP-15, SHP-20 (Ocean NanoTech, USA), having mean cores sizes of about 10 nm, 15 nm, and 20 nm, respectively, as documented in the corresponding data sheets and in the case of SHP-20 proved by TEM-measurements [3]. Furthermore, we investigated (ii) two MNP-systems with small particles, MNP-C-A and MNP-C-B (Institute for Radiology, Charité, Germany), coated with citrate. (iii) The system M4E with large magnetite cores were produced precipitating a $2.5 \cdot 10^{-2}$ M iron (II) salt ($FeSO_4$) in the presence of $7.0 \cdot 10^{-2}$ M NaOH and a mild oxidant (0.1 M KNO_3) at 90ºC in a mixture of solvents water/ethanol according to procedure described in [4,5].

For all size distributions, we assumed spherical particles with "magnetic" diameters d_m here also termed domain sizes, obeying a lognormal function $f(d_\mathrm{m})$ which is parameterised by the diameter of the mean volume, $d_\mathrm{m,V}$, and the dispersion parameter σ. The size distributions for the magnetic part of the MNP, i.e. the effective domain diameters, were estimated fitting a model of lognormally distributed noninteracting MNP-moments [6] supplemented with a quasiparamagnetic term [7] to the M(H)-curves, measured with a MPMS-XL (Quantum Design).

By magnetorelaxometry (MRX) [8] we measured the relaxation of the magnetisation of immobilised MNPs after a polarising field was switched off. The fit of a Moment Superposition Model (MSM) to MRX-curves yields also $f(d_\mathrm{m})$ and the mean effective anisotropy constant K_eff [9]. Note, that given MRX-setup samples the relaxation curves starting from t_1=400 µs so that typical magnetite MNP with d<20 nm do not contribute to the signal, significantly.

MPS-measurements were performed on fluid suspensions of the MNPs at H=10 mT/μ_0 and 25 kHz by means of a Magnetic Particle Spectrometer from Bruker BioSpin.

In order to compare the data quantitatively, the iron concentration of the MNP suspensions were measured by Prussian Blue Staining after dissolution of MNP in hydrochloric acid.

3 Results

Structure

The distributions of core sizes, estimated from TEM-pictures (Figure 1), and of the domain sizes, estimated from M(H) and MRX-data, agree well for the single core MNP (Table 1). The magnetisation behaviour of M4E was successfully described introducing a bimodal size distribution, only, as it was previously found for Resovist, too [2], yielding $d_{\mathrm{m,V}}$=12(2) nm (57%) and $d_{\mathrm{m,V}}$=35(6) nm (43%).

In contrast to Resovist, the MRX-result for M4E yields a dispersion parameter of about σ=0.7±0.1 exceeding the value of the larger size fraction of M(H)-analysis, being 0.1±0.03, significantly. This might be caused by the second size fraction which is obviously also MRX-active, probably due to a high anisotropy constant. In table 1 the mean K_{eff} are listed.

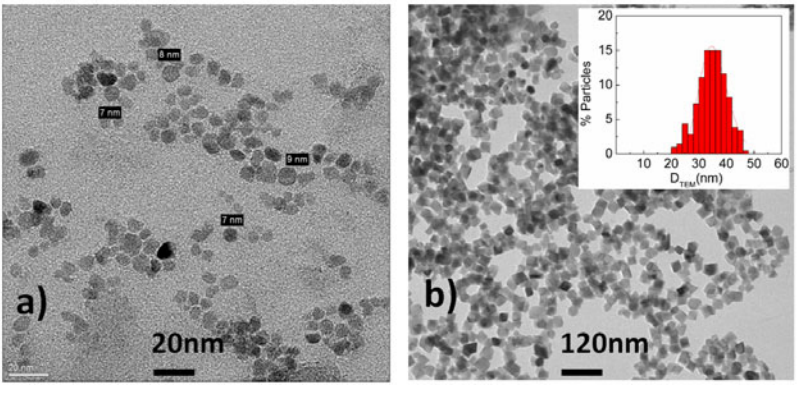

Fig. 1. TEM-pictures from MNP-C-B (a) and M4E (b). The inset of (b) shows the histogram of the largest length of the M4E particles (diagonals of the cubes).

MPS

The measure MPS amplitudes, e.g. A_3, increase and the relative magnitude of higher harmonics, represented by A_5/A_3, decreases with increasing MNP size (Table 1). The exception M4E with the largest mean domain size will be discussed below. As explained in [2], we calculated the MPS-amplitudes $A_{\mathrm{k,s}}$ from quasistatic M(H) curves, i.e. they are not influenced by time dependent processes. Accordingly, the $A_{\mathrm{k,s}}$ of the systems with small MNP, SHP-10, SHP-15, MNP-C-A and MNP-C-B, agree well with the measured ones. On the other hand A_{k}<$A_{\mathrm{k,s}}$. for the systems of larger MNP Resovsit, SHP-20 and M4E (Tab. 1) indicating, that the moments of the MNP can not follow the drive field instantaneously, also confirmed by

the occurrence of a phase lag between harmonics and drive field, e.g. approx 50° for Resovist. This effect is most pronounced for M4E presenting the largest domain size, where $A_3/A_{3,s}$=0.14, only.

Table 1. Measured (A_3) and from M(H) calculated ($A_{3,s}$) MPS-Amplitudes (3rd harmonic) together with the mean magnetic size $d_{m,V}$ (MRX) and mean magnetic anisotropy. The uncertainties of d and $A_{3,s}$ are of order of 10%, that of measured A_3 less than 1%, respectively.

Sample	d_{TEM} nm	$d_{m,V}$ nm	E_A/k_BT K	A_3 Am²/mol(Fe)	A_5/A_3	$A_{3,s}/A_3$
Resovist	4.6	21 [2]	7	0.20	0.24	0.63
SHP-10	10 [1]	10	-	4E-04	0.01	0.80
SHP-15	15 [1]	15	-	0.02	0.04	0.89
SHP-20	19	19	9	0.17	0.19	0.56
MNP-C-A	-	4	-	3E-04	0.01	1.03
MNP-C-B	6.4	7	-	0.01	0.14	1.07
M4E	35	35 [2]	76	0.08	0.04	0.14

[1] Data from data sheet.

[2] Larger size fraction of the bimodal distribution model.

On the base of the hydrodynamic diameters, estimated from MRX-data, we found $\omega\tau_B$=5.5, 2.5 and 2.3 (f=25 kHz) for Resovist, SHP-20 and M4E, respectively, indicating that the Brownian relaxation is considerably restricted. Hence, the Néel mechanism plays a crucial role and we can attribute the difference between A_k and $A_{k,s}$ to the magnetic anisotropy energy of the MNP, E_A=$K_{eff}V$, estimated by MRX, which attains the largest value for M4E, while Resovist and SHP-20 with a 10 times smaller E_A show a much smaller gap between A_3 and $A_{3,s}$, i.e. $A_3/A_{3,s}$=0.63 and 0.56, respectively (Tab. 1).

4 Conclusion

It is clearly shown that the measured MPS-amplitudes increase with increasing core size and decrease with increasing effective anisotropy constant. In particular, because M4E exhibit a large effective magnetic anisotropy, it

shows a small MPS-signal although the core size of about 50% of the MNP is near the expected ideal size range of 30 nm…60 nm.

Acknowledgements. Sample M4E were provided by M. Andrés-Vergés (Department of Organic and Inorganic Chemistry, Universidad de Exremadura, Spain) and M.P. Morales and C.J. Serna (Department of Biomaterials and Bioinspired Materials, Instituto de Ciencia de Materiales de Madrid, ICMM, CSIC, Spain). Samples SHP-10, -15, -20 were supplied by A. Wang (Ocean NanoTech). The research was supported by the German Ministry for Education and Research, Grant No. FKZ 13N11092.

References

[1] Gleich, B.: WO2004/091398 A2 (December 28, 2004)
[2] Eberbeck, D., Wiekhorst, F., Wagner, S., Trahms, L.: How the size distribution of magnetic nanoparticles determines their magnetic particle imaging performance. Appl. Phys. Let. 98, 182502 (2011)
[3] Braun, K.-F., Sievers, S., Eberbeck, D., Gustafsson, S., Olsson, E., Schumacher, H.W., Siegner, U.: arXiv:1002.3739 (unpublished)
[4] Andres Verges, M., Costo, R., Roca, A.G., Marco, J.F., Goya, G.F., Serna, C.J., Morales, M.P.: Uniform and water stable magnetite nanoparticles with diameters around the monodomain-multidomain limit. J. Phys. D: Appl. Phys. 41, 134003 (2008)
[5] Morales, M.P.: Private communication (2011)
[6] Chantrell, R.W., Popplewell, J., Charles, S.W.: Measurements of particle size distribution parameters in ferrofluids. IEEE Trans. Mag. 14(5), 975–977 (1978)
[7] Eberbeck, D., Müller, R., Schmidt, C., Wagner, S., Löwa, N., Trahms, L.: Evidence of bimodal distribution of the effective magnetic sizes of magnetic nanoparticles. In: Book of Abstracts of the 11th German Ferrofluid Workshop, Benediktbeuern, September 28–30, pp. 16–17 (2011)
[8] Matz, H., Drung, D., Hartwig, S., Groß, H., Kötitz, R., Müller, W., Vass, A., Weitschies, W., Trahms, L.: A SQUID measurement system for immunoassay. Appl. Supercond. 6(10-12), 577–583 (1999)
[9] Eberbeck, D., Wiekhorst, F., Steinhoff, U., Trahms, L.: Aggregation behaviour of magnetic nanoparticle suspensions investigated by magnetorelaxometry. J. Phys. Condens. Matter 18, S2829–S2846 (2006)

Determination of System Functions for Magnetic Particle Imaging

Matthias Graeser, Sven Biederer, Mandy Grüttner, Hanne Wojtczyk, Timo F. Sattel, Wiebke Tenner, Gael Bringout, and Thorsten M. Buzug

Institute of Medical Engineering, University of Lübeck,
Ratzeburger Allee 160, 23562 Lübeck, Germany
{graeser,buzug}@imt.uni-luebeck.de

Abstract. In Magnetic Particle Imaging, a new medical imaging modality, the relation between measured signals and the spatial distribution of the tracer particles is described by the system function. In existing scanners the system function is measured by moving a delta probe through the field-of-view and the particle response is measured. This procedure is time consuming, caused by the mechanical movement, and makes great demands on the hardware, because of the huge data amount that is measured. To speed up the determination of the system functions other methods have to be considered. In this work the model based and the hybrid system function will be compared to the measured one.

1 Introduction

In Magnetic Particle Imaging (MPI), an imaging modality that was invented in 2005, the nonlinear response of the magnetization of nanoparticles is measured [1]. By using a combined field generating device, which superimposes a gradient field by a sinusoidal oscillating field (the drive field), the nanoparticles change their magnetization only in the field-free point (FFP) of the gradient field. All other particles stay in saturation. If the field amplitude of the drive field is high enough, the movement of the FFP, caused by the drive field, cannot be neglected. In this case all particles in the FOV change magnetization and induce a voltage in the receive coil.

Due to the fact that particles are exposed to different gradient fields in space, the signal differs according to their spatial position, as shown in fig. 1.

T.M. Buzug and J. Borgert (Eds.): Magnetic Particle Imaging, SPPHY 140, pp. 59–64.
springerlink.com

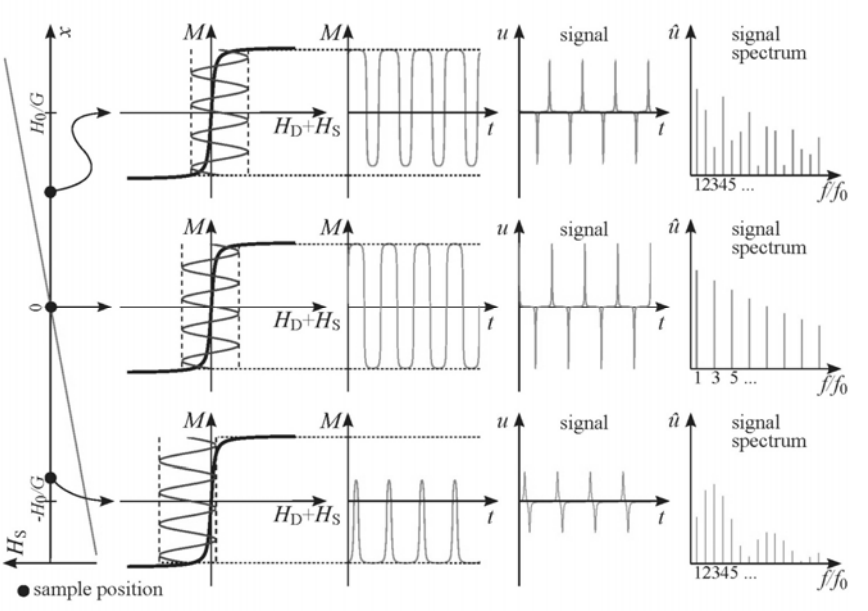

Fig. 1. Particle behaviour according to the superimposed gradient field and the voltage and spectrum induced in a receive coil. H_s = gradiend field amplitude, M = particle magnetisation, u = voltage induced in the receive coil, û = FFT of the received signal.

The spectrum of the different positions is a fingerprint of particles positioned at this very point.

In a real scanner device the signals $\hat{u}_k$ in the receive coil depend on the particle concentration $c(\mathbf{r})$ and the system function $\hat{s}_k(\mathbf{r})$.

$$\hat{u}_k = \int_{FOV} \hat{s}_k(\mathbf{r}) c(\mathbf{r}) d^3 r \tag{1}$$

The system function itself depends on the transfer function a_k, the particle magnetization $\hat{M}(\mathbf{r},t)$ and the coil sensitivity $p(\mathbf{r})$.

$$\hat{s}_k = a_k \int_0^T \frac{\partial}{\partial t} \frac{\hat{M}(\mathbf{r},t)}{c_0} p(\mathbf{r}) e^{\frac{-2\pi i k t}{T}} dt \tag{2}$$

Until now, three different techniques are known to acquire these quantities: the measurement based, the model based and the hybrid strategy to obtain the system function.

2 Material and Methods

The measurement based system function is acquired directly by recording the response of a delta probe. A delta probe, with the dimensions of one voxel is moved mechanically to every later voxel position in the FOV. The answer of the system to the drive field excitation induces a voltage in the receive coil. This voltage consists of the fundamental frequency and many harmonics that are caused by the nonlinear magnetization characteristic of the particles. This spectrum can be inserted as one column in the system matrix as it represents the answer of the whole system of the particles in this specific spatial position. The particle magnetization curve, the scanner gradient field distribution and the receive coil sensitivities are already included in the received signal. Due to the desire of a high spatial resolution, many positions have to be measured. This leads to a long measurement time as well as to a large amount of data. In case of a FOV with 128 x 256 x 256 voxels and 40 harmonics with 8 byte per harmonic a data amount of

$$128 \cdot 256 \cdot 256 \cdot 40 \cdot 8 \text{ byte} = 2.5 \text{ GB}$$

is generated. This causes great demands on the hardware. Another disadvantage is the high system noise caused by the distance of the probe to the receive coil.

The model based system function uses mathematical calculations to simulate the independent parts of the system function [2, 3]. For the magnetic fields the Biot-Savart law is used (3).

$$\mathbf{B}(\mathbf{r}) = \frac{\mu_0}{4\pi} \int_V \mathbf{J}(\mathbf{r}') \times \frac{\mathbf{r} - \mathbf{r}'}{|\mathbf{r} - \mathbf{r}'|^3} d^3 r \tag{3}$$

These calculations are very precise. The measured fields have a NRMSD of less than 3 percent. This is within the measurement error of our measurement instrumentation. The particle magnetization is calculated by the Langevin equation:

$$M(\xi) = M_0(\coth \xi - 1/\xi) \tag{4}$$

with

$$\xi = \frac{\mu_0 m H}{k_B T} \tag{5}$$

As a last step, some measurements are needed to obtain the transfer function of the system. This is done by moving the delta probe described above and acquiring the signal at specific points. By comparing the calculated data with the measured ones the transfer function a_k of (2) is determined. With this technique it is possible to speed up the determination process. Due to the fact that the system function can be calculated within the reconstruction process it is not necessary to store the whole system function in the memory

of the computer. Unfortunately, the reconstruction results show less resolution compared to the measurement based ones. The largest error is the imprecise particle model that neglects the imperfections of the tracer material.

As the modeled system function, the hybrid system function simulates the magnetic fields and coil sensitivities using the law of Biot-Savart (3), because the results of this simulation are satisfying. To measure the particle magnetization in (1) a magnetic particle spectroscope (MPS) is used [3]. Actually, an MPS is a zero-dimensional MPI scanner device. It has the complete signal chain of an MPI scanner without the gradient field. Thus, all particles within the testing chamber are responding to the oscillating field, which allows for a high signal to noise ratio. Because the receive coil is very close to the probe a very high sensitivity is achieved. In our MPS a homogenous offset field replaces the gradient field of a scanner device. This additional field allows for simulating the response of particles in every position of the scanner. By mapping the measured particle answers to the respective points in the scanner, a system function can be acquired. In addition, the transfer function has to be measured according to the modeled system function. This method also speeds up the measurement process. The advantage of the hybrid system function is that the particle errors are incorporated within the MPS measurements and therefore in the system function. In addition, a very low noise level is achieved.

3 Results

Fig. 2 shows a modeled system function of an ideal scanner meaning perfect gradient and drive fields and ideal coil sensitivities. For the same values of field amplitudes fig. 3 shows the respective hybrid system function. As it can be seen the system functions are very similar. In fig. 4 an error plot is shown. It is demonstrated that the errors are mostly in the area of higher harmonics and higher offset field values.

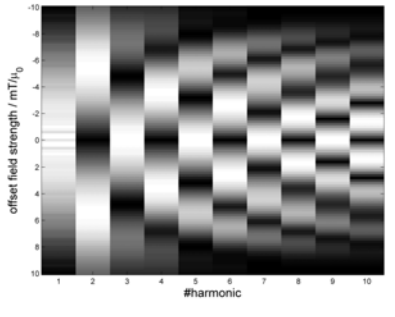

Fig. 2. Modelled system function. Amplitude of harmonics normalized to maximum of each column. H_{ac} = 10 mT H_{dc} = 0-10 mT

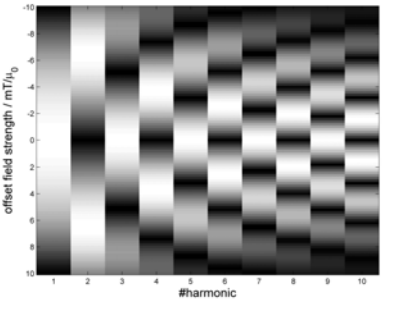

Fig. 3. Hybrid system function. Amplitude of harmonics normalized to maximum of each column. H_{ac} = 10 mT H_{dc} = 0-10 mT

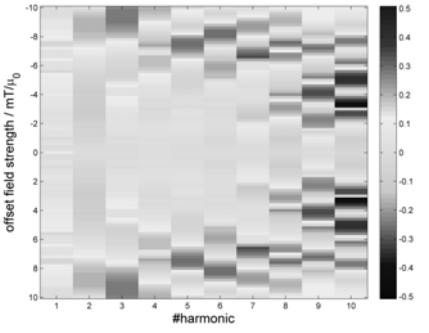

Fig. 4. Difference plot of the modeled and hybrid system function.

4 Discussion

We demonstrated that the hybrid system functions could speed up the acquisition of the system function. Compared to the model based system function a high similarity has been shown. The low noise level caused by the MPS should be one advantage of this method compared to measurement based system functions. The hybrid method also solves the data-handling problem, because less data has to be stored in the memory due to the fact that the system function can be calculated within the reconstruction process. For evaluation of the hybrid method a comparison not only to the modeled system function but also to the measured system function is necessary.

5 Conclusion

We compared different methods to acquire system functions of an MPI scanning device. The hybrid approach is promising from different points of view but has to be validated by reconstruction results. Also, a 3D MPS with additional drive fields is required to apply these methods for 3D MPI scanning devices.

Acknowledgements. We acknowledge the support of the Federal Ministry of Education and Research, Germany (BMBF) (grant numbers 01EZ0912 and 13N11090), the European Union and the State Schleswig-Holstein (Programme for the Future – Economy: 122-10-004) (MGrä, MGrü, HW, GB) and Germany's Excellence Initiative [DFG GSC 235/1] (WT).

References

1. Gleich, B., Weizenecker, J.: Tomographic imaging using the nonlinear response of magnetic particles. Nature 435, 1214–1217 (2005)
2. Knopp, et al.: Model-Based Reconstruction for Magnetic Particle Imaging. IEEE Trans. Med. Imag. 29(1), 12–18 (2010)
3. Knopp, et al.: 2D Model-based reconstruction for magnetic particle imaging. Medical Physics 37, 485–491 (2010)
4. Biederer, S., Sattel, T., Knopp, T., Lüdtke-Buzug, K., Gleich, B., Weizenecker, J., Borgert, J., Buzug, T.M.: A Spectrometer for Magnetic Particle Imaging. In: Vander Sloten, J., Verdonck, P., Nyssen, M., Haueisen, J. (eds.) ECIFMBE 2008. IFMBE, vol. 22, pp. 2313–2316. Springer, Heidelberg (2008)

Magnetic Particle Separation

Microfluidic System as a Tool for Magnetic Separation of Human Cells with Diagnostic Relevance

J. Schemberg[1], J. Bertram[2], M. Hottenrott[3], T. Legler[4], S. Howitz[5], K. Lemke[1], G. Gastrock[1], and J. Metze[1]

[1] Institute for Bioprocessing and Analytical Measurement Techniques, Rosenhof, Heilbad-Heiligenstadt, Thuringia, 37308, Germany
joerg.schemberg@iba-heiligenstadt.de
[2] IBA GmbH, Rudolf-Wissell-Str. 28, Göttingen, Lower Saxony, 37079, Germany
Bertram@iba-go.com
[3] Intros GmbH, Rudolf-Diesel Str.3, Heilbad-Heiligenstadt, Thuringia, 37308, Germany
hottenrott@intros.de
[4] Abteilung Transfusionsmedizin, Universitätsmedizin Göttingen, Stiftung Öffentlichen Rechts, Robert-Koch-Straße 40, Göttingen, Lower Saxony, 37075, Germany
tlegler@med.uni-goettingen.de
[5] GeSiM mbH, Bautzner Landstrasse 45, Großerkmannsdorf, Saxony, 01454, Germany
howitz@gesim.de

A new microfluidic system was realized by means of a specially designed chip from silicon and glass. Magnetic disks were located above and below this chip. The transportation, mixing, incubation and the chip based separation procedure of the cell-magnetic bead suspension is caused by pumps and the rotation of permanent magnets arranged outside the chip.

A high efficiency of attachment to the appropriate target cells from blood or other fluids is realized since the magnetic beads were functionalized with antibodies or a special Fab-Streptamer® technology. In comparison with monoclonal antibodies this technology allows the release of the beads from the target cells after separation by means of added D-Biotin to the target cell-magnetic bead suspension. The unlabelled target cells and the beads are ready for further use.

In comparison with commercial separation systems, the benefit of the new microfluidic system in combination with the Fab-Streptamer-magnetic beads is the continuous fluid flows is the increased cost-effectiveness based on reduced incubation time, reduced magnetic bead concentration and re-usable target cells. Automized measurement of real blood samples

T.M. Buzug and J. Borgert (Eds.): Magnetic Particle Imaging, SPPHY 140, pp. 67–71.
springerlink.com

from cancer patients and the detection of the separated cells by means of a flow-cytometer (FACS) are ongoing.

1 Introduction

Magnetic cell separation is based on specific functionalized magnetic particles called magnetic beads. The structure and volume of magnetic beads varies depending on their usage. Due to their material properties and interface shape magnetic beads have special magnetic characteristics. Different issues like finite-size and surface effects especially in the condition of decreased particle size exhibits no remanence or coercivity. The energetic definition for such magnetic beads is well described [1]. A more deep theoretical understanding about superparamagnetism will be described elsewhere [2, 3]. The processes of synthesis, protection and functionalization of magnetic beads were reviewed in several papers [4, 5]. This procedure should be aligned with the requirements of biocompatibility, biodegradability, stability in different media combined with uniform size distribution and a correct shape. With the appropriate magnetic features of the magnetic beads basic manipulation in microfluidic systems are feasible. Non-magnetic cells can be labeled with magnetic beads through antigen-antibody interactions or by means of a Streptavidin-Streptamer binding. Magnetic forces applied perpendicular to the flow direction diverting labelled from non-labelled cells into different trajectories [6]. An alternative is based on the cyclic magnetic field-flow fractionation effect. A rotating permanent magnet is placed above a capillary coil to provide a cyclic magnetic field across the capillary [7].

2 Material and Methods

The work flow is divided into the following modules i) Mixing and incubation of the cell-magnetic bead suspension, ii) Chip-based microfluidic cell separation, iii) Sampling and purification of the cell-magnetic bead suspension, iiii) Analysis by means of FACS or manual cell counting. To avoid non-specific cell separation the temperature during the separation was 4^{o}C.

Cell Lines

The system was tested using leukemia cells (Tab.1). They were suspended in PBS buffer, and human whole blood from appropriate contributors. Their concentration respectively was 1.3E+05cells/mL.

Table 1. Cell lines (DSMZ GmbH, Braunschweig, Germany) and their immunology

cell line	name	immunology
CMK	Human acute megakaryocytic leukemia	CD34+, CD71+, CD15-
KG-1	Human acute myeloid leukemia	CD34+, CD15+
K-562	Human chronic myeloid leukaemia in blast crisis	CD71+, CD15+

Magnetic Beads

The cells were separated using two types of magnetic beads commercial antibody functionalized and specially designed Fab-Streptamer coated magnetic beads (Tab.2). The magnetic bead concentration was between 2E+08 and 1E+10beads/mL. The diameter of the magnetic beads varied between 0,5-3,5µm.

Table 2. Magnetic beads with different functionalized interface

magnetic beads	manufacturer	interface coating
MagStrep Type2	IBA GmbH, Göttingen, Germany	Anti-CD34+ IgG; Anti - CD15+ IgG
Strep-Tactin Microbeads	IBA GmbH, Göttingen, Germany	Fab-Strep Anti-CD34+
MACSi-Beads	Miltenyi Biotech, GmbH	Anti-CD15+ IgM

Chip-Based Microfluidic Cell Separation

After the mixing and incubation of 500µL cell-magnetic bead suspension (10min.) a silicon-glass chip was used for the cell separation. Rotating disks above and below the chip, contain up to 30 permanent magnets (ibs-magnet GmbH, Berlin, Germany). The cell separation and subsequent washing process was automized by a special regime using syringe pumps (Cetoni GmbH, Korbußen, Germany. After sampling and purification of the sample, analysis by means of counting chambers (Neubauer, Malassez, Nageotte) and FACS (Beckton Dickinson Company) was realized.

3 Results

Separation of KG-1 Cells in Buffer

After several preliminary microfluidic and computer simulated tests (Comsol GmbH, Göttingen, Germany) to optimize the fluidic stream, the maximum cell separation yield of KG-1 in buffer with CD34+ IgG-coated magnetic beads reached ~90% (Fig.1). Further investigations indicated a

dependency between bead concentration (c_b) and the number of antibodies coated on the interface of the magnetic beads (n_m) with the cell separation yield. If (c_b) is halved, the cell separation yield was decreased by nearly the same percentages like the bead concentration. If (n_m) was reduced by a factor ten, the cell separation yield was halved.

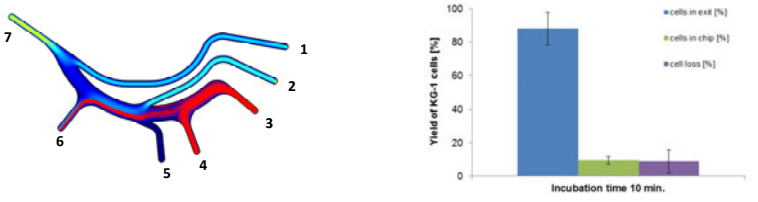

Fig. 1. Left: Simulated ideal flow profile to separate the origin media (blood, plasma) from the target cell-magnetic bead-suspension in specially designed silicon-glass-chip. Number 1-7 are the inlet-outlet channels. Right: Separation of KG-1 cells from buffer. Cells in exit means directly separated cells while cells in chip were the eluted cells only after removal of the permanent magnets.

Separation of KG-1 Cells in Human Plasma and Blood

In comparison with buffer as media, the cell separation yield with the same magnetic beads was explicitly less (~4%). However further investigations with MACSiBeads (Miltenyi Biotech GmbH) indicates the same cell separation yield as with buffer (80-90%). The usage of the same antibody-coated (CD15+ IgG) Typ 2 Beads (IBA GmbH) showed much less cell separation yield (~50%). Cell separation from blood as medium was comparable to separation from plasma. Further agglomeration effects between the MACSiBeads and blood plugged near the permanent magnets caused by a high cell loss.

Separation of KG-1 Cells in Human Buffy Coat

Agglomeration and interaction-effects between the cell-bead-complexes and the appropriate media (plasma and blood) was a big drawback for reliable cell separation results. To prevent this problems human blood was separated by means of centrifugation. The buffy coat showed better cell separation results with Fab-Streptamer and IgG-coated magnetic beads than in plasma or blood. Additionally, the Fab-Streptamer magnetic beads showed stronger magnetization effects than the IgG-coated beads.

4 Discussion

The results indicate that viscosity and agglomeration effects between the red blood cells (RBC) and the magnetic beads are especially problematic with human blood. Additionally components or effects in human plasma

inhibit the binding process between the target cells and the magnetic beads. Further tests with smaller sized magnetic beads (Ø~100nm) should show if these effects can be minimized. On the contrary cell separation from buffy-coat indicates nearly the same results as from buffer. The release process of Fab-Streptamer functionalized beads from the target cells after the separation procedure is inefficient.

5 Conclusion

By means of an optimized syringe pump work-flow the replacement of media (blood, plasma, buffy coat) to separate only the target cell-magnetic bead suspension was successful. In comparison with commercial cell separation protocols, the special modular assembly of the magnetic separator reduced the incubation time of the target cell sample with the appropriate magnetic beads from 30 to 10 minutes without a loss of cell separation effectiveness. Further investigations will focus on automatization and validation of the whole process to create a prototype and to optimize the efficiency of the used magnetic beads to enhance the cell separation yield.

References

[1] Lu, A.-H.L., Sabalas, E.L., Schüth, F.: Magnetic Nanoparticles: Synthesis, Protection, Functionalization and Application. Angew. Chem. Int. Ed. 46, 1222–1244 (2007)
[2] Gijs, M.A.M., Lacharme, F., Lehmann, U.: Microfluidic Applications of magnetic particles for biological analysis and catalysis. Chem. Rev. 110, 1518–1563 (2010)
[3] Batlle, X., Labarta, A.: Finite-size effets in fine particles: magnetic and transport properties. J. Phys. D: Appl. Phys. 35, R15–R42 (2002)
[4] Horak, D., Babic, M., Mackova, H., Benes, M.J.: Preparation and properties of magnetic nano- and microsized particles for biological and environment separations. J. Sep. Sci. 30, 1751 (2007)
[5] Safarik, I., Horska, K., Safarikova, M.: Magnetic nanoparticles for biomedicine. In: Prokop, A. (ed.) Intracellular Delivery: Fundamentals and Applications, Fundamental Biomedical Technologies, vol. 5, pp. 362–372 (2011)
[6] Tsutsui, H., Ho, C.-M.: Cell separation by non-intertial force fields in microfluidic systems. Mechanics Research Communications 36, 92–103 (2009)
[7] Bi, Y., Pan, X., Chen, L., Wan, Q.-H.: Field-flow fractionation of magnetic particles in a cyclic magnetic field. Journal of Chromatography A 1218, 3908–3914 (2011)

Potential of Improving MPI Performance by Magnetic Separation

N. Löwa, D. Eberbeck, U. Steinhoff, F. Wiekhorst, and L. Trahms

Physikalisch-Technische Bundesanstalt, Abbestr. 2-12,
10587 Berlin, Germany
norbert.loewa@ptb.de

Abstract. The present article reports on the experimental results of applying magnetic separation to DDM128, a magnetic fluid very similar to Resovist®, with superior MPI performance. Larger particle diameters are assumed to perform better in MPI signal generation. Thus particle size fractionation is expected to result in significant MPI signal enhancement. We separated DDM128 using magnetic separation at different field strengths. In the following we investigated the particle size distribution of the fractions by magnetization measurements and magnetic particle spectroscopy.

1 Introduction

Magnetic Particle Imaging (MPI) is a novel modality for imaging magnetic nanoparticles (MNP) [1]. The magnetic properties of the tracer material, i.e. the MNP, determine the spatial resolution of the method.

Initial MPI experiments with the MRI liver contrast agent Resovist® have shown a high spatial resolution [2]. Regarding the bimodal distribution of Resovist®, the good performance was attributed to MNPs of the larger fraction [1,3]. Hence, separation can be expected to improve the MPI signal [6].

We present experimental results of magnetic separation applied to DDM128 at different field strengths. To evaluate the potential of this method we estimated the resulting size distribution from magnetization measurements and analyzed the particle performance with a Magnetic Particle Spectrometer (MPS).

2 Materials and Methods

2.1 Sample

We investigated DDM128 (Meito Sangyo, Japan) which is a precursor of Resovist®. In Resovist, the magnetic cores of the iron oxide nanoparticles

T.M. Buzug and J. Borgert (Eds.): Magnetic Particle Imaging, SPPHY 140, pp. 73–78.
springerlink.com

are coated with carboxymethyl dextran. Before fractionation 1.5 ml of the diluted sample (c_{Fe}=11 mmol/l) was centrifugated at 1200 rpm for 1 min. In the following the removed supernatant will be denoted as feed sample.

2.2 Fractionation

Before performing magnetic fractionation using a commercially available separation column (MS column, Miltenyi Biotec, Germany), we devolatilized every solution. To generate magnetic fields up to 36 mT we used a 10 layer copper coil (200 mm height, 125 windings/layer). Additionally, for the field strength of 500 mT a commercial separator (MiniMACS™, Miltenyi Biotec, Germany) was used.

For one separation cycle the sample was poured onto the column while the magnetic field was applied. After collecting the discharge the column was washed with 200 µl of water. A second washing step with 200 µl carboxyl dextran solution (0.25 g/ml) was performed after the field was switched off. The rinsed eluate was collected as well. For fractionation the procedure was iterated using magnetic fields of 4 mT, 12 mT, 36 mT and 500 mT starting with 1 ml feed sample volume and in the following using the discharge of the previous step.

2.3 Measurements

The discharges and eluates of each separation step were filled in polycarbonate caps of 75 µl sample volume. Using a commercial magnetometer (MPMS XL, Quantum Design, USA) the static magnetization of the sample at room temperature was measured as a function of the applied field strength. We used the moment superposition model (MSM) [3,5] assuming a bimodal distribution of particles magnetic core sizes, i.e. we described the magnetization curve $M(H)$ by the superposition of the magnetization curves of two fractions 1-β_2 and β_2:

$$M(H) = (1-\beta_2)\, M_1(H)+\beta_2\, M_2(H). \quad (1)$$

Assuming the diameter distribution to be log-normal we estimated two medians μ_i and two dispersion parameters σ_i by fitting the MSM. We used $d_{i,V}$ as the mean diameter corresponding to the volume of the effective magnetic domain of the particle.

To evaluate the iron concentration we scaled the saturation magnetization of the fraction to the feed sample of known concentration.

MPI signal performance of the samples was analyzed using a magnetic particle spectrometer (MPS3, Bruker, Germany). For the measurement 30 µl sample volume were filled in conventional PCR tubes and measured at 25 mT drive field to generate the characteristic signal spectra.

3 Results and Discussion

3.1 Magnetization Behaviour

Magnetization curves of the feed sample, discharges and eluates at the 12 mT, 36 mT and 500 mT separation steps are plotted in Fig. 1. Characteristics of the obtained size distributions are given in Table 1.

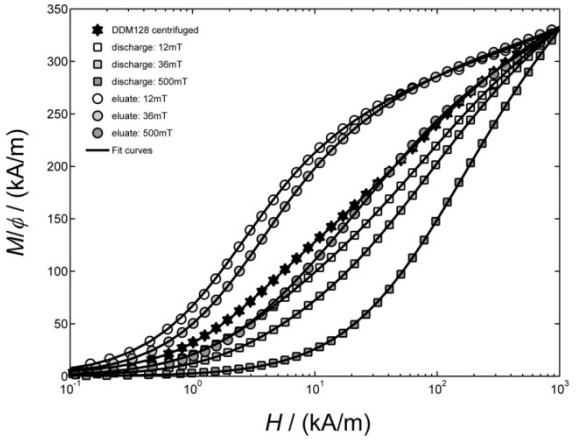

Fig. 1. *M(H)* curves of magnetic separated fractions of DDM128, analyzed by (1) assuming a bimodal size distribution. A mono-modal size distribution was assumed for the discharge separated with 500mT.

We found good agreement of the bimodal model of the size distribution to the measurement data of the feed sample. In agreement with earlier measurements on Resovist® [3] we obtained a volume weigthed diameter $d_{1,V}$=(4.8±1) nm magnetic core size representing the smaller fraction and a larger fraction with $d_{1,V}$=(20.6±0.4) nm and β_2=(31±1) %.

Comparing β_2 over the separation steps we found that the larger fraction gradually decreased in the discharges with increasing separation field strengths. At 500 mT separation field no reasonable result using a bimodal distribution function according to eq. (1) could be found. The conventional monomodal fit yielded a size distribution appropriate to the smaller fraction.

In the eluates β_2 was significantly increased for separation field strengths of 12mT and 36 mT and mounted to about 73 %. Note, that each separation step was performed with the discharge of the previous.

The variations in estimated mean diameters were in the range of the measurement uncertainty for the smaller fraction $d_{1,V}$ as well as for the second fraction $d_{2,V}$.

3.2 MPS Analysis

Fig. 2 shows the MPI spectra of the different samples normalized to iron concentration (mmol). The amplitudes of 3rd and 11th harmonic normalized to the corresponding amplitudes of the feed sample are listed in Table 1.

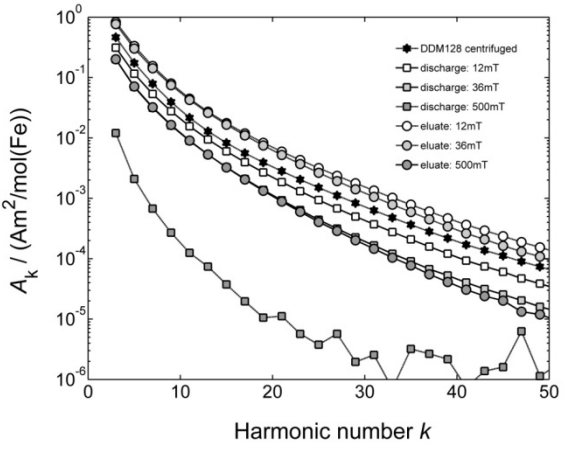

Fig. 2. Odd harmonics of the MPS spectra normalized to iron concentration. The samples are excited by a drive field of 25 mT and f_0 = 25.25 kHz. Odd harmonics are connected by a solid line to guide the eye.

Whereas the sample containing no larger particles (discharge 500 mT) showed a considerably smaller signal than the feed sample, the MPS data of the 12 mT and 36 mT eluates yielded an increase about 1.8 times signal amplitude in the 3rd harmonic. Examination of higher harmonic amplitudes resulted in even two times signal enhancement, e.g. in A_{11}. Note, that the iron concentration of the samples was roughly estimated by normalization of saturation magnetization to that of the feed sample.

Table 1. Size distribution parameters of DDM128 for three steps of magnetic separation obtained by magnetization measurements listed with amplitude ratio of 3rd and 11th harmonic of the separation sample to feed sample.

field	sample	size distribution					MPI-amplitude changes	
		$d_{1,V}$ (nm)	σ_1	β_2	$d_{2,V}$ (nm)	σ_2	$A_{3,n}/A_{3,feed}$	$A_{11,n}/A_{11,feed}$
-	*feed*	*4.8(1)*	*0.52(1)*	*0.31(1)*	*20.6(4)*	*0.23(1)*	*1*	*1*
12mT	discharge	4.8(2)	0.52(1)	0.19(1)	20.6(8)	0.19(2)	0.67	0.70
	eluate	4.5(2)	0.55(1)	0.74(5)	21(1)	0.27(2)	1.79	2.08
36mT	discharge	4.9(2)	0.50(1)	0.09(1)	20(1)	0.15(4)	0.43	0.42
	eluate	5.1(8)	0.5(1)	0.72(3)	19.6(5)	0.23(1)	1.65	1.98
500mT	discharge	5.0(1)	0.52(1)	-	-	-	0.03	0.01
	eluate	6(1)	0.5(1)	0.3(4)	15(6)	0.26(2)	0.43	0.42

4 Conclusion

We demonstrated the potential of improving MPI performance by magnetic separation of DDM128.

As it was expected low signal amplitudes were obtained for the isolated smaller fraction of the discussed samples, since these particles do not meet ideal parameters for MPI. However, increasing the larger fraction up to 73 % by magnetic separation, improves MPI signal about a factor of two.

Note that only a 3 % fraction of Resovist® is suggested to contribute to the overall signal [1]. Hence, further fractionations using this setup, with lower fields than 12mT, seems to be a promising path for further optimization of MPI tracers.

Acknowledgements. The research was supported by the German Ministry for Education and Research (Grant No. FKZ 13N11092).

References

1. Gleich, B., Weizenecker, J.: Tomographic imaging using the nonlinear response of magnetic particles. Nature 435, 1214–1217 (2005)
2. Weizenecker, J., Borgert, J., Gleich, B.: A simulation study on the resolution of magnetic particles imaging. Physics in Medicine and biology 52, 6363–6374 (2007)

3. Eberbeck, D., Wiekhorst, F., Wagner, S., Trahms, L.: How the size distribution of magnetic nanoparticles determines their magnetic particle imaging performance. Applied Physics Letters 98, 182502 (2011)
4. Eberbeck, D., Wiekhorst, F., Trahms, L.: Evidence of Aggregates of Magnetic Nanoparticles in Suspensions Which Determine the Magnetisation Behavior. In: Buzug, T.M., Borgert, J., Knopp, T., Biederer, S., Sattel, T.F., Erbe, M., Lüdtke-Buzug, K. (eds.) Magnetic Nanoparticles: Particle Science, Imaging Technology and Clinical Applications, pp. 66–72. World Scientific Publishing Company (2010)
5. Eberbeck, D., Hartwig, S., Steinhoff, U., Trahms, L.: Description of the magnetization decay in ferrofluids with a narrow particle size distribution. Magnetohydrodynamics 39, 77–83 (2003)
6. Schütz, G., Lohrke, J., Hütter, J.: Use of Resovist in Magnetic Particle Imaging. In: Buzug, T.M., Borgert, J., Knopp, T., Biederer, S., Sattel, T.F., Erbe, M., Lüdtke-Buzug, K. (eds.) Magnetic Nanoparticles: Particle Science, Imaging Technology, and Clinical Applications, pp. 32–36. World Scientific Publishing Company (2010)

Magnetic Nanoparticles

Fractionated Magnetic Multicore Nanoparticles for Magnetic Particle Imaging

Silvio Dutz[1], Dietmar Eberbeck[2], Robert Müller[1], and Matthias Zeisberger[1]

[1] Institute of Photonic Technologies
A.-Einstein-Str. 9, 07745 Jena, Germany
silvio.dutz@ipht-jena.de
[2] Physikalisch-Technische Bundesanstalt
Abbestraße 2-12, 10587 Berlin, Germany

Abstract. Aim of this study was the investigation of the suitability of magnetic multicore nanoparticles (MCNP) for magnetic particle imaging. For this, MCNP of different cluster sizes were investigated. To obtain a set of samples which differ in their cluster sizes the MCNP were classified into fractions of different mean sizes by centrifugation. By the fractionation particles with hydrodynamic diameters from 100 to 800 nm were obtained. Magnetic measurements confirmed a correlation of the hydrodynamic size with the effective magnetic volume of the particles in these fractions – e.g., with increasing particle size the coercivity of the particles varied from 3.5 to 25.8 Oe. Magnetic particle spectrometry investigations showed a clear dependence of the quality of MPS signal on the hydrodynamic diameter of the particles and thus the cluster size. In particular the amplitude ratio of the higher (15...40) harmonics to the 3rd harmonic span over one order of magnitude, where the smaller MCNP showed the highest values.

1 Introduction

The performance of magnetic particle imaging (MPI) strongly depends on the magnetic properties magnetic moment, coercivity, and initial susceptibility of the magnetic nanoparticles acting as imaging agents. Ideal particles show a very steep slope of the magnetisation during magnetic reversal combined with a high saturation magnetisation and a low coercivity. Usually, an increase in magnetic moment entails also in enhancement in magnetic anisotropy energy, i.e. the coercive force. Thus, beside the enhancement of the magnetic volume of the tracers one has to reduce the anisotropy constant. In previous investigations it was shown that MCNP are promising candidates for suitable MPI tracers [1]. Present MCNP consist of single domain cores in the size range from 10 to 15 nm which form

T.M. Buzug and J. Borgert (Eds.): Magnetic Particle Imaging, SPPHY 140, pp. 81–85.
springerlink.com

larger clusters with diameters of 20 nm up to a few hundred nm. Aim of this study was the investigation of the suitability of MCNP for MPI in more detail. For this, MCNP of different cluster sizes were investigated. To obtain a set of samples which differ in their cluster sizes the MCNP were classified into fractions of different mean sizes by means of a centrifuge [2]. In this contribution we describe the preparation and fractionation of the MCNP. We show the results of the samples characterisation and give an interpretation of the correlation between the different determined parameters and the quality of the MPS signal. Finally, we discuss the design of promising future MCNP for MPI based on our findings in this study.

2 Material and Methods

2.1 Sample Preparation

Two samples of MCNP of different mean size (by synthesis at different temperatures) were prepared as described before [3]. In short: a 1 M $NaHCO_3$ solution was slowly added to a $FeCl_2/FeCl_3$ solution (total Fe-concentration: 1.25 M; Fe^{2+}/Fe^{3+} ratio = 1/1.3) with a rate of 1.2 ml/min under permanent stirring up to pH = 8, leading to the formation of a brownish precipitate. Afterwards, the solution was boiled for 5 minutes to form an almost black precipitate. The magnetic nanoparticles were then washed with water. To produce sedimentation stable suspensions, the particles were coated with a carboxymethyl dextran (CMD) shell. The magnetic particle concentration in the suspension was adjusted to a value of about 1 % by mass.

From these suspensions fractions of MCNP of different cluster sizes were prepared by means of centrifugation fractionation. For this, the initial MCNP fluids were filled in a cylindrically shaped centrifugation vessel made of glass (sample height 70 mm and diameter 20 mm). The sample was centrifuged in a laboratory centrifuge at 500 g with a temperature of 20 °C. The sediment was stored and the supernatant was recovered. A portion of the supernatant was centrifuged again. This procedure was repeated 9 times with increasing centrifugal accelerations (up to 4000 g). In consequence, 10 sediments and 10 supernatants were obtained representing 20 fractions of the MCNP for each sample. From these fractions samples of suitable size increments were chosen for further investigations.

2.2 Sample Characterisation

Differences in the cluster size for the obtained fractions were determined by means of photon correlation spectroscopy (PCS). For this, the z-ave value from cumulants fit method assuming spherically shaped clusters was used. Additionally to this the effective magnetic core size was measured by magneto relaxometry (MRX) by investigation of the relaxation behaviour of liquid samples [3]. The overall core size of selected samples was determined by means of transmission electron microscopy (TEM). A measure

for the size of the single cores (assumed to be single crystalline) in the clusters were obtained from X-ray diffractometry (XRD) analysing the size dependent broadening of the 440 Debye-Scherrer line using the Scherrer formula. Magnetic characterisation of the quasistatic properties of the clustes was done by vibrating sample magnetometry (VSM) as well as by SQUID-magnetometry. The behaviour of the particles regarding the suitability as tracers for MPI was investigated via analysis of the ratio of the higher harmonics measured in a magnetic particle spectrometer (MPS).

3 Results

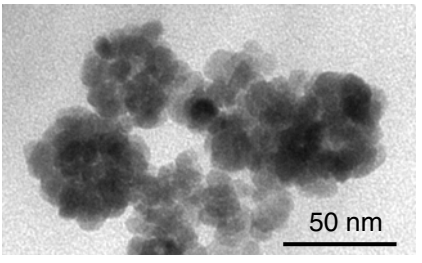

Fig. 1. Typical TEM image of a MCNP sample (sample B).

In the TEM images (Figure 1) clusters in the size range from 20 to 80 nm as well as a small proportion of single cores were found. These are good preconditions for a size dependent fractionation of clusters of different size. The clusters in the starting fluids consist of cores of 11.2 nm (sample A) and 12.7 nm (sample B), as measured by XRD. The success of the fractionation procedure was confirmed by PCS, MRX, and VSM (Table 1). By the fractionation clusters with hydrodynamic diameters (PCS, z-ave) from 100 to 800 nm were obtained. VSM measurements confirmed a correlation of the hydrodynamic cluster size with the effective magnetic volume of the particles in these fractions – e.g., with increasing particle size the coercivity (Hc) of the B-particles increased from 3.5 to 25.8 Oe.

Table 1. Particle size obtained from different methods and coercivity *Hc* of all samples.

Sample	D(PCS) [nm]	D(MRX) [nm]	D(XRD) [nm]	Hc [Oe]	
				liquid	powder
A	268	288	11.2	3.1	6.4
A-1	267	287	11.3	2.6	6.1
A-2	209	252	10.9	1.0	4.1
A-3	151	188	10.5	0.2	3.0
A-4	102	119	10.5	0.1	1.9
B	801	433	12.7	20.1	25.8
B-1	791	457	13.2	20.1	24.0
B-2	701	504	12.8	19.5	22.4
B-3	496	400	13.1	18.5	21.0
B-4	363	350	12.9	16.6	21.0
B-5	205	174	12.4	10.2	15.6
B-6	124	123	12.3	7.8	3.5

In the frame of the measurement accuracy the size of the cores D(XRD) in each sample set is constant. This means that here only the influence of the cluster size on the MPS signal in each sample set was investigated. Partially, clusters of identical size from both sample sets were prepared (e.g. A-2 and B-5). For this case the influence of the core size is dominating the magnetic dynamic behaviour: Analysing the SQUID M(H) data of the original fluids A and B by a method slightly modified with respect to Chantrell method [Eberbeck et al within this book], we found that about 90% (by volume) of the MCNP have diameters D_V corresponding to the mean volume of 10.5 nm and 12 nm for A and B, respectively, where the width of the distribution σ is significantly larger for A (σ=0.43) then for B (σ=0.29). On the other hand, the analysis of MRX data, probing the magnetisation dynamics in the range of f = 1 Hz...3 kHz in immobilised MCNP, reveals in the framework of the applied model of non-interacting magnetic moments a huge width of the effective anisotropy energy barrier distribution of σ=0.65 for B, whereas σ=0.33 for sample A. To explain this difference we propose two possible hypotheses: (i) The hydrodynamic diameters are much larger and (ii) the sizes of single cores are slightly larger in B than in A. Both facts may lead to a broader distribution of the effective energy barriers due to (i) stronger dipole-dipole interaction and in case of hypothesis (ii) due to a larger anisotropy energy of the single cores leading to a higher fraction of single crystal moments the Néel relaxation of which is blocked.

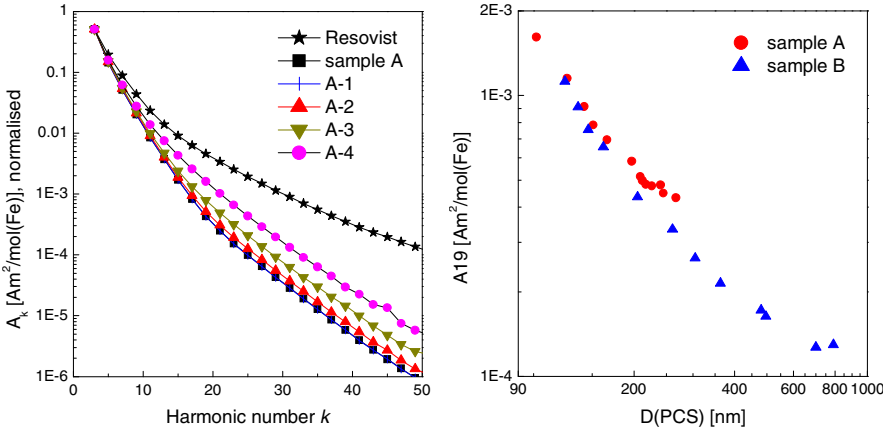

Fig. 3. a) Amplitudes of higher harmonics scaled to 3rd one for all fractions of sample A in comparison to Resovist® (asterisks). b) Attenuation of the 19th harmonic, scaled to the 3rd one, in dependence on cluster size.

Suitable tracers for MPI require a low degree of decrease of the amplitudes of higher harmonic for increasing numbers of harmonics. Up to now Resovist® shows nearly the best signal. The MPS investigation of our

particles showed a clear dependence of the quality of MPS signal on the hydrodynamic diameter of the particles and thus the cluster size. In Figure 3a it is clearly to see that the smallest particles show the best MPS signal. Figure 3b shows the ratio of the 19^{th} to the 3^{rd} harmonic in dependence on particle size. Fractions with smaller clusters from sample A and B show similar behaviour and the best ratio. The ratio decreases with increasing cluster size and found a really low value for the largest clusters from sample B. The reason for this behaviour is the increasing magnetic energy barrier in bigger particles (represented by an increasing coercivity) which inhibits a sufficient magnetic excitation of the large clusters.

4 Conclusion

In this work a clear correlation between primary particle size, cluster size, and MPS signal was found. For the investigated size range the smallest clusters show the best signal. For clusters of comparable size but different primary particle size the MCNP with the smallest primary particles show the best signal. Altogether the investigated samples are magnetically too hard to achieve the performance of Resovist regarding MPI suitability. That why, for further investigations we suggest to decrease cluster size and primary particle size – clusters in the range from 20 to 30 nm consisting of 5 to 8 nm cores seem to be promising for further investigations.

References

1. Eberbeck, D., et al.: Evidence of aggregates of magnetic nanoparticles in suspensions which determine the magnetisation behaviour. In: Magnetic Nanoparticles – Proceedings of the First International Workshop on Magnetic Particle Imaging, pp. 66–72. World Scientific (2010)
2. Dutz, S., et al.: Ferrofluids of magnetic multicore nanoparticles for biomedical applications. J. Magn. Magn. Mater. 321(10), 1501–1504 (2009)
3. Eberbeck, D., et al.: Aggregation behaviour of magnetic nanoparticle suspensions investigated by magnetorelaxometry. J. Phys. Condens. Matter. 18, 2829 (2006)

Precision Synthesis of Iron Oxide Nanoparticles and Their Use as Contrast Agents

Jan Niehaus[1], Sören Becker[2], Christian Schmidtke[2], Katja Werner[1], and Horst Weller[1,2]

[1] Center for Applied Nanotechnology GmbH,
[2] Institute Of Physical Chemistry, University Hamburg, Grindelallee 117, 20146 Hamburg, Germany
Niehaus@can-hamburg.de

Abstract. The use of magnetic nanoparticles as contrast agents in biomedical applications requires highly reproducible markers soluble in aqueous media. Here we present a modular approach for the formation of a magnetic contrast agent, which is composed of an inorganic core like iron oxide and a water solubility mediating polymer shell. The shell can also be a carrier for specific affinity molecules like antibodies or peptides, which offer the possibility to selectively target surface receptors upon cells.

1 Introduction

The detection of chronic diseases like cancer and infectious diseases often the visualization of changes down to cellular level is required to monitor changes and progression of the malady.[1, 2] The most popular imaging method using magnetic phenomena for readout is the magnetic resonance imaging (MRI), detecting changes in nuclear spin arrangement of the sample. In 2004 Gleich and Weizenecker presented another imaging method using magnetism, the magnetic particle imaging (MPI). This method is using iron oxide nanoparticles as direct markers.[3]

However the spatial resolution of magnetic imaging methods is limited by the quality of the contrast agent. For the use of iron oxide as magnetic material highly monodispers particles are needed due to size dependence of the magnetic behavior.[4, 5]

2 Material and Methods

Materials

All chemicals were bought at Sigma-Aldrich with purities higher than 90% and were used without further purification.

T.M. Buzug and J. Borgert (Eds.): Magnetic Particle Imaging, SPPHY 140, pp. 87–91.
springerlink.com

The poly(isoprene-*b*-ethylene oxide) (PI-PEO) and the polyisoprene-diethylenetriamine (PI-N3) were produced by anionic polymerization in the group of Prof. Weller.

Synthesis of Iron Oxide Nanoparticles

The 10 nm iron oxide particles were synthesized using standard inert gas techniques. 10.5 g (45.8 mmol) *N,N*-Dimethyldodecylamine *N*-oxide and 14.5 mL (45.6 mmol) oleic acid were dissolved in 400 mL dioctyl ether at 100 °C. 2.0 mL (15 mmol) $Fe(CO)_5$ were quickly added to the solution and stirred for 2 h at 130 °C. Finally the reaction solution was slowly heated up to 295 °C and grown for 1 h at this temperature. At room temperature the particles were separated by the addition of ethanol and centrifugation. The particles were dissolved in an unpolar media e.g. hexane or toluene and purified by further precipitation and dissolving steps.

For the synthesis of 15 nm iron oxide nanoparticles 172 mg (1.94 mmol) FeO(OH) were suspend in a mixture of 3.69 mL (11.6 mmol) oleic acid and 6.4 mL 1-octadecene. The mixture was heated up to 315 °C within 15 min. After 30 min under reflux the mixture was cooled to room temperature, and the nanoparticles were precipitated using an excess of polar solvent like acetone or ethanol and separated by a centrifugation step. The particles were purified in the same way a described above.

The 20 nm particles were synthesized using the reaction conditions described for the 15 nm particles using FeO(OH) as a precursor. A FeO(OH) to oleic acid ratio of 1:7.5 was used and the reaction time was elongated to 4 h.

Continuous Flow Phase Transfer Approach

The particles (10 nmol) were added to a solution of PI-N3 (6 µmol) in hexane. The coated particles were precipitated using an excess of ethanol and separated by centrifugation. A solution of particles, diblock copolymer (500 nmol) and AIBN (41 µmol) in THF (3.3 mL) was formed. This solution was transferred into water using a microfluidic mixing chamber and a syringe pump. The resulting dispersion was heated to 75 °C for 2 h. Finally the concentration of the aqueous solution was adjusted by filtration.

3 Results and Discussion

Synthesis of Magnetic Cores

The synthesis of the iron oxide nanoparticles were performed in high-boiling solvents like 1-octadecene or dioctyl ether to achieve nucleation and growth temperatures around 300 °C. These temperatures were needed for the thermal decomposition of the *in situ* formed iron oleate complexes. To obtain cores with different magnetic behavior the sizes of the particles were tuned by varying the reaction parameters.[6, 7]

Using $Fe(CO)_5$ and dioctyl ether in combination with *N,N*-Dimethyldodecylamine *N*-oxide as an oxidizing agent it was possible to form iron oxide nanoparticles with a diameter around 10 nm. A TEM image is shown in figure 1.

The use of FeO(OH) as an iron precursor and 1-octadecene led to a particle diameter of 15 nm and 20 nm respectively. The variation of iron source to ligand ratio as well as the reaction time allowed a differentiation between both diameters. The resulting particles are shown in figure 1.

The yielded nanoparticles show a high degree of monodispersity and crystallinity. The oleic acid coating of the particles ensures solubility in non-polar media like hexane without formation of agglomerates or sedimentation.

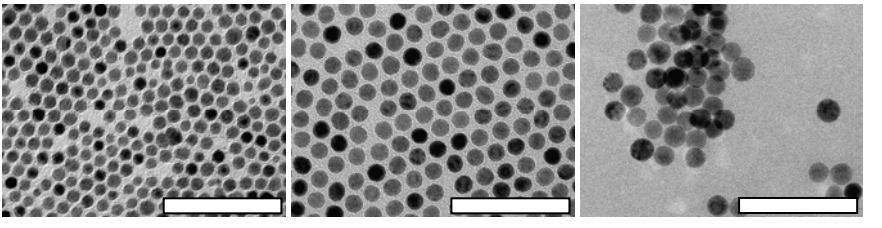

Fig. 1. TEM images of iron oxide particles with different diameters: 10 nm (left), 15 nm (middle) and 20 nm (right), scale bar: 100 nm

Formation of Nanocapsules

A phase transfer from non-polar to aqueous media is essential for the biological use of the described particles. This was achieved by the formation of nanosized capsules using tailor-made copolymers in a two-step process. First the inorganic cores were coated with PI-N3 via a ligand exchange in solution. This step is necessary to stabilize the particles during the final encapsulation to avoid uncontrolled aggregation of the particles. The coated particles were mixed with an amphiphilic PI-PEO copolymer. The resulting solution was injected into water. During this mixing step the amphiphilic copolymer forms micelles encapsulating the nanoparticles. After the transfer into water, the capsules get crosslinked by radical polymerization at 75 °C. This procedure is shown in figure 2.

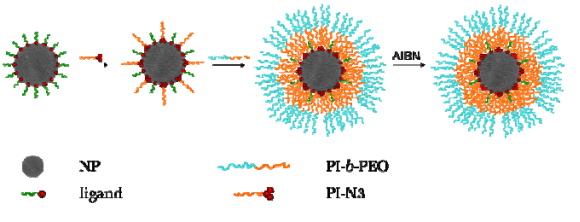

Fig. 2. Schematic overview of the encapsulation procedure

The most crucial step during the described process is the mixing of the organic and the aqueous phase. Here the dispersity and stability of the capsules are getting defined. To ensure a high degree of reproducibility, a continuous flow phase transfer approach for the encapsulation using microfluidic components was developed. These microfluidic components enhance the reproducibility of the capsule's formation by the control of mixing conditions and offer the possibility of easy scale-up. Figure 3 shows the size distribution of the capsules in water for different batches and over time.

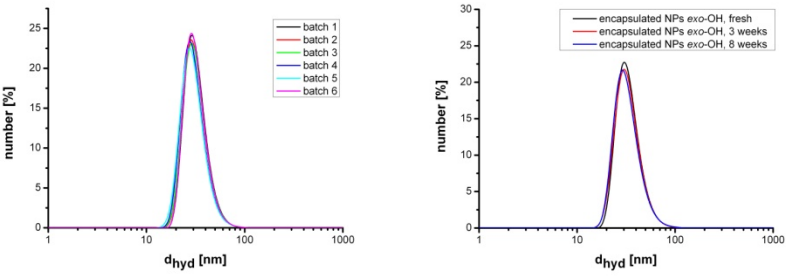

Fig. 3. DLS measurements of the PI-PEO capsules containing iron oxide particles

For the formation of a molecular contrast agent, functional groups on the outer sphere are needed for the attachment of specific antibodies or peptides. The used PI-PEO can be modified so that the following groups are accessible on the surface of the capsule: OH, COOH and NH_2. The synthesis and modification of the polymers was done at Prof. Weller's group. In figure 4 it can be seen that the functional group has only little influence on the capsule size.

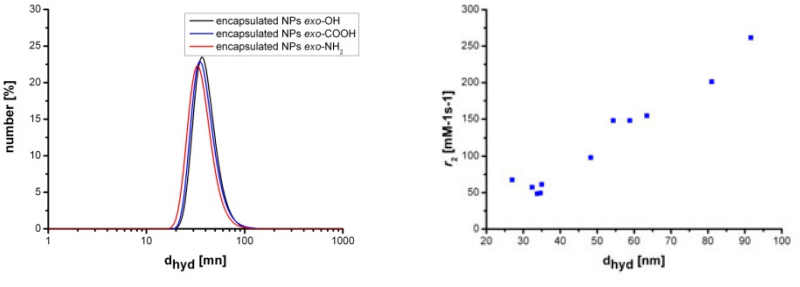

Fig. 4. DLS measurements of functionalized capsules (left) and capsule size dependence of r_2 (right)

Using nanoparticles like iron oxide it is possible to influence the number of particles per capsule by variation of the mixing speed. If a quick mixing step is used, uniform capsules with a small size and just one particle inside are formed. A less powerful mixing steps leads to the formation of bigger capsules with clustered iron oxide particles inside. This is very interesting especially for magnetic nanoparticles as the magnetic properties changes with the number of particles per capsule. Figure 4 shows the correlation of the hydrodynamic diameter and the transvers relaxivity r_2.

All different sizes of capsules were made using the continuous flow phase transfer approach but with different flow rates and mixing chambers. Figure 4 shows that single encapsulated particles exhibit a small r_2. With increasing cluster size an increase of r_2 from 50 up to 250 mM-1s-1 can be observed. Even larger clusters do not form stable dispersions in water anymore.

4 Conclusion

Using thermal decomposition methods it was possible to synthesis iron oxide particles with a small size distribution and different diameters. In combination with the developed continuous flow phase transfer approach a highly stable and reproducible magnetic contrast agent could be formed. The resulting capsules can be produced with different functional groups on the surface. The r_2 can be tuned by controlled clustering of the iron oxide particles.

References

1. Yoo, D., Lee, J.-H., Shin, T.H., Cheon, J.: Theranostic Magnetic Nanoparticles. Accounts of Chemical Research 44, 863–874 (2004)
2. Jun, Y.-W., Lee, J.-H., Cheon, J.: Chemisches Design von leistungsfähigen Nanosonden für die Kernspintomographie. Angewandte Chemie 120, 5200–5213 (2008)
3. Gleich, B., Weizenecker, J.: Tomographic imaging using the nonlinear response of magnetic particles. Nature 435, 1214–1217 (2005)
4. Tromsdorf, U.I., Bruns, O.T., Salmen, S.C., Beisiegel, U., Weller, H.: A Highly Effective, Nontoxic T1 MR Contrast Agent Based on Ultrasmall PEGylated Iron Oxide Nanoparticles. Nano Letters 9, 4424–4440 (2009)
5. Weizenecker, J., Borgert, J., Gleich, B.: A simultation study on the resolution and sensitivity of magnetic particle imaging. Physics in Medicin and Biology 52, 6363–6374 (2007)
6. Yu, W.W., Falkner, J.C., Yavuz, C.T., Colvin, V.L.: Synthesis of monodisperse iron oxide nanocrystals by thermal decomposition of iron carboxylate salts. Chemical Communication, 2306–2307 (2004)
7. Hyeon, T., Lee, S.S., Park, J., Chung, Y., Na, H.B.: Synthesis of Highly Cristalline and Monodisperse Maghemite Nanocrystallites without a Size-Selection Process. Journal of the American Chemical Society 123, 12798–12801 (2001)

Synthesis of Single-Core Iron Oxide Nanoparticles as a Tracer for Magnetic Particle Imaging

Aidin Lak, Thilo Wawrzik, Frank Ludwig, and Meinhard Schilling

Institut für Elektrische Messtechnik und Grundlagen der Elektrotechnik,
TU Braunschweig, Hans-Sommer-Str. 66, 38106 Braunschweig, Germany
a.lak@tu-bs.de

Abstract. Superparamagnetic single-core iron oxide nanoparticles coated with oleic acid have been synthesized via high temperature decomposition of iron-oleate precursor. The particle's core and hydrodynamic size distributions are characterized utilizing a variety of methods including Fluxgate Magnetorelaxometry (MRX) and Photon Cross-correlation Spectroscopy (PCCS). The harmonic spectra of mobile and immobile samples were measured using our homebuilt Magnetic Particle Spectrometer (MPS) whereby the suitability of the synthesized particles as a tracer for MPI is analyzed. Furthermore, the MPS spectra of the fabricated single-core nanoparticles are compared with the harmonic spectra of Resovist® (Bayer Schering Pharma, Berlin) and Ocean NanoTech nanoparticles.

1 Introduction

The Magnetic Particle Imaging (MPI) technique has been attracting lots of attention since it has emerged due to its simplicity and low cost in comparison with other imaging methods. Since the invention of MPI by Gleich and Weizenecker [1], the fabrication of magnetic nanoparticles (MNPs) as a suitable tracer for MPI has been an issue of several research studies [2].

Having reviewed the recent research studies about the fabrication of optimum MNP tracers for MPI, it was found that in most studies commercially available multi-core particles with an approximate hydrodynamic and core sizes of ~60 nm and ~6 nm, respectively, such as Resovist® (Bayer Schering Pharma, Berlin), have been used even though their mass sensitivity and spatial resolution are relatively low [1,2]. Considering that the particle's harmonic spectra are related to the nonlinearity of the magnetization curve, minimum magnetic excitation field amplitudes are desirable for MPI contrast agents. On the other hand, it is known that the bigger the primary particles core size, the lower is the driving field frequency that has to be applied to observe the harmonic spectra. Bearing these criteria in mind,

T.M. Buzug and J. Borgert (Eds.): Magnetic Particle Imaging, SPPHY 140, pp. 93–97.
springerlink.com

single-core monodisperse MNPs with an approximate core size of ~20 nm are unquestionably candidates of interest for further investigations. Noteworthy, both image spatial resolution and mass sensitivity, which depend on the particle size distribution, are not fully achieved when multi-core particles are used. In spite of what was mentioned above, few studies have been carried out to characterize the suitability of single-core MNPs for MPI.

In this work, ~20 nm superparamagnetic single-core monodisperse iron oxide nanoparticles have been fabricated via high temperature decomposition of iron-oleate precursor. The suitability of the synthesized particles for MPI was studied by performing Magnetic Particle Spectroscopy (MPS) measurements. The comparison of the harmonic spectra of the self-synthesized nanoparticles and the commercially available ferrofluids, such as Resovist®, will be presented and discussed.

2 Material and Methods

Chemicals

$FeCl_3 \cdot 6H_2O$ (Sigma-Aldrich, 98%), docosane (Sigma-Aldrich, 99%), hexane (95%), ethanol (99.8%), chloroform (HPLC grade, 99.9%), oleic acid (TCI, 99%), and sodium oleate (TCI, 97%) were utilized “as received” and without further purification.

Synthesis

For the synthesis of the iron-oleate precursor, initially 80 mmol of sodium oleate was poured into a round bottom flask connected to a Schlenk line and degassed three times using evacuation-filling with argon. Afterwards, 24 mmol of $FeCl_3 \cdot 6H_2O$ dissolved in 36 mL distilled water, 48 mL of ethanol, and 84 mL of hexane were loaded into the flask using the Schlenk-line technique. The mixture was heated to reflux under flow of argon for 4 h. The obtained dark reddish top layer was intensively washed three times with 60 mL distilled water in a separatory funnel and next hexane was evaporated off using a rotary evaporator. The resultant reddish waxy product was dried in a vacuum oven at 70ºC for 24 h.

In a typical MNPs synthesis procedure, 2 mmol iron-oleate, 6 mmol oleic acid and 7.8 gr docosane (hydrocarbon $C_{22}H_{46}$, solid at room temperature) were loaded into a three-neck round bottom flask attached to a Schlenk-line, and were degassed for 30 minutes at 100ºC, ending with filling with argon. After that, the solution was heated to 370 ºC at the rate of 3 ºC/min (using a temperature controller) to reflux under flow of argon for 30 minutes. The resulting black suspension was cooled down to 60ºC. Afterwards, MNPs were washed and separated by adding a 4:1 acetone/hexane mixture and centrifuging the obtained solution. This process

was repeated two times. The obtained MNPs are readily dispersible in chloroform due to the presence of oleic acid molecules on their surfaces.

Characterization

To trace the particle's Néel relaxation, the MNP's Brownian motion was blocked by solidification of 100 µL suspension with 140 mg gypsum (so-called immobile sample). The particle's Néel relaxation was measured by performing fluxgate magnetorelaxometry (MRX) measurements at a magnetizing field of 2 mT on the immobile samples and the core size distribution was derived from the relaxation curves using the magnetic moment superposition model (MSM). Details of the model can be found in [3]. The size and morphology of the particles were characterized by Field-emission Scanning Electron Microscopy (FE-SEM). The hydrodynamic diameter of the particles was determined by Photon Cross-correlation Spectroscopy (PCCS) (Nanophox, Sympatec GmbH). To study the capability of the particles as a tracer for MPI, MPS measurements were conducted using our homebuilt Magnetic Particle Spectrometer [4] with an excitation field amplitude of 20 mT and a frequency of 9.96 kHz. The iron molar mass of the synthesized particle's suspension was estimated via the Prussian blue method. The results were used to correct the MPS spectra for different iron contents.

3 Results

Fig. 1(a) shows the particle core and hydrodynamic size distributions which were acquired from MRX and DLS measurements, respectively. As can be seen, the particle core and hydrodynamic sizes are around 20 and 30 nm, respectively. Apparently, the particles show a narrow distribution of core (σ_{core}=0.14) and hydrodynamic (σ_{hydro}=0.17) diameters. By knowing that the particle's shell (i.e., oleic acid) thickness is about 3 nm and comparing the core and hydrodynamic sizes, it is deduced that the particles are sparsely distributed in the medium. Moreover, no trace of clusters in the sample has been observed in DLS measurements. Besides, the fact that the MRX signal of the immobile sample decreased to zero after switching off the magnetizing field indicates that the particles are superparamagnetic. Fig. 1(b) depicts a typical FE-SEM micrograph of the synthesized iron oxide nanoparticles. A monolayer of the nearly spherical particles is formed on the substrate, representing the particle's size and shape uniformity.

The harmonic spectra of the fabricated 20 nm single-core particles in both mobile and immobile states are shown in Fig. 2. It can be seen that both spectra show harmonics up to 500 kHz and they are virtually identical which indicates that almost all of the particles are able to follow the driving field frequency (i.e. 9.96 kHz). For comparison, MPS spectra of Resovist® (hydrodynamic size of ~60 nm) and Ocean NanoTech iron oxide nanocrystals (SHP-20, nominal core size of 20 nm) suspensions were plotted in the same graph.

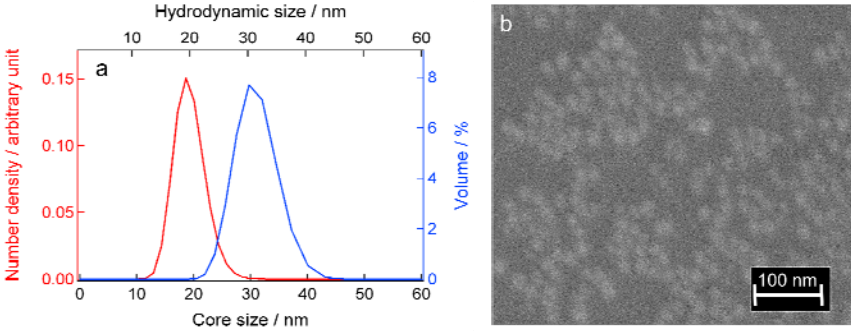

Fig. 1. (a) The core and hydrodynamic size distributions of the single-core iron oxide nanoparticles obtained from MRX and DLS measurements, respectively. (b) A typical FE-SEM micrograph of the iron oxide nanoparticles.

As can be seen, the spectral magnitude of harmonics of the synthesized 20 nm single-core particles is slightly larger than Resovist® up to about 190 kHz, where both reach the same level. This observation can be explained by the fact that in Resovist® (crystallite size of ~6 nm) only the large clusters contribute to the MPS signal [5] whereas nearly all of the synthesized 20 nm single-core particles are involved. Conversely, from 200 kHz to 500 kHz, the spectral magnitude of harmonics of Resovist® exceeds the 20 nm single-core particles. The slower decay of the harmonic magnitudes is attributed to the bigger effective magnetic moments of the clusters (~60 nm) of Resovist® than those of the self-synthesized particles.

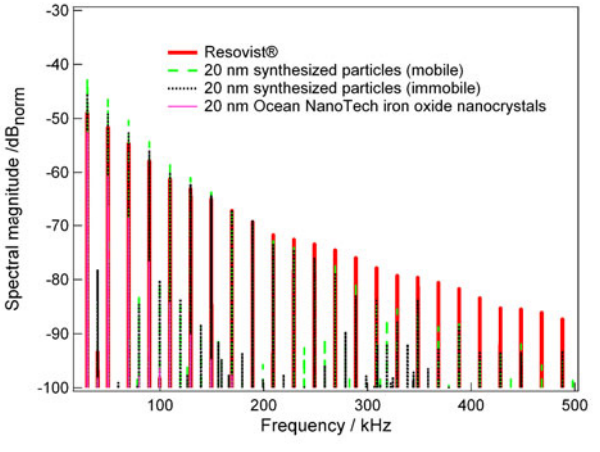

Fig. 2. Harmonic spectra of the synthesized 20 nm single-core nanoparticles (both mobile and immobile samples), Resovist® and Ocean NanoTech 20 nm iron oxide nanocrystals. All spectra were normalized to 70mM (Fe).

In contrast, the harmonics of the SHP-20 drop dramatically fast and can be seen solely up to 150 kHz. This behavior can be related to a smaller magnetically active core size and a lower surface crystallinity of the SHP-20 compared to the self-synthesized particles.

4 Conclusion

To sum up, it has been demonstrated that the self-synthesized particles shows a sufficient number of harmonics with substantially large magnitudes, allowing one to reconstruct images with a reasonable quality. Moreover, these particles reveal narrow core and hydrodynamic size distributions, as can also be seen from the linearity of the harmonics decay, eventually leading to a better spatial resolution. By and large, the self-synthesized particles with the large iron core and relatively narrow hydrodynamic size distribution have been found as an appropriate compromise between Resovist® consisting of clusters of small primary crystallites and the monodisperse SHP-20 MNPs from Ocean NanoTech.

Acknowledgments. This work was financially supported by the DFG via SFB 578. Financial support by the International Graduate School of Metrology at Braunschweig (igsm) for PhD thesis (A.L.) is appreciated.

References

1. Gleich, B., Weizenecker, J.: Tomographic imaging using the nonlinear response of magnetic particles. Nature 435, 1214–1217 (2005)
2. Ferguson, R.M., Minard, K.R., Khandhar, A.P., Krishnan, K.M.: Optimizing magnetite nanoparticles for mass sensitivity in magnetic particle imaging. Med. Phys. 38(3), 1619–1626 (2011)
3. Ludwig, F., Heim, E., Schilling, M.: Characterization of superparamagnetic nanoparticles by analyzing the magnetization and relaxation dynamics using fluxgate magnetometers. J. Appl. Phys. 101, 113909 (2007)
4. Wawrzik, T., Ludwig, F., Schilling, M.: Magnetic particle spectroscopy for the evaluation of eld-dependent harmonics generation, pp. 86–91. World Scientific (2010)
5. Eberbeck, D., Wiekhorst, F., Wagner, S., Trahms, L.: How the size distribution of magnetic nanoparticles determines their magnetic particle imaging performance. Appl. Phys. Lett. 98, 182502 (2011)

New Perspectives for MPI: A Toolbox for Tracer Research

Nicole Gehrke[1], Andreas Briel[1], Frank Ludwig[2], Hilke Remmer[2], Thilo Wawrzik[2], and Stefan Wellert[3]

[1] nanoPET Pharma GmbH, Robert-Koch-Platz 4, 10115 Berlin, Germany
nicole.gehrke@nanopet.de
[2] Institut für Elektrische Messtechnik und Grundlagen der Elektrotechnik, TU Braunschweig, Hans-Sommer-Str. 66, 38106 Braunschweig, Germany
f.ludwig@tu-bs.de
[3] Stranski Laboratorium, TU Berlin, Straße des 17. Juni 124, 10623 Berlin, Germany
s.wellert@tu-berlin.de

Abstract. Since its invention, magnetic particle imaging (MPI) has gained increasing attention in academic as well as industrial research and development. It requires the application of an imaging agent, but the structure-efficacy relations are far from being fully understood and no ideal MPI tracer has been found so far. Here, we present a systematic investigation of the size dependence of the MPI spectra of identically composed, but differently sized iron oxide nanoparticles. We furthermore present a small angle X-ray scattering (SAXS) study as a route to assess the particle core structure. To that goal we used FeraSpin™ R and the FeraSpin™ Series (XS to XXL). We show that FeraSpin R offers an equal whereas FeraSpin L to XXL offer an improved MPI signal as compared to the hitherto "gold-standard" Resovist®. Moreover, the FeraSpin Series constitutes a versatile "toolbox" for MPI tracer research.

1 Introduction

Magnetic particle imaging (MPI) is a new imaging modality with a high potential impact on diagnostic imaging due to its unique properties such as its fast scanning speed and the highly sensitive and quantitative tracer detection [1-3]. Promising tracer materials are iron oxide nanoparticles which are already safely used as MRI contrast agents in humans. In particular, yet unmet clinical needs such as the rapid and reliable differentiation between stroke and cerebral hemorrhage or the non-invasive diagnostics of coronary heart diseases could highly benefit from MPI. So far, the currently known tracer materials do not provide sufficient MPI signal and are far from their theoretical limit. Even the hitherto "gold-standard" Resovist® [1,4,5] was estimated to contain only a 3% fraction of particles with the desired signal [1].

T.M. Buzug and J. Borgert (Eds.): Magnetic Particle Imaging, SPPHY 140, pp. 99–103.
springerlink.com

Furthermore, Resovist is no longer available and, therefore, Resovist cannot be used for MPI tracer research. Thus, to bring MPI to clinical practice there is an urgent need to understand the structure-efficacy relation of the magnetic nanoparticles so as to subsequently generate MPI tracers with the desired performance - while still providing a material suitable for human application.

2 Material and Methods

FeraSpin™ R and the FeraSpin™ Series are manufactured by nanoPET Pharma GmbH (Berlin) and internationally distributed by Miltenyi Biotec (Bergisch-Gladbach). The FeraSpin Series comprises six products of different particle sizes (FeraSpin XS, S, M, L, XL and XXL) which have been extracted from FeraSpin R and therefore contain narrowly size distributed particles of identical composition. Their mean hydrodynamic diameters are 60 nm for FeraSpin R and 18, 25, 35, 45, 55 and 65 nm for FeraSpin XS, S, M, L, XL and XXL respectively. Resovist® was still stocked in the author's labs. MPS measurements were performed with a homebuilt spectrometer [6]. The excitation field had an amplitude of 20 mT at a frequency of 9.96 kHz, no dc field was applied. Small angle X-ray scattering (SAXS) was measured using a SAXSess mc^2 system in line collimation, operated at 40 kV and 50 mA producing Cu Kα radiation of a wavelength of 0.154 nm. Initial data treatment, background subtraction and desmearing was done using the SAXSquant 3.5 software package.

3 Results

MPS measurements showed that FeraSpin R exhibits the same harmonic spectrum as Resovist. As expected, systematic differences were observed for the FeraSpin Series. Fig. 1 depicts the spectra measured at the highest iron concentration investigated here (roughly 70 mM) normalized to the same iron content.

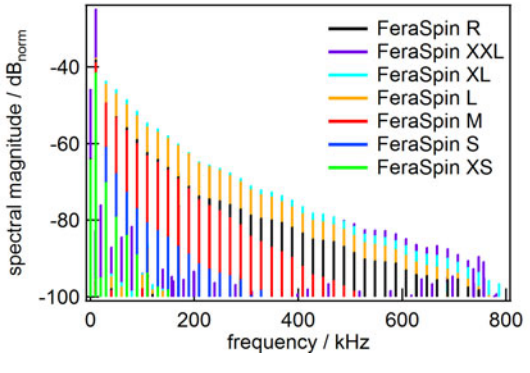

Fig. 1. Harmonic spectra of FeraSpin R and the FeraSpin Series (XS to XXL) in suspension. All spectra were normalized to 67 mM iron.

The slope of the harmonic spectra gradually decreases with hydrodynamic particle size, i.e., from FeraSpin XS to FeraSpin XXL, and the overall spectral magnitude of the harmonics increases. Thereby, the magnitude of FeraSpin XXL is almost identical to that of XL for frequencies up to 500 kHz and a factor of 1.3 larger for higher frequencies. In comparison to FeraSpin R, a 2.5-fold increase of the magnitude is observed. The MPS spectra were also recorded after dilution by a factor of 10 and 100, and no differences are discernible after normalization to account for the different concentrations (data not shown). Fig. 2 depicts the harmonic spectra of the immobilized reference samples. For FeraSpin L, XL, XXL and R the harmonics decay much faster than those of the respective suspensions, however, for FeraSpin XS, S and M the spectra of the suspensions and immobilized samples are similar.

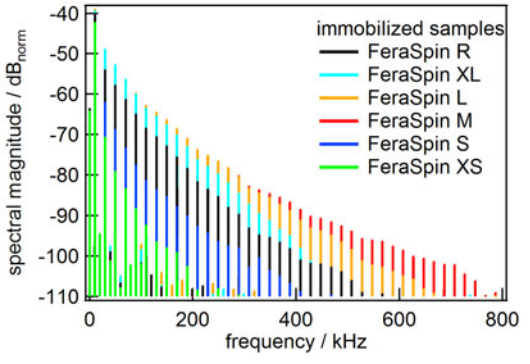

Fig. 2. Harmonic spectra of the immobilized FeraSpin samples. All spectra were normalized to the same iron content.

Fig. 3 shows the scattered X-ray intensity I(Q) as a function of the scattering vector Q in double-logarithmic representation for FeraSpin XS to XXL. The signal originates from the particle cores as a contribution from the outer coating can be neglected due to its low contrast with the solvent. The intensity at Q=0 increases from FeraSpin XS to XXL. The inset shows the measured data transformed into a Kratky type representation in the form $I(Q)*Q^2$ as a function of Q. The bell-shaped curves show a maximum in the low Q range shifting towards lower Q from FeraSpin XS to XXL.

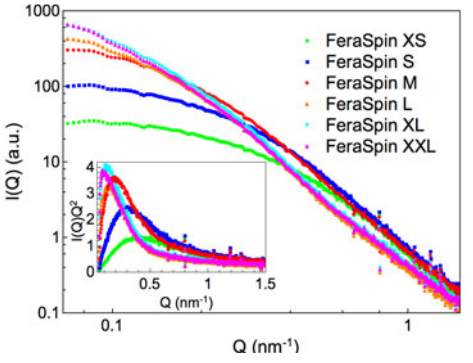

Fig. 3. SAXS spectra and Kratky plot of the FeraSpin Series (XS to XXL).

4 Discussion

FeraSpin R appears to be ideally suited as a new standard reference material for MPI research due to the equality of its MPS spectrum to that of Resovist. The identical particle composition of all FeraSpin products allows us to exclusively investigate the influence of particle size. Our findings show that the MPS signal can be improved by adjusting the particle size as can be concluded from the richer harmonic spectrum, i.e., the decreased slope and the higher spectral magnitude of the large particles FeraSpin L to XXL as compared to FeraSpin R (Fig.1). The stronger harmonics above 500 kHz of FeraSpin XXL as compared to XL may be indicative of a remanence occurring only for FeraSpin XXL having the largest size studied here. Due to the exclusive influence of size it is feasible to evaluate these results quantitatively in more detail which is subject of ongoing work. A potential influence of interparticular interactions can be excluded from the comparison of the spectra of different dilutions. In contrast to that, the spectra of the immobilized reference samples (Fig. 2) of FeraSpin L to XXL are different from those of the respective suspensions (Fig. 1) which can be attributed to the fact that in the immobilized state only internal Néel relaxation can occur. However, the spectra of FeraSpin XS to M show no such significant differences between the dispersed and immobilized state which led us to the conclusion that for FeraSpin XS, S and M the internal Néel relaxation dominates also in the suspension [7]. This is in congruence with the smaller iron oxide core size (as well as overall particle size) of FeraSpin XS to M as compared to FeraSpin L to XXL. In this context it is important to point out that the iron oxide cores of the FeraSpin particles are differently sized “clusters” of the same elementary crystallites having a diameter of about 5 nm. As such crystallites should possess very short Néel time constants, all particles should follow the 9.95 kHz excitation field [7]. Consequently, the differences for FeraSpin L to XXL must be attributed to the formation of clusters, their size and the crystallites interaction inside the clusters.

Furthermore, it must be noted that now FeraSpin M exhibits the richest spectrum which is of particular interest for MPI applications where immobilized particles are involved, e.g. when bound to a certain target or accumulated in a certain tissue. In congruence with the MPS results, the SAXS data indicate an increasing size of the scattering objects, i.e. the particle cores, from FeraSpin XS to XXL. Moreover, the Kratky plot suggests a rigid, eventually globular structure with length scales of 5-7 nm for FeraSpin XS to 30-40 nm for FeraSpin XXL which is in agreement with the latter having the richest MPS spectrum. Further analysis by a mass fractal analysis will provide more insight into distinct structure and size distribution of the clusters comprising the particle cores.

5 Conclusion

The particle size dependence of the MPS spectra was investigated using FeraSpin^{TM} nanoparticles. SAXS measurements were performed to study the particle cores. We show that FeraSpin R can serve as a new standard material, while the size-selected FeraSpin Series particles (XS to XXL) offer versatile opportunities for MPI tracer research and the optimization for both *in vitro* as well as *in vivo* applications. In a next step, a more detailed, quantitative evaluation of the results reported here will provide a deeper understanding of the nanoparticle parameters defining the MPS characteristics to allow for more focused MPI tracer optimization.

References

1. Gleich, B., Weizenecker, J.: Tomographic imaging using the nonlinear response of magnetic particles. Nature 435, 1214–1217 (2005)
2. Weizenecker, J., et al.: A simulation study on the resolution and sensitivity of magnetic particle imaging. Phys. Med. Biol. 52, 6363–6374 (2007)
3. Biederer, S., et al.: Trajectory analysis for magnetic particle imaging. Phys. Med. Biol. 54, 385–397 (2009)
4. Biederer, S., et al.: Magnetization response spectroscopy of superparamagnetic nanoparticles for magnetic particle imaging. J. Phys. D: Appl. Phys. 42, 1–7 (2009)
5. Weizenecker, J., et al.: Three-dimensional real-time in vivo magnetic particle Imaging. Phys. Med. Biol. 54, L 1–10 (2009)
6. Wawrzik, T., et al.: Multivariate Magnetic Particle Spectroscopy for Magnetic Nanoparticle Characterization. Proc. of AIP Conf., vol. 1311, pp. 267–270 (2010)
7. Ferguson, R.M., et al.: Optimization of nanoparticle core size for magnetic particle imaging. J. Magn. Magn. Mater. 321(10), 1548–1551 (2009)

Superparamagnetic Iron Oxide Nanoparticles: Evaluation of Stability of SPIONs in Different Milieu for Magnetic Particle Imaging

Kerstin Lüdtke-Buzug and Céline Borchers

Institute of Medical Engineering, University of Luebeck, Ratzeburger Allee 160
Lübeck, 23562, Germany
luedtke-buzug@imt.uni-luebeck.de

Abstract. Today, a variety of different nanoparticles are used in various applications. In particular, super-paramagnetic iron oxide nanoparticles (or SPIONs) are used *in vitro* for cell separation and *in vivo* for hyperthermia or as contrast agent for magnetic resonance imaging (MRI). However, in Magnetic Particle Imaging (MPI), SPIONs play a fundamental role as tracer material. In addition to the overall size of the particles and the particle coating, which are important for medical applications, it is the magnetic core diameter that is relevant for the performance in MPI applications. In general, for *in vivo* applications, the stability of the particles is of key importance. Therefore, in this paper, the stability of the SPIONs have been analyzed in different particle suspension media.

1 Introduction

Due to their rather scientifically interesting and technically attractive properties nanoparticles have been in the focus of numerous research activities [1-3], which may have also great potential for use in medicine [4], magnetic resonance imaging [5] (MRI) or even in environmental sciences [6]. Nowadays, nanoparticles come more and more to the focus in medical research directions as, for instance, for innovative carrier agents that may transport therapeutic substances [7] or the particles act as tracer material for imaging applications [8]. For example, magnetic nanoparticles play an essential role in MRI, where they are typically used as contrast media leading to an enhancement of structured of the acquired images [9] due to the decrease of the T_2 relaxation time.

T.M. Buzug and J. Borgert (Eds.): Magnetic Particle Imaging, SPPHY 140, pp. 105–109.
springerlink.com

A well established and approved nanoparticle-based contrast agent in MRI is Resovist (Bayer Schering Pharma). This agent falls into the class of super-paramagnetic iron oxide nanoparticles (SPIONs). It consists of magnetite (Fe_3O_4) coated with carboxydextran, which prevents the particles from agglomeration. Due to the structure and size of these very particles, Resovist is a reticuloendothelial system (RES) specific MRI contrast media, originally used for imaging of liver lesions.

However, recently, Resovist has been used to show the feasibility of magnetic particle imaging (MPI). MPI is a novel imaging modality, which is directly based on the nonlinearity of the magnetization characteristics of the nanoparticles that can be described by the Langevin theory of superparamagnetism. Already in the first publication on MPI by Gleich and Weizenecker [10] it has been mentioned that Resovist does not meet all the requirements for MPI and, unfortunately, it has been withdrawn by Bayer Schering Pharma in the end of 2008. Therefore, there is a high demand on the design of new MPI-optimized and stable magnetic nanoparticles. In this contribution, the results are reported of a stability study of self-designed nanoparticle [11-13] in different suspension media.

2 Material and Methods

A simple strategy to design a suitable nanoparticle tracer for MPI based on precipitation has been described in [11-13]. The magnetic core size of these particles can be estimated by a novel magnetic particle spectrometer (MPS) [14]. However, to characterize the nanoparticle long-term stability in different suspension media, here, we used the photon cross correlation spectroscopy (PCCS). The fundamental principle of PCCS is a 3D cross-correlation technique in a special scattering geometry. For small *Reynolds* numbers, the mean squared displacement of the particles is related to the diffusion coefficient D and the dynamic viscosity η of the liquid. From theses parameters, the hydrodynamic diameter d_h can be estimated via $d_h = k_B T / (3\pi\eta D)$.

Indeed, under certain conditions, the particle coating may become instable and the particles start to agglomerate. Here, the variation of the hydrodynamic diameter d_h is measured as a particle stability indicator. Different media have been selected - from simple buffer solutions used in cell biology to culture media - and monitored over periods of several weeks. Table 1 gives an overview of the used media and the pH value.

Table 1. Media used for nanoparticle suspension

Media	pH
$CH_3COOH/NaCH_3COO$	4,6
MES (2-(N-Morpholino)ethansulfonsäure	5,8
MES	6,8
TRIS Tris(hydroxymethyl)-aminomehtan	8,0
NH_3/NH_4Cl	10,0
DMEM, high Glucose	6,8-7,2
Demin. H_2O (Reference)	7,0

3 Results and Discussion

In a first measurement campaign the different nanoparticle suspensions given in table 1 have been analyzed with PCCS over 8 hours at equidistant time points in intervals of one hour. As a reference value, particle diameters have been measured immediately after synthesis, indicated as 0 h in the following figures. Similarly, a dilution series of particle suspensions has been set up and evaluated every hour up to eight hours. In the next evaluation step, the time interval was prolonged. In a second measurement campaign the solutions were measured with PCCS after one, two and three weeks.

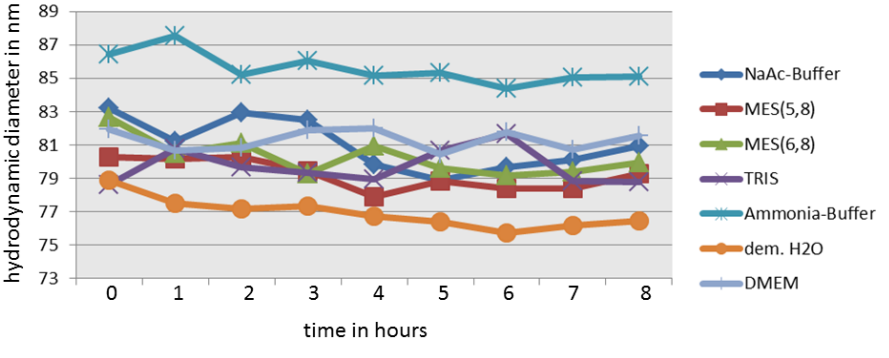

Fig. 1. First Campaign: Measurement of the hydrodynamic diameter during 8 hours.

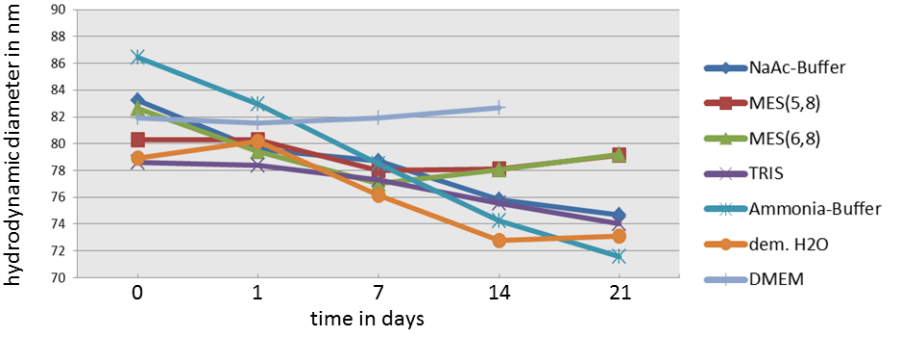

Fig. 2. Second Campaign: Measurement of the hydrodynamic diameter during 21 days.

Figures 1 and 2 show the hydrodynamic particle diameter d_h at different time points. Depending on the solvent and the particle concentration, the particles show slightly different behavior. However, even in culture media the hydrodynamic diameter of the particles remains stable within the first two weeks after synthesis. Table 2 summarizes the results.

Table 2. Measured hydrodynamic diameters for different SPIO suspension media.

	NaAc-Buffer	MES (5,8)	MES (6,8)	TRIS	Ammonia-Buffer	dem. H_2O	DMEM
mean diameter in nm	81,03	79,23	80,29	79,70	85,58	76,94	81,31
standard deviation in nm	± 3,34	± 2,61	± 2,75	± 2,58	± 2,80	± 2,44	± 2,27

4 Conclusion

In this project, the hydrodynamic diameter of our SPIONs has been used as indicator of the stability of the magnetic nanoparticles. A range of different pH values from 4.6 to 10 and also a typical culture media (DMEM) has been chosen to monitor the hydrodynamic diameter over three weeks. The mean SPION diameter over all the different media is 80.58 nm with standard deviation of 2.44 nm. We also measured with three different concentrations, by doubling and tripling the initial concentration of the suspensions of the SPIONs. No significant changes of the hydrodynamic diameter visible have been observed.

For certain media the hydrodynamic diameter increases for a period of more than two weeks. This is interpreted as a consequence of agglomerate

processes. However, the stability interval of two weeks in different media is more than sufficient for the application as contrast media.

Acknowledgement. Parts of this work have been funded by the Innovation Fund Schleswig-Holstein (Innovationsstiftung Schleswig-Holstein – ISH: Grant number: 2007-60).

References

1. Paschen, H., Coenen, C., Fleischer, T., Grünwald, R., Oertel, D., Revermann, C.: Nanotechnologie – Forschung, Entwicklung, Anwendung. Springer, Heidelberg (2004)
2. Leyendecker, S.: Nanomaterialien in Architektur. In: Innenarchitektur und Design, Birkhäuser, Basel (2008)
3. Bönnemann, H., Brijour, W., Brinkmann, R.: Angew. Chemie 103(10), 1344–1346 (1991)
4. Gupta, A.K., Gupta, M.: Synthesis and surface engineering of iron oxide nanoparticles for biomedical applications. Biomaterials 26(18), 3995–4021 (2005)
5. Mornet, S., Vasseur, S., Grasset, F., Verveka, P., Goglio, G., Demourgues, A., Portier, J., Pollert, E., Duguet, E.: Prog. Solid State Chem. 34, 237 (2006)
6. Elliott, D.W., Zhang, W.X.: Environ. Sci. Technol. 35, 4922 (2001)
7. Gulyaev, A.E., et al.: Significant transport of doxorubicin into brain with polysorbate 80-coated nanoparticles. Pharm. Res. 16(10), 1564–1569 (1999)
8. Lanza, G.M., Lamerichs, R., Caruthers, S., Wickline, A.S.: Molekulare Bildgebung in der MRT mit paramagnetischen Nanopartikeln. MEDICAMUNDI 6, 11–17 (2004)
9. Groman, E.V., Josephson, L.: US Patent 4.770.183 (1983)
10. Gleich, B., Weizenecker, J.: Tomographic imaging using the nonlinear response of magnetic particles. Nature 435, 1214–1217 (2005)
11. Lüdtke-Buzug, K., Biederer, S., Sattel, T., Knopp, T., Buzug, T.M.: Preparation and Characterization of Dextran-Covered Fe3O4 Nanoparticles for Magnetic Particle Imaging. In: Vander Sloten, J., Verdonck, P., Nyssen, M., Haueisen, J. (eds.) IFMBE Proceedings. ECIFMBE 2008, vol. 22, pp. 2343–2346. Springer, Heidelberg (2008)
12. Lüdtke-Buzug, K., Biederer, S., Sattel, T.F., Knopp, T., Buzug, T.M.: Particle-Size Distribution of Dextran- and Carboxydextran-Coated Superparamagnetic Nanoparticles for Magnetic Particle Imaging. In: World Congress on Medical Physics and Biomedical Engineering. IFMBE, vol. 25/VIII, pp. 226–229. Springer, Heidelberg (2009)
13. Lüdtke-Buzug, K., Rapoport, D., Schneider, D.: Characterization of Iron-Oxide Loaded Adult Stem Cells for Magnetic Particle Imaging in Targeted Cancer Therapy. In: Proc. of AIP Conf., vol. 1311, pp. 244–248 (2010)
14. Biederer, S., Knopp, T., Sattel, T.F., Lüdtke-Buzug, K., Gleich, B., Weizenecker, J., Borgert, J., Buzug, T.M.: Magnetization Response Spectroscopy of Superparamagnetic Nanoparticles for Magnetic Particle Imaging. Journal of Physics D: Applied Physics 42(20), 7 (2009)

3D Semi-quantification of Nanoparticle Content in Tissue on Experimental and Commercial µCT-Scanner

Helene Rahn[1], Katharina Bayer[1], Stefan Odenbach[1], Stefan Lyer[2], Christoph Alexiou[2], Frank Wiekhorst[3], Lutz Trahms[3], Michael Baumann[4], Julia Buckwar[4], and Mechthild Krause[4]

[1] Institute of Fluid Mechanics, Chair of Magnetofluiddynamics, University, Address Dresden, 01069, Germany
Helene.Rahn@tu-dresden.de, Stefan.Odenbach@tu-dresden.de
[2] Section for Experimental Oncology and Nanomedicine at the ENT-Department of the University Erlangen-Nürnberg, Waldstr. 1, 91054 Erlangen,
Stefan.Lyer@uk-erlangen.de, C.Alexiou@web.de
[3] PTB, Abbestr. 2-12, Berlin, Germany
Frank.Wiekhorst@ptb.de, Lutz.Trahms@ptb.de
[4] OncoRay - National Center for Radiation Research in Oncology Medizinische Fakultät Carl Gustav Carus, Fetscherstr. 74, PF 41, Dresden
Michael.Baumann@oncoray.de,
Mechthild.Krause@uniklinikum-dresden.de

X-ray computed tomography is a widely used imaging technique nowadays. Especially in medicine it takes an important role for visualization and diagnostics. Micro-computed tomography (µCT) follows the same principle as conventional medical CT-Scanner. But the objects analyzed are smaller, thus an improvement in spatial resolution down to few micrometers is possible. In the work field of biomedical application of magnetic nanoparticles µCT has been used for the visualization of the nanoparticle accumulations within tumoral regions after magnetic drug targeting. Further on, a calibration procedure has been developed and applied with a µCT-apparatus. The calibration procedure enables a semi-quantification of the nanoparticle content within the tissue samples. The next step stone in visualization process is the observation of the nanoparticle accumulation during the application of magnetic drug targeting in an animal. Thus, we have tested the calibration procedure on a commercial animal scanner. In this paper we compare the semi-quantitative results figured out in two different µCT-equipments.

1 Introduction

Since several years minimal-invasive cancer treatments are explored with the aim to treat a tumor locally. For these therapeutic approaches magnetic

T.M. Buzug and J. Borgert (Eds.): Magnetic Particle Imaging, SPPHY 140, pp. 111–115.
springerlink.com

nanoparticles gained an important role. In case of magnetic drug targeting nanoparticles are used as drug carriers. For this purpose a chemotherapeutic agent is connected to nanoparticles of a magnetic fluid and then injected into the tumor supplying artery. A strong magnetic field gradient, which is positioned over the target region, influences the magnetic fluid. Thus, the magnetic nanoparticles carrying drugs can be directed to the tumor region and fixated there. Due to this magnetically supported cancer therapy a higher dose rate of the chemotherapeutic agent can be reached within the target region while the total amount of the drug within the body is reduced [1].

The success of the local cancer treatment described above depends among other things of the nanoparticle distribution and also if they are available in an appropriate amount. X-ray micro-computed tomography enables the 3-dimensional examination of biological tissue samples with a spatial resolution in the micrometer range. Because of the polychromasy and the respective artifacts the tomographic data of biological tissue samples could be analyzed in a qualitative way, yet [2].

In this paper we present a calibration procedure which enables a semi-quantitative evaluation of the tomographic data. Thereby the quantitative Magnetorelaxometry (MRX) data is used as reference for the semi-quantification based on digital images.

The developed calibration procedure has been applied to a self-made experimental µCT-equipment LeTo, which is placed at the chair of Magnetofluiddynamics at TU Dresden in Dresden/Germany [3] as well as to a commercial animal scanner [4], located at the Carl Gutstav Carus university hospital Dresden. After the calibration two tumors have been measured with both µCT-equipments and the subsequent analysis reveals a very good agreement between the tomographic data and the reference data.

2 Material and Methods

2.1 Tumor Model

For the magnetic drug targeting a tumor model has been used. VX2-tumors were grown on rabbits and then treated with MDT. The chemotherapeutic agent mitoxantrone was connected to the magnetite nanoparticles. In the following the fluid was injected into the tumour supplying artery. A strong external magnetic field gradient of 72 T/m has been applied to direct the magnetic fluid to the tumor region. The magnetic fluid carrying drugs has been retained in the target region for 1.5 hours. After the local cancer treatment the rabbits were euthanized, the tumour was resected, fixated in formalin and embedded in paraffin [1]. In this paper 2 tumors measured with MRX and 2 different µCT-equipments are presented.

2.2 Reference Phantom

The reference phantom is composed of polyurethane gel (PUR) and magnetic nanoparticles. Thereby the pure PUR-gel is used as a body material for biological tissue, while the PUR-gel with immobilized magnetic nanoparticles represents the biological tissue which is enriched with magnetic nanoparticles. For the calibration a batch of 6 cuboids with nanoparticle concentrations from 0 to 33.49 mg/ml have been produced [5].

2.3 µCT-Apparatus LeTo (Low Energy Tomography) and Animal Scanner

The phantoms and tumors were measured with the polychromatic tomography apparatus named LeTo and with a commercial animal scanner. The main parameters of the scans are listed in Tab.1

Table 1. Main parameters for the tomographic scans of the phantoms and tumors.

µCT equipment	LeTo	animal scanner
acceleration voltage [kV]	50	40
emission current [mA]	1	1
spatial resolution [µm]	57	80
X-ray source	X-ray tube	X-ray tube

2.4 Magnetorelaxometry (MRX)

Magnetorelaxometry (MRX) is known as a very sensitive method for magnetic nanoparticle detection with a mass resolution of several hundred nanograms but providing only a poor spatial resolution. This method is also non destructive and yields the absolute nanoparticle value for the validation of the calibration procedure. The MRX measurements are performed by our cooperation partners at PTB in Berlin [6].

3 Results

The digital image processing of the tomographic data sets has been performed with the open source software ImageJ [7]. The obtained grey values and the magnetic nanoparticle concentrations provide calibration curves for

the two particular µCT-equipments. A linear fit of the experimental data provides calibration equations, which are shown together with the calibration curves in Fig.1. These calibration equations are then used for the conversion of grey values into nanoparticle concentrations.

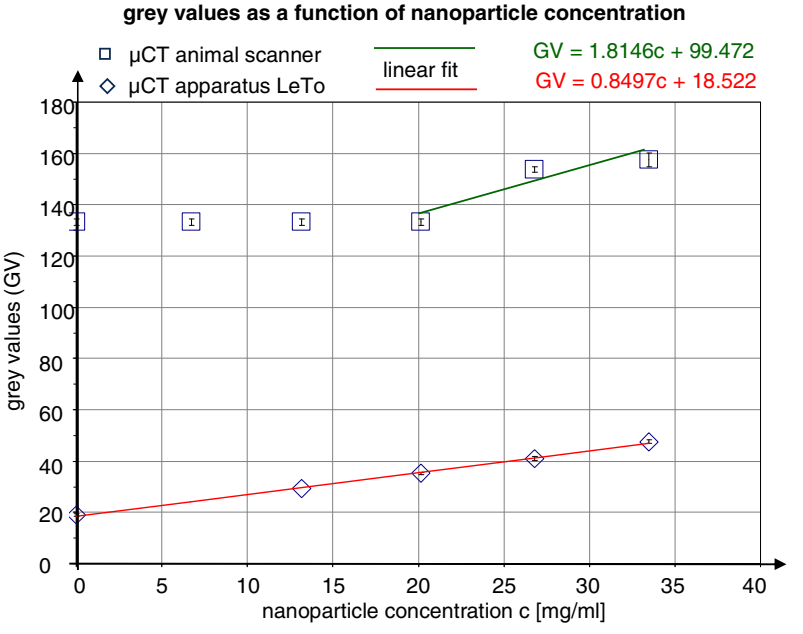

Fig. 1. Calibration curves for the different µCT-equipments. The density resolution of the animal sanner is limited to nanoparticle concentrations above 20 mg/ml.

The nanoparticle content as quantified by MRX was (24.46 +-1) mg for tumor 1 and (25.0 +-1) mg for tumor 2. The semi-quantification of the tomographic data has been performed with self-written software [5]. This software allows a voxel wise conversion of grey values into concentration values. It has been figured out that the nanoparticle content obtained with the help of the calibration procedure can be detected in adequate approximation with respect to the reference MRX values. The semi-quantitative nanoparticle content in tumor 1 amounts to 20.85 mg (LeTo) and to 20.61 mg (animal scanner). The deviation of the semi-quantitative data to MRX-data is 14.76 % (LeTo) and 15.74 % (animal scanner). The semi-quantification of tumor 2 reveals a nanoparticle content of 24.41 mg (LeTo) and 24.999 mg (animal scanner). The calculated deviation between the semi-quantitative tomographic results and quantitative MRX-results amounts to 2.36 % (LeTo) and 0.0045 % (animal scanner). The results of the semi-quantitatively evaluated 3-dimensional tomographic data and MRX data are summarized in Tab.2.

Table 2. Nanoparticle content in biological tissue samples detected with an absolute MRX measurement as well as by a calibrated µCT-examination.

	quantitative nanoparticle content		
object measured with LeTo	MRX [mg]	XµCT [mg]	deviation (%)
tumor 1	24.46 +-1	20.85	14.76
tumor 2	25 +-1	24.41	2.36
object measured with animal scanner	MRX [mg]	XµCT [mg]	deviation (%)
tumor 1	24.46	20.61	15.74
tumor 2	25	25	0.0045

4 Conclusion

The developed calibration method allows a semi-quantitative evaluation of polychromatic tomographic data sets of biological tissue samples enriched with magnetic nanoparticles. This has been successfully shown with an experimental µCT-equipment as well as with a commercial animal scanner.

Acknowledgments. The authors would like to thank the DFG OD18/9 & OD18/16 & DFG PAK 151 and the BMBF (FKZ:01EX1012B) for their financial support.

References

1. Alexiou, C., Arnold, W., Klein, R.J., Parak, F.G., Hulin, P., Bergemann, C., Erhardt, W., Wagenpfeil, S., Lübbe, A.S.: Locoregional cancer treatment with Magnetic Drug Targeting. Cancer Research 60, 6641–6648 (2000)
2. Rahn, H., Odenbach, S.: X-ray micro-tomography as tool for the investigation of the biodistribution of magnetic nanoparticles. Nanomedicine 4(8), 981–990 (2009)
3. Brunke, O., Odenbach, S., Jurgons, R., Alexiou, C., Hilger, I., Beckmann, F.: J. Phys. Condens. Matter 18, S2903–S2917 (2006)
4. CT-Imaging, http://www.ct-imaging.de/en/index.php
5. Rahn, H., Odenbach, S.: Calibration phantom for 3-dimensional semi-quantitative detection of nanoparticle content in biological tissue samples after magnetically supported cancer treatment (in Preparation)
6. Wiekhorst, F., et al.: Quantification of magnetic nanoparticles by magnetorelaxometry and comparison to histology after magnetic drug targeting. Journal of Nanoscience and Nanotechnology 6, 222–3225 (2006)
7. ImageJ, http://rsbweb.nih.gov/ij/

Biomaterials for Regenerative Medicine: Cytotoxicity of Superparamagnetic Iron Oxide Nanoparticles in Stem Cells

D. Schneider and K. Lüdtke-Buzug

Institute of Medical Engineering, University of Luebeck, Ratzeburger Allee 160, Luebeck, 23562, Germany
schneider@imt.uni-luebeck.de

Abstract. Detrimental effects of nanoparticles on cell viability, cell growth and morphology have been an ongoing topic in the field of nanoparticle tissue engineering, cell labeling, and drug delivery. Establishing biocompatible nanoparticles is particularly important for stem cell -based therapies and cell-tracking by magnetic particle imaging in regenerative medicine. Recently, magnetic particle imaging (MPI) has been presented as a new method for the measurement of the spatial distribution of superparamagnetic iron oxide nanoparticles (SPIOs). Spatial resolution and signal to noise ratio of MPI depend on the particle quality. Here we developed dextran-coated SPIOs for magnetic particle imaging and analyzed their stability and hydrodynamic diameter by photon cross correlation spectroscopy (PCCS). The uptake of SPIOs and the morphology of labeled human adult stem cells were examined by confocal laser scanning microscopy. Labeled stem cell growth was monitored by the xCELLigence system. We focused on commonly used *in vitro* assays for estimation of cell viability and cell death. The newly developed SPIOs revealed a low signal to noise ratio. Dextran-coated SPIOs had no significant influence on cell growth and viability of human adult stem cells. Our data support dextran-coated magnetic nanoparticles as a well-tolerated and promising tool for further surface modifications and stem cell -based therapies.

1 Introduction

During the last few years nanoparticles have been advanced to one of the most interesting materials in several different areas of life [6]. Particular in medicine, these particles are in the focus of research for new active agents that may carry therapeutic substances or act as tracer material for imaging purposes [1,6]. Especially nano-sized superparamagnetic materials based on iron oxide, so called SPIOs (superparamagnetic iron oxide particles), became more and more interesting due to an increasing variety of applications

T.M. Buzug and J. Borgert (Eds.): Magnetic Particle Imaging, SPPHY 140, pp. 117–122.
springerlink.com

from cancer therapy to contrast enhancement in magnetic resonance imaging (MRI). In this study we analyzed the uptake and influence on cell growth and viability on human adult stem cells of newly developed SPIOs.

2 Material and Methods

2.1 Synthesis of Iron Oxide Nanoparticles

All reagents were of analytical grade and used without further purification. Dextran T70 (M~70.000 g/mol, Roth), Iron(II) chloride tetrahydrate (Merck), Iron(III) chloride hexahydrate (Roth) were dissolved in deionized water. A 7.5% Ammonia solution (Roth) was used. To synthesize superparamagnetic iron oxide nanoparticles here the classical co-precipitation of iron oxide in an alkaline solution in the presence of dextran was realized as described in [1].

Steps of precipitation:

$$2Fe^{3+} + Fe^{2+} + 8OH^- \xrightarrow[\text{temperature}]{\text{at room}} Fe(OH)_2 + 2Fe(OH)_3$$

$$Fe(OH)_2 + 2Fe(OH)_3 \xrightarrow[\text{for 30-60 minutes}]{\text{heating (≈70 °C)}} Fe_3O_4 + 4H_2O$$

2.2 Photon Cross-Correlation Spectroscopy

The hydrodynamic diameter, d_h of dextran-coated SPIOs was measured by PCCS, (NANOPHOX, Sympathec GmbH) [2]. Therefor dextran-coated SPIOs were incubated for 8h in different media. The nanoparticles exhibited a hydrodynamic diameter in the range between d_h 80 nm and d_h 90 nm.

2.3 Stem Cell Preparation and Cultivation

Adult glandular stem cells were obtained from human *glandula submandibularis* biopsies from healthy donors following Helsinki guidelines and ethics committee approval and cultured as previously described in [3,4,5]. Cell viability before experiments was measured by trypan blue exclusion and was always greater than 97%.

2.4 Analysis of Stem Cell Growth

Human adult stem cells were cultured with different concentrations from 0 - 1 mg/ml of dextran-coated SPIOs in 5 ml cell culture flasks. To determine cell numbers cells were counted after 1 week of culturing with a cellometer (Nexcelom Bioscience). xCELLigence:$1x10^4$ human adult stem cells/well of a 96 well-E-Plate were incubated for 90 hours with concentrations as indicated in figure 2 of dextran-coated SPIOs. As control stem cells grown

without SPIOs were used. The electrical impedance was measured continuously by the xCELLigence System (Roche).

2.5 Cytochemistry

2 x 10^4/well human adult glandular stem cells were cultivated in µ-dishes (Ibidi) with FITC-dextran-coated SPIOs for 4h at 37 °C and 5% CO_2. Cells were fixed with 4% PFA/PBS and stained with 0,2 nmol/l Phalloidin Fluo-Probes 547 (Interchim) and with 1 µg/ml DAPI (Roche). To determine the intracellular localization of the SPIOs, samples were analyzed by confocal microscopy (LSM7, Zeiss).

2.6 MTT-Viability Assay

The analysis of stem cell viability after incubation with SPIOs was performed using MTT-viability assay (Invitrogen) following manufacturer´s guidelines.

3 Results

3.1 Uptake of Nanoparticles by Human Adult Stem Cells

Human adult stem cells were incubated for 4h with 10 µg/ml FITC-dextran-coated SPIOs and stained for fluorescence microscopy. SPIOs were localized in the cytoplasm without disruption of the cell membranes of adult stem cells. A nuclear localization was not observed. Displayed is one representative of three independent experiments with cells of three different donors (figure 1).

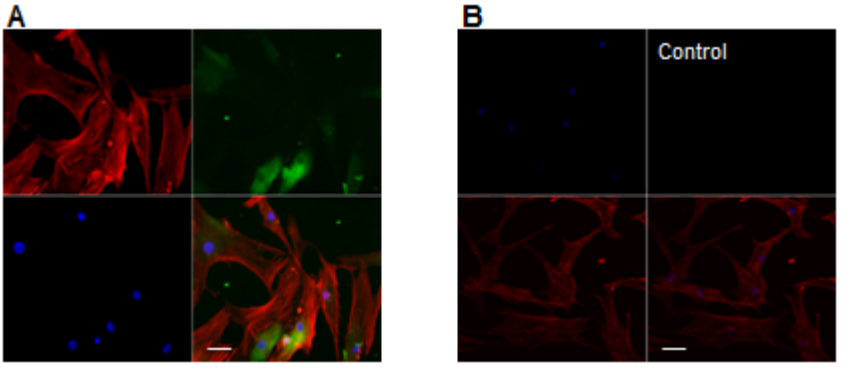

Fig. 1. Uptake of SPIOs into human adult stem cells: human adult stem cells were grown on cover slips and incubated for 4h with 10 µg/ml FITC-dextran-coated SPIOs (A). (B) control: stem cells incubated without SPIOs. Displayed in green: FITC-dextran-coated SPIONS, red F-actin filaments, blue: nuclei of the stem cells. White bars indicate 10 µm.

3.2 Influence of SPIONs on Stem Cell Growth

The xCELLigence System measures electrical impedance across interdigitated micro-electrodes integrated on the bottom of tissue culture E-Plates. The impedance measurement provides quantitative information about the biological status of the cells, including cell number and viability. Adult stem cells were incubated for 90 hours with dextran-coated SPIOs continuously measuring the impedance by xCELLigence. Adult stem cells grown without SPIOs served as control. Higher concentration (100-1000 µg/ml) of SPIOs slightly reduced cell growth of adult stem cells, but without significance. Displayed is one representative of three independent experiments with cells from three different donors (figure 2).

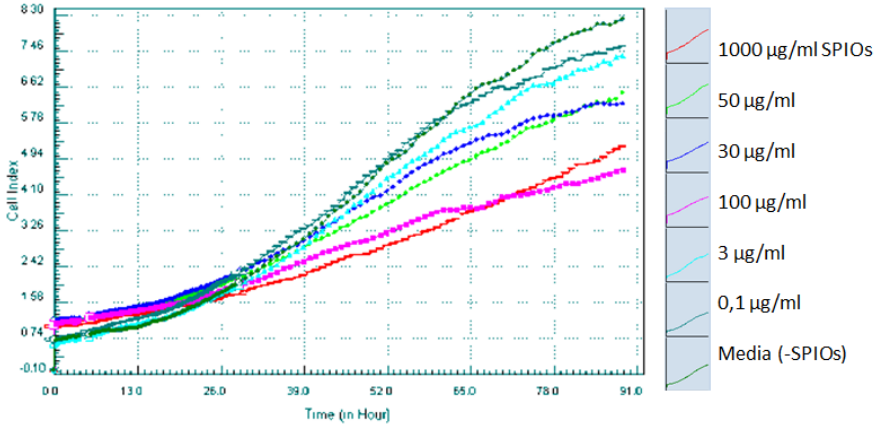

Fig. 2. Influence of dextran-coated SPIOs on adult stem cell growth. Adult stem cells were grown on E-plates for 90 hours with dextran-coated SPIONs and the impedance was measured continuously by the xCELLigence system. Higher concentration of SPIONs slightly reduced cell growth, but not significantly. Control: stem cells grown without SPIOs (media, -SPIOs).

For analysis of cell growth of human adult stem cells in the presence of SPIOs, cell numbers were determined with an automated cell counter after one week incubation time with up to 1 mg/ml dextran-coated SPIOs. SPIOs had no influence on cell numbers after one week incubation time. No significant differences between unlabeled and labeled stem cells were observed.

3.3 No Significant Influence on Stem Cell Viability

The MTT-assay revealed no significant influence of dextran-coated SPIOs on human adult stem cell viability (figure 3). Based on these observations

annexinV /propidium iodide stainings were performed to analyze cell death using flow cytometry with regard to apoptosis and necrosis. No significant increase of cell death was observed (data not shown).

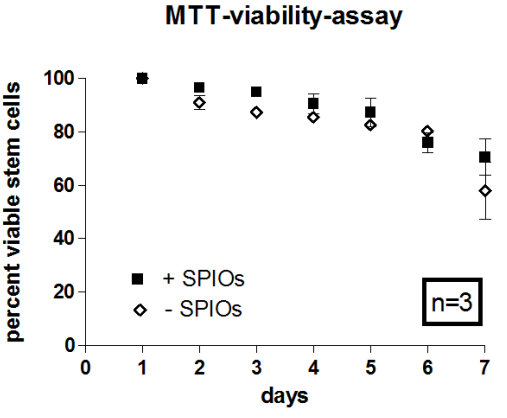

Fig. 3. No influence on cell viability by SPIONs. Human adult stem cells were cultured with 1 mg/ml dextran-coated SPIOs (+SPIOs) and without (-SPIOs; control) for the indicated time. The nanoparticles revealed no significant influence on cell viability of human adult stem cells up to 7 days of incubation time. Displayed are means $\pm$ SD of three independent experiments performed with cells from three donors.

Statistical analysis was performed using the non-parametric Mann Whitney U test. Differences were considered significant for P-values < 0,05.

4 Discussion

In this study we investigated the uptake and cytotoxicity of dextran-coated SPIOs on human adult stem cells. Due to their lack of cytotoxic effects, their intracellular localization in the cytoplasm of stem cells without nuclear localization we conclude high stability and biocompatibility of dextran-coated SPIOs. These findings were supported by measurable fluorescence of FITC-dextran-SPIO labeled stem cells after 4 days. Brunner et al. postulated 2006 that the toxic effects of nanoparticles may be attributed to two different actions: (i) a chemical toxicity based on the chemical composition, e.g., release of (toxic) ions and particle surface catalyzed reactions, e.g., formation of reactive oxygen species; or (ii) due to stress or stimuli caused by the surface, size and/or shape of the particles [8]. The intralysosomal degradation of SPIOs and the ability of stem cells of self-renewal and repair possibly contribute to the good tolerability of dextran-coated SPIOs. Untreated oxide nanoparticle dispersions undergo rapid agglomeration in cell culture medium [7]. The results obtained from PCCS measurements of SPIOs in different

media corroborate these findings and led to size and surface optimized stable particles. In order to elucidate the molecular mechanisms underlying the complexity of nanoparticle-related cytotoxicity further investigation with different cell types and molecular biological tests is needed. Only early toxicity assessment leads to safe nanoparticle -based medical applications and tracer media for magnetic particle imaging.

5 Conclusion

Our data support that newly developed nanoparticles are well tolerated by human adult stem cells and have great potential for a variety of medical applications and for magnetic particle imaging.

References

1. Lüdtke-Buzug, K., Biederer, S., Sattel, T., Knopp, T., Buzug, T.M.: Preparation and Characterization of Dextran-Covered Fe_3O_4 Nanoparticles for Magnetic Particle Imaging. In: Vander Sloten, J., Verdonck, P., Nyssen, M., Haueisen, J. (eds.) IFMBE Proceedings. IFMBE, vol. 22, pp. 2343–2346. Springer, Heidelberg (2008)
2. Lämmle, W.: Nanometre particle sizing and stability measurement using a tabletop PCCS system. LabPlus International, 19–24 (2005)
3. Kruse, C., Birth, M., Rohwedel, J.: Pluripotency of adult stem cells derived from human and rat pancreas. Applied Physics A 79, 1617–1624 (2004)
4. Kruse, C., Kajahn, J., Petschnik, A.E., Maass, A., Klink, E., Rapoport, D.H., Wedel, T.: Adult pancreatic stem/progenitor cells spontaneously differentiate in vitro into multiple cell lineages and form teratoma-like structures. Ann. Anat. 188(6), 503–517 (2006)
5. Gorjup, E., Danner, S., Rotter, N., Habermann, J., Brassat, U., Brummendorf, T.H., Wien, S., Meyerhans, A., Wollenberg, B., Kruse, C., von Briesen, H.: Glandular tissue from human pancreas and salivary gland yields similar stem cell populations. Eur. J. Cell. Biol. 88(7), 409–421 (2009)
6. Singh, R., Nalwa, H.S.: Medical applications of nanoparticles in biological imaging, cell labeling,antimicrobial agents, and anticancer nanodrugs. J. Biomed. Nanotechnol. (4), 489–503 (2011)
7. Limbach, L.K., Li, Y.C., Grass, R.N., Brunner, T.J., Hintermann, Stark, W.J.: Oxide nanoparticle uptake in human lung fibroblasts: Effects of particle size,agglomeration, and diffusion at low concentrations. Environ.Sci. Technol. 39, 9370–9376 (2005)
8. Brunner, T.J., Wick, P., Manser, P., Spohn, P., Grass, R.N., Stark, W.J.: In vitro cytotoxicity of oxide nanoparticles: comparison to asbestos, silica, and the effect of particle solubility. Environ. Sci. Technol. 40(14), 4374–4381 (2006)

Tracer Development for Magnetic Particle Imaging

Harald Kratz[1], Dietmar Eberbeck[2], Susanne Wagner[1], Jörg Schnorr[1], and Matthias Taupitz[1]

[1] Department of Radiology, Charité - Universitätsmedizin Berlin, Charitéplatz 1, 10117 Berlin, Germany
Harald.Kratz@charite.de, Susanne.Wagner@charite.de, Jörg.Schnorr@charite.de, Matthias.Taupitz@charite.de
[2] Physikalisch-Technische Bundesanstalt, Abbestr. 2-12, 10587 Berlin, Germany
Dietmar.Eberbeck@ptb.de

Abstract. Magnetic particle imaging (MPI) allows quantitative evaluation of the spatial distribution of superparamagnetic iron oxide (SPIO) nanoparticles in the body. With a spatial resolution similar to magnetic resonance imaging (MRI), but superior temporal resolution, MPI has potential for different diagnostic applications. In addition to technical requirements, preclinical and clinical applications of this novel imaging modality require SPIO tracers optimized for MPI. This article discusses the suitability of Resovist as an MPI tracer and challenges and future prospects of tracer development.

1 Introduction

Magnetic particle imaging (MPI) was first described as a new tomographic imaging modality by Gleich and Weizenecker in 2005. MPI visualizes the spatial distribution of superparamagnetic iron oxide (SPIO) nanoparticles by exploiting the nonlinear magnetization curve of SPIO nanoparticles in a rapidly oscillating magnetic field to inductively detect overtones in addition to the applied basic frequency [1]. Direct detection of the magnetization from SPIO using MPI potentially offers high spatial resolution, excellent contrast, and good signal-to-noise ratio (SNR) [2]. With a SPIO concentration of 20 nmol Fe/l, resolution in the submillimeter range can be achieved in vivo [3]. When a small volume is imaged, up to 50 3D datasets can be acquired per second. Hence, MPI appears to have potential for real-time in vivo imaging of fast dynamic processes, for instance, in angiographic applications [3]. As MPI exclusively detects the magnetization from SPIO nanoparticles, information on the underlying anatomy is not available. Hence, MPI should ideally be combined with an imaging modality providing anatomic information such as

T.M. Buzug and J. Borgert (Eds.): Magnetic Particle Imaging, SPPHY 140, pp. 123–127.
springerlink.com

computed tomography (CT) or magnetic resonance imaging (MRI). On the other hand, the performance of MPI crucially depends on the physical properties of the tracers. In order to obtain a high resolution, the tracers should have a large magnetic moment so that significant nonlinearity of the magnetisation set on already at small fields. In case of magnetite core diameters of 30 nm...60 nm are envisaged by a narrow size distribution [4]. Furthermore, the intrinsic magnetic anisotropy sould be small, ensuring that the moments can follow the high frequency field. In the following, we outline the state of the art in the development of tracers for MPI and propose directions for future research in this field.

2 Resovist

Resovist (Schering, Berlin, Germany), a hepatocellular MRI contrast agent approved in 2001, was the first tracer successfully used in experimental in vivo studies of MPI. Resovist consists of SPIO nanoparticles with a carboxydextran coating and a hydrodynamic diameter of approx. 60 nm [5, 6]. Resovist was used for the first phantom experiments of MPI [1] and the first in vivo studies in animals [3]. These initial experiments revealed MPI‘s potential as a clinical imaging modality. The Resovist doses used in these early experiments were equal to or higher than the clinically approved dose of 40 µmol Fe/kg body weight; hence, higher spatial resolution was not achievable with this contrast medium. Moreover, Resovist was taken off the market as an MRI contrast agent at the end of 2008. An analysis of the efficiency of Resovist as an MPI tracer showed that only 3% of the iron in Resovist accounts for its MPI performance [1]. The iron oxide cores in Resovist have a size range of approx. 3-5 nm (average, 4 nm) [6] and are partially clustered; it is to these clusters of iron oxide cores that the MPI properties of Resovist have been attributed [7].

3 Prospects for Future Tracer Development

3.1 Synthesis

Recent physical investigations suggest that the good MPS signal of Resovist is provided by cluster-like MNP having an effective magnetic diameter of 22 nm [7]. It has been proposed that the magnetic moments of elementary cores within the clusters in zero field might cancel out each other, providing good colloidal stability due to attenuation of dipolar interaction of such clusters [7]. SPIOs used for MPI should ideally be monodisperse in order to optimize the yield of MPS signal per unit iron [8]. Based on reports in the literature, thermal decomposition yields nearly monodisperse SPIO preparations [9]. Known synthesis methods for magnetite/ maghemite systems lead to different particle properties in terms of anisotropy and magnetizability. Hence, available SPIOs synthesized

with different methods are likely to differ in their shape, exact composition, and crystal structure. As there are so many different approaches for synthesizing SPIO nanoparticles, one aim of future research should be to identify the approach that yields the best MPI tracers and to investigate how these can be stabilized for in vivo application. For particles intended for clinical use, attention must be paid to biocompatibility and biodegradability.

3.2 Separation

Suitable SPIO particle preparations can be separated on the basis of magnetic momonent (magnetic separation) or density (centrifugation), among others [10,11]. Both separation methods allow narrowing down the size range present within a sample, thereby improving the MPS signal. A disadvantage of magnetic separation is that large SPIOs (over approx. 30 nm) may aggregate due to magnetization by the applied magnetic field. The forces occurring during centrifugation can also induce particle aggregation. Moreover, centrifugation prevents the accurate and reproducible size separation of particles, critical steps in nanoparticle synthesis. Other methods for size separation of nanoparticles reported in the literature [12,13] include so-called quadrupole magnetic flow sorting of magnetically labeled cells after loading [14].

4 Challenges and Outlook

4.1 SPIO Synthesis

The challenge confronting scientists working on SPIO synthesis is to produce tracers with optimal MPS performance. A narrow size distribution of the resulting particles might be achieved by controlled aggregation using solvent mixtures [15]. The SPIOs must form stable dispersions in saline solutions, and the nanoparticle sizes and magnetic properties must be well reproducible.

4.2 Outlook

The primary aim of work in this field must be to synthesize tracers for MPI that have properties in biological systems allowing their later preclinical and clinical development. It is also conceivable that SPIOs of different sizes might be developed for different applications. For instance, SPIO nanoparticles with a size of less than 30 nm have potentially longer circulation times, making them suitable for angiography and imaging of cardiovascular diseases in general. Larger SPIO particles are potentially suitable for passive targeting of cells and in vivo tracking [16,17]. Passive targeting might also be of interest for accomplishing selective uptake of larger SPIO particles up to 100 nm in size by tumors [18]. In a further step, SPIO could be specifically funcionalized for active targeting. The signal

produced by a tracer is pivotal. A high signal yield may allow administration of smaller amounts of MPI tracers, increasing the chance of good tolerability in human clinical applications.

Acknowledgements. We thank Bettina Herwig and Randall Lindquist for language editing. The research was supported by the German Ministry for Education and Research, Grant No. FKZ 13N11092.

References

1. Gleich, B., Weizenecker, J.: Tomographic imaging using the nonlinear response of magnetic particles. Nature 435, 1214–1217 (2005)
2. Goodwill, P.W., Tamrazian, A., Croft, L.R., Lu, C.D., Johnson, E.M., Pidaparthi, R., et al.: Ferrohydrodynamic relaxometry for magnetic particle imaging. Applied Physics Letters 98, 262502 (2011)
3. Weizenecker, J., Gleich, B., Rahmer, J., Dahnke, H., Borgert, J.: Three-dimensional real-time in vivo magnetic particle imaging. Physics in Medicine and Biology 54, L1 (2009)
4. Gleich, B.: WO2004/091398 A2 (December 28, 2004)
5. Reimer, P., Tombach, B., Daldrup, H., Hesse, T., Sander, G., Balzer, T., et al.: Neue MR-Kontrastmittel in der Leberdiagnostik Erste klinische Ergebnisse mit hepatobiliärem Eovist®(Gadolinium-EOB-DTPA) und RES-spezifischem Resovist®(SH U 555 A). Der Radiologe 36, 124–133 (1996)
6. Lawaczeck, R., Bauer, H., Frenzel, T., Hasegawa, M., Ito, Y., Kito, K., et al.: Magnetic iron oxide particles coated with carboxydextran for parenteral administration and liver contrasting. Pre-clinical profile of SH U555A. Acta Radiol. 38, 584–597 (1997)
7. Eberbeck, D., Wiekhorst, F., Wagner, S., Trahms, L.: How the size distribution of magnetic nanoparticles determines their magnetic particle imaging performance. Applied Physics Letters 98, 182502–182502 (2011)
8. Ferguson, R.M., Minard, K.R., Krishnan, K.M.: Optimization of nanoparticle core size for magnetic particle imaging. J. Magn. Magn. Mater. 321, 1548–1551 (2009)
9. Hyeon, T., Lee, S.S., Park, J., Chung, Y., Na, H.B.: Synthesis of highly crystalline and monodisperse maghemite nanocrystallites without a size-selection process. J. Am. Chem. Soc. 123, 12798–12801 (2001)
10. Qiu, P., Mao, C.: Viscosity gradient as a novel mechanism for the centrifugation-based separation of nanoparticles. Adv. Mater. 23, 4880–4885 (2011)
11. Bai, L., Ma, X., Liu, J., Sun, X., Zhao, D., Evans, D.G.: Rapid separation and purification of nanoparticles in organic density gradients. J. Am. Chem. Soc. 132, 2333–2337 (2010)
12. Novak, J.P., Nickerson, C., Franzen, S., Feldheim, D.L.: Purification of molecularly bridged metal nanoparticle arrays by centrifugation and size exclusion chromatography. Anal. Chem. 73, 5758–5761 (2001)
13. Hanauer, M., Pierrat, S., Zins, I., Lotz, A., Sönnichsen, C.: Separation of nanoparticles by gel electrophoresis according to size and shape. Nano. Lett. 7, 2881–2885 (2007)

14. Moore, L.R., Rodriguez, A.R., Williams, P.S., McCloskey, K., Bolwell, B.J., Nakamura, M., et al.: Progenitor cell isolation with a high-capacity quadrupole magnetic flow sorter. Journal of Magnetism and Magnetic Materials 225, 277–284 (2001)
15. Larsen, B.A., Haag, M.A., Serkova, N.J., Shroyer, K.R., Stoldt, C.R.: Controlled aggregation of superparamagnetic iron oxide nanoparticles for the development of molecular magnetic resonance imaging probes. Nanotechnology 19, 265102 (2008)
16. Moghimi, S.M., Hunter, A.C., Murray, J.C.: Long-circulating and target-specific nanoparticles: theory to practice. Pharmacol. Rev. 53, 283–318 (2001)
17. Raynal, I., Prigent, P., Peyramaure, S., Najid, A., Rebuzzi, C., Corot, C.: Macrophage endocytosis of superparamagnetic iron oxide nanoparticles: mechanisms and comparison of ferumoxides and ferumoxtran-10. Invest. Radiol. 39, 56–63 (2004)
18. Perrault, S.D., Walkey, C., Jennings, T., Fischer, H.C., Chan, W.C.: Mediating tumor targeting efficiency of nanoparticles through design. Nano Lett. 9, 1909–1915 (2009)

The Potential of Magnetic Particle Imaging in the Competitive Environment of Cardiac Diagnostics

Gunnar Schütz

MR & CT Contrast Media Research, Bayer Pharma AG, Müllerstr. 178
13467 Berlin, Germany
gunnar.schuetz@bayer.com

Abstract. Magnetic particle imaging (MPI) is a novel real-time imaging technique visualizing magnetic nanoparticles. Due to its intrinsic features it is especially suited for functional cardiac diagnosis, including angiography, cardiac wall motion assessment and quantitative myocardial perfusion imaging. In addition it may be suitable for cardiac intervention. MPI may reduce the overall diagnostic procedure duration and the complexity of recommended diagnostic pathways, thereby providing medical benefits to patients and economical benefits to hospitals / cardiologists due to the expected increased patient throughput.

1 Introduction

Magnetic particle imaging (MPI) is a novel tomographic imaging method for visualizing nanoparticles with defined magnetic properties first published in 2005 [1]. It is a real-time imaging method which can acquire more than 25 volumes of interest per second. The magnetic nanoparticles used as imaging tracer are measured directly and quantitatively. Thus, MPI generates PET-like images without a tissue background. Due to the supposed size range of the tracer particles of 40 to 100 nm hydrodynamic diameter, those are strictly intravascular after intravenous injection. These facts, real-time imaging, lack of tissue background and the vascular tracer, renders MPI ideally suited for angiography and perfusion imaging in rapidly moving tissues. Therefore, MPI will be a perfect imaging modality for functional cardiac diagnostic and intervention. The cardiac diagnostic pathways as currently recommended by national organizations such as the "NICE clinical guideline 95" for the United Kingdom [2] contain a complicated decision tree involving multiple diagnostic tests including imaging by several modalities. MPI may offer significant reduction in complexity of functional cardiac diagnostic by combining favourable features from established imaging techniques.

T.M. Buzug and J. Borgert (Eds.): Magnetic Particle Imaging, SPPHY 140, pp. 129–134.
springerlink.com

2 Imaging in Current Functional Cardiac Diagnostics

Invasive coronary angiography including percutaneous coronary intervention (PCI; vessel dilatation by insertion of a stent) are integral part of the diagnostics in chest pain patients who may suffer from coronary artery disease (CAD). The complication rate of these invasive methods is reported to be approximately 1% [3] which is low compared to surgical interventions but high compared to non-invasive diagnostic imaging procedures. As only approximately 35% of all catheter based coronary angiographies include an intervention [4], several diagnostic imaging methods have been introduced to support the functional assessment of the myocardium in order to reduce the number of invasive coronary angiographies. SPECT and PET are radioactive imaging methods which use ^{99m}Tc Sestamibi or ^{82}Rb, respectively, for direct and quantitative assessment of tissue perfusion [5, 6]. FDG-PET in combination with tissue perfusion data can provide information on remaining viability, which can be important for the therapy decision (i. e. to place a stent and re-perfuse the tissue or not). Dynamic CT angiographic examinations for tissue perfusion assessment are also possible; however, the radiation exposure is significantly higher compared to standard CT examinations including CTA [7]. In principle, contrast enhanced transthoracical ultrasound imaging can be used to determine myocardial perfusion, as well. However, it has some limitations due to sound wave attenuations by the sternum and ribs [8]; the image quality is also limited in overweight and obese patients. Cardiac MRI is a sophisticated radiation free imaging method for acquiring functional information of the myocardium, including tissue viability assessment. Like FDG-PET it thus offers additional data to support a therapy decision. However, visualization of coronary artery stenosis and quantitative assessment of myocardial perfusion are time consuming and remain challenging [9, 10].

The involvement of the mentioned imaging modalities, SPECT, PET and CT as well as cardiac echo within the recommended diagnostic pathway for CAD is indicated in Fig. 1. Stable chest pain patients who may suffer from CAD including stable angina will enter this diagnostic pathway. Because these patients are usually free of pain at rest, they are not treated as emergency cases. A diagnostic workup begins with an assessment of the patient's history and risk factors, such as age, gender, diabetes, smoking and hyperlipidaemia. The primary anamnesis either leads directly to a diagnosis of CAD or a clinical assessment including electrocardiography (ECG), risk factor analysis and cardiac echo will be conducted to reach firm diagnosis. Therapy for CAD / stable angina includes invasive coronary angiography and PCI [11]. As outlined in Fig. 1 the diagnostic pathway for stable chest pain patients splits into 4 major routes and contains several decision points. The overall diagnostic procedure is thus time consuming and may include the use of multiple different imaging modalities.

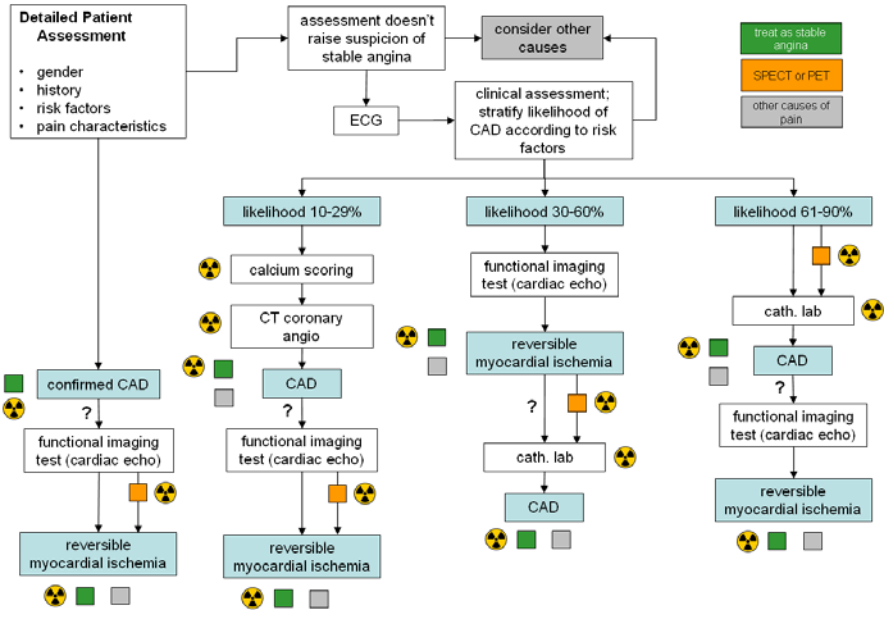

Fig. 1. CAD diagnostic pathway according to NICE clinical guidelines 95. Squares represent diagnostic or therapeutic options: orange indicates possible involvement of SPECT or PET; green indicates the need to treat as stable angina including invasive methods and PCI; grey indicates other causes of pain and "?" represents an uncertain diagnosis. Radioactivity symbols indicate involvement of X-ray or γ-radiation. Adapted from [2]

3 Expected Advantages of MPI in Functional Cardiac Diagnostics

The complexity of cardiac diagnostic may be resolved by introduction of MPI into the CAD diagnostic procedure. MPI would replace imaging by SPECT. It could further replace myocardial perfusion imaging by PET or MRI in patients where viability information is not required. One bolus injection of an MPI tracer at rest and one injection at stress may be sufficient for stenosis detection, the assessment of cardiac wall motion alterations and the detection of cardiac perfusion deficits. Thus, MPI can provide immediate information on the functional relevance of a detected stenosis.

MPI may therefore gain significant share of invasive coronary artery imaging, which may considerably lower the rate of invasive imaging procedures. It is reported, that MPI scanners can be constructed in a rather open configuration [12]. This could offer sufficient patient access to allow for MPI based PCI. Such an MPI device could thus enable the integration of MPI-driven functional cardiac diagnostics and cardiac

intervention. Invasive coronary diagnosis could be avoided while maintaining the option to continue from the diagnostic to intervention stages without the need for patient relocation. To minimize time from patient arrival to intervention, functional imaging tests are currently not performed for cardiac emergency patients. Stenosis detection occurs during PCI and functional relevance is not assessed at all. MPI can provide the addition of functional information without increasing the procedure time and may thus decrease the number of stents to be implanted.

4 A Potential Scenario for the Use of MPI in the CAD Diagnostic Pathway

In terms of diagnostic workflow this means that MPI may become the major imaging modality for CAD diagnosis and intervention, thereby significantly reducing the complexity of the diagnostic pathway. The four diagnostic routes may be reduced to a single approach that provides all of the required diagnostic information.

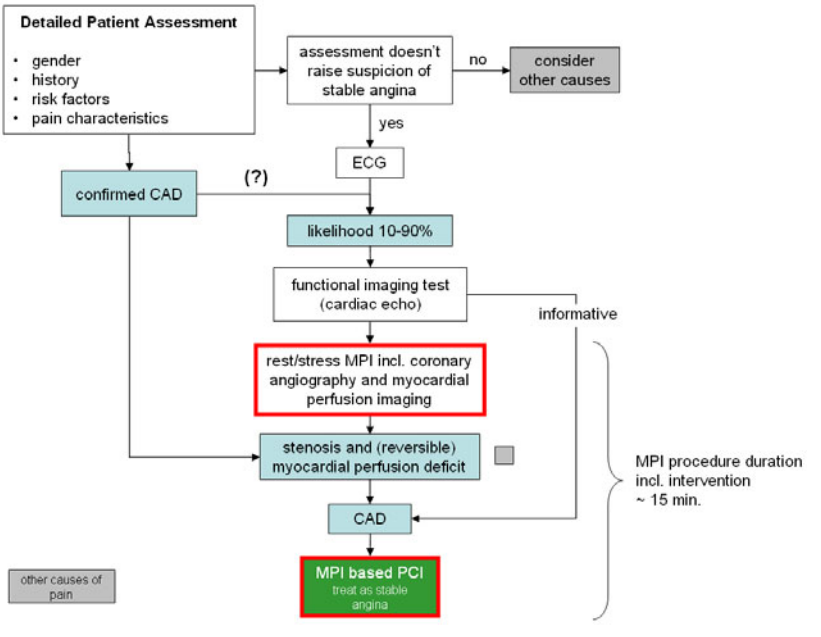

Fig. 2. A Potential scenario for use of MPI in CAD diagnostic pathway. The red frame indicates that MPI is involved. The therapeutic options are indicated as follows: green indicates treat as stable angina including PCI; grey indicates other causes of pain; and "?" indicates uncertain diagnosis. No radioactive exposure for patient or examiner is involved.

A reduction in complexity may not only minimize the time necessary to obtain a conclusive diagnosis but also has the potential to reduce the overall expenses associated with CAD / stable angina diagnosis by an expected increase in patient throughput. A diagnostic scenario as proposed in Fig. 2 may therefore not only provide medical benefits to patients but also economical benefits to hospitals / cardiologists. To become a preferred and reimbursed procedure for cardiac diagnosis MPI, of course, has to compete economically with the established diagnostic pathways while providing improved diagnostic quality.

5 Conclusion

The considerations presented here propose that MPI may become an important imaging method for the cardiac diagnostic processes due to possible reductions in complexity, time to conclusive diagnosis and diagnostic costs. To achieve economic success in medical imaging MPI should gain a share of the market from cardiac SPECT, PET and CTA. Ideally, as outlined above, MPI should also be used for coronary angiography and in support of PCI. The prerequisite for the successful implementation of MPI is, of course, the excellent technical performance of the MPI system including the instrumentation and the tracer. The spatial resolution and detection sensitivity are considered to be critical parameters. A human MPI scanner or a suitable MPI tracer is currently not available; however, ongoing research has shown promising initial preclinical results.

References

1. Gleich, B., Weizenecker, J.: Tomographic imaging using the nonlinear response of magnetic particles. Nature 435(7046), 1214–1217 (2005)
2. Walker, R., et al.: Chest pain of recent onset: Assessment and diagnosis of recent onset chest pain or discomfort of suspected cardiac origin. National Institute for Health and Clinical Excellence (2003)
3. Dangas, G., et al.: Vascular complications after percutaneous coronary interventions following hemostasis with manual compression versus arteriotomy closure devices. J. Am. Coll. Cardiol. 38(3), 638–641 (2001)
4. Bruckenberger, E.: Herzbericht 2010, vol. 23, p. 56 (2010)
5. Iida, H., Eberl, S.: Quantitative assessment of regional myocardial blood flow with thallium-201 and SPECT. J. Nucl. Cardiol. 5(3), 313–331 (1998)
6. Di Carli, M.F., et al.: Clinical myocardial perfusion PET/CT. J. Nucl. Med. 48(5), 783–793 (2007)
7. Bamberg, F., et al.: Dynamic myocardial stress perfusion imaging using fast dual-source CT with alternating table positions: initial experience. Eur. Radiol. 20(5), 1168–1173 (2010)
8. Porter, T.R., Xie, F.: Myocardial perfusion imaging with contrast ultrasound. JACC Cardiovasc. Imaging 3(2), 176–187 (2010)

9. Bluemke, D.A., et al.: Noninvasive coronary artery imaging: magnetic resonance angiography and multidetector computed tomography angiography: a scientific statement from the american heart association committee on cardiovascular imaging and intervention of the council on cardiovascular radiology and intervention, and the councils on clinical cardiology and cardiovascular disease in the young. Circulation 118(5), 586–606 (2008)
10. Breton, E., et al.: Quantitative contrast-enhanced first-pass cardiac perfusion MRI at 3 tesla with accurate arterial input function and myocardial wall enhancement. J. Magn. Reson. Imaging (2011)
11. Serruys, P.W., et al.: Percutaneous coronary intervention versus coronary-artery bypass grafting for severe coronary artery disease. N. Engl. J. Med. 360(10), 961–972 (2009)
12. Sattel, T.F., et al.: Single-sided device for magnetic particle imaging. Journal of Physics D: Applied Physics 42(2) (2009)

Iron Oxide Nanoparticles – Tracer for Magnetic Particle Imaging

Ulrich Pison[1], Cordula Grüttner[2], Fritz Westphal[2], Barbara Kleiner[3], Nicole Barthel[3], and Katharina Roepke[3]

[1] Charité-Universitätsmedizin Berlin, CC 7
Augustenburger Platz 1, 13353 Berlin, Germany
ulrich.pison@charite.de
[2] micromod Partikeltechnologie GmbH
Friedrich-Barnewitz-Straße 4, 18119 Rostock, Germany
gruettner@micromod.de
[3] Topass GmbH
Drakestr. 42, 12205 Berlin, Germany
info@topass.eu

Abstract. Magnetic Particle Imaging (MPI) is a tomographic imaging technique, which relies on the nonlinearity of the magnetization curves of magnetic particles such as iron oxide nanoparticles and the fact that the particle magnetization saturates at some magnetic field strength (1). Sensitivity of MPI highly depends on the magnetic characteristics of used tracer. We have developed colloidal stable iron oxide nanoparticles with different sizes and coatings and optimized their magnetic properties using a variety of fractionation techniques to improve tracer sensitivity. MPI spectra were obtained on the various iron oxide nanoparticles to select the most sensitive tracer for plaque imaging in homozygous mice for the Apoe^{tm1Unc} mutation. We conclude that iron oxide nanoparticles with appropriate magnetic properties are useful tracers for MPI.

1 Introduction

Imaging technologies such as computer tomography (CT), ultrasound imaging, magnetic resonance imaging (MRI), and positron emission tomography (PET) are useful tools for the diagnosis and therapy control in routine clinical practice (4). MPI is a new imaging technology that relies on the nonlinearity of the magnetization curves of magnetic particles such as iron oxide nanoparticles and the fact that the particle magnetization saturates at some magnetic field strength (1, 7). Resolution and sensitivity of MPI depends on the appropriate tracer (6). Since the current tracer for MPI, Resovist® is not available anymore on the market we aimed to develop new tracer material for MPI and summarize our current data on this approach.

T.M. Buzug and J. Borgert (Eds.): Magnetic Particle Imaging, SPPHY 140, pp. 135–139.
springerlink.com

2 Material and Methods

Iron oxide nanoparticles were synthesized by alkaline precipitation of iron(II) and iron(III) salts in the presence of dextran or carboxydextran (2, 5). The obtained material was further purified using alternating and permanent magnetic fields. Resovist® was obtained from Bayer-Schering-Pharma, Berlin, Germany. Iron concentration was measured using phenanthroline standard calorimetric assay.

Size of nanoparticles was determined by dynamic light scattering (DLS) and ξ-potential was measured by electrophoretic mobility using a Nano-ZS Zetaziser (Malvern Instruments, Herrenberg, Germany) according to the manufacturer's instructions. Colloidal stability was defined as the aggregation tendency of nanoparticles in various conditions including water, Hank's balanced salt solution at pH 7.4 containing 1 mM $MgCl_2$, 1 mM $CaCl_2$ and 1 g/l glucose (HBSS) and HBSS supplemented with 4 % bovine serum albumine (BSA). Briefly, 1 mg nanoparticles were diluted in 1 mL indicated media, incubated for 30 minutes at room temperature and measured by DLS. The ξ-potential was determined in 1 mM NaCl. Atomic Force Microscopy (AFM) was performed using a NanoWizard AFM device (JPK Instruments AG, Berlin, Germany) equipped with a microscope (Axiovert 200, Zeiss Jena, Germany). Diluted nanoparticles were briefly incubated on a fresh cleaved mica sheet, rinsed with aqua bidest and air dried for 5 minutes. Images were taken using the intermitted contact mode using a cantilever tip with a force constant of 7.5 N/m (3).

MPI spectra were obtained using a Magnetic Particle Spectrometer (Philips Hamburg, Germany). Transition electron microscopy (TEM) was performed on an EM 902 (Zeiss, Oberkochen, Germany).

Animal experiments were performed according to the German Animal Welfare Act of 1998 and with approval from the responsible authorities. Plaque imaging was performed on the thoracic aorta of homozygous mice with mutation for the $Apoe^{tm1Unc}$. One day before the aorta was explanted for imaging $Apoe^{tm1Unc}$ mice received purified macrophages ($CD11b^{+}$-cells) that were obtained from spleen explants of BL/6 mice. These macrophages were labeled with MM4 iron oxide nanoparticles *in vitro* prior use.

3 Results and Discussion

Iron oxide nanoparticles that were obtained by alkaline precipitation were further purified using alternating and permanent magnetic fields. We obtained magnetic particle fractions termed MM1 to MM8. All fractions of particles were colloidal stable as depicted for MM4 in Fig. 1. Particles remained stable over at least 3 months.

The polydispersity index as obtained with DLS was below 0.2 for all our particle preparations. For comparison, we measured a larger polydispersity index of about 0.25 and Dh = 37 nm for Resovist®, a carboxydextrane stabilized iron oxide nanoparticle, which is commercially available and used as contrast agent in magnetic resonance tomography.

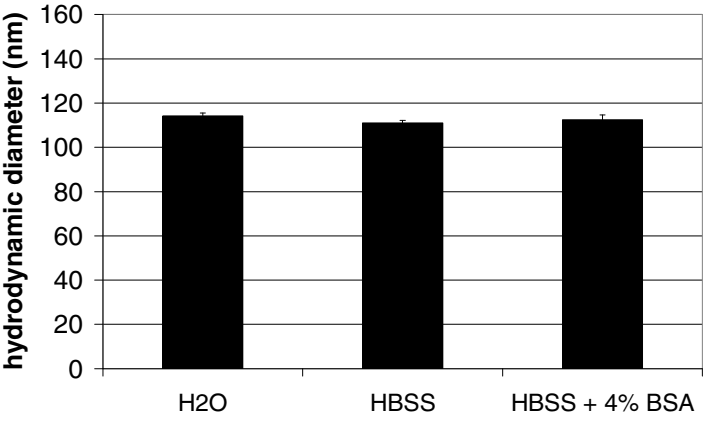

Fig. 1. Colloidal stability of MM4 particles in H_2O, HBSS and HBSS in the presence of 4 % BSA

AFM and TEM displayed monodispersed particles as shown in Fig. 2.

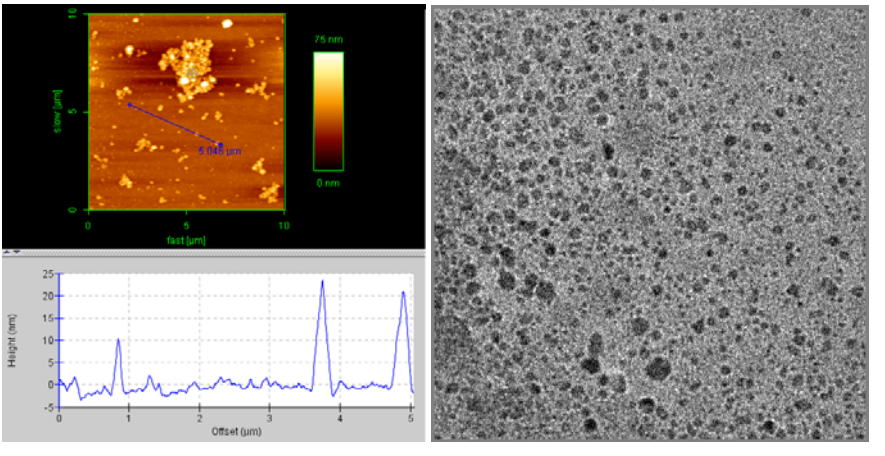

Fig. 2. AFM and TEM image of MM 8 particles.

To select the most sensitive tracer for MPI we obtained MPI spectra for our iron oxide nanoparticles at an iron concentration of 50mM and compared data with the data for Resovist® at the same iron concentration. We found that MM4 outperformed the magnetic behavior of Resovist® in terms of MPI sensitivity by an order of two.

We selected MM4 to demonstrate feasibility of the new tracer material for *in vivo* applications. Macrophages ($CD11b^+$-cells) from BL/6 mice were labeled with MM4 and the labeled cells were injected intravenously into $Apoe^{tm1Unc}$ mice. After 24 hours the aorta was explanted and MPI spectra

of the explanted aorta obtained. We found positive MPI spectra indicating that the MM4 labeled macrophages migrated to the inflammatory sites of the vessel in this animal model of arteriosclerosis.

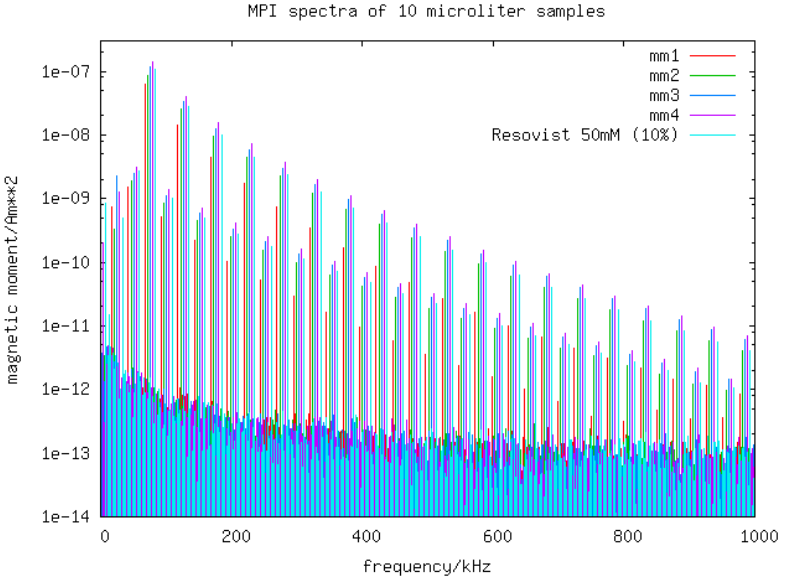

Fig. 3. MPI spectra of MM1, MM2, MM3, MM4 and Resovist® at 50mM Fe.

4 Conclusion

MPI relies on available tracers that fulfill certain criteria depending on their intended use. For the *in vivo* use in clinical and preclinical imaging tracer material need to be colloidal stable and non-toxic. Resovist® has been used in the past due its availability, approval as contrast agent in clinical medicine and appropriate magnetic characteristics for MPI. Since Resovist® is not available any more on the market we set out to develop a substitute for clinical and preclinical use. Current data on MM4 to MM8, new iron oxide nanoparticles obtained through alternating and permanent magnetic field fractionation, demonstrate that colloidal stable particles with optimized magnetic properties could be synthesized with reproducible characteristics. These tracers will become available in the near future for preclinical applications, but further experiments are necessary before such new material could be used in a clinical setting.

Acknowledgement. The authors would like to thank Bernhard Gleich from Philips Technology GmbH in Hamburg for MPI spectra. This work was in part financial supported by a grant form the BMBF.

References

1. Gleich, B., Weizenecker, R.: Tomographic imaging using the nonlinear response of magnetic particles. Nature 435, 1214–1217 (2005)
2. Grüttner, C., Teller, J., Schütt, W., Westphal, F., Schümichen, C., Paulke, B.: Preparation and Characterization of Magnetic Nanospheres for in vivo Application. In: Häfeli, U.O., Schütt, W., Teller, J., Zborowski, M. (eds.) Scientific and Clinical Applications of Magnetic Carriers, pp. 53–68. Plenum Press, New York (1997)
3. Kaufner, L., Cartier, R., Wustneck, R., Fichtner, I., Pietschmann, S., Bruhn, H., Schutt, D., Thunemann, A.F., Pison, U.: Poly(ethylene oxide)-block-poly(glutamic acid) coated maghemite nanoparticles: in vitro characterization and in vivo behaviour. Nanotechnology 18 (2007)
4. Kiesslich, R., Goetz, M., Hoffman, A., Galle, P.R.: New imaging techniques and opportunities in endoscopy. Nature Reviews Gastroenterology & Hepatology 8, 547–553 (2011)
5. Molday, R.S., Mackenzie, D.: Immunospecific Ferromagnetic Iron-Dextran Reagents for the Labeling and Magnetic Separation of Cells. Journal of Immunological Methods 52, 353–367 (1982)
6. Weizenecker, J., Borgert, J., Gleich, B.: A simulation study on the resolution and sensitivity of magnetic particle imaging. Physics in Medicine and Biology 52, 6363–6374 (2007)
7. Weizenecker, J., Gleich, B., Rahmer, J., Dahnke, H., Borgert, J.: Three-dimensional real-time in vivo magnetic particle imaging. Physics in Medicine and Biology 54, L1–L10 (2009)

Magnetic Particle Imaging Theory

Experimental Evaluation of Correlation-Based Image Reconstruction Method for Magnetic Particle Imaging

Takumi Honma and Yasutoshi Ishihara

School of Science and Technology, Meiji University
1-1-1, Higashimita, Tama-ku, Kawasaki-shi, Kanagawa, Japan
ee84030@isc.meiji.ac.jp, y_ishr@meiji.ac.jp

Abstract. In a conventional magnetic particle imaging (MPI) method, a reconstructed image is mainly calculated from odd harmonics of the magnetization response. However, the image blurring and artifacts appear due to the interference of the magnetization response generated from magnetic nanoparticles (MNPs) around the field free point (FFP), so that the image resolution is degraded. Therefore, we proposed a new image reconstruction method that was focused on the difference between a waveform of electromotive force generated from inside and outside of an object region. Then, a numerical analysis and a phantom experiment were performed in order to confirm validity of the proposal method, and an experiment system was constructed. As results, it was indicated that image artifacts was reduced by the proposal method. However, since the image blurring was seen on the reconstructed image, the image resolution needs to be improved.

1 Introduction

In a magnetic particle imaging (MPI), a local magnetic field distribution is scanned, and the magnetization signal generated from magnetic nanoparticles (MNPs) within the field free point (FFP) is detected [1] ~ [3]. In a conventional (fundamental) method, a reconstructed image is mainly calculated from odd harmonics of the magnetization response. However, the image blurring and artifacts appear due to the interference of magnetization response.

Therefore, we have proposed the image reconstruction methods to solve this problem. One of these methods could correct the image blurring and artifacts by adjusting frequency components of observed magnetization response, and another could suppress the image artifacts by evaluating a saturation time of the magnetization response [4]. Although we have shown that an exact particle image of an isolated unit particle could be reconstructed with this method, we were not able to obtain an exact particle

T.M. Buzug and J. Borgert (Eds.): Magnetic Particle Imaging, SPPHY 140, pp. 143–148.
springerlink.com

image when MNPs existed as a spatially continuous distribution since the edge parts of an object on the reconstructed image were emphasized excessively.

In this study, we propose the new image reconstruction method that is focused on the difference between the waveform of electromotive force generated from inside and outside of an object region (FFP) [5][6]. A numerical analysis and a phantom experiment are carried out in order to confirm validity of this proposal method.

2 Material and Methods

2.1 Concept of Proposal Method

In order to improve the image blurring and artifacts for the MPI, we propose the method based on the correlation information between a system function and the waveform of an electromotive force detected with a receiver coil around a field of view (FOV). The outline of the proposal method is indicated in Fig.1. In this explanation, the FOV is treated as one-dimensional matrix. When an MNP exists in a left end matrix, the FFP is scanned for every matrix and an observation signal is generated as Vx(t) at each FFP (Fig.1, left column). A calculated waveform generated from an MNP that is located at each scanning point (FFP) is defined as a system function (Fig 1, central column). This system function is expressed as Gx(t) in this paper. An image intensity of a reconstruction image is calculated from the correlation between the observation signal Vx(t) and the system function Gx(t) at each scanning point. Therefore, the two-dimensional image intensity F(x,z) in the x-z plane is reconstructed by using Eq. (1)

$$\mathrm{F}(\mathrm{x},\mathrm{z}) = \int V_{x,z}(t) G_{x,z}(t) dt \tag{1}$$

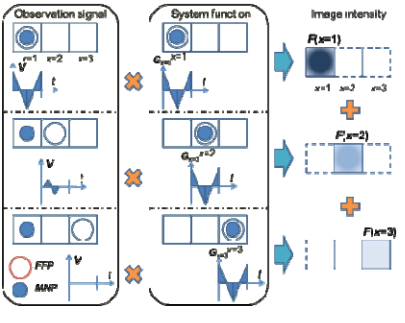

Fig. 1. One-dimensional image reconstruction by the proposal method

2.2 Condition of Numerical Analysis

A numerical analysis was carried out on a condition corresponding to our prototype system. The Maxwell pair coil (diameter: 180mm, distance: 50mm) was used. The FOV was set to 40 mm × 40 mm with a matrix size of 21 × 21, and an MNP were located at the center of FOV. A gradient field of 1.45 T/m generated in the z-direction was applied into the MNP. In addition, an alternative magnetic field of 32 mT with a frequency of 39 Hz was applied.

2.3 Condition of Experiment for One-Dimensional Image Reconstruction

Bipolar current sources were controlled with a function generator, and then an alternating magnetic field and the FFP were generated by the Maxwell pair coil (diameter: 180 mm, coil turns: 250-turn, distance between coils: 50 mm). A phantom that was enclosed magnetic fluid (ferucarbotran: 500 mmol/l, 0.5 cc) was located at the center between coils, and magnetization responses were measured with a receiver coil (diameter: 19 mm, coil turns: 350-turn). In order to examine the validity of the proposal method, an electromotive force generated from an MNP at each FFP was detected. An alternative current of 6.0 A was applied to the Maxwell pair coil with frequency of 39 Hz in the same direction to generate an alternative magnetic field of 32mT. In addition, direct current of 12 A was also applied to it in the opposite direction to generate a gradient field of 1.45 T/m in z direction as the FFP. The current value required to move the FFP-interval (corresponds to the resolution of the image matrix) was evaluated by the preliminary experiment, and the FFP was scanned by controlling the function generator. Measured image point was divided into 21 points in the range of ±20 mm-FOV.

3 Results

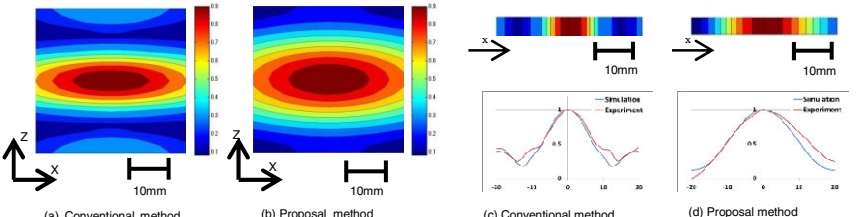

(a) Conventional method (Numerical analysis)
(b) Proposal method (Numerical analysis)
(c) Conventional method (Phantom experiment)
(d) Proposal method (Phantom experiment)

Fig. 2. Reconstructed image by each method

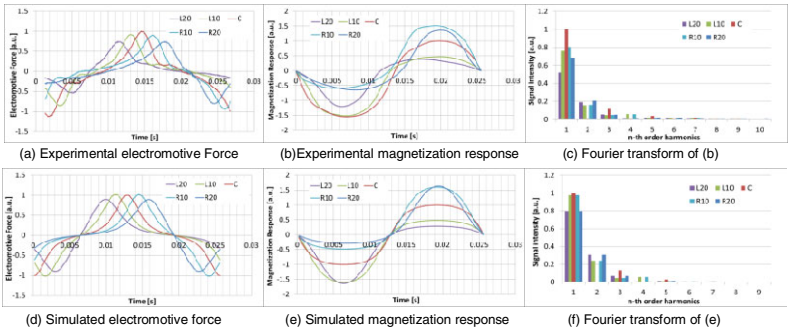

(a) Experimental electromotive Force (b)Experimental magnetization response (c) Fourier transform of (b)

(d) Simulated electromotive force (e) Simulated magnetization response (f) Fourier transform of (e)

Fig. 3. Electromotive force and magnetization response at each FFP

The reconstructed two-dimensional images by each method in the numerical analysis were shown in Fig.2 (a), (b), respectively. The image artifacts appeared upper and lower side of the region where the MNPs were actually located in the conventional method. On the other hand, image artifacts were not appeared in the proposal method. The image resolution was calculated by using a full width at half maximum (FWHM). An evaluated image resolution in z-direction for each method was 7.2 mm and 10.3 mm, respectively (Fig.2 (a), (b)). Image resolutions in the x-direction were, however, unmeasurable.

The waveforms of electromotive forces, magnetization signals that were integrated electromotive forces, and Fourier decomposition of magnetization signals in the experiments were described in Fig.3 (a), (b), and (c), respectively. The results of numerical analysis obtained under the same condition were also shown in Fig.3 (d), (e), and (f). Figure 2 (c) and (d) showed the reconstructed images in one-dimension and theirs profiles. Ideally, the system functions of the proposal method need to be defined at each scanning point. In contract to this, since the system functions of our experimental condition were little difference between each scanning point, all system functions were defined as the same at each scanning point. In this experiment, therefore, the waveform observed when an MNP and the FFP were located at the center of FOV was made into the system function. As experimental results, the spatial resolution of each method was 8 mm and 10mm, respectively (Fig.2 (c), (d)).

4 Discussion

It was confirmed that the numerical analysis is effective owing to detecting the same electromotive forces between the numerical analysis and the phantom experiment. Furthermore, image artifacts reconstructed by using the conventional method were suppressed by using the proposal method although the image blurring was appeared around real particle location (Fig.2 (a), (b)).

As the first cause, it is difficult to generate a sharp gradient field by a general Maxwell pair coil. Therefore, in particular, the image blurring was easy to appear in the x-direction. This solution is to average each reconstructed image obtained by exchanging the direction of the gradient field. As the second cause, the correlation information cannot be calculated correctly by using the system function obtained from only the scanning point. Because of this reason is that the system function of the proposal method (Fig.1, central column) ignored interference signals generated from the MNPs that located the boundary regions of the FFP. A reconstruction algorithm considered this interference signals has been attempted in our study.

Furthermore, image artifacts may be able to appear depending on the conditions of MNP's location and the value of gradient field in this proposal method. This is because the interference signal generated from the MNPs may be included in a response waveform as the odd harmonics at the scanning point (FFP), even when an FFP is located at the position separated from the MNPs. Since these components are also included into a system function, it becomes impossible to calculate exact correlation information. We need further studies to determine the condition in cases image artifacts appear on the reconstructed images.

5 Conclusion

In this paper, we proposed new reconstruction method for suppressing image artifacts, and confirmed the validity of the proposal method by performing the numerical analysis and the phantom experiment. The algorithm of proposal image reconstruction used correlation information between the observed signal and the system function. Although we obtained the image resolution of about 12 mm and image artifacts were suppressed in experiment of one-dimensional reconstruction, the proposal method needs to be improved since the image blurring was seen on the reconstructed image.

References

1. Gleich, B., Weizenecker, J.: Tomographic imaging using the nonlinear response of magnetic particles. Nature 435, 1214–1217 (2005)
2. Weizenecker, J., Borgert, J., Gleich, B.: A simulation study on the resolution and sensitivity of magnetic particle imaging. Phys. Med. Biol. 52, 6363–6374 (2007)
3. Gleich, B., Weizenecker, J., Borgert, J.: Experimental results on fast 2D-encoded magnetic particle imaging. Phys. Med. Biol. 53, N81–N84 (2008)

4. Kusayama, Y., Ishihara, Y.: High-resolution Image Reconstruction Method on the Molecular Imaging Using Magnetic Nanoparticles. Technical Report of IEICE, MBE2009-92, pp. 1653–1662 (2009)
5. Ishihara, Y., Kuwabara, T., Wadamori, N.: Sensitivity improvement of a molecular imaging technique based on magnetic nanoparticles. In: Proc. SPIE, vol. 7965, pp. 79652J-1-j-8 (2011)
6. Ishihara, Y., Kuwabara, T., Honma, T., Nakagawa, Y.: Correlation-based image reconstruction methods for magnetic particle imaging. IEICE Trans. Electron (in press)

Relaxation in x-space Magnetic Particle Imaging

Laura R. Croft[1], Patrick Goodwill[1], Matt Ferguson[3], Kannan Krishnan[3], and Steven Conolly[1,2]

[1] Departments of Bioengineering & [2] EECS, University of California, Berkeley
340 Hearst Memorial Mining Bldg, Berkeley, CA 94709, USA
lcroft@berkeley.edu, sconolly@berkeley.edu
[3] Department of Materials Science & Engineering, University of Washington
Box 352120, Seattle, WA 98195, USA

Abstract. Magnetic particle imaging (MPI) is an emerging medical imaging modality capable of high-sensitivity images with unprecedented contrast and without ionizing radiation [1]. Our laboratory previously developed the x-space theory for MPI, which describes MPI as a scanning process in the spatial domain [2,3]. X-space MPI is particularly critical as it permits real-time image reconstruction, orders of magnitude faster than the traditional harmonic space system matrix reconstruction methods. The x-space theory was derived assuming adiabatic and instantaneous alignment of ultra-small superparamagnetic iron oxide nanoparticles (USPIOs) with the applied magnetic field. However, in reality the magnetization lags behind the applied field due to relaxation. Here, we include relaxation in the x-space MPI theory and show that real-time reconstruction is still feasible even with relaxation effects.

To validate our theoretical predictions, we built an x-space MPI relaxometer, which measures the USPIO diameter, relaxation time constant, and point spread function (PSF) without an imaging gradient. We show that the inclusion of these relaxation effects is essential for theoretical predications to agree with experimental MPI data, and we demonstrate experimentally and theoretically how relaxation adversely affects image quality. This knowledge will enable us to understand how to design MPI x-space scanning to mitigate the negative effects of relaxation and to achieve desirable image resolution, accuracy, and signal strength.

1 Introduction

Magnetic particle imaging is a new imaging modality with excellent contrast and sensitivity to the family of superparamagnetic iron oxide nanoparticles contrast agents (SPIOs and USPIOs). MPI also offers the safety benefits of no ionizing radiation [1]. The ferumoxide contrast agents employed in MPI

T.M. Buzug and J. Borgert (Eds.): Magnetic Particle Imaging, SPPHY 140, pp. 149–153.
springerlink.com

have been found safe even for Chronic Kidney Disease (CKD) patients, who cannot tolerate conventional contrast agents, iodine and gadolinium [4]. MPI senses only the contrast agent, and human tissue is completely transparent to the low-frequency magnetic fields used in MPI. Hence, the contrast to background ratio of MPI is *unprecedented* in the history of medical imaging.

To create a MPI scan, we employ a linear magnetic gradient, which creates a so-called field-free point (FFP) at the origin of the gradient. We translate the FFP across the image field of view (FOV) in a sinusoidally varying manner, causing USPIO magnetic moments to "flip" and induce a signal in an inductive receiver coil.

The x-space theory for MPI provides an elegant description of MPI as a scanning process in the image domain [2,3]. The x-space theory also provides a real-time image reconstruction algorithm, orders of magnitude faster than traditional system matrix reconstruction methods. However, the original x-space theory neglected relaxation effects. Relaxation includes Brownian, Neel or any other effect that that causes a time delay between applied field and magnetization response. Here we amend the x-space theory to include relaxation and compare it to experimentally measured results in a x-space MPI relaxometer. We demonstrate experimentally how relaxation affects image resolution, and we also investigate methods to minimize these effects.

2 Theory

To update the one-dimensional x-space theory to include relaxation effects, we developed a phenomenological description of magnetization *M(x,t)* (measured in A/m) based on first-order Debye relaxation process, as previously described in [5,6].

$$M(x,t) = M_{adiab}(x,t) * r(t)$$

where $M_{adiab}(x,t)$ (A/m) is the adiabatic magnetization solved for in the original x-space analysis [2], and *r(t)* represents a relaxation term. We assumed that the relaxation blur could be well-modeled by the generic function $r(t) = \frac{1}{\tau} e^{-\frac{t}{\tau}} u(t)$ where *u(t)* is the heavyside function and τ is the relaxation time constant, in seconds. It follows that the x-space MPI image equation with relaxation is:

$$\hat{\rho}(x_s(t)) = \hat{\rho}_{adiab}(x_s(t)) * r(t)$$

where $x_s(t)$ is the instantaneous FFP position. Note that this equation assumes that first-harmonic information, which must be rejected due to direct feedthrough, can be fully restored by methods experimentally validated in [3,7]. We also assumed that the sinusoidal FFP velocity is well approximated as a constant-velocity waveform, which incurs errors smaller than

5% under our partial FOV scanning conditions [3,7]. Hence the ramp FFP velocity is modeled accurately as

$$RG = H_{amp} 2\pi f$$

where H_{amp} is the excitation field strength amplitude (T) and f is the excitation frequency (Hz). We use this value of field ramp rate to characterize the scanning rate of the relaxometer.

3 Material and Methods

We performed theoretical calculations using MATLAB and compared these predicted signals to those acquired in the Berkeley x-space relaxometer (see Figure 1), which measures the 1D x-space point spread function (PSF) [2,8].

The relaxometer has a resonant excitation coil, which scans the FFP using oscillating magnetic fields of 20-200 mT-pp strength at nine frequencies ranging from 1.4 kHz to 22.25 kHz. Here we selected four frequencies of these frequencies (2.245, 4.4, 7.775, and 8.9125 kHz), since they are close enough in frequency to be capable of producing comparable field ramp rates. During excitation, the signal from the USPIO magnetization response is received by an inductive receiver coil. The relaxometer also has a bias coil, which we vary up to ± 130 mT to simulate moving a point source sample in a gradient field.

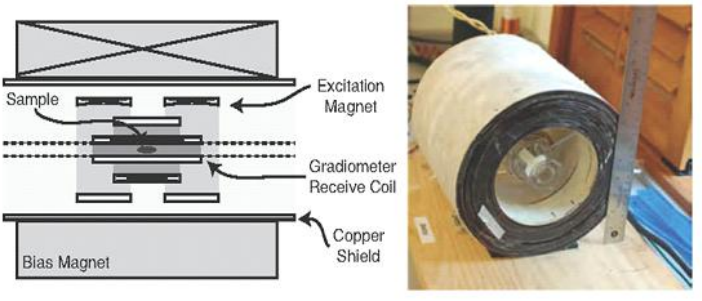

Fig. 1. (left) Schematic and (right) photo of the Berkeley x-space MPI relaxometer

Using an unconstrained nonlinear optimization method and assuming a log-normal particle size distribution and a single relaxation time constant, we adapted the theoretical simulation to fit to experimental signals. Using this method we derived a measurement of the relaxation time of an experimentally measured USPIO sample.

4 Results

Figure 2 (left) displays an experimentally measured PSF of Resovist as well as two theoretically calculated PSFs: the adiabatic x-space PSF and the x-space PSF with relaxation effects included. Clearly, the x-space theory matches experimentally-measured signals far better after including relaxation effects. Note also that relaxation causes *blurring* as well as a gross shift in the scanning direction. Both of these artifacts are significant and efforts must be made to mitigate their effects.

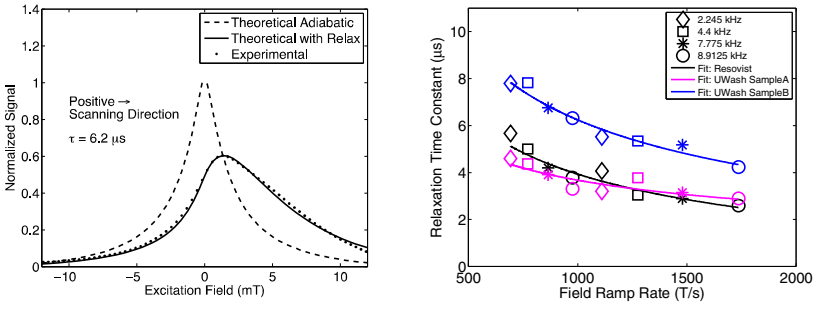

Fig. 2. (left) An experimentally measured PSF of Resovist acquired at 4.4 kHz and 37.4 mT-pp in the positive scanning direction compared to the adiabatic x-space predicted PSF and the updated x-space predicted PSF. (right) Measured relaxation time constants decrease with field ramp rate.

The measured relaxation time constants decreased with faster scanning rate as displayed in Figure 2 (right). Peak signal also varied with field ramp rate; Figure 3 (right) depicts a linear increase in peak signal with increasing field ramp rate. However, increasing field strength, which increases scanning rate, widened resolution as measured by the full-width at half-maximum (see Figure 3 (left)).

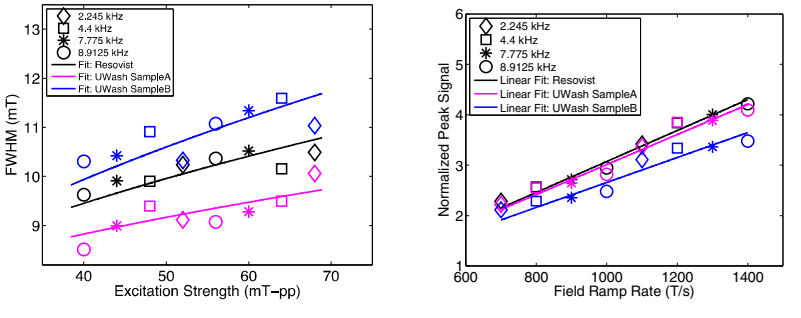

Fig. 3. (left) Resolution measured as full-width at half-maximum (FWHM) worsens with increasing excitation strength. (right) Peak signal increases linearly with field ramp rate.

5 Discussion

Incorporating relaxation effects into the x-space theory greatly improved our ability to model the shape of experimentally measured signals. We have found experimentally that relaxation effects will asymmetrically blur the MPI image and shift the image in the scanning direction.

Relaxation time decreases with increasing scanning rate as the magnetic torque acting on the USPIOs increases. However, we have found that overall image resolution improves with a smaller excitation field strength. We believe this resolution enhancement occurs because smaller excitation strengths require less rotation of the nanoparticle, and the particle is able to respond with less blurring. Fortunately, increasing scanning rate increases the peak signal and overall image SNR. Selecting a scanning rate is clearly a tradeoff between image resolution and SNR. We are currently working to better understand these tradeoffs.

6 Conclusion

Allowing for non-negligible relaxation improves the accuracy of the x-space theory. We have found that relaxation introduces a delay on scans as well as significant asymmetric blurring of the image, both effects acting in the scanning direction. We are testing scanning parameters to reduce these artifacts.

References

1. Gleich, B., Weizenecker, J.: Tomographic imaging using the nonlinear response of magnetic particles. Nature 435, 1214–1217 (2005)
2. Goodwill, P., Conolly, S.: The x-space formulation of the magnetic particle imaging process: 1-D signal, resolution, bandwidth, SNR, SAR, and magnetostimulation. IEEE Transactions on Medical Imaging 29, 1851–1859 (2010)
3. Goodwill, P., Conolly, S.: Multidimensional x-space magnetic particle imaging. IEEE Transactions on Medical Imaging 30, 1581–1590 (2011)
4. Lu, M., et al.: FDA report: ferumoxytol for intravenous iron therapy in adult patients with chronic kidney disease. American Journal of Hematology 85, 315–319 (2010)
5. Debye, P.: Polar Molecules. The Chemical Catalog Company, New York (1929)
6. Shliomis, M.: Magnetic fluids. Sov. Phys.-Usp. 17, 153–169 (1974)
7. Lu, K., Goodwill, P., Zheng, B., Conolly, S.: The impact of filtering direct-feedthrough on the x-space theory of magnetic particle imaging. In: Proceedings of SPIE, vol. 7965, p. 79852I (2011)
8. Goodwill, P., et al.: Ferrohydrodynamic relaxometry for magnetic particle imaging. Applied Physics Letters 98, 262502–262502-3 (2011)

Linear and Shift Invariance of Magnetic Particle Imaging

Kuan Lu[1], Patrick Goodwill[1], and Steve Conolly[2]

[1] Bioengineering, UC Berkeley, 340 HMMB
Berkeley, CA 94720-1762, United States
luckylukuan@berkeley.edu
[2] UC Berkeley, Department of Bioengineering and EECS
Berkeley Imaging System Laboratory, 340 HMMB
Berkeley, CA 94720, United States
sconolly@berkeley.edu

Abstract. MPI is intrinsically a linear and shift-invariant (LSI) system as described in x-space theory [3,4] assuming perfect signal acquisition and that the imaging equation can be written as a convolution in real space. However, the received MPI signal is corrupted by a direct feedthrough signal from the excitation source at the drive frequency, which is 10^6 times larger than the nanoparticle signal. Hardware filtering is required to suppress the feedthrough signal but also inevitably removes this frequency component from the particle signal. This signal loss in the received particle signal breaks the LSI properties of x-space MPI. This study will investigate the impact of losing the fundamental frequency component in the image domain and propose an algorithm to recover the lost information. Finally, experimental results demonstrate that LSI properties can be restored after applying a simple and robust baseline recovery algorithm.

1 Introduction

Magnetic Particle Imaging [1] (MPI) is a new medical imaging modality that holds great promise. There have been many efforts toward understanding MPI's imaging theory and image reconstruction, including harmonic domain system matrix theory [2] and x-space theory [3,4]. The harmonic domain theory is the first established method to analyze MPI signals in the frequency domain and to reconstruct MPI images. Unfortunately, the system matrix methods require the inversion and multiplication of a very large matrix, which makes real-time MPI image reconstruction difficult. X-space reconstruction has already been demonstrated to provide a real-time and well-conditioned image reconstruction; moreover, it is the first theory that indicates MPI is an LSI system.

T.M. Buzug and J. Borgert (Eds.): Magnetic Particle Imaging, SPPHY 140, pp. 155–160.
springerlink.com

Linearity and shift-invariance (LSI) are critical characteristics for quantitative imaging. X-space theory shows that MPI can be modeled as an LSI system [3] assuming perfect signal acquisition. However, MPI does suffer from signal loss in data acquisition. Unlike MRI, where the received signal and excitation are temporally decoupled, MPI drives the excitation coil and detects the particle signal simultaneously. Thus the excitation field will undesirably "feed through" to the receiver and corrupt the particle signal. This contamination from the excitation signal is more than 10^6 times stronger; therefore, significant electronic filtering is needed to suppress the feedthrough contamination. However, the filtering operation also removes most of the particle signal around the fundamental drive frequency, and compromises the LSI properties of the MPI system (see **Fig.1**).

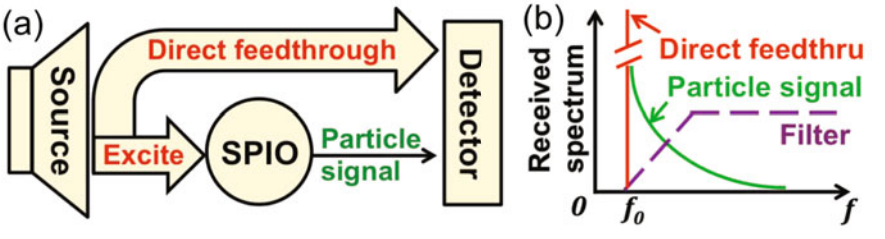

Fig. 1. Direct feedthrough challenge. **(a)** Particle signal is corrupted by the direct feedthru signal from the source, which is 10^6 times stronger than the desired particle signal. **(b)** Significant filtering is needed to remove the direct feedthrough signal, but it also removes part of the particle spectrum, thus breaks LSI in MPI and introduces artifacts.

In order to use MPI as a quantitative imaging technique, it is important to recover MPI's LSI properties by recovering the lost signal. In this study, we show that filtering out the fundamental frequency signal only leads to low spatial frequency loss in x-space and is recoverable with robust image processing methods [5]. Our preliminary imaging experiments show excellent match to the theoretical simulations using LSI x-space theory.

2 Material and Methods

Theoretically, the ideal particle signal from a single scan in temporal domain can be decomposed into a sum of temporal harmonics. Since we lose the fundamental frequency component of the particle signal, it is prudent to isolate its contribution to the MPI. We have shown mathematically that the loss of fundamental frequency in the signal spectrum leads to a constant offset in the image domain (see **Fig.2a**), with its amplitude

varying with the particle concentration distribution within each scan. It can be proven that the lost information can be recovered by enforcing positivity of the reconstructed image with the boundary condition that the image intensity goes to zero at the edge of the field of view (see **Fig.2b**).

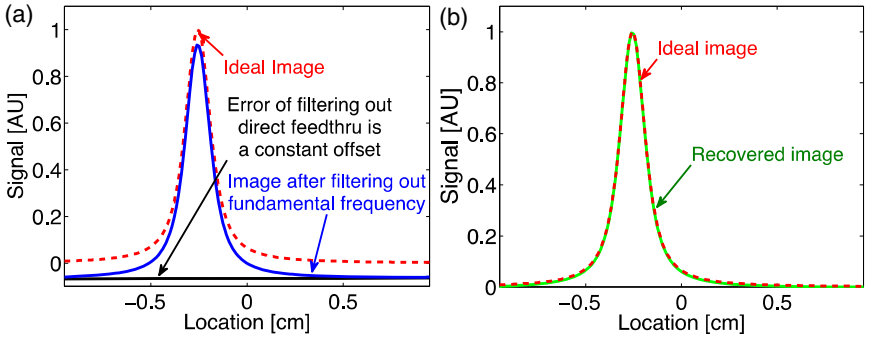

Fig. 2. (a) Langevin simulation of the MPI image of a point source before & after filtering. It shows that fundamental frequency loss leads to an unknown constant offset in the filtered image. **(b)** The constant loss can be robustly recovered via enforcing positivity of the image across the scanning FOV.

In a realistic MPI scanning scheme, the excitation field is limited due to safety concerns, which directly translates to a small scanning field of view (FOV). Therefore, to cover the entire sample, multiple partial FOVs (pFOV) are acquired and the final image is formed by stitching all the pFOVs together. As mentioned above, the constant offset of each pFOV scan correlates with the actual particle concentration within that pFOV and varies from scan to scan (see **Fig.3c**). Similar to the single scan scheme, the constant loss from each pFOV scan can be easily estimated and compensated by enforcing positivity and continuity of the overall image, and the stitching can be realized through constrained nonlinear optimization.

3 Results

Experiment on a point source phantom (**Fig.3b**) is carried out on the Berkeley MPI scanner (**Fig.3a**) to validate the baseline recovery method. **Fig.3c,d,e** shows the raw scans, scans after baseline recovery, and the final reconstructed image.

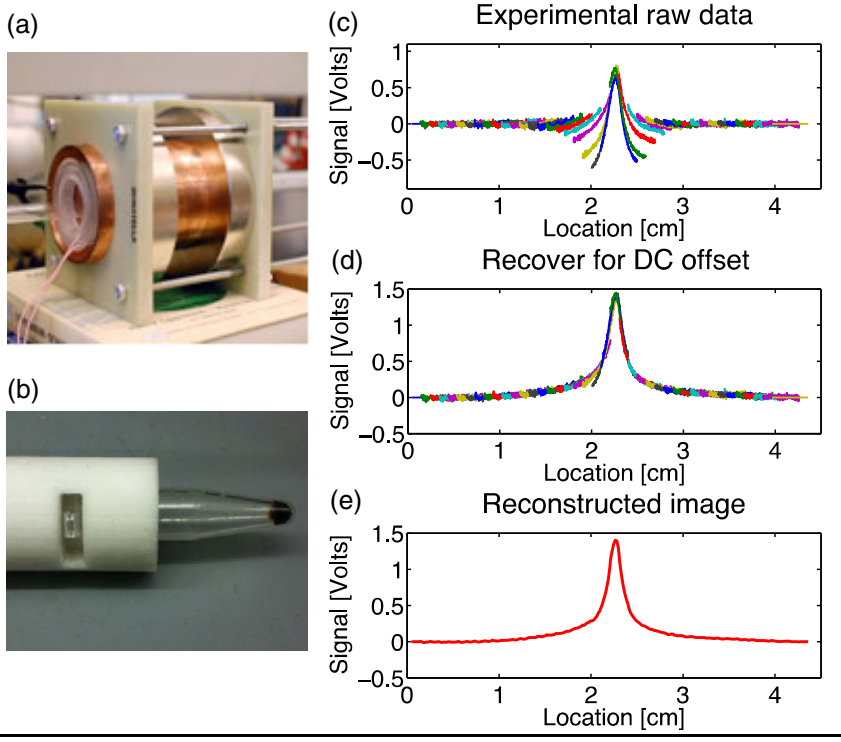

Fig. 3. Experimental data of point source phantom. **(a)** Berkeley MPI scanner. **(b)** Point source concentration (undiluted Resovist, 0.5 mmol Fe/mL). **(c)** The raw scanning data, it can be seen that there is a DC offset lost for each scan. **(d)** The result after applying the DC recovery to each scan. **(e)** Reconstructed image indicates the experimental success of the baseline recovery and pFOV stitching algorithm.

Furthermore, the linearity and shift-invariance of MPI system with baseline recovery is experimentally tested on Berkeley Field Free Line (FFL) scanner (**Fig.4a**). The LSI phantom is constructed using four polyethylene tubings injected with Resovist of different concentration (**Fig.4b**). The resulting image is shown is **Fig.4c**, and it shows that MPI is indeed linear and shift-invariant with baseline recovery and stitching algorithm.

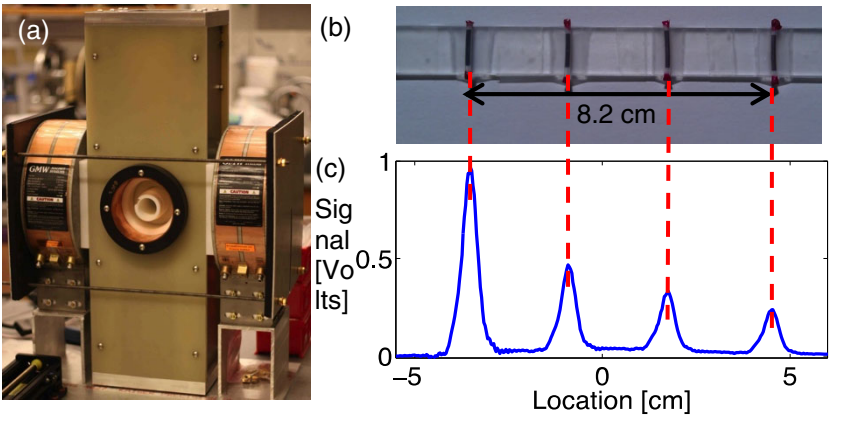

Fig. 4. Experimental demonstration of linearity and shift-invariance (LSI) in MPI with baseline recovery and pFOV stitching. **(a)** Berkeley Field Free Line (FFL) scanner. **(b)** Shift-invariant phantom w/ iron quantity (from left to right) of: 0.5, 0.25, 0.167, and 0.125 mmol Fe in each acrylic tubing. **(c)** The recovered 1D image shows that the image response of the SPIO channel of the same width is linear with respect to the iron quantity and has the same shape at different locations, thus LSI properties of MPI are restored.

4 Discussion

In **Fig.3**, the raw experimental data shows serious discontinuities in between adjacent scans. Without any recovery, the overall reconstructed image would suffer from significant artifacts, and the LSI properties break down due to the varying constant loss from each pFOV scan. Here we proposed and experimentally validated a fast and robust algorithm to restore the lost baseline information at fundamental frequency using a constrained nonlinear optimization method that enforces continuity and positivity across all the pFOVs. We found our algorithm is robust and produces no SNR degradation in our experimental image reconstructions. This new imaging algorithm restores linearity and shift-invariance for any MPI scanner, which will be critical for future MPI biomedical applications.

It is necessary to have the boundary condition for an accurate recovery, which is the particle signal should die off to zero at the edge of the field of view. In a practical scan, it can be achieved by extending the imaging field of view slightly beyond the sample region to ensure the boundary condition.

5 Conclusion

Direct feedthrough filtering breaks the linear and shift-invariant property of MPI imaging process. Here we demonstrated an image reconstruction algorithm that restores LSI in MPI, which will greatly broaden MPI's role as a quantitative molecular, cellular and vascular imaging modality.

Acknowledgments. The authors would like to acknowledge: California Institute for Regenerative Medicine, UC Discovery Grant, and National Institutes of Health.

References

1. Gleich, B., Weizenecker, J.: Tomographic imaging using the nonlinear response of magnetic particles. Nature 435, 1214–1217 (2005)
2. Rahmer, J., Weizenecker, J., Gleich, B., Borgert, J.: BMC Med. Imaging 9(1), 4 (2009)
3. Goodwill, P., Conolly, S.: IEEE Trans. Med. Imaging (2010)
4. Goodwill, P., Conolly, S.: IEEE Trans. Med. Imaging (2011)
5. Lu, K., Goodwill, P., Conolly, S.: SPIE Conference Proceeding (2011)

Efficient Positioning of the Field-Free Point in Magnetic Particle Imaging

Tobias Knopp*, Timo F. Sattel, and Thorsten M. Buzug

Institute of Medical Engineering, University of Lübeck, Ratzeburger Allee 160
Lübeck, 23562, Germany
knopp@imt.uni-luebeck.de, buzug@imt.uni-luebeck.de

Abstract. Magnetic particle imaging uses a field with a single field-free point for spatial encoding. Such a gradient field can be generated by a Maxwell coil pair consisting of two opposing coils driven by current flowing in converse directions. In order to sample the volume in-between the coils, the field-free point has to be moved through space. When keeping the gradient strength constant the electrical power loss of the Maxwell coil pair setup drastically increases when moving the field-free point off-center. In this paper a coil configuration is proposed, which consists of four coils and considerably reduces the electrical power loss for off-center field-free point generation.

1 Introduction

Magnetic particle imaging (MPI) is a quantitative method for determining spatial distributions of magnetic nanoparticles [1]. The method is based on the nonlinear magnetization behavior of the particles, which saturate even for low field strengths of few $mT\mu_0^{-1}$. By applying a magnetic gradient field featuring a field-free point (FFP) at one specific position, the majority of particles in space are saturated such that only particles in the close vicinity of the FFP respond when the applied magnetic field changes. By moving the FFP in space along a sufficiently dense trajectory, the region of interest is scanned.

Conventionally, the FFP gradient field is generated by a Maxwell coil pair consisting of two opposing coils driven by current flowing in converse directions (see figure 1). In this way, the field components at the center cancel out such that an FFP is established.

An alternative topology was proposed in [2], which consists of two coils as well. However, they differ in diameter and are arranged concentrically in the same plane (see figure 1). Due to different coil sensitivities, an FFP field is generated in front of the assembly when both coils are fed with opposite currents.

* Now with Bruker Biospin MRI, Ettlingen, Germany.

T.M. Buzug and J. Borgert (Eds.): Magnetic Particle Imaging, SPPHY 140, pp. 161–165.
springerlink.com

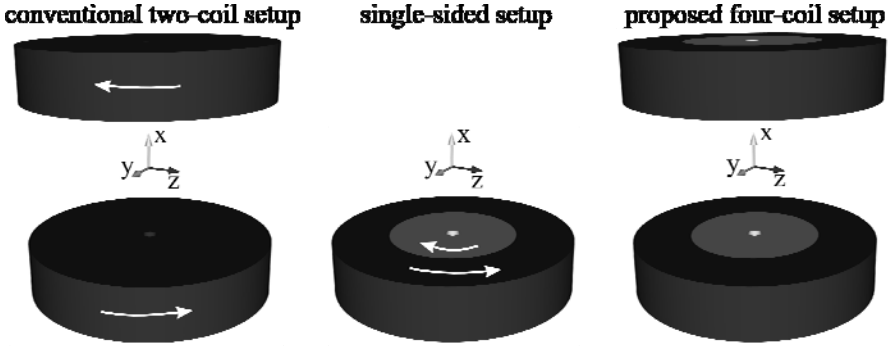

Fig. 1. Different coil topologies for generating a gradient field featuring an FFP.

When the currents in both coils of the conventional two-coil setup have the same absolute value, the FFP is generated at the center. To generate the FFP at another position on the axial coil axis, a current is superimposed on one or both coils. For a given gradient strength, the conventional coil design has the property that the least power is necessary to establish an FFP at the center, while moving the FFP off-center considerably increases the power loss. In contrast, the single-sided coil topology needs less power for generating an FFP in the vicinity of the coils than for generating an FFP in larger distance to the coils.

In this work, a coil topology is proposed that combines the advantages of the single-sided and the conventional concept for FFP generation leading to a drastically reduced power loss for off-center FFP generation.

2 Material and Methods

We propose a coil arrangement as shown on the right in figure 1. It consists of two sets of axial coils, where each set can be interpreted as gradient field generator of a single-sided 1D MPI scanner. These coils are mounted symmetrically on a common axis. The basic idea is to use the scanner in a conventional mode for generating an FFP at the center and use the scanner in a single-sided mode for generating the FFP near the coils. In between, a combination of both concepts is used. In the conventional mode, the currents in the interleaved coils flow in the same direction to maximize the gradient strength at the center. Instead, in the single-sided mode, mainly the two coils closer to the FFP are used for field generation. In these coils, the currents flow in converse directions like in the coils of a single-sided scanner.

Instead of switching between two defined modes, we optimize the currents to generate the FFP at a specific position with a given gradient strength. Here, we minimize the total electrical power loss of all coils.

3 Results

The proposed four-coil topology is compared in a simulation study to the conventional two-coil pair arrangement used in MPI to date. For a fair comparison, both setups are chosen to have the same total volume (weight).

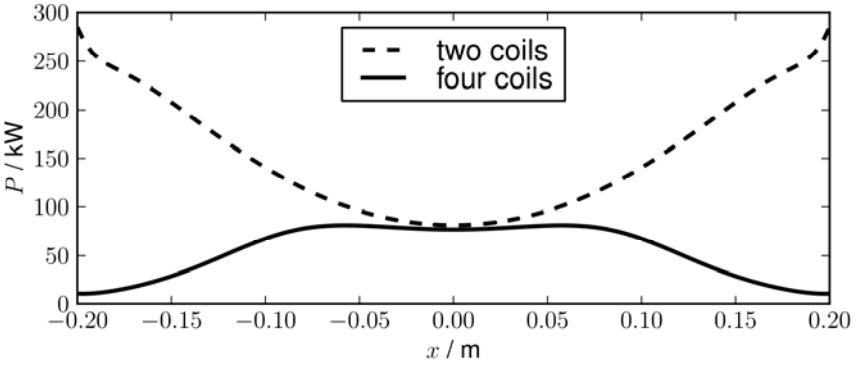

Fig. 2. Total power loss of the conventional two-coil setup and the proposed four-coil setup as a function of the FFP location.

The free space in-between the coils is chosen to be 40 cm, which should suffice to fit a normal sized human adult. The gradient strength is adjusted to be 2 $Tm^{-1}\mu_0^{-1}$. The coils of the conventional two-coil setup have an outer diameter of 70 cm, a length of 15 cm, and a radial width of 33 cm.

To achieve a four-coil setup with similar dimensions, each of the coils is split up in two separate coils of equal radial width of 16.5 cm. In this way, the four-coil setup is actually a generalization of the two-coil setup and can emulate the latter by choosing equal currents in both of the coils. Hence, the four-coil setup is at least as efficient as the two-coil setup.

The total power loss of both setups is plotted in figure 2. As can be seen, with the FFP at the center, both setups have nearly the same power loss. When moving the FFP off-center, the power loss of the conventional setup drastically increases, since it scales quadratically with the current. Therefore, an increase in the power loss cannot be compensated for by the decrease of the current amplitude in the other coil.

The four coil setup is characterized by a slight increase of the power loss, which reaches its maximum at x = ±5.9 cm. From this point on, the power loss decreases, as the currents in the FFP afar coils are reduced. For a linear FFP movement along the complete field-of-view, the two-coil setup needs 155 kW on average, while the four-coil setup needs 55 kW on average.

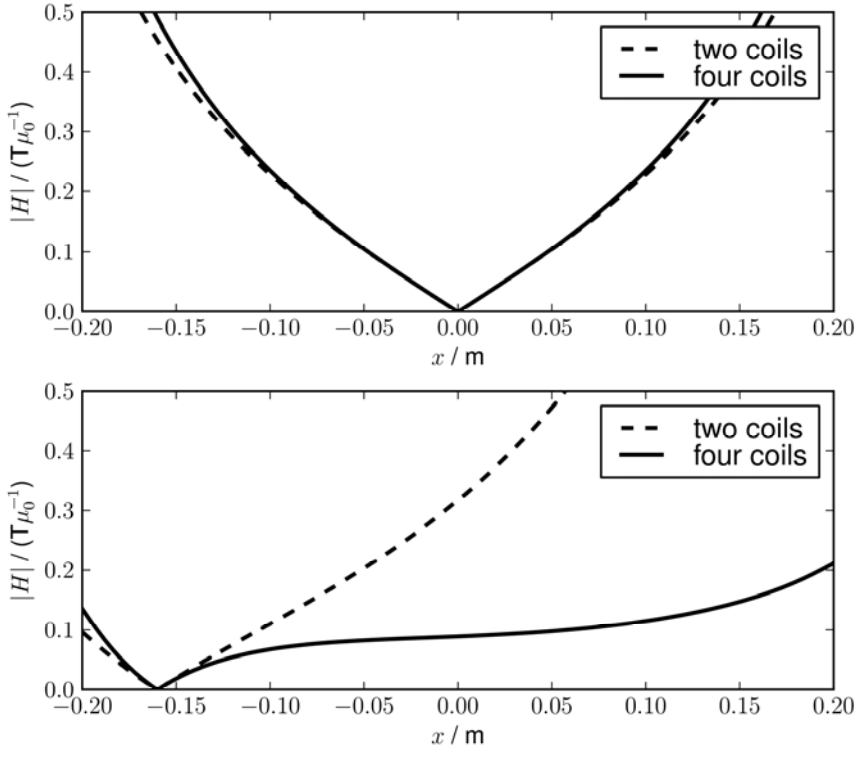

Fig. 3. Absolute value of the magnetic fields generated by the conventional two-coil setup and the proposed four-coil setup for two different FFP locations.

In figure 3, the generated magnetic fields are shown for several FFP positions. If the FFP is at the center, both setups generate a similar magnetic field, which is nearly linear at the center and has a higher gradient near the coils. When moving the FFP close to the coils, the field has a typical single-sided behavior, i.e. the strong increase of the field at the FFP flattens with distance to the FFP. However, for imaging with MPI this is not a drawback as it is sufficient to reach certain field strength to saturate the particles. The strong increase of the field even in farther distance to the FFP, which can be identified for the conventional two-coil setup, is thus associated with an unnecessary dissipation of energy.

4 Conclusion and Discussion

In this paper, a new coil topology for the generation of a magnetic gradient field featuring a field-free point for the application in magnetic particle imaging was proposed. The currents were optimized to generate an FFP with minimal total power loss. As it was shown, the proposed coil topology is

considerably more efficient than the two coil setup used in previously published work.

As the currents determined using the optimization approach are non-sinusoidal when moving the FFP through the FOV, the movement has to be controlled by slowly varying currents. Hence, the sinusoidal drive field still has to be realized by a dedicated coil pair (see [3]).

The coil topologies considered in this paper were only capable of moving the FFP in one dimension. A major question that is worth investigating is how the principles developed in this paper can be extended to move the FFP efficiently in 2D and 3D.

Acknowledgement. We acknowledge the support of the Federal Ministry of Education and Research, Germany (BMBF) (grant numbers 01EZ0912 and 13N11090).

References

1. Gleich, B., Weizenecker, J.: Tomographic imaging using the nonlinear response of magnetic particles. Nature 435, 1214–1217 (2005)
2. Sattel, T.F., Knopp, T., Biederer, S., Gleich, B., Weizenecker, J., Borgert, J., Buzug, T.M.: Single-sided device for magnetic particle imaging. Journal of Physics D: Applied Physics 42, 1–5 (2009)
3. Gleich, B., Weizenecker, J., Timminger, H., Bontus, C., Schmale, I., Rahmer, J., Schmidt, J., Kanzenbach, J., Borgert, J.: Fast MPI demonstrator with enlarged field of view. In: Proc. ISMRM, Stockholm, vol. 18, p. 218.

Visualization of Instruments in interventional Magnetic Particle Imaging (iMPI): A Simulation Study on SPIO Labelings

Hanne Wojtczyk[1], Julian Haegele[2], Mandy Grüttner[1], Wiebke Tenner[1], Gael Bringout[1], Matthias Graeser[1], Florian M. Vogt[2], Jörg Barkhausen[2], and Thorsten M. Buzug[1]

[1] Institute of Medical Engineering, University of Lübeck, Ratzeburger Allee 160, 23562 Lübeck, Germany
wojtczyk@imt.uni-luebeck.de, buzug@imt.uni-luebeck.de
[2] Clinic for Radiology and Nuclear Medicine, University Hospital Schleswig-Holstein, Ratzeburger Allee 160, 23562 Lübeck, Germany

Abstract. Due to its ability for quantitative 3D real time imaging with high sensitivity and spatial resolution but without ionizing radiation and iodine-based contrast agents, Magnetic Particle Imaging shows great promise for the application to the image guidance of cardiovascular interventions. For this purpose, the blood in the vessels and the instruments would have to be visualized, e.g. using a SPIO-based contrast agent and a SPIO labeling, respectively (SPIO: superparamagnetic iron oxide). In a simulation study of this situation, simple models of a guide wire and a catheter with a coated tip as well as a filled balloon catheter have been examined under a variety of conditions. The appearance of the instruments in the reconstructed images has been shown to be strongly dependent on the imaging parameters (gradient strength), the difference of the SPIO concentrations in adjacent structures as well as the geometric extensions of the instrument and its position inside the vessel (partial volume effect). It has been demonstrated that the visualization of instruments in a vessel may be possible with positive or negative contrast, depending on the individual circumstances.

1 Introduction

Magnetic Particle Imaging (MPI) can determine SPIO concentrations quantitatively in 3D with high temporal and spatial resolution and high sensitivity

T.M. Buzug and J. Borgert (Eds.): Magnetic Particle Imaging, SPPHY 140, pp. 167–172.
springerlink.com

[1,2]. Unlike Computed Tomography (CT) and Digital Subtraction Angiography (DSA), which only yields 2D projections, it does not require the use of ionizing radiation and iodine-based contrast agents. Therefore, MPI shows great promise for the application to the image guidance of cardiovascular interventions. For this purpose, the blood in the vessels and the instruments would have to be visualized, e.g. using a SPIO-based contrast agent and a SPIO labeling, respectively. A simulation study of this situation has been performed, examining three models of labeled instruments under a variety of conditions.

2 Material and Methods

2D software phantoms of a guide wire and a catheter with a coated tip as well as a filled balloon catheter inside a vessel have been created using Matlab (see fig. 1a, 2a and 3a). The SPIO labeling of the instruments and the vessel filled with SPIO-based contrast agent were modeled as static compartments containing the same sort of solution of mono-sized nanoparticles (diameter 30 nm), only in different concentrations (500 mmol(Fe)/l for the labeling, varying concentrations for the contrast agent in the blood). The size of the software phantoms was 200x400 pixels, corresponding to a field of view of 2x4 cm^2 with a pixel width of 100 µm. The vessel compartment was chosen to have a diameter of 9 mm, representing the *aorta abdominalis* in adult female Göttingen minipigs [3]. The catheter had a diameter of 2 mm and a coating of 1.5 cm length and 300 µm thickness, while the guide wire had a diameter of 600 µm and a coating of 1.5 cm length and 200 µm thickness. The balloon catheter had a shaft diameter of 2 mm, a balloon diameter of 4.8 mm, a balloon length of 1.5 cm and a wall thickness of 200 µm. The devices were located in the center of the vessel. Additionally, the guide wire was examined in a position 0.3 mm above the center. In-house written software was employed to perform the simulation of the 2D imaging process using ideal fields and neglecting any noise. Unless stated otherwise, the gradient strength was set to 2 T/m perpendicular to the vessel and 1 T/m along the vessel. The drive fields had an amplitude of 20 mT and frequencies around 25 kHz. In addition, the guide wire was studied using a gradient strength of 5 T/m perpendicular to the vessel and 2.5 T/m along the vessel. In this case the drive fields had an amplitude of 50 mT (this value, which is higher than the amplitudes applied in experiments so far, was chosen to reach the same field of view as with the lower gradient strength). Using the iterative Kaczmarz method, the images were reconstructed as a matrix of 40x80 pixels, corresponding to a pixel width of 0.5 mm.

3 Results

The results of the simulations are shown in fig. 1-3. It can be seen that the appearance of the instruments in the reconstructed images strongly depends on the imaging parameters (gradient strength), the difference of the SPIO concentrations in adjacent structures as well as the geometric extensions of the instrument and its position inside the vessel (partial volume effect). Depending on the situation there may be positive contrast (see e.g. fig. 1c-d, 2d,f,h,j and 3b-c), negative contrast (e.g. due to a signal void caused by a displacement of the bolus by the device, see fig. 1b and 2b-c,e,g,i) or a blurring with the background (see esp. fig. 2c,e). In the study of the guide wire, the influence of increasing the gradient strength from 2 T/m to 5 T/m, which improves the inherent spatial resolution from 1.2 mm to 0.5 mm according to [4], is visible: the difference between the positions in the center and 0.3 mm off-center becomes more prominent as the partial volume effects leading to blurring are less pronounced (see. fig. 1g,i compared to fig. 1c,e).

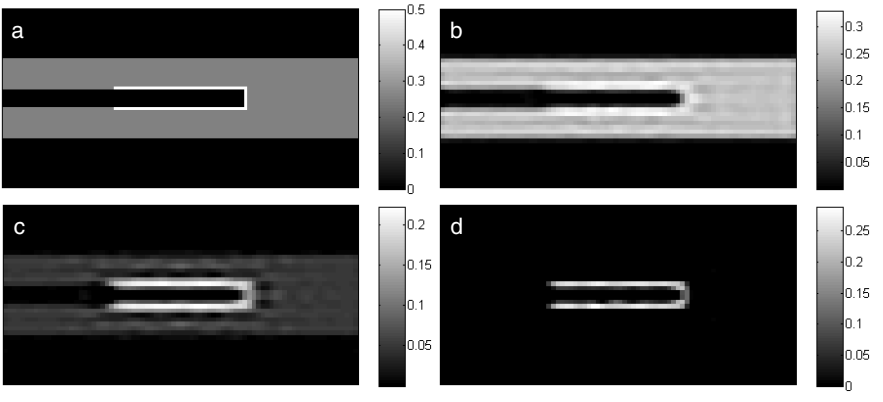

Fig. 1. Original (a) and reconstructed (b-d) images (2x4 cm^2) of the catheter inside the vessel. Depicted is the SPIO concentration in mol(Fe)/l. a-b: bolus concentration 250 mmol(Fe)/l; c: bolus concentration 50 mmol(Fe)/l; d: without contrast agent in the blood.

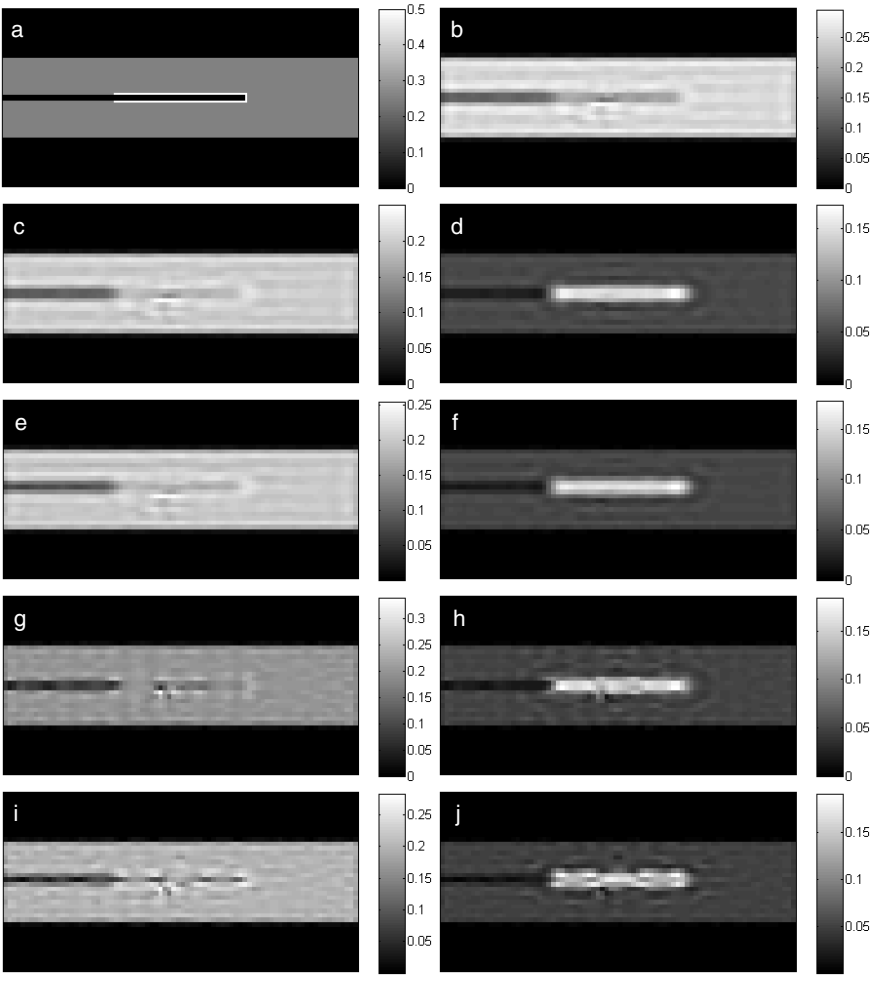

Fig. 2. Original (a) and reconstructed (b-j) images (2x4 cm^2) of the guide wire inside the vessel. Depicted is the SPIO concentration in mol(Fe)/l. a-b: bolus concentration 250 mmol(Fe)/l; c: bolus concentration 200 mmol(Fe)/l; d: bolus concentration 50 mmol(Fe)/l; e-f : like c-d, but with the guide wire 0.3 mm above the center; g-j: like c-f, but with the higher gradient strength.

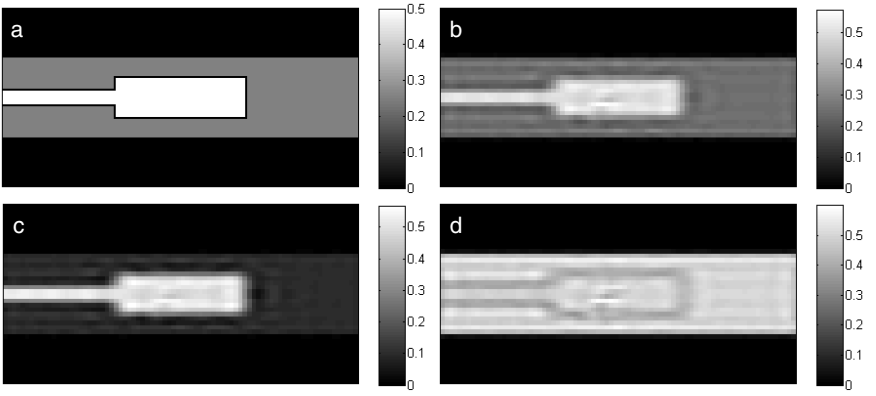

Fig. 3. Original (a) and reconstructed (b-d) images (2x4 cm^2) of the balloon catheter inside the vessel. Depicted is the SPIO concentration in mol(Fe)/l. a-b: bolus concentration 250 mmol(Fe)/l; c: bolus concentration 100 mmol(Fe)/l; d: bolus concentration 500 mmol(Fe)/l.

4 Discussion

Taking into account the assumptions of this study (ideal fields, no noise), the findings are directly transferable to instruments that can be labeled using a solution of SPIOs, e.g. double lumen catheters and balloon catheters. Recently, the visualization of a balloon catheter *in vitro* was accomplished in this way [5]. A precondition for this approach is that the device itself does not disturb the imaging process. As for the SPIOs inside a coating, it remains to be seen whether they will be represented sufficiently well by the same system function as SPIOs in solution. Using magnetic spectroscopy of Brownian motion (MSB), multiple types of magnetic nanoparticles or multiple nanoparticle bound states can be quantified concurrently [6,7]. In general, techniques for the simultaneous detection of different SPIOs or SPIOs in different surroundings would be desirable for MPI as well. Furthermore, the influence of other magnetizable and/or electrically conductive materials on the imaging process in MPI is an interesting area of research. This concerns both the instruments themselves and dedicated labelings or visualization approaches that may be conceivable. For example, it seems worth investigating whether at all and, if so, under which conditions, image reconstruction will be possible in the presence of relevant eddy currents induced during the process of MPI, and whether their effects might even be exploited for device tracking.

5 Conclusion

A simulation study on using SPIO labelings for the visualization of instruments inside a vessel containing a SPIO-based contrast agent has been

performed. It has been demonstrated that the visualization of devices may be possible with positive or negative contrast, depending on the individual circumstances.

Acknowledgments. The authors gratefully acknowledge the financial support of the German Federal Ministry of Education and Research (BMBF) under grant number 13N11090, of the European Union and the State Schleswig-Holstein (Programme for the Future – Economy) under grant number 122-10-004 and of Germany's Excellence Initiative [DFG GSC 235/1].

References

1. Gleich, B., Weizenecker, J.: Tomographic imaging using the nonlinear response of magnetic particles. Nature 435, 1214–1217 (2005)
2. Weizenecker, J., Gleich, B., Rahmer, J., Dahnke, H., Borgert, J.: Three-dimensional real-time in vivo magnetic particle imaging. Phys. Med. Biol. 54, L1–L10 (2009)
3. Hieb, B., Müller, C., Jung, F., Hünigen, H., Hamm, B., Plendl, J., Niehues, S.M.: Macro- and micromorphometric studies of the vascular structures from the Göttingen® minipig. Applied Cardiopulmonary Pathophysiology 13(4), 318–321 (2009)
4. Rahmer, J., Weizenecker, J., Gleich, B., Borgert, J.: Signal encoding in magnetic particle imaging: properties of the system function. BMC Medical Imaging 9(4), 21 pages (2009)
5. Haegele, J., Rahmer, J., Gleich, B., Bontus, C., Borgert, J., Wojtczyk, H., Buzug, T.M., Barkhausen, J., Vogt, F.M.: Visualization of instruments for cardiovascular intervention using MPI. In: 2nd International Workshop on Magnetic Particle Imaging, IWMPI 2012 (accepted, 2012)
6. Rauwerdink, A.M., Giustini, A.J., Weaver, J.B.: Simultaneous quantification of multiple magnetic nanoparticles. Nanotechnology 21(45), 5 pages (2010)
7. Rauwerdink, A.M., Weaver, J.B.: Concurrent quantification of multiple nanoparticle bound states. Med. Phys. 38(3), 1136–1140 (2011)

Medical Applications

Red Blood Cells as Magnetic Carriers for MPI Applications

A. Antonelli[1], C. Sfara[1], M. Magnani[1], J. Rahmer[2], B. Gleich[2], J. Borgert[2], and J. Weizenecker[3]

[1] Department of Biomolecular Sciences, University of Urbino, Via Saffi 2 Urbino, 61029, Italy
mauro.magnani@uniurb.it
[2] Philips Technologie GmbH Innovative Technologies, Research Laboratories, Röntgenstraße 24-26, 22355 Hamburg, Germany
juergen.rahmer@philips.com
[3] University of Applied Sciences, Moltkestr. 30, 76133 Karlsruhe, Germany
juergen.weizenecker@hs-karlsruhe.de

Magnetic Particle Imaging (MPI), a method that takes advantage of the non-linear magnetization curve of superparamagnetic iron oxide (SPIO) nanoparticles, promises to deliver high spatial and temporal resolution with a sensitivity exceeding that of magnetic resonance imaging (MRI). However, SPIO nanoparticles have a short blood retention time which limits the applicability of such compounds for MPI. We propose the use of red blood cells (RBCs) as carriers of SPIO nanoparticles to realize a blood pool tracer with longer blood retention time. Previously, we described a method of SPIO nanoparticle encapsulation into RBCs. The loading procedure consists of a hypotonic dialysis of cells in the presence of magnetic nanoparticles and successive resealing and reannealing of cells using isotonic solutions. Here, we report for the first time Magnetic Particle Spectroscopy (MPS) and MPI results obtained after intravenous administration of murine Resovist-loaded RBCs in an *in vivo* MPI experiment.

1 Introduction

Magnetic Particle Imaging (MPI) uses the response of superparamagnetic iron oxide (SPIO) nanoparticles as tracer material to determine their local concentration (1). Because the tracer material is formulated for intravenous injection, the obvious MPI applications are those that can capitalize on material staying in the blood stream for a certain time. One widespread application that meets this criterion is the diagnosis and assessment of cardiovascular disease (CVD), caused by partial closure (stenosis) or a complete obstruction (occlusion) of one or more coronary arteries that lead to the condition known as myocardial infarction. However, SPIO-contrast

T.M. Buzug and J. Borgert (Eds.): Magnetic Particle Imaging, SPPHY 140, pp. 175–179.
springerlink.com

agents, such as Resovist®, have a short blood half-life due to rapid uptake by the reticuloendothelial system (RES), which limits the applicability of such compounds for MPI. Previously, we have proposed a method of SPIO nanoparticle encapsulation into red blood cells (RBCs) in order to overcome the fast clearance of these particles by the RES, and thus, increase their blood retention time (2). The encapsulation of magnetic nanomaterials into erythrocytes was performed by a loading procedure consisting of a dialysis of red blood cells in the presence of nanomaterials against a hypotonic solution, in order to open pores of the red cell membrane such that nanoparticles can be taken up, and successive resealing and reannealing of dialysed cells using isotonic buffer. In this manner, SPIO loaded RBCs can be successfully utilized as biomimetic constructs that escape RES clearance, preserving the main properties of the native cells as well as the properties of the nanoparticles. It is known that RBCs have a longer lifespan in circulation compared to synthetic carriers that are currently available (soluble macromolecules as synthetic polymers or complex particulate structures such as microparticles and liposomes) and their use as potential biocompatible carriers for different bioactive substances including proteins, nucleotide analogues, and cancer chemotherapeutics has been reported (3). Recently, Markov *et al*. have reported on the characterization of SPIO-loaded RBCs for use as new MPI tracer material with a long blood retention time for imaging of the circulatory system (4). These analyses have revealed a high iron oxide concentration in loaded erythrocytes and despite the fact that SPIO-loaded erythrocytes have shown a reduced performance in MPS compared to their respective bulk materials, the data obtained from nuclear magnetic resonance (NMR) and vibrating sample magnetometry (VSM) characterization confirm the attractiveness of RBCs in MPI using a suitable nanoparticle-based contrast material. Here, we present data obtained from an *in vivo* experiment, where mice were imaged 3 and 24 hours after intravenous injection of Resovist-loaded RBCs using a prototype MPI scanner as described in (5).

2 Material and Methods

The loading of magnetic nanomaterial into murine red blood cells was attempted by a procedure that has been reported in Antonelli *et al*. (2). Essentially, 1 ml of RBCs at 70% was dialysed in the presence of 5.6 mg Fe of Resovist contrast agent (0.5 mmol Fe/ml or 28 mg/ml, from Bayer Healthcare) for 75 min using a tube with a 12–14 kDa cut-off in 50 vol of a dialysis buffer (10 mM $NaHCO_3$, 10 mM NaH_2PO_4, 20 mM glucose, 4 mM $MgCl_2$ pH 7.4), containing 2 mM ATP and 3 mM reduced glutathione. Resealing of RBCs was obtained by adding 0.1 vol of PIGPA (5 mM adenine, 100 mM inosine, 2 mM ATP, 100 mM glucose, 100 mM sodium pyruvate, 4 mM $MgCl_2$, 194 mM NaCl, 1.606 M KCl, 35 mM NaH_2PO_4, pH 7.4) per vol of dialysed RBCs and by incubating at 37 °C for 45 min. The resealed cells were recovered by centrifugation at 400 g and washed four times with

Hepes buffer to remove unentrapped magnetic particles. All these procedures were performed a 4°C under sterile conditions. The loading of RBCs was controlled by measuring the T1 and T2 relaxation times in erythrocytes in an NMR experiment to determine the Resovist concentration. The loaded erythrocyte suspensions with a hematocrit of 44% were measured at 9.4 Tesla at 37°C using a 400 MHz NMR spectrometer (Bruker BioSpin). In the *in vivo* experiment, a bolus of 0.5 ml Resovist-loaded RBCs was injected into the tail vein of a 29 g ICR (CD-1) mouse. The presence of Resovist-loaded RBCs in the mouse circulation was evaluated by MPS measurements of blood withdrawals at 3 and 24 hours after injection. At the same points in time, dynamic volumetric images were acquired using the MPI scanner with a FOV of about 20x17x12 mm^3 (5). The animal experiments were performed in accordance with local laws and regulations and were approved by the local authorities.

3 Results

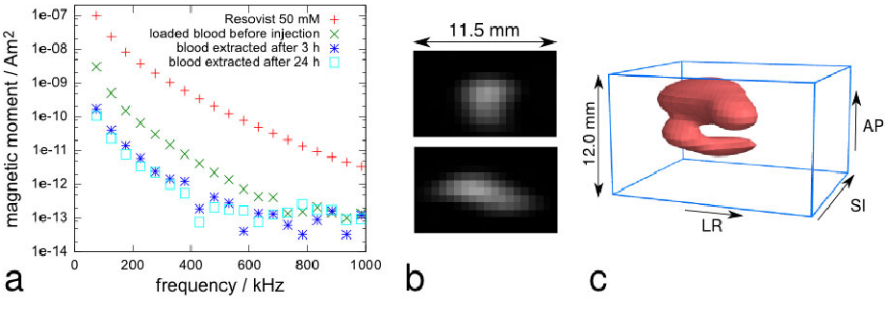

Fig. 1. (a) MPS spectra of loaded RBC samples before injection (green crosses), withdrawn from the mouse after 3 h (blue stars) and 24 h (blue squares), in comparison with Resovist 1:10 (red crosses). (b) MPI images of Resovist 1:1000 in a vial (top) and the Resovist-loaded blood sample (bottom). (c) Surface rendering of 3D MPI data of the heart region of the mouse acquired 3 hours after RBC injection.

The concentration of Resovist encapsulated in murine RBCs was found to be around 2 mM Fe evaluated by T1 and T2 from NMR measurements. This concentration was later confirmed by the MPS measurements of Resovist-loaded RBCs, the harmonic spectrum of which was compared to diluted Resovist as shown in Fig. 1a. A steeper drop in higher harmonics is found for the loaded RBCs compared to the aqueous solution of Resovist. This indicates a size selection during the loading process of the RBCs (4). Figure 1b shows images of 0.5 mM Resovist (top) and a loaded blood sample with 2 mM (bottom). Despite this concentration difference, the image signal level of the loaded RBCs is only about 15 % above that for the Resovist sample. The reason is that imaging relies on the (rapidly

dropping) higher harmonics, whereas the concentration has been determined using the lower harmonics in the MPS spectra.

After i.v. injection of 0.5 ml blood containing Resovist-loaded RBCs (or 1 μmole Fe) into the mouse tail vein, the presence of Resovist-loaded RBCs in the circulation was evaluated by MPS measurements of blood withdrawals performed 3 and 24 hours later as shown in Fig. 1a. At these times, the Fe concentrations in the mouse blood stream was 250 μM and 150 μM, respectively, corresponding to 0.5 and 0.3 μmoles total Fe (that is 17.45 μmoles Fe/kg and 10.3 μmoles Fe/kg).

3D MPI images of the living mouse acquired 3 hours after Resovist-loaded RBCs injection show signal from various anatomical regions. In Fig. 1c, the FOV is positioned over the heart region. We assume to see the heart in the upper part of the volume and a large vessel, possibly the vena cava, in the lower part of the volume. To gain additional information, the temporal signal behavior of a voxel in the upper structure and a voxel in the lower structure was determined. In the upper region, a signal variation of 210 bpm was found, which can be assigned to the heart rate of the sedated mouse. In the lower region, a signal variation of 126 bpm was found, which is a frequency found at other locations in the abdomen as well and which might be attributed to breathing motion.

4 Discussion

Ex-vivo MPI of blood containing loaded RBCs (Fig. 1b) demonstrates the basic feasibility of imaging of particles encapsulated in RBCs. Due to the steeper drop in the spectrum of higher harmonics compared to particles in aqueous solution, the imaging performance is reduced. The MPS results from withdrawn blood show that the loaded RBCs stay in the blood for many hours. MPS measurements of blood withdrawals from mice treated with Resovist-loaded RBCs show that 50% and 30% of administered dose are still visible at 3h and 24h after intravenous injection, respectively. The remaining iron concentrations in the blood are close to the detection limit of the scanner prototype. Thus, only in the scan 3h after injection, a clear signature of the beating heart and thus of signal generated from loaded RBCs still flowing in the blood is found. After 24h, the signal of particles accumulated in organs like the liver dominated the images. The drop in loaded RBCs between 3 and 24 hours is larger than expected, but it is assumed that during the loading process, SPIO-loaded murine RBCs could be partially damaged and are taken up by liver and spleen macrophages more rapidly than healthy RBCs. Therefore, we have developed a new procedure to perform future *in vivo* experiments that involves first the treatment of mice or rats with bisphosphonate clodronate that can be effective in macrophage depletion and secondly the injection of SPIO-loaded human erythrocytes containing higher nanomaterial concentrations. In the future, the availability of a new preclinical MPI scanner with a larger bore allowing rapid imaging with enlarged FOVs will provide full mouse coverage.

5 Conclusion

The MPS data obtained after the administration of Resovist-loaded RBCs to mice suggest the potential of RBCs as nanoparticle tracer carriers in MPI. We expect that more detailed results can be obtained with future experiments using commercially available MPI systems and new procedures of SPIO-loading and administration with the aim to investigate the circulation survival of RBC-encapsulated MPI tracers.

Acknowledgements. We acknowledge support in animal provision and handling by Dr. Tiemann (University Medical Center Hamburg-Eppendorf) and funding by the German Federal Ministry of Education and Research (BMBF) under the grant numbers FKZ 13N9079 and 13N11086.

References

1. Gleich, B., Weizenecker, J.: Tomographic imaging using the nonlinear response of magnetic particles. Nature 435, 1214–1217 (2005)
2. Antonelli, A., Sfara, C., Mosca, L., Manuali, E., Magnani, M.: New biomimetic constructs for improved in vivo circulation of superparamagnetic nanoparticles. J. Nanosci. Nanotechnol. 8, 2270–2278 (2008)
3. Magnani, M., Serafini, S., Fraternale, A., Antonelli, A., Biagiotti, S., Pierigé, F., Sfara, C., Rossi, L.: Red Blood Cell-Based Delivery of Drugs and Nanomaterials for Therapeutic and Diagnostic Applications. Encyclopedia of Nanoscience and Nanotechnology 22, 309–354 (2011)
4. Markov, D.E., Boeve, H., Gleich, B., Borgert, J., Antonelli, A., Sfara, C., Magnani, M.: Human erythrocytes as nanoparticle carriers for magnetic particle imaging. Phys. Med. Biol. 55, 6461–6473 (2010)
5. Weizenecker, J., Gleich, B., Rahmer, J., Dahnke, H., Borgert, J.: Three-dimensional real-time in vivo magnetic particle imaging. Phys. Med. Biol. 54, L1–L10 (2009)

Ex Vivo Magnetic Sentinel Lymph Node Detection in Colorectal Cancer with a SPIO Tracer

Joost J. Pouw[1], Raluca M. Fratila[1], Aldrik H. Velders[2], Bennie ten Haken[1], Quentin A. Pankhurst[3], and Joost M. Klaase[4]

[1,2] MIRA Institute for Biomedical Technology & Technical Medicine, NeuroImaging Group[1]/Biomedical Chemistry Group[2], University of Twente P.O. Box 217, 7500AE Enschede, The Netherlands
J.J.Pouw@utwente.nl

[3] The Royal Institution of Great Britain, Davy-Faraday Research Laboratory 21 Albemarle Street, W1S 4BS, London, UK
Q.Pankhurst@endomagnetics.com

[4] Medisch Spectrum Twente, Department of Surgery P.O. Box 50.000, 7500 KA Enschede, The Netherlands
J.Klaase@mst.nl

Abstract. A new method for selecting sentinel lymph nodes (SNs) in colorectal cancer tissue was investigated in 12 patients. A tracer consisting of superparamagnetic ironoxide (SPIO) nanoparticles was injected in the resected tissue. A handheld magnetic probe was used to select SNs to which the SPIO was drained. Vibrating sample magnetometry was performed on the lymph nodes to quantify the amount of SPIO in the nodes. High-field MRI allowed to depict the distribution of SPIO in the node, and revealed small anatomical structures. One or more SPIO containing nodes were successfully selected with the magnetic probe in all 12 patients.

1 Introduction

Colorectal cancer is the third most common cancer in men and the second in women, with a total of approximately 1.2 million new cases annually worldwide.[1] In treatment of patients suffering from colorectal cancer and other solid cancers it is very important to determine whether metastatic cells from the primary tumor have migrated to the lymph nodes (LNs). The presence or absence of metastasis in the LNs determines if the patient is treated with chemotherapy or not.

Nodal metastasis can be diagnosed by analyzing a section of surgically resected LNs by light microscopy. Sentinel Lymph Node Mapping (SLNM) is a technique used to select the most relevant LNs. A tracer is injected

T.M. Buzug and J. Borgert (Eds.): Magnetic Particle Imaging, SPPHY 140, pp. 181–185.
springerlink.com

near the tumor, after which it is drained to the LNs via the lymph vessels that drain the tumor area. The LNs to first receive drainage from the tumor area, are also the nodes first reached by the tracer. Since metastatic cells are drained via the same lymphatic route, these nodes are also most likely to be the first nodes to contain metastasis.[2] The current most commonly used tracer for SLNM in colorectal cancer is a blue dye, which can be visually detected.[3] Recent studies propose to introduce SLNM in colorectal cancer to identify very small metastasis in the SNs which are missed during regular light microscopic analysis.[4, 5]

We have used a SPIO tracer and a commercially available handheld magnetic detection device (SentiMag®, Endomagnetics LTD., London, UK) to select the Sentinel Nodes (SNs) in colorectal cancer tissue. The SentiMag® is originally developed to intraoperatively detect SNs in breast cancer.[6]

2 Material and Methods

In surgical treatment of colorectal cancer the tumor and complete adjacent draining lymphatic tissue is resected in one piece. This allows to perform SLNM after resection, ex vivo. When the tracer is injected after resection the patient is not exposed to the substance, and there is no chance of adverse events. Because the patient is not exposed, also newly developed substances not (yet) approved for use in humans can be tested. Ex vivo SLNM can be performed as effective as in vivo in colorectal cancer.[7]

We analysed the distribution of a SPIO tracer consisting of nanoparticles, approved for use in humans (Endorem**®,** Guerbet Nederland BV, Gorinchem, The Netherlands; diameter: 80-150 nm, 11.2 mg Fe mL^{-1}), to the LNs in colorectal tissue. We aimed to select the SNs with the SPIO tracer and SentiMag® handheld probe.

12 patients undergoing surgical resection for colorectal cancer in the MST Enschede hospital gave informed consent. Immediately following resection of the colorectal segment, approximately 2 mL of Endorem was injected submucosally near the tumor. A gentle massage of the injection site was performed to promote lymphatic transport of the tracer. A blue dye (Patent Blue V, Guerbet Nederland BV, Gorinchem, The Netherlands) was administered as a reference, in a similar fashion, because this is currently the most used method in colorectal SLNM studies.

After resection of all the LNs from the tissue by the pathologist, the SentiMag® was used to select the lymph nodes containing SPIO. The nodes were placed on the probe, and the measured signal intensity was recorded for each node (Fig. 1).

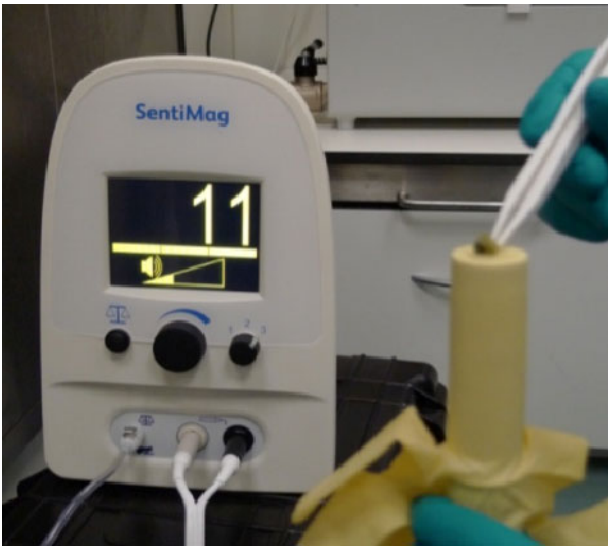

Fig. 1. SentiMag® control unit and handheld probe (covered by surgical glove to prevent contamination) with LN placed on the probe to asses the presence of SPIO in the node.

Blue discoloration of the LNs due to the presence of Patent Blue V was visually detected and noted.

In a subset of the patients, all SPIO containing LNs were subjected to a Vibrating Sample Magnetometry (VSM) measurement to accurately quantify the amount of iron present.

High-field (14.1 T, Bruker Avance II NMR spectrometer) T1- and T2-weighted MR imaging was carried out in order to assess the distribution of SPIO inside the individual LNs.

As a final step, the LNs were subjected to histopathological examination to determine whether metastasis was present, and iron specific staining with Perls Prussian Blue to microscopically investigate the iron distribution in the nodes.

3 Results

The SPIO tracer was successfully transported through the lymphatic system into the SNs in all patients. One or more SPIO containing LNs were selected in each of the 12 patients using the SentiMag®. The amount of iron in the LNs measured by VSM ranged between 2-142 µg. The measured amount of iron by VSM was linearly related to the signal intensity displayed by the SentiMag®, which indicates that the SentiMag® can be used as an indication of the amount of iron present in the lymph nodes.

High-field MR images of some of the nodes showed hypointense areas due to the presence of SPIO. Small anatomical structures were also revealed on these images. An example in which both the hypointense areas and the small anatomical structures (follicles) can be distinguished can be seen in Fig. 2.

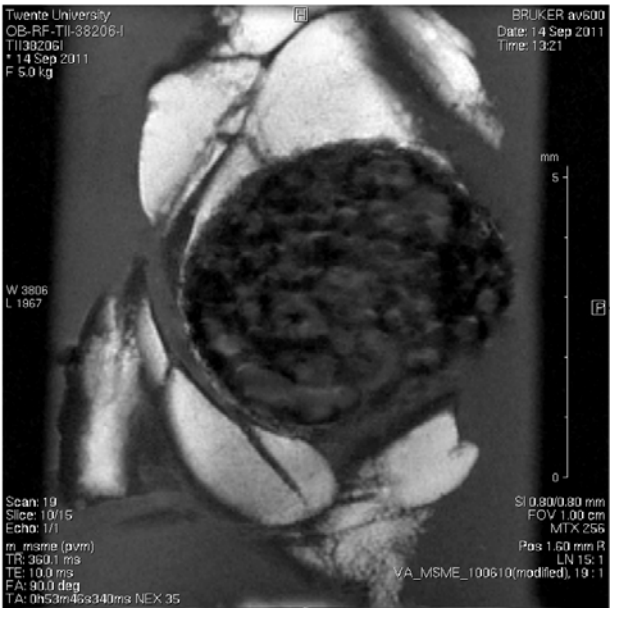

Fig. 2. T1-weighted image of a SN, surrounded by fat tissue. The image was acquired using a multi-slice-multi-echo (MSME) sequence.

4 Discussion and Conclusion

These initial experiment showed that it is possible to select SNs in colorectal tissue with the SentiMag® after ex vivo administration of a SPIO tracer. To validate the clinical applicability of this method in colorectal cancer, it is necessary to correlate the presence of metastasis in the LNs to the presence and/or amount of iron found in nodes. We are currently performing this analysis on the cohort of 12 patients, and including a larger number of patients to be able to draw firm conclusions.

Acknowledgments. This work was supported by the Dutch Technology Foundation STW under Project Radiation free localization and diagnosis of sentinel lymph nodes with magnetic nano-particles.

References

1. International Agency for Research on Cancer, GLOBOSCAN (2008), http://globoscan.iarc.fr
2. Tan, K.Y., et al.: Distribution of the first metastatic lymph node in colon cancer and its clinical significance. Colorectal Dis. 12(1), 44–47 (2010)
3. Cahill, R.A., Leroy, J., Marescaux, J.: Could lymphatic mapping and sentinel node biopsy provide oncological providence for local resectional techniques for colon cancer? A review of the literature. BMC Surg. 8, 17 (2008)
4. van der Zaag, E.S., et al.: Diagnosing occult tumour cells and their predictive value in sentinel nodes of histologically negative patients with colorectal cancer. Eur. J. Surg. Oncol. 36(4), 350–357 (2010)
5. van Schaik, P.M., et al.: Ex vivo sentinel lymph node "mapping" in colorectal cancer. Eur. J. Surg. Oncol. 33(10), 1177–1182 (2007)
6. Joshi, T., et al.: Magnetic nanoparticles for detecting sentinel lymph nodes. ESJO 33, 1135 (2007)
7. Park, J.S., et al.: Comparison of ex vivo and in vivo injection of blue dye in sentinel lymph node mapping for colorectal cancer. World J. Surg. 33(3), 539–546 (2009)

Distribution of Superparamagnetic Nanoparticles in Lymphatic Tissue for Sentinel Lymph Node Detection in Breast Cancer by Magnetic Particle Imaging

Dominique Finas[1], Kristin Baumann[1], Katja Heinrich[1], Britta Ruhland[1], Lotta Sydow[1], Ksenija Gräfe[2], Timo Sattel[2], Kerstin Lüdtke-Buzug[2], and Thorsten Buzug[2]

[1] Department of Obstetrics and Gynecology, University of Lübeck, Ratzeburger Allee 160, Lübeck, 23538, Germany
finas.d@arcor.de
[2] Institute of Medical Engineering, University of Lübeck, Ratzeburger Allee 160, Lübeck, 23538, Germany
buzug@imt.uni-luebeck.de

Abstract. Breast cancer diagnostic and treatment consists of surgical tumor removal and axillary lymph node resection. Radical axillary lymph node removemend is associated with high morbidity and significant loss of quality of life. The concept of sentinel lymph node biopsy (SNLB) by the use of dye and radio nuclides strongly reduced those side effects. To further reduce the side effects when axillary lymph nodes are removed, super paramagnetic iron oxide nano particles (SPIOs) could replace these marker substances. The magnetic particle imaging (MPI)-procedure will be used to visualize these SPIOs. Intraoperative three-dimensional MPI imaging and distinct localization probably by the use of a MPI hand probe will facilitate the axillary SNL detection and moreover makes it more precise. A mouse model was applied to prove the mentioned principle of SNLB by MPI. We are presenting first results of this approach and, additionally the qualitative and semi-quantitative distribution of SPIOs in lymph-fat tissue is shown for the first time. SPIOs are moving from the injection site through the lymph-fat tissue to the axillary region and finally into the axillary lymph nodes. This was approved by histology and prussian blue iron staining of the slides, electron transmission microscopy and in vivo magnetic resonance imaging. The concept of SNLB by MPI can be applied in principle in all solid tumors.

T.M. Buzug and J. Borgert (Eds.): Magnetic Particle Imaging, SPPHY 140, pp. 187–191.
springerlink.com

1 Introduction

The most frequent malignant tumor of the female population worldwide in western industrialized countries is the cancer of the breast. Tumors of the mammary gland are draining to the axillary lymph nodes. Therefore, axillary lymph nodes were primarily radically dissected from the ipsilateral axilla (ALND) as part of the staging [2]. A decrease of the prognosis occurs, when tumor cells are detected in lymph nodes. But, the ALND is associated with high morbidity and loss of quality of life because of surgery related side effects. Therefore, a new standard was developed to reduce those side effects by introducing the concept of sentinel lymphonodectomy (SNLB). It was based on the theory of mammary lymphatic draining to axillary lymph nodes in a hierarchic manner, whereas one or few lymph nodes are draining lymphatic fluids from the breast tissue. Within this method dye and radio nuclides are injected into the breast. The sentinel lymph nodes (SNLs) are identified by visualization of blue dye traces and use of a gamma camera for a targeted extraction. To further reduce the side effects when axillary lymph nodes are removed, super paramagnetic iron oxide nano particles (SPIOs) could replace these marker substances under the use of real-time intraoperative three-dimensional imaging and localization by magnetic particle imaging (MPI), probably by the use of a MPI hand probe. This eliminates the exposure of patient and medical staff to ionizing radiation. Qualitative and quantitative enrichment of SPIOs in the axillary lymphatic tissue is unexplored until now. Moreover, the MPI procedure was not applied in vivo within this setting so far.

2 Material and Methods

We applied a healthy mouse model to prove the mentioned principle of SNLB by MPI [4]. SPIOs (Resovist®, Bayer Shering Pharma AG, Germany) were injected into the mammary gland next to the axillary region of healthy female C57B6 mice. After sacrifice, we examined the mammary glands, the axillary lymph nodes and environmental tissues for SPIO accumulation and distribution by histological examination at formalin fixed and paraffin embedded tissue, stained with hematoxilin-eosin, nuclear fast red and iron sensitive Prussian blue stain correlated by electron microscopy and MRI (3 Tesla microscopy coil) [7].

2.1 Ethics

This animal study protocol was approved by the ministry of agriculture, environment and rural areas of Schleswig-Holstein, Germany under the registry number V 312-72241.122-10 (35-3/09).

3 Results

Movement of SPIOs from the injection site at the mammary gland through the lymph-fat tissue to the axillary region and lymph nodes was shown and approved through MRI by in vivo visualizing (pictures not shown). The SPIOs are following the traces of lymphatic vessels, respecting the borders and spaces between different tissues e.g. muscle fibers, they were found in the neighborhood of collagen fibers (Figure 1).

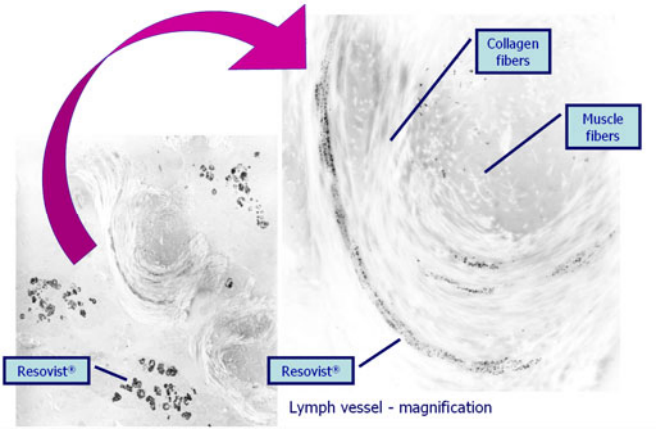

Fig. 1. Tissue section with lymph vessel between mammary gland and axillary region. SPIOs are not located within cells, but between tissues e.g. muscle fibers and near collagen fibers. They are forming a kind of trace to the axillary region.

The SPIOs accumulates in the lymph nodes cortex region (Figure 2). They could not be located within cells by light microscopy, but they were found in the neighborhood of collagen fibers and around fat cells (Figure 3). These findings were demonstrated under the use of electron transmission microscopy. Also using electron transmission microscopy, SPIOs were not detectable within other cells except macrophages. SPIOs are incorporated by endocytosis by these monocytotic cells (pictures not shown).

We present first results of the approach of SNLB by MPI. Qualitative and semi-quantitative distribution of SPIOs in lymph-fat tissue is shown here for the first time. SPIOs are moving from the injection site through the lymph-fat tissue to the axillary region and finally into the axillary lymph nodes.

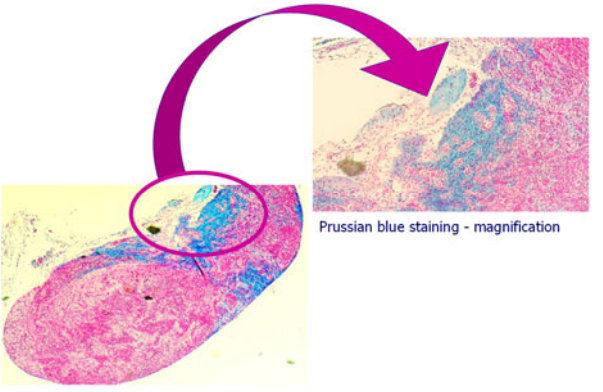

Fig. 2. Complete axillary lymph node, formalin fixed and paraffin embedded. The slide was stained with nuclear fast red aluminium sulphate solution and iron sensitive Prussian blue. SPIOs are clearly located in the cortex region.

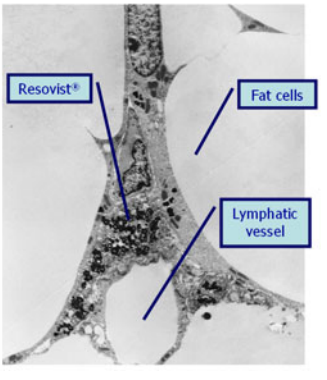

Fig. 3. Magnification of an axillary lymph node 3 hours after SPIO (Resovist®) injection into the mammary gland. The SPIOs are distributes between the fat cells and around a lymph vessel.

4 Discussion

We aim to show that SPIOs and the MPI technique are effective to be used as SNLB tracer and finder. Therewith the sentinel lymph node detection can be easily performed after intra operative tracer application. A new MPI hand probe with unilateral solenoid arrangement designed for use in the operating theater is under construction [5]. This project is part of a comprehensive test program to develop the new SNLB technique. This will be less complex and incriminating for the patient and the staff [1]. Compared with the standard SNLB this method will be less expensive and a

less burdensome diagnostic process. At that time, experiments with magnetic particle spectroscopy (MPS) are ongoing.

5 Conclusion

For conventional SNLB the axilla has to be widely explored to identify the SNL. The presented results show the feasibility of the use of SPIOs for SNLB under the use of MPI. Further investigation will show the quantitative distribution of SPIOs in the lymph-fat tissue and lymph nodes and we will proof the SNL concept within a tumor bearing and metastatic mouse model [3,6]. Intra operative three-dimensional imaging with the MPI hand probe facilitates the axillary SNL detection and moreover makes it more precise. Through the avoidance of intensive surgical exploration of the axilla the morbidity is dramatically reduced. The tracer for MPI is easy to obtain. This makes the method accessible to all patients. The concept of SNLB by MPI can be applied in principle in all solid tumors [1].

Acknowledgements. This project is supported by the German Federal Ministry of Education and Research (BMBF Grant number 01EZ0912). It is also part of the University Research Program “Imaging of Disease Processes", University of Lübeck.

References

1. Finas, D., Baumann, K., Ruhland, B., Heinrich, K., Lüdtke-Buzug, K., Buzug, T.: Sentinel Lymph node detection in breast cancer through superparamagnetic nanoparticles for magnetic particle imaging. Biomed. Tech. 56, 1–7 (2011)
2. Kuehn, T., Bembenek, A., Decker, T., Munz, D.L., Sautter-Bihl, M.L., Untch, M., Wallwiener, D.: A concept for the clinical implementation of sentinel lymph node biopsy in patients with breast carcinoma with special regard to quality assurance. Cancer 103, 451–461 (2005)
3. Ling, L.J., Wang, S., Liu, X.A., Shen, E.C., Ding, Q., Lu, C., Xu, J., Cao, Q.H., Zhu, H.Q., Wang, F.: A novel mouse model of human breast cancer stem-like cells with high CD44+CD24-/lower phenotype metastasis to human bone. Chin. Med. J. (Engl.) 121, 1980–1986 (2008)
4. Robe, A., Pic, E., Lassalle, H.P., Bezdetnaya, L., Guillemin, F., Marchal, F.: Quantum dots in axillary lymph node mapping: biodistribution study in healthy mice. BMC Cancer 8, 111 (2008)
5. Sattel, T., Knopp, T., Biederer, S., Gleich, B., Weizenecker, J., Borgert, J., Buzug, T.: Single-sided device for magnetic particle imaging. J. Phys. D: Appl. Phys. 42, 1–5 (2009)
6. Tsunoda, N., Kokuryo, T., Oda, K., Senga, T., Yokoyama, Y., Nagino, M., Nimura, Y., Hamaguchi, M.: Nek2 as a novel molecular target for the treatment of breast carcinoma. Cancer Sci. 100, 111–116 (2009)
7. Weissleder, R., Elizondo, G., Wittenberg, J., Lee, A.S., Josephson, L., Brady, T.J.: Ultrasmall superparamagnetic iron oxide: an intravenous contrast agent for assessing lymph nodes with MR imaging. Radiology 175, 494–498 (1990)

Behavior of Superparamagnetic Iron Oxides in Magnetic Targeting Models

Ioana Slabu[1], Anjali Roeth[2], Gernot Güntherodt[3], Thomas Schmitz-Rode[4], and Martin Baumann[4]

[1] Applied Medical Engineering, Medical Faculty, Helmholtz-Institute, RWTH Aachen University, Pauwelsstr. 20, 52074 Aachen, Germany
slabu@hia.rwth-aachen.de
[2] Department of Surgery, Medical Faculty, University Hospital Aachen, 52074 Aachen, Germany
[3] II. Physical Institute, RWTH Aachen University, 52074 Aachen, Germany
[4] Applied Medical Engineering, Medical Faculty, Helmholtz-Institute, RWTH Aachen University, 52074 Aachen, Germany

Abstract. In order to improve the specificity of chemotherapeutic drugs towards pathological tissue, we investigated minimally invasive delivery methods by simulation of a magnetic targeting system. This system aims at the concentration of superparamagnetic nanoparticles at a tumor site in the body under the influence of external magnetic forces after injection of the particles into the circulatory system. Therefore, the properties of differently synthesized superparamagnetic iron oxides (SPIOs) were analyzed and implemented in a simulation model. FEM simulations were performed using the Navier-Stokes equation of fluid motion, which describes the hydrodynamic forces that act on the SPIOs in blood flow, with an additional magnetic term caused by the interaction between the SPIOs and the external magnetic field. As a result, we could show the feasibility of magnetic targeting by combining the optimization of both the magnetic fields and the SPIOs' properties.

1 Introduction

A very important objective of therapeutic drug delivery is the ability to precisely target any tissue or region in the body with high specificity in order to allow a controlled drug release, e. g. in a tumor. A promising current approach is magnetic drug targeting which describes the selective targeting of therapeutics by external magnetic field guided delivery. The concept is based on binding a drug of choice to colloidal superparamagnetic nanoparticles, injection of the composite into the circulatory system and direction to a specific body region using an external magnetic field. The field exerts an attractive force on the particles and concentrates them in vivo at a target

T.M. Buzug and J. Borgert (Eds.): Magnetic Particle Imaging, SPPHY 140, pp. 193–197.
springerlink.com

site where the strongest magnetic force and the highest magnetic field gradient dominate. Finally, by the application of a high-frequency magnetic field the medical drugs can be released. This enhances the efficiency of the therapy by reducing the initial required dose of the drug and minimizes its side effects. The generated heat can also be used for hyperthermia treatment [1].

In this work, we develop a targeting model using FEM simulations of magnetic nanoparticles in blood flow under the influence of a magnetic field considering the characteristics of the nanoparticles. Therefore, we synthesized and investigated the physical and chemical properties of two types of superparamagnetic iron oxides (SPIOs) nanoparticles with different sizes, morphologies, relaxivities and magnetization values. The inductive heating characteristics of the SPIOs were also measured in order to determine their therapeutic features for hyperthermia applications.

2 Materials and Methods

We synthesized two kinds of SPIOs (Fe_3O_4) using the thermal decomposition approach by applying the method of Sun [2] with different tenside to precursor ratios of 20:1 for sample S1 and of 3:1 for sample S2. In both cases, the particles were synthesized in an organic phase, stabilized with dodecanoic acid and then transferred to water phase by mixing Pluronic F-127 [3]. We analyzed the SPIOs using four different modalities: superconducting quantum interference, magnetic resonance imaging, transmission electron microscopy and laser diffraction spectrometry. In this way, we determined the susceptibility value, the relaxivity, the core and shell sizes and the morphology of the nanoparticles. The heating characteristics were determined using an induction heating generator TIG 5/300 (Hüttinger GmbH, Germany) operated at 20 A and 188 kHz.

The FEM simulations were performed with the software COMSOL Multiphysics (COMSOL Group, Sweden). A model that describes the interaction of an external magnetic field with blood flow containing homogeneous suspended SPIOs with a mass fraction of particles in the blood (SPIOs concentration) between 0.033 and 0.1 was developed. The description of the motion of the fluid composed of blood and particles is based on the Navier-Stokes equation of anisotropic fluid motion (1) which describes the velocity $\vec{u}$ of the fluid.

$$\rho\left(\frac{\partial}{\partial t}+\vec{u}\cdot\vec{\nabla}\right)\vec{u}=\vec{\nabla}\left[\eta(\dot{\gamma})\cdot(\nabla\mathbf{u}+(\nabla\mathbf{u})^{T})-p_{tot}\mathbf{I}\right]+\vec{f} \tag{1}$$

where ρ is the density of the fluid, p_{tot} is the total pressure acting on the fluid, **I** is the unit matrix and $(\nabla\mathbf{u})^T$ the Jacobian matrix of the velocity $\vec{u}$ [4].

This equation has an additional term, the magnetic force density $\vec{f}$ that acts on the SPIOs in blood flow (2), which is derived from the Maxwell's equations:

$$\vec{f} = \mu_0 M(\vec{\nabla} H) \tag{2}$$

where H is the magnitude of the magnetic field, M is the magnitude of the magnetization and μ_0 is the vacuum permeability [4].

The non-Newtonian dependency of the viscosity η from the shear rate $\dot{\gamma}$ is described by the Generalised Power Law [5]:

$$\eta(\dot{\gamma}) = 0.1\,\lambda(\dot{\gamma})\,|\,\dot{\gamma}\,|^{n(\dot{\gamma})-1} \tag{3}$$

with

$$\lambda(\dot{\gamma}) = \eta_\infty + \Delta\eta \cdot \exp\left[-\left(1+\frac{|\,\dot{\gamma}\,|}{a}\cdot\exp\left(-\frac{b}{|\,\dot{\gamma}\,|}\right)\right)\right] \tag{4}$$

$$n(\dot{\gamma}) = n_\infty - \Delta n \cdot \exp\left[-\left(1+\frac{|\,\dot{\gamma}\,|}{c}\cdot\exp\left(-\frac{d}{|\,\dot{\gamma}\,|}\right)\right)\right] \tag{5}$$

where a = 50 s^{-1}, b = 3 s^{-1}, $\Delta\eta$ = 450 mPa·s, η_∞ = 3.5 mPa·s, c = 50 s^{-1}, d = 4 s^{-1}, Δn = 0.45 and n_∞ = 1.

The model was applied for a simulation of the carotid artery using the following description for the pulsatile blood flow:

$$u(t) = 2u_0 s(1-s)\left(\sin(\omega t) + \sqrt{\sin^2(\omega t)}\right) \tag{7}$$

where t is the time, ω the pulse frequency and u_0 = 70 cm/s the peak blood velocity. Furthermore, a quadratic velocity profile is implemented by the term $s(1\text{-}s)$ where the parameter s linearly increases from 0 to 1 from one side of the vessel wall to the other side.

3 Results

The characteristics of the SPIOs samples S1 and S2 are listed in table 1. Both samples show a superparamagnetic behavior and a narrow size distribution.

Table 1. Core size (D_{TEM}), hydrodynamic radius (R_{DLS}), saturation magnetization (M_S), susceptibility (χ), relaxivities R1 and R2 as well as specific absorption rate (SAR) of samples S1 and S2 with an iron concentration of 0.274 mg ml^{-1}.

Sample	D_{TEM} [nm]	R_{DLS} [nm]	M_S [emu/g]	χ	R1 [s^{-1} mM^{-1}]	R2 [s^{-1} mM^{-1}]	SAR [W g^{-1}]
S1	6.3 ± 0.6	27.8 ± 1.8	29.4 ± 0.5	1.19 ± 0.06	4.1 ± 0.3	54.9 ± 5.4	0.400 ± 0.001
S2	4.5 ± 1.1	28.2 ± 1.4	61.7 ± 0.4	1.14 ± 0.06	1.4 ± 0.2	33.5 ± 5.6	0.534 ± 0.002

In the simulations of the targeting model, the velocity change of the fluid in the carotid artery caused by the magnetic interaction of the SPIOs with the permanent magnet, which is placed at an angle α to the normal component of the chosen geometry and at a fixed distance of 0.35 mm to the vessel, is obtained (figure 1). The remanence of the magnet is set to 1.19 T. The simulations were performed with four different SPIOs concentrations and nine different angular settings of the magnet. The results show the largest velocity change of 10 % at α = 0° and for a SPIOs concentration of 0.1.

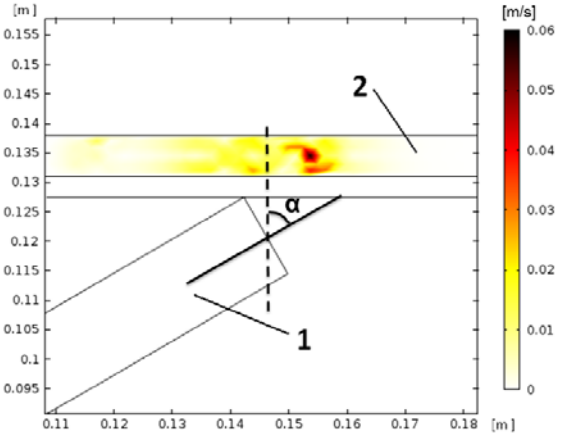

Fig. 1. Velocity magnitude of the fluid for a permanent magnet (1) near the carotid artery (2). Here: α = 60°, SPIOs concentration 0.1.

4 Discussion

The small size of the particles influences their properties tremendously, showing SAR values 100 times lower in comparison to particles with approx. 10 times bigger volume [6]. From their relaxivity values, it can be deduced that the particles can be used as contrast agents only for T1 weighted images. However, both samples show good magnetization values which are even higher for smaller particles (S2).

From the simulation results it can be concluded that for the same concentration of nanoparticles different settings of the magnet lead to different velocity changes in the magnitude in the range from 2 to 10 % of the maximal velocity. This indicates the importance of the geometry of the applied magnetic fields. Furthermore, a minimum SPIOs concentration of 0.033 could be identified below which no targeting efficiency was observed.

5 Conclusion

The simulations proved to be suitable for further investigation of magnetic targeting systems. The system thus can be advanced to a tumor model with capillary vessels, optimized geometries of the magnetic field and nanoparticles with stronger therapeutic (e. g. hyperthermia) and magnetic resonance imaging features.

References

1. Krishnan, K.M.: Biomedical nanomagnetics: A spin through possibilities in imaging, diagnostics, and therapy. IEEE Trans. Magn. 46(7), 2523–2558 (2010)
2. Sun, S., et al.: Monodisperse MFe_2O_4 (M = Fe, Co, Mn) Nanoparticles. J. Am. Chem. Soc. 126, 273–279 (2004)
3. Jeong, Y.Y., et al.: Antibiofouling amphiphilic polymer-coated superparamagnetic iron oxide nanoparticles: synthesis, characterization, and use in cancer imaging in vivo. J. Mater. Chem. 19, 6412–6417 (2009)
4. Rosensweig, R.E.: Ferrohydrodynamics. Cambridge University Press (1985)
5. Johnston, B., et al.: Non-Newtonian blood flow in a bifurcation model with a non-planar branch. Journal of Biomechanics 37, 1899–1911 (2004)
6. De Cuyper, M., et al.: Specific heating power of fatty acid and phospholipid stabilized magnetic fluids in an alternating magnetic field. J. Phys. Condens. Matter 20, 204131–204136 (2008)

Diagnostic Imaging in Cancer Therapy with Magnetic Nanoparticles

Stefan Lyer[1], Rainer Tietze[1], Stephan Dürr[1], Tobias Struffert[2], Tobias Engelhorn[2], Marc Schwarz[2], Arnd Dörfler[2], Lubos Budinsky[3], Andreas Hess[3], Wolfgang Schmidt[4], Roland Jurgons[5], and Christoph Alexiou[1]

[1] Department of Oto-Rhino-Laryngology, Head and Neck Surgery, Section for Experimental Oncology and Nanomedicine, Else Kröner-Fresenius-Stiftung-Professorship, University Hospital Erlangen, Waldstraße 1, 91054 Erlangen, Germany
Stefan.Lyer@uk-erlangen.de
[2] Department of Neuroradiology, University Hospital Erlangen, Schwabachanlage 6, 91054 Erlangen, Germany
[3] Chair of Pharmacology and Toxicology, Friedrich-Alexander University Erlangen, Fahrstraße 17, 91054 Erlangen, Germany
[4] Siemens AG, Corporate Technology, Erlangen, Germany
[5] Franz-Penzoldt-Zentrum, University Hospital Erlangen and Friedrich-Alexander University Erlangen, Palmsanlage 5, 91054 Erlangen, Germany

The unfavorable application-to-tumor-dose-ratio is a drawback of conventional systemic chemotherapy, implying an often insufficient drug dose in the tumor being associated with severe side effects for the patient. The use of chemotherapeutics bound to magnetic nanoparticles offers several advantages. On the one hand it is possible to concentrate the chemotherapeutics in the tumor region by the use of magnetic fields, like it is done in Magnetic Drug Targeting (MDT). On the other hand magnetic particles can serve as contrast agent for magnetic resonance imaging (MRI) that is bound to the therapeutics. Hence, the particles possibly are opening an insight into drug distribution in the tumor region directly after administration.

Another important factor for a successful MDT-application is detailed knowledge about tumor vascularization.

In this pilot study we investigated vascularization and size of an tumor in an experimental *in vivo* tumor model via flat-panel angiography and DYNA-CT before MDT and the particle distribution with MRI after MDT.

We could show that the tumor could be displayed by MRI and DYNA-CT before and after MDT. Flat panel angiography revealed clearly the pathological tumor vascularization before MDT, while MRI imaging afterwards displayed the tumor as well as the particle distribution in the tumor.

T.M. Buzug and J. Borgert (Eds.): Magnetic Particle Imaging, SPPHY 140, pp. 199–203.
springerlink.com

1 Introduction

Personalized and individualized medicine [1, 2] are keywords describing the ambition of medical and medicine orientated basic science and an actual need for an improvement in treating especially threatening disorders like malignant tumors [3, 4], but also cardiovascular [5], pulmonary [6], and other diseases [7, 8]. Theranostics is another keyword promising an improvement in treatment and diagnostic of such disorders often by combining personalized approaches with nanotechnological tools [9, 10].

Different imaging techniques are crucial for these up-to-date approaches to a better medicine. Especially in Magnetic Drug Targeting biocompatible iron-oxide based nanoparticles offer these opportunities. On the one hand these particles can serve as shuttles for chemotherapeutics and other drugs to the desired region, where they can be concentrated by external magnetic fields [11-14]. On the other hand, magnetic particles can be used as contrast agents for MRI by causing a signal-extinction. For successfully completing the personalized nanomedical theranostics-approach of MDT, a diagnostic angiography displaying the tumor supplying vessels is necessary.

In this pilot study, we investigated the combination of MRI, DYNA-CT and flat panel angiography before MDT and the correlation of the particle distribution in the tumor by MRI afterwards.

2 Material and Methods

A VX-2 tumor was implanted at the left hind limb of rabbits. Mitoxantrone was bound to superparamagnetic Fe_3O_4-nanoparticles in an aqueous solution. This drug loaded ferrofluid was applied in a 1:500 dilution through the femoral artery close to the tumor. The magnetic nanoparticles were attracted to the tumor by a focused external magnetic field (field gradient max. 72 T/m) during the application. Imaging of the tumor vascular system and size before MDT was done using a biplane angiographic system with rotational flat-panel CT (DYNA-CT, Siemens Axiom Artis dBA) with a standard contrast agent. Tumor imaging was realized with an experimental MRI (BRUKER BIOSPEC) before and after MDT, additionally.

3 Results

MRI and DYNA-CT revealed a tumor, situated lateral at the rabbits' leg. Using both imaging methods, in transversal slices the tumor could be distinguished clearly from the muscle tissue (Fig.1).

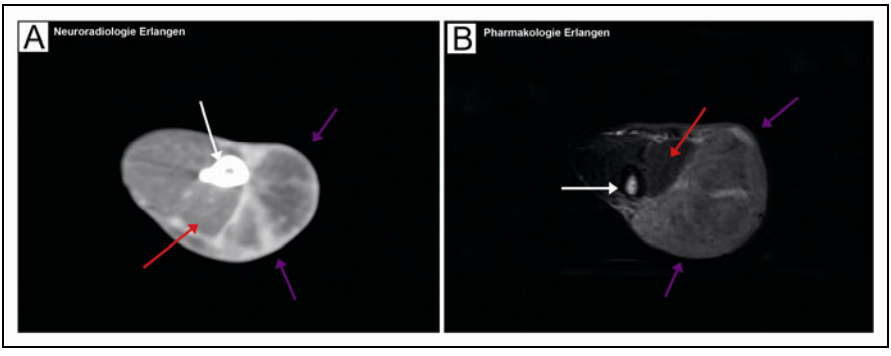

Fig. 1. 2D-Imaging before MDT. A) Transversal DYNA-CT imaging and B) transversal magnetic resonance tomography shows a big VX2-tumor situated lateral at the left shank of the rabbit. White and red arrows depict bone and muscle of the left hind limb, purple arrows depict the tumor.

The tumor and the supplying vessels could be displayed clearly by flat panel on day one (Fig.2A). The angiography showed the pathological vascularization of the tumor branching from the *Arteria femoralis*. Three main artery branches with heterogeneous and irregular vessels supported the tumor from ventral at its' proximal and distal part, respectively (Fig.2A.).

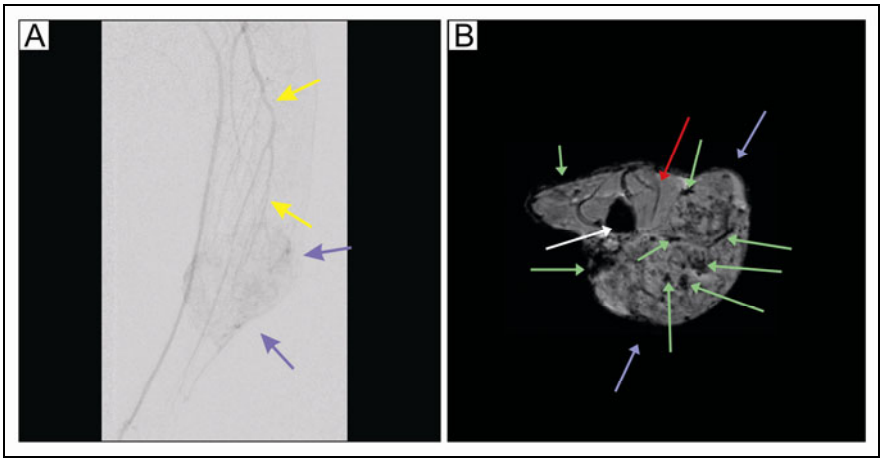

Fig. 2. A) 2D-angiography before MDT. Yellow arrows: irregular vessel supporting the tumor; purple arrows: tumor. B) Transversal MRI image of the tumor region 3 days after MDT. The tumor (purple arrows) can be distinguished clearly from the muscle tissue (red arrow). Signal extinction caused by the magnetic nanoparticles occurs throughout the whole tumor (green arrows).

On day two a 1:500 dilution of a regularly used dose was applied during MDT. During the treatment no complications occurred and the wound healing proceeded normally. Three days after MDT (day 6) MRI imaging of the treated region was done (Fig.2B). The tumor could be displayed lateral at the left shank, again. It could be distinguished very clearly from the normal muscle tissue. Additionally, MRI showed signal extinction caused by the magnetic particles. Compared to the image received one day before MDT (Fig.1B) throughout the treated tumor big parts without signal displayed the areas of particle accumulation. The analysis of all transversal slices showed, that this signal extinction occurred correspondingly to the vascularization pattern revealed by CT-angiography.

4 Conclusion

In medicine oriented science a personalized treatment of each patient is pushed forward by a growing knowledge about the networks and molecular relationships that are keeping us alive. It is the ambition of scientists as well as clinicians to treat patients better, more cost effective and with lower side effects, especially in cancer treatment. One example of a promising attempt to fulfill these ambitions is Magnetic Drug Targeting [11, 14]. A critical part of local tumor treatment with MDT is a sufficient drug load in the tumor region. Since MDT is using the tumor supporting vessels directly, a detailed knowledge of the tumor vascularization is necessary. This can be achieved by flat-panel CT based angiography, like we could show in this study. But magnetic nanoparticles as drug carriers also offer the possibility of a drug deposition control directly after the application and even some days afterwards. By using MRI we were able to visualize qualitatively the particle distribution of the used 1:500 dilution in the tumor region with a 4.7 Tesla machine three days after MDT. Taken into account the progress in the field of MRX-measurement, the combination with imaging methods even could lead to a quantitative measurement of the iron content and indirectly of the drug content in the tumor region. As shown, flat-panel angiography combined with DYNA-CT before and MRI after Magnetic Drug Targeting with magnetic iron oxide nanoparticles offer excellent tools to realize the Theranostic approach of this new and innovative cancer treatment.

Acknowledgment. This study was supported by the German Ministry of Education and Research (BMBF, FKZ:01EX1012B), the DFG (PAK 151) and the Else Kröner-Fresenius-Stiftung, Bad Homburg v.d.H., Germany.

References

1. Morrison, K.E.: Whole-genome sequencing informs treatment: personalized medicine takes another step forward. Clin. Chem. 57(12), 1638–1640 (2011)
2. Natoli, G., Capalbo, C.: The end of the beginning of personalized medicine. Ann. Oncol. 22(12), 2695 (2011)
3. Chiang, A., Million, R.P.: Personalized medicine in oncology: next generation. Nat. Rev. Drug. Discov. 10(12), 895–896 (2011)
4. Corless, C.L.: Personalized cancer diagnostics. Science 334(6060), 1217–1218 (2011)
5. Degoma, E.M., et al.: Personalized vascular medicine: individualizing drug therapy. Vasc. Med. 16(5), 391–404 (2011)
6. Shapiro, S.D.: Merging personalized medicine and biology of aging in chronic obstructive pulmonary disease. Am. J. Respir. Crit. Care Med. 184(8), 864–866 (2011)
7. Zarco, M., Vess, T., Ginsburg, G.: The oral microbiome in health and disease and the potential impact on personalized dental medicine. Oral. Dis (2011)
8. Wong, E.H., et al.: Toward personalized medicine in the neuropsychiatric field. Int. Rev. Neurobiol. 101, 329–349 (2011)
9. Kelkar, S.S., Reineke, T.M.: Theranostics: combining imaging and therapy. Bioconjug. Chem. 22(10), 1879–1903 (2011)
10. Cole, A.J., Yang, V.C., David, A.E.: Cancer theranostics: the rise of targeted magnetic nanoparticles. Trends Biotechnol. 29(7), 323–332 (2011)
11. Alexiou, C., et al.: Locoregional cancer treatment with magnetic drug targeting. Cancer Research 60(23), 6641–6648 (2000)
12. Alexiou, C., et al.: Magnetic drug targeting - Biodistribution of the magnetic carrier and the chemotherapeutic agent mitoxantrone after locoregional cancer treatment. J. Drug Target 11(3), 139–149 (2003)
13. Jurgons, R., et al.: Drug loaded magnetic nanoparticles for cancer therapy. Journal of Physics-Condensed Matter 18(38), S2893–S2902 (2006)
14. Lyer, S., et al.: Visualization of Tumor Regression after Local Chemotherapy with Magnetic Nanoparticles. Anticancer Research 28(6B), 4079–4080 (2008)

Engineering Contrast Agents for Gastrointestinal Magnetic Particle Imaging: The Biological Perspective

Katrin Ramaker, Niels Röckendorf, and Andreas Frey

Division of Mucosal Immunology & Diagnostics, Department of Pneumology, Research Center Borstel, Parkallee 22, 23845 Borstel, Germany
kramaker@fz-borstel.de, nroeckendorf@fz-borstel.de, afrey@fz-borstel.de

Abstract. Cancers of the gastrointestinal tract are one of the leading causes of death in affluent countries. Although they are usually curable if detected at an early enough stage, the compliance to undergo routine screenings for gastrointestinal cancers in a presymptomatic stage is low, mostly due to the discomfort which current diagnostic measures, such as gastroscopy, colonoscopy, digital rectal exams or feces examinations pose to the patient. Magnetic particle imaging (MPI) has the potential to overcome this hurdle as the procedure is noninvasive, radiation-free and assumed to be more sensitive than most other imaging modalities used today. Yet, MPI bears a catch as it requires special magnetizable contrast agents in the nanoscale range. These contrast agents have to meet a number of requirements. They must be detectable in the magnetic field, be manufacturable in a cost-effective manner, display a certain shelf life, be administrable in a compliant way, be stable in vivo, be specific and sensitive in labeling the neoplastic tissue and must not be harmful to the individual who incorporates them. Due to this complex requirement profile MPI contrast agent engineering lags behind imaging hardware development. In order to close in on this field it is important to identify, rate and define the relevant players which ingested MPI contrast agents have to deal with en route to their destination in the body. Potential players are the anatomy and microanatomy of the gastrointestinal tract, the chemical and biological composition of the luminal constituents as well as potential degradation and scavenger mechanisms. Once the possible impact of these factors has been established contrast agents can be designed to master these challenges. Yet, reaching the destination without causing harm is a necessary but not sufficient requirement. In order to fully exploit the potential of MPI and to qualify it for mass screening the method must be highly sensitive and specific. This may be achieved by targeting systems that direct the contrast agent exclusively and efficiently to the neoplastic tissue in question. In this paper we provide an overview on our current knowledge

T.M. Buzug and J. Borgert (Eds.): Magnetic Particle Imaging, SPPHY 140, pp. 205–210.
springerlink.com

of the fate of magnetizable contrast agents in the gut, the players which determine this fate, measures to properly endow contrast agents for this task and means to equip them with the necessary specifity and sensitivity.

Malignancies of the digestive system account for about 30% of new cancer cases and 40% of cancer-related deaths in the world's population every year. Which organ is affected largely depends on diet and life style. In developing countries stomach and liver cancer claim most of the victims whereas in developed countries most casualties are caused by colorectal tumors. Whether or not a person is likely to survive such a disease depends on the stage at which the malignancy is diagnosed. For colorectal cancer the five-year survival rate is 90% when the tumor is detected at a local stage but less than 10% when the disease is diagnosed after distant metastases have already formed. As the odds to develop a gut tumor increase with age, it is recommended in most affluent countries for everyone beyond age 50 to undergo screening for colorectal neoplasia.

Currently, three screening procedures are in use: the fecal occult blood test (FOBT), endoscopy (sigmoidoscopy or colonoscopy) and X-ray investigation after barium enema. The FOBT is rapid, cheap and noninvasive but with a sensitivity of 24-87% and a specificity of 88-98% the least dependable test. X-ray examination is more reliable with sensitivities of 62-100%, while endoscopy reaches a sensitivity of 70-100% for sigmoidoscopy/colonoscopy, and a specificity of 84% for sigmoidoscopy. Accordingly, it was shown that already a single flexible sigmoidoscopy screening on probands between 55 and 64 years of age reduces colon cancer incidence by 33% and mortality by 43% among these individuals [1,2]. Yet, compliance to enroll in such screenings is low, mostly due to the discomfort of an invasive rectal examination. To overcome this reluctancy and to gain broad acceptance for colorectal cancer screening there is an urgent need for new, noninvasive screening procedures of high sensitivity and specificity.

Magnetic particle imaging (MPI) is a novel imaging modality that holds the potential to fill this gap. MPI is a radiation-free technology that operates on the recording of the nonlinear response of magnetic particles in an oszillating magnetic field [3]. To prevent thermal injury with such particles, the oszillating magnetization must not undergo a hysteresis cycle. Thus, only anhysteretic superparamagnetic particles in the nanoscale range are suitable for MPI.

The need for nanoparticles has pros and cons. An upside should be the particles' ability to rapidly disseminate to and to homogeneously decorate the target. Problems may arise on the manufacturing and safety side. Especially the latter is of particular importance in light of the ongoing concerns about nanotechnology in the public. The few biological studies with MPI [e.g. 4,5] do not provide an answer for this, nor do the some 1700 studies conducted on small or ultrasmall superparamagnetic iron oxide

particles (SPIOs or USPIOs) in the neighbouring field of magnetic resonance imaging (MRI). Two (U)SPIO-MRI-formulations, Endorem®/Feridex® and Resovist® have already been abandoned although they had a good safety profile [6,7]. A third one, GastroMARK®/Lumirem®, which consists of siloxane-coated USPIOs [8], is still on the market despite some concerns about its safety and usefulness. A tentative conclusion from this may be: performance, safety, shelf life and ease of manufacturing of anhysteretic superparamagnetic contrast agents primarily depend on the size, shape, homogeneity and surface properties of the particles and the intended site of use and delivery.

In this respect the gastrointestinal (GI) tract is a very special case. In biological terms the lumen of the GI tract is outside of the body, and the mucosal lining is an outer surface, much like the skin. But unlike the skin the mucosa does not represent a strong mechanical barrier nor does the gastrointestinal surface comprise multilayers of dead cells that prevent uptake of foreign matter. The epithelia of the mucosa consist of a single layer of live cells. Uptake of luminal content is prevented by tight junctions which sustain close contact between the cells, by a mesh of glycoproteins, termed glycocalyx, that allows trespassing of solutes only, and by a mucus gel coat that lubricates the mucosal surface and traps pathogens, solid food constituents and the like (Fig. 1).

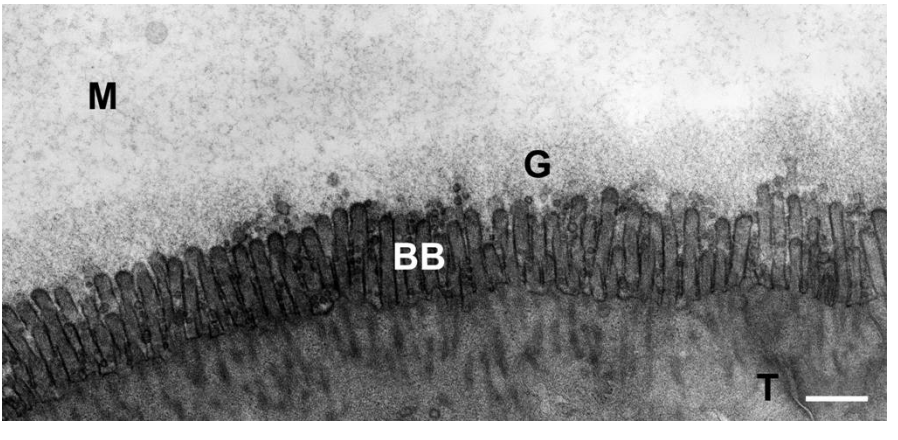

Fig. 1. Ultrastructure of the surface of the human large intestinal epithelium. The transmission electron micrograph depicts the brush border (BB) of the tight junction-sealed (T) colonic epithelium that is covered by a continuous glycocalyx (G) which in turn is coated by a mucus (M) gel. Preparation, fixation and staining of the tissue was performed as described by Frey et al. [9]. The biopsy was obtained with written informed consent of the donor and used according to a study protocol that was approved by the research ethics committee of the University of Luebeck. Scale bar: 500 nm

The apical cell membrane of the intestinal epithelium is organized as brush border to increase the surface for rapid transport of water, salts and nutrients. Particles do not belong to the standard cargo but there are certain sites and cell types for the sampling of microorganisms where particles may occasionally be misclassified as microbes and be taken up [10]. Yet, the amount of translocated particles will be low compared to that contained in systemically administered (U)SPIO-based contrast agents. Moreover, the recurring epithelial renewal will eliminate particles accidentally endocytosed at non-sampling sites. Thus, it is likely that the majority of ingested particulate contrast agents leave the body via the natural route without need for breakdown and detoxification. The small fraction of particles that is taken up may still present a problem. They must be broken down or excreted via liver or kidney.

Particles usually do not display a certain tissue- or cell-tropism which a contrast agent must have in order to specifically highlight a small neoplastic lesion. Hence, the (U)SPIO-based contrast agents mentioned above cannot be used for early colon cancer detection. Endorem®/Feridex® and Resovist® rely on phagocytosis of particulate matter by the reticuloendothelial system in the healthy liver. GastroMARK®/Lumirem® fills the lumen of the gut and/or decorates the mucosal surface thereby revealing large lesions and indentations. Although some polyps may be visible this way, the lack of target specificity must be overcome if MPI is to become a routine screening procedure for colorectal cancer. To meet this goal suitable particles must be surface customized such that they bind specifically to cancerous tissue. Several preclinical studies on (U)SPIO-targeting to colon cancer (cells) have been performed [e.g. 11,12] but the results are scarcely clinically useful. For systemic administration the safety issue persists which may negatively affect the compliance with MPI-based screening of asymptomatic individuals. For oral delivery compliance should be higher since clearance is not a major problem and with GastroMARK®/Lumirem® an approved formulation is already at hand. However, orally administered particles face other challenges. They must not be trapped in mucus, food or by the intestinal flora and the surface modification that guides the particles to the cancerous lesions must withstand the digestive environment of the alimentary canal. Antibodies and other protein ligands often used for systemic targeting will not survive this environment. Besides that, they are expensive and difficult to couple to a particle surface in a defined manner. In contrast, peptide ligands are cheaper to manufacture and can be coupled to particle surfaces in a reproducible manner. Unfortunately, they are not very stable in the gastrointestinal tract either (Fig. 2). Unlike protein ligands, however, they may be designed as peptidomimetics with critical amino acids replaced by nonnatural moieties.

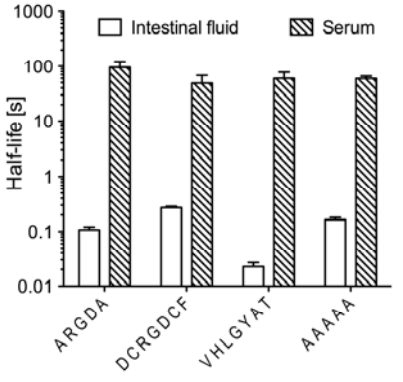

Fig. 2. Different stabilities of peptides in intestinal fluid and serum. Peptides containing the integrin-binding-motif RGD and/or described as "tumor-specific" [13,14] were chosen as model targeting ligands, an alanine 5mer served as control. Murine intestinal fluid was harvested by aqueous lavage and the dilution factor determined via its IgA content [15]. Peptide half-lifes in serum and intestinal fluid were measured as described [16]. Data represent geometric mean ± SD of three experiments and demonstrate the dramatic differences of peptide stability in serum and intestinal fluid.

An unsolved problem with site-specific delivery remains the identification of suitable targets - no general surface marker for colorectal tumor tissue has been described as yet - and of the matching ligand. We address both problems. Novel surface markers are identified that can be targeted by ligand-coated (U)SPIOs, and a plattform is under development with which peptide and peptidomimetic ligands for such targets can be identified [17].

References

1. Jemal, A., et al.: Global cancer statistics. CA Cancer J. Clin. 61, 69–90 (2011)
2. Helfmann, J., et al.: Early Diagnosis of cancer. In: Popp, J., Strehle, M. (eds.) Biophotonics: Visions for Better Health Care, pp. 231–300. Wiley-VCH, Weinheim (2006)
3. Gleich, B., Weizenecker, J.: Tomographic imaging using the nonlinear response of magnetic particles. Nature 435, 1214–1217 (2005)
4. Weizenecker, J., et al.: Three-dimensional real-time in vivo magnetic particle imaging. Phys. Med. Biol. 54, L1–L10 (2009)
5. Markov, D.E., et al.: Human erythrocytes as nanoparticle carriers for magnetic particle imaging. Phys. Med. Biol. 55, 6461–6473 (2010)
6. Bluemke, D.A., et al.: Hepatic MR imaging with ferumoxides: multicenter study of safety and effectiveness of direct injection protocol. Radiology 228, 457–464 (2003)
7. Reimer, P., Balzer, T.: Ferucarbotran (Resovist): a new clinically approved RES-specific contrast agent for contrast-enhanced MRI of the liver: properties, clinical development and applications. Eur. Radiol. 13, 1266–1276 (2003)
8. Hahn, P.F., et al.: First clinical trial of a new superparamagnetic iron oxide for use as an oral gastrointestinal contrast agent in MRI imaging. Radiology 175, 695–700 (1990)
9. Frey, A., et al.: Role of the glycocalyx in regulating access of microparticles to apical plasma membranes of intestinal epithelial cells: implications for microbial attachment and oral vaccine targeting. J. Exp. Med. 184, 1045–1059 (1996)

10. Shepherd, N.A., et al.: Exogenous pigment in Peyer's patches. Hum. Pathol. 18, 50–54 (1987)
11. Toma, A., et al.: Monoclonal antibody A7-superparamagnetic iron oxide as contrast agent of MR imaging of rectal carcinoma. Brit. J. Cancer 93, 131–136 (2005)
12. Creixell, M., et al.: Preparation of epidermal growth factor (EGF) conjugated iron oxide nanoparticles and their internalization into colon cancer cells. J. Magnetism Magnet. Mater. 322, 2244–2250 (2010)
13. de Groot, F.M.H., et al.: Design, synthesis, and biological evaluation of a dual tumor-specific motive containing integrin-targeted plasmin-cleavable doxorubin prodrug 1. Mol. Cancer Ther. 1, 901–911 (2002)
14. Zhang, Y., et al.: Panning and identification of a colon tumor binding peptide from a phage display peptide library. J. Biomol. Screen. 12, 429–435 (2007)
15. Bade, S., et al.: Quantitation of major protein constituents of murine intestinal fluid. Anal. Biochem. 406, 157–165 (2010)
16. Gorris, H.H., et al.: Rapid profiling of peptide stability in proteolytic environments. Anal. Chem. 81, 1580–1586 (2009)
17. Röckendorf, N., et al.: Peptide-based optical contrast agents for targeting of intestinal malignancies. In: Proc. SPIE, vol. 6633, pp. 66332A1–66332A9 (2007)

Visualization of Instruments for Cardiovascular Intervention Using MPI

Julian Haegele[1], Jürgen Rahmer[2], Bernhard Gleich[2], Claas Bontus[2], Jörn Borgert[2], Hanne Wojtczyk[3], Thorsten M. Buzug[3], Jörg Barkhausen[1], and Florian M. Vogt[1]

[1] Clinic for Radiology and Nuclear Medicine, University Hospital Schleswig Holstein Campus Lübeck, Ratzeburger Allee 160, 23538 Lübeck
haegele@radiologie.uni-luebeck.de
[2] Philips Technologie GmbH Innovative Technologies, Research Laboratories, Röntgenstraße 24-26, 22335 Hamburg, Germany
[3] Institute of Medical Engineering, University of Lübeck, Ratzeburger Allee 160, 23562

Abstract. Due to the possibility of high temporal and spatial resolution, high sensitivity and three-dimensional imaging, Magnetic Particle Imaging is a promising new imaging approach for interventional cardiovascular procedures. In this contribution we present first MPI-images of a specifically labeled, though commercially available device for cardiovascular intervention. Furthermore, different approaches to label those instruments are discussed.

1 Introduction

Magnetic Particle Imaging (MPI) determines the spatial distribution of superparamagnetic iron oxide particles (SPIOs) using oscillating and static magnetic fields. It is a tomographic imaging method capable of high temporal and spatial resolution and high sensitivity [1]. Thus, high resolution, three-dimensional real-time imaging is feasible. These conditions and the absence of ionizing radiation render MPI very interesting for application in cardiovascular intervention as there is no other single method providing all of those characteristics. As MPI in principle displays only the concentration of SPIOs, visualization of interventional devices is a challenge, but also a precondition. We labeled a commercially available balloon catheter for percutaneous intraluminal angioplasty (PTA) by filling the balloon afferent lumen and the balloon itself with a Resovist dilution. Imaging was performed on an experimental MPI-scanner.

T.M. Buzug and J. Borgert (Eds.): Magnetic Particle Imaging, SPPHY 140, pp. 211–215.
springerlink.com

2 Material and Methods

We used an experimental MPI-scanner setup ("pre-clinical demonstrator") described by Rahmer et al. [2] providing a gradient field strength of 2.5 Tm^{-1} in z-direction and 1,25 Tm^{-1} in x- and y-direction. The drive field amplitude was set to 13 mT while the excitation frequency was around 25 kHz. The sample rate was 46 volumes per second, corresponding to an acquisition time of 21.54 ms per image. The resulting field of view FOV was 3.4x3.4x2.0 cm^3. For reconstruction, a system function was acquired prior using a 1.6 µl probe of undiluted Resovist.

A balloon catheter for PTA of larger arteries originally designed for intra-arterial digital subtraction angiography (i.a. DSA) (Abbot Vascular, Fox plus PTA-catheter, shaft diameter 1.72 mm, balloon diameter 10 mm and balloon length 30 mm) was used. The afferent lumen to the balloon was filled with diluted Resovist (1:20, 25mmol (Fe)/l, Bayer Schering Pharma). The catheter was inserted in a basic vascular phantom (tube-shaped, inner diameter 16 mm) containing sodium chloride solution (0.9 %). During image acquisition, the catheter was moved forward and backward through the FOV to image the shaft and the deflated balloon, respectively. Subsequently, the balloon was inflated using the diluted Resovist.

The system function based reconstruction was done using three different regularization parameters (λ = 0.1, 1, 10) as described by Weizenecker et al. in [3]. In general, with higher regularization parameter λ, the signal to noise ratio (SNR) increases up to a certain point, but spatial resolution decreases.

3 Results

Both, the shaft and the balloon of the catheter could be visualized. Despite the small Resovist-containing lumen (approximately 0.3 mm^3) of the catheter the shaft could be visualized with all regularization schemes (see Fig 1.). The inflation and the deflation as well as the inflated balloon itself could be monitored very well. Contrast and sensitivity were best using the regularization parameter λ=1. The higher SNR especially improved not only the visualization of the shaft, but also the delineation of the balloon compared to the lower regularization (λ=0.1). The theoretical decrease of spatial resolution was not comprehensible in this regularization scheme. With higher regularization (λ=10) the image blurred out as both, the resolution and the SNR, decreased. The stainless steel radiopaque markers of the balloon did not interfere with image acquisition.

4 Discussion

Commercially available catheters can be visualized relatively easily using appropriate SPIOs like Resovist. Especially catheters with two lumina can be labeled by filling one with a dilution of SPIOs. This refers mainly to therapeutic balloon- and balloon-expandable stent-catheters. We could demonstrate

even the visualization of the deflated balloon and the very small afferent lumen to the balloon within the shaft. However, before those therapeutic instruments can be used to e.g. dilate an arterial stenosis, instruments to navigate to the site of interest and to guide the therapeutic catheters are crucial and indispensable. These are mostly diagnostic catheters and guide wires. As diagnostic catheters have only one lumen and the guide wire has no lumen at all, other strategies for labeling are necessary. Coating these instruments with SPIO-based enamel may be the easiest alternative. As guide wires are commonly between 0.5 and 0.9 mm thin, the coating needs to be very thin, too. Consequently, for a good signal of the coating, the concentration of SPIOs has to be very high and the SPIOs inherently need to generate a strong signal as well. Furthermore, the coating must neither change the mechanical properties of the instrument nor splinter even under

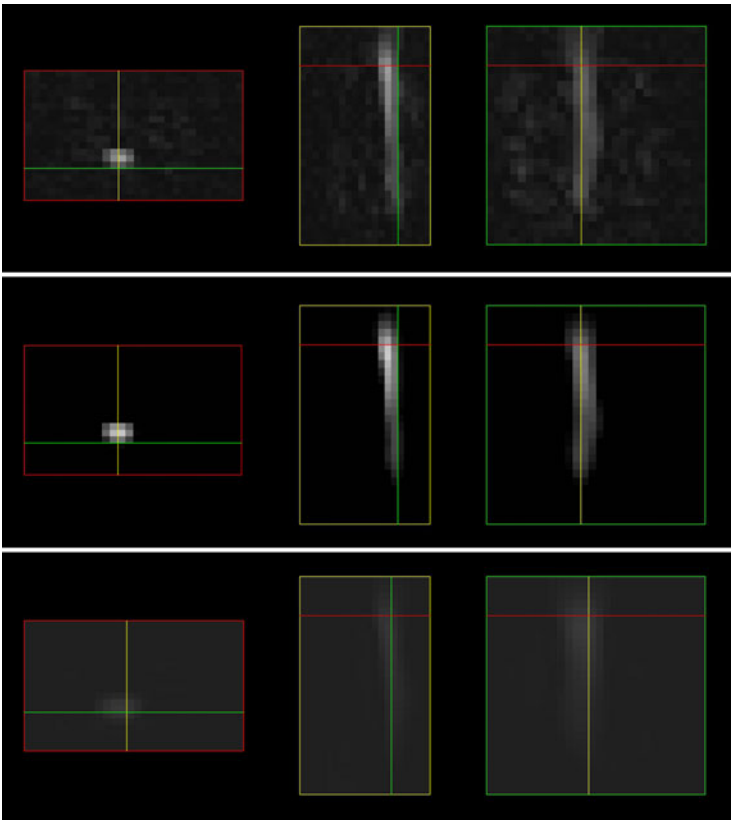

Fig. 1. Visualization of the Resovist-filled shaft (left to right: axial, sagittal and coronal view) using different regularization schemes (top λ=0,1, middle λ=1, bottom λ=10): The shaft is clearly delineable in all three planes and regularization schemes. With λ=1 (middle) the balance between spatial resolution and SNR seems best. By lowering regularization the SNR decreases too much while using higher regularization the gained resolution is too low and the SNR decreased again.

strong mechanical burden. Another alternative is the integration of SPIOs in the polymeric structure of the instrument. Working with a system function based reconstruction, which to date is necessary for rapid 3D imaging, two issues have to be taken into account:

First, it is only possible to reconstruct images using one system function until now. Thus, the intravascular tracer has to be the same as the one labeling the instruments and the delineation of instrument and intravascular tracer has to be achieved using different concentrations thereof. Alternatively, the instrument could have a pattern that is easily discerned.

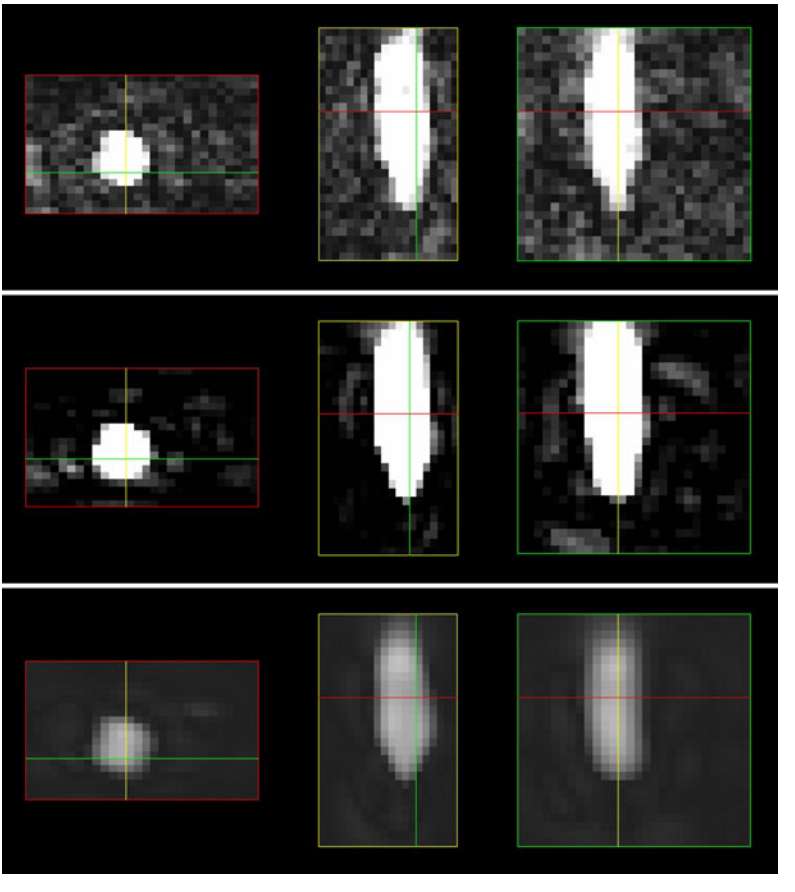

Fig. 2. Inflated Ballon filled with Resovist dilution (left to right: axial, sagittal and coronal view). The difference between the three regularization schemes (λ=0.1, 1, 10, top to bottom) is comparable to differences evaluation the shaft part of the catheter. Again regularization with λ=1 reveals the most satisfying image quality.

Second, a tradeoff exists between resolution and SNR [3]. In this study, the application of a moderate regularization scheme showed the best results. High SNR and sensitivity are important for imaging very small structures, but regularization could increase the SNR only up to a certain point. In accordance with Weizenecker et al., a higher regularization led to a decrease of SNR combined with an even lower resolution resulting in a blurred image. However, this problem may be solved by the development of dedicated SPIOs for MPI with a higher inherent magnetic moment leading to higher sensitivity and spatial resolution.

Another crucial point for guidance of a cardiovascular intervention via MPI is real-time device tracking. Currently the image reconstruction is too slow for real-time visualization, but expected improvements in data processing and computer performance will solve this problem.

5 Conclusion

We were able to visualize a commercially available instrument for cardiovascular intervention in an MPI setting using luminal loading with Resovist. This is a first step towards cardiovascular intervention using MPI. For an encompassing intervention procedure using MPI, visualization of several other instruments is mandatory. Furthermore, instruments have to be delineable from the intravascular tracer. Real-time reconstruction of the images is another crucial point that needs to be realized as well.

Acknowledgement. The authors acknowledge funding by the German Federal Ministry of Education and Research (BMBF) under the grant numbers FKZ 13N9079, FKZ 13N11086 and FKZ 13N11090 and the State Schleswig-Holstein (Program for the Future-Economy: 122-10-004).

References

1. Gleich, B., Weizenecker, J.: Tomographic imaging using the nonlinear response of magnetic particles. Nature 435, 1214–1217 (2005)
2. Rahmer, J., et al.: Rapid 3D in vivo Magnetic Particle Imaging with a Large Field of View. In: 19th Annual Meeting International Society for Magnetic Resonance in Medicine, Montreal, p. 3285 (2011)
3. Weizenecker, J., Borgert, J., Gleich, B.: A simulation study on the resolution and sensitivity of magnetic particle imaging. Physics in Medicine and Biology 52(21), 6363–6374 (2007)

Efficient Encoding Methods for Small Numbers of Pixels to Achieve High Sensitivity for Screening

John B. Weaver

Department of Radiology, Dartmouth College, One Medical Center Drive
Lebanon, NH, 03756, USA
john.b.weaver@dartmouth.edu

Abstract. Screening for early ovarian cancer is critical because it would increase survival dramatically. Ovarian cancer is cured at very high rates when found early but is almost never found until it has metastasized and the survival rate is very low. Ovarian cancer screening might be possible using immunologically targeted magnetic nanoparticles (mNP). mNP injected into the peritoneum are delivered to the cancer by phagocytic cells using the bodies own immune system. Magnetic detection of the mNP does not require ionizing radiation and can be made at low mNP concentrations. Screening only requires the number of nanoparticles in each ovary so minimal localization is required: only two pixels. We present simulation results showing that spatial encoding for two pixels can be achieved using many sets of harmonics ranging from only two harmonics to essentially all the harmonics. However, the highest SNR measurements are achieved using only two harmonics that approximate a wavelet basis.

1 Introduction

Magnetic detection of immunologically targeted magnetic nanoparticles (mNP) has demonstrated promise for early detection of ovarian cancer in a mouse model [1-3]. Early detection of ovarian is critical because it would increase survival dramatically. When found early, ovarian cancer is cured at very high rates. However, ovarian cancer is rarely found until it has metastasized and the survival rate at that time is very low. Immunologically targeting has two elements: 1) the immune system gathers the mNP and 2) immune signaling collects the mNPs in the cancer. The mNPs were injected into the peritoneum where they were delivered to the cancer by the immune system. The phagocytes avidly collect all objects in the 10nm to 200nm size range including mNPs because objects of that size include viruses and cellular debris. Cytokine and chemokine signaling then draws the phagocytes with their mNP payload to the cancer.

T.M. Buzug and J. Borgert (Eds.): Magnetic Particle Imaging, SPPHY 140, pp. 217–221.
springerlink.com

Magnetic detection of the mNP is a very sensitive method that does not require ionizing radiation. In the context of ovarian cancer screening, magnetic detection only requires the number of nanoparticles in each ovary so minimal localization of only two pixels is required.

The combination of immunological targeting and magnetic detection allowed us to detect lesions in a mouse model while they were still microscopic and effectively treated [1-3].

The previous results on mice used a small pickup coil to limit the signal detected to one ovary or the other. Pickup coil localization is sufficient for mouse work and probably for screening smaller patients where the coil can be placed relatively close to the ovaries. However, for the general population screened alternatives might be required.

This paper presents simulation results demonstrating that localization to the ovary is possible with a relatively small magnetic field gradient and a single measurement of multiple harmonics.

2 Material and Methods

We used a Langevin function to estimate the magnetization assuming relatively low frequency steady state magnetization resulting from relatively fast relaxation. We assumed the combination of a static gradient field and a spatially uniform field that is sinusoidal in time. The maximum amplitude of both fields was varied between 1mT and 50mT in all integer combinations. Single measurements of multiple harmonics were used to estimate the number of nanoparticles at both pixels; i.e. at both values of the gradient field. The physical constants appropriate for 80nm iron oxide nanoparticles were used. The response matrix was the signal from each pixel at each harmonic used. The condition number of the response matrix was used to estimate the stability of the reconstruction. The signal was estimated at each harmonic and the noise was assumed to be proportional to the number of harmonics included. The SNR was the product of the signal and the inverse condition number divided by the number of harmonics employed. The energy norm was used.

3 Results

The signal to noise ratio (SNR) achieved by different combinations of harmonics is provided in Table 1. The magnitudes of the gradient and the sinusoidal fields where the maximum SNR was achieved are also provided. The maximum sinusoidal field, or nearly the maximum, always achieves the best SNR. However, the gradient required is higher for fewer harmonics than for many harmonics.

Table 1. The maximum SNR acheived using each set of harmonics (last column). The amplitude of the gradient field and sinusoidal fields where the maximum SNR was achieved are columns two and three.

Harmonics,	Grad Amp,	Sinusoidal Amp,	Max SNR
1 - 63	10.3	60.0	0.0752
1 - 7	23.0	60.0	0.1318
1 - 2	**30.5**	**60.0**	**0.1825**
2 - 63	4.2	60.0	0.0720
2 - 7	55.3	58.6	0.1415
2 - 3	**47.3**	**58.1**	**0.2097**
3 - 63	4.2	60.0	0.0733
3 - 7	56.7	60.0	0.1219
3 - 4	**54.4**	**60.0**	**0.2050**
4 - 63	26.7	59.5	0.0708
4 - 7	57.7	60.0	0.1527
4 - 5	**56.7**	**60.0**	**0.1887**

The underlined combinations are examples of wavelet-like bases with one even and one odd harmonic. The wavelet-like bases consistently achieved the highest SNRs.

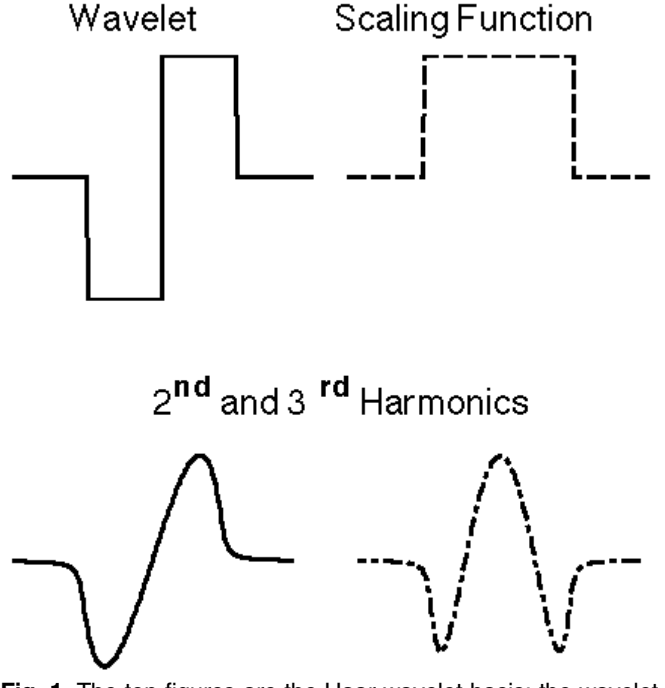

Fig. 1. The top figures are the Haar wavelet basis: the wavelet and the scaling function. The bottom figures show the second and third harmonics as a function of static field (the axis spans -50mT to 50mT for 80nm iron oxide nanoparticles). The similarity between the even harmonic (2^{nd}) and the wavelet is clear. There is also clear similarity between the odd harmonic (3^{rd}) and the scaling function. A wavelet like reconstruction can be achieved by scaling and translating these basic functions [4,5].

4 Discussion

The use of just two harmonics is reasonable: The reconstruction mimics a lower order wavelet transform as described previously [4,5] and, therefore, produces stable solutions. The even harmonics are analogous to the wavelet function and the odd harmonics are analogous to the scaling function. For only two pixels the Haar transform is achieved by measuring the sum of the signal from the two pixels and the difference in signal between the two pixels. That is nearly achieved using adjacent harmonics. The signal is high for lower harmonics and the noise is minimized by minimizing the bandwidth sampled. This framework does not attempt to include the sequential measurements with different applied field gradient fields. The highest sensitivity was always achieved using the largest amplitude sinusoidal field but not the largest gradient field.

NPs off the two positions for which the transform is defined will alias the solution because the basis will become very different from the wavelet basis used to reconstruct mNPs at the proper position. This phenomenon might not be a significant problem for ovarian screening because the ovaries positions are relatively discrete. However, for more general applications, this phenomenon might suggest multiple measurements with different gradient fields to minimize or eliminate this aliasing.

5 Conclusion

The simulations of the magnetization are valid for low frequencies and fast relaxation and they show that two-pixel localization can be achieved from a single measurement of the magnetization at multiple harmonic frequencies. Sensitivity is critical so the SNR achieved is the critical metric of any localization scheme. However, lower magnetic field gradients are also important to minimize cost so the method can be used in a screening environment. Wavelet-like imaging is superior for two-point localization in terms of a) optimal SNR achieved, and b) minimizing the gradient field required. The wavelet-like encoding methods allow significantly lower gradient amplitudes with the same SNR.

References

1. Weaver, J.B.: Magnetic Nanoparticle Biomarkers in Thermal Therapy and Screening. In: Annual Meeting of American Association of Physicists in Medicine (AAPM) TH-E-214-5; Medical Physics 38(6), 3872 (2011) (abstract, invited Presentation)
2. Weaver, J.B.: The Use of Magnetic Nanoparticles in Thermal Therapy Monitoring and Screening. Magnetism and Magnetic Materials Conference; Journal of Applied Physics FA-05 (2011) (abstract, invited Presentation)

3. Weaver, J.B., Scarlett, U.K., Rauwerdink, A.M., Fiering, S.N., Conejo-Garcia, J.R.: Potential Ovarian Cancer Screening Method: Immunologically Targeted Nanoparticles Detected with Magnetic Spectroscopy of Nanoparticle Brownian Motion. In: RSNA 2011, 11034641, LL-PHS-TU7B (2011)
4. Weaver, J.B.: Alternative Methods of Imaging Magnetic Nanoparticles. DOD Breast Cancer Research Program Era of Hope Meeting P44-12-35, 2642 (2008)
5. Weaver, J.B., Rauwerdink, A.M.: An Alternative Spatial Encoding Method for Magnetic Nanoparticle Imaging. In: American Association of Physicists in Medicine (AAPM) SU-EE-A4-5, 35-8484-19379-655 (2008)

Magnetic Particle Imaging

Influence of Magnetic Field Optimization on Image Quality Achieved for Efficient Radon-Based Reconstruction in Field Free Line Imaging in MPI

Marlitt Erbe, Tobias Knopp, Timo F. Sattel, and Thorsten M. Buzug

Institute of Medical Engineering, University of Lübeck,
Ratzeburger Allee 160, 23562 Lübeck, Germany
{erbe,buzug}@imt.uni-luebeck.de

Abstract. The use of a field free line in magnetic particle imaging promises a considerable increase in sensitivity of this new imaging technique. Furthermore, efficient reconstruction algorithms emerge for line acquisition in MPI, since it is possible to transform the data into Radon space. This allows for the use of well-known and powerful reconstruction algorithms like for instance the filtered backprojection, which will substantially speed up reconstruction time. In this work, a simulation study is presented, which analyzes the influence of magnetic field optimization on the image quality achieved for efficient Radon-based reconstruction.

1 Introduction

By means of the novel tomographic imaging method magnetic particle imaging (MPI) [1] real-time three dimensional highly resolved imaging of the artery of a patient will be possible without harmful radiation. Conventionally, MPI is a sensitive spot method. The field of view (FOV) is scanned with a field free point (FFP), at which iron-oxide nanoparticles, used as tracer, produce a measurable signal and can therefore be spatially resolved.

The concept of MPI data acquisition along a field free line (FFL) has recently been introduced [2] and promises an increase in sensitivity by one order of magnitude. Since that first introduction substantial achievements in optimizing the scanner geometry used to generate the required fields have been made [3, 4]. With respect to that, a FFL field demonstrator was implemented and tested [5]. Furthermore, it was shown that efficient Radon-based reconstruction algorithms may be used to considerably speed up reconstruction time [6]. This is of special importance for applications

T.M. Buzug and J. Borgert (Eds.): Magnetic Particle Imaging, SPPHY 140, pp. 225–229.
springerlink.com

requiring online reconstruction. However, this was only shown for a very small FOV compared to the bore of the scanner. It was not yet analyzed how the image quality is influenced by the use of efficient Radon-based reconstruction for larger FOVs. Furthermore, an optimized FFL scanning device, which provides a considerable enhancement in FFL homogeneity as well as very low electrical power consumption has been introduced [7]. It was not yet examined, however, how the increase in FFL homogeneity influences the image quality achieved using efficient Radon-based reconstruction algorithms. Therefore, a simulation study is presented in this work, which shows results for a phantom covering a large region of the scanner bore diameter where at the same time the optimized design is compared to the conventional design used in [6].

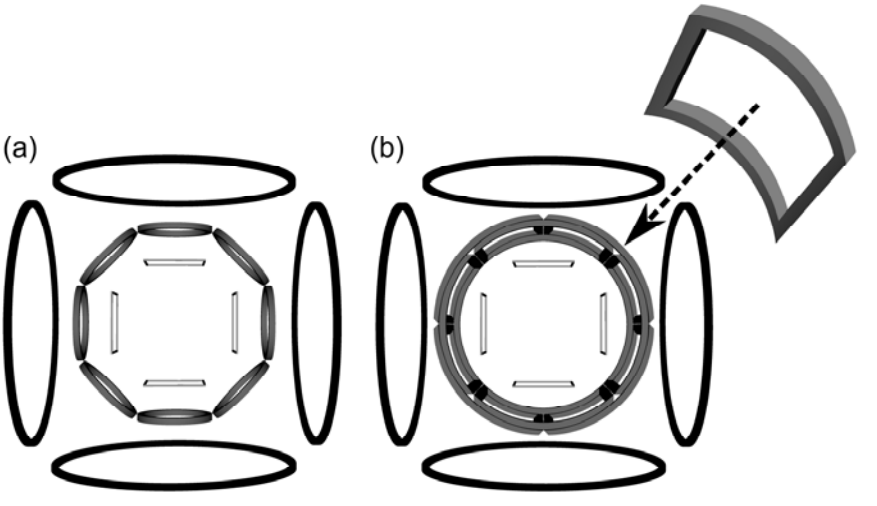

Fig. 1. Scanner geometries used for the simulation study. (a) shows the conventional MPI scanner consisting of a ring of 4 coil pairs. In (b) an optimized scanning device of curved rectangular coils is illustrated.

2 Material and Methods

A simulation study is performed covering the whole MPI process for two different scanner geometries, which are illustrated in **Fig. 1**. The scanner design shown in (a) was used for the first simulation study on efficient reconstruction in FFL imaging in MPI [6] and was therefore chosen as ground truth. The design illustrated in (b) has recently been introduced and promises a decrease in electrical power loss up to a factor of 4 while concurrently increasing the FFL field homogeneity by a factor of almost 5 [7].

Here, curved rectangular coils are used for the generation of the selection field. Both geometries have a bore diameter of 40 mm and will therefore accommodate a mouse even if receive coils including mountings are placed inside of the bore. The gradient of the selection field perpendicular to the FFL is chosen to be 2.5 $Tm^{-1}\mu_0^{-1}$. The trajectory of the FFL is realized at 80 discrete FFL angles by a drive field with an amplitude of 20 mT. The phantom is illustrated in **Fig. 2** and covers a region of 10.4 x 10.4 mm^2. The reconstruction is performed on a field of view of 14 x 14 mm^2. As a comparison, in [6] a phantom of the same size was used for reconstruction with a scanner of a bore diameter of 30 cm. Hence, the current results represent reconstruction on a much larger FOV compared to the bore diameter of the scanner.

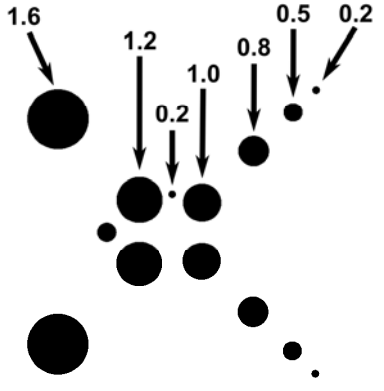

Fig. 2. Phantom used for the simulation study. All specifications are given in mm.

3 Results

The resulting images illustrated in **Fig. 3** show a resolution of about 0.5 mm for both tested scanner geometries. The smallest dots of the phantom with a size of 0.2 mm are nearly not visible. Since dots of the same size were slightly better resolved in [6] this is an effect arising due to the larger ratio of FOV size and bore diameter of the scanner. Still, the results show that efficient Radon-based reconstruction can be used even for large FOV sizes.

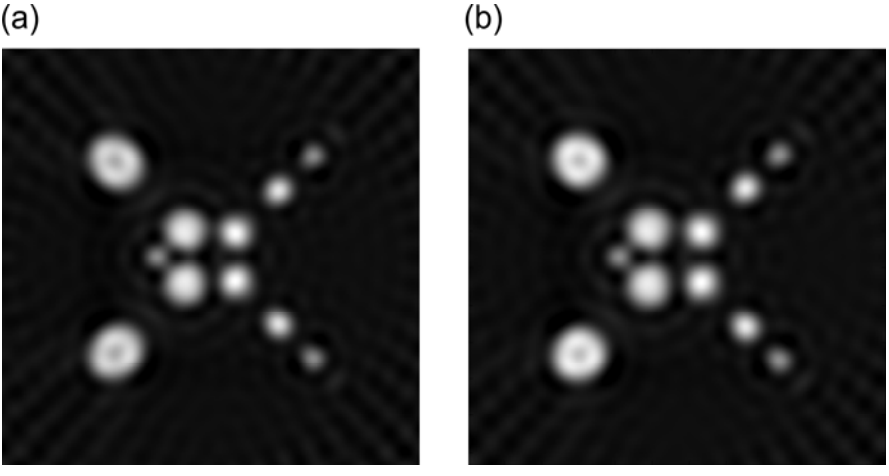

Fig. 3. Reconstructed images for the two different scanner geometries and a FOV size of 14 x 14 mm^2. (a) shows the result for the conventional design of a ring of coils, whereas (b) illustrates the result for the optimized design of curved rectangular coils. It is clearly visible that for the conventional design the outer points are egg-shaped, while for the optimized design they stay almost circle-shaped due to the enhanced magnetic field quality.

The comparison of the two images, resulting from the two different scanner designs introduced in **Fig. 1,** only shows significant differences for the 1.6 mm dots as well as for the 0.5 mm dots, which have the largest distance to the center of the FOV. In **Fig. 3** (a) the result for the conventional design is pictured. The outer dots are clearly egg-shaped, which results from a decreasing homogeneity of the field along the FFL as well as parallel to its alignment when approaching the scanner setup. The results from the design, where curved rectangular coils were used for selection field generation, show only very little deformation of the outer coils. Hence, the enhancement of magnetic field quality is visible in the achieved image quality using efficient Radon-based reconstruction.

4 Discussion

The presented results constitute a first step on the way towards optimized FFL imaging for large FOV sizes and short reconstruction times due to the use of efficient reconstruction algorithms. However, a more detailed simulation study including different phantom sizes and shapes as well as an optimized drive field generator design is needed to further analyze the possibilities arising from this alternative data acquisition scheme. The origin and nature of the artifacts occurring for the conventional design and in a less intensive manner also for the optimized design need to be analyzed in more detail to further optimize the imaging process.

Furthermore, implementation of the curved rectangular coils is of crucial importance, since it needs to be shown that the simulated image quality can be achieved in an implemented FFL scanning device. First implementation results have shown, however, that no large field deviations occur for the use of curved rectangular coils due to an optimized implementation process. A FFL scanner of this optimized design is currently implemented.

5 Conclusion

It has been shown that the use of efficient Radon-based reconstruction is possible for FFL imaging in MPI even for FOV sizes, which cover a large area of the bore diameter of the scanner. Enlarging the FOV size while simultaneously decreasing reconstruction time is of great importance for many applications addressed by MPI. Furthermore, the influence of magnetic field quality optimization on image quality achieved for FFL imaging and efficient Radon-based reconstruction in MPI was analyzed. The optimized design of curved rectangular coils does not only lead to a considerably reduced electrical power loss but does moreover outperform the conventional design in achieved image quality.

References

1. Gleich, B., Weizenecker, J.: Tomographic imaging using the nonlinear response of magnetic particles. Nature 435, 1214–1217 (2005)
2. Weizenecker, J., Gleich, B., Borgert, J.: Magnetic particle imaging using a field free line. J. Phys. D Appl. Phys. 41
3. Knopp, T., Sattel, T.F., Biederer, S., Buzug, T.M.: Field-free line formation in a magnetic field. Journal of Physics A: Mathematical and Theoretical 43(1), 012002 (2010)
4. Knopp, T., Erbe, M., Biederer, S., Sattel, T.F., Buzug, T.M.: Efficient generation of a magnetic field-free line. Medical Physics 37(7), 3538–3540 (2010)
5. Knopp, T., Erbe, M., Sattel, T.F., Biederer, S., Buzug, T.M.: A Fourier slice theorem for magnetic particle imaging using a field-free line. Inverse Problems 27, 095004 (2011)
6. Erbe, M., Knopp, T., Sattel, T.F., Biederer, S., Buzug, T.M.: Experimental generation of an arbitrarily rotated field-free line for the use in magnetic particle imaging. Medical Physics 38(9), 5200–5207 (2011)
7. Erbe, M., Sattel, T.F., Knopp, T., Biederer, S., Buzug, T.M.: An optimized field free line scanning device for magnetic particle imaging. Biomed. Tech. 56(suppl.) (2011), doi:10.1515/BMT.2011.298

Slicing Frequency Mixed Traveling Wave for 3D Magnetic Particle Imaging

P. Vogel[1,2], M.A. Rückert[1,2], P. Klauer[1,2], W.H. Kullmann[2], P.M. Jakob[1,3], and V.C. Behr[1]

[1] Department of Experimental Physics 5 (Biophysics), University of Würzburg, Am Hubland, D-97074 Würzburg, Germany
[2] Electrical Engineering, University of Applied Sciences Würzburg-Schweinfurt, Ignaz-Schön-Str. 11, D-97421 Schweinfurt, Germany
[3] Research Center Magnetic Resonance Bavaria (MRB) e.V., Am Hubland, D-97074 Würzburg, Germany
Patrick.Vogel@physik.uni-wuerzburg.de,
Martin.Rueckert@physik.uni-wuerzburg.de,
Peter.Klauer@physik.uni-wuerzburg.de,
Walter.Kullmann@fhws.de,
PeJa@physik.uni-wuerzburg.de,
Behr@physik.uni-wuerzburg.de

Abstract. Magnetic **P**article **I**maging is based on the nonlinear response of ferro- and superparamagnetic particles to magnetic fields [1]. For imaging, a field free point (FFP) within a string magnetic gradient on the order of 1–5 T/m is moved through the sample. A new gradient system design allows performing dynamic imaging in a linear sampling scheme by using a traveling wave approach [2]. We present an extension for doing 3D imaging using a traveling wave in combination with frequency mixing [3] and a sliced field of view (FoV). This approach provides the possibility of an arbitrarily large FoV in one direction without increasing the specific absorption rate (SAR) and allows the spatial encoding in the additional 2 dimensions.

1 Introduction

Magnetic Particle Imaging is a tomographic method for the quantitative determination of spatial distributions of superparamagnetic iron-oxide nanoparticles (SPIO). Recently high resolution real time imaging of a beating mouse heart was presented [1][4]. Since the introduction of the method in 2005 by B. Gleich and J. Weizenecker several different types of scanners have been developed [4][5][6]. But a significant issue of these approaches is the usage of permanent magnets for creating the required strong gradient strength of about 3–5 T/m. Because of the static generation of the magnetic field, it is difficult to scan a large field of view (FoV). The problem

T.M. Buzug and J. Borgert (Eds.): Magnetic Particle Imaging, SPPHY 140, pp. 231–235.
springerlink.com

is the required high magnetic field (drive-field) to move the field free point (FFP) away from the center of scanner. For a ten times higher FoV the necessary receiver bandwidth increases ten times and the energy increase even hundred times for a given acquisition time. Thus the specific absorption rate (SAR) rises with the increasing FoV enormously [6]. Respecting the maximum allowed SAR for in-vivo measurement [7] the FoV for a static permanent scanner type is limited to approximately 16x32x32 mm^3 for humans [6]. For mice a factor of about 5 is possible but the required energy increases dramatically [7]. In 2011 we presented a new approach to generate the strong magnetic field gradient in a more effective way, the dynamic linear gradient array (dLGA) [2]. With the traveling wave concept the FFP can move fast in a linear way over the sample. The FoV of the dLGA can be arbitrarily increased in one dimension without increasing the SAR. Based on this 1D concept an extension was presented to perform 2D acquisitions with a slice size of about 20x60 mm^2 and a thickness of about 2–3 mm with an orthogonal frequency mixing technique [8]. For 3D acquisitions the whole 2D slice is being moved step by step linear through the volume of interest. This results in a sliced 3D image with a FoV of about 60x20x20 mm^3 without the complexity of 3D reconstruction.

2 Material and Methods

Hardware:
The dLGA requires no permanent magnets and also replaces the drive coils for one direction. It is a modular array of 16 consecutive coils for generating two FFPs dynamically, one with a positive and one with a negative gradient slew (gradient strength: z-axis: 3.5 T/m, x and y-axis: 1.75 T/m, 1.6 kW) [2]. The FFPs travel in the z-direction by applying a sinusoidal current at a frequency of f_1=1 kHz with an increasing phase shift to adjacent coils, this concept was named “traveling wave” (see fig. 1A). The full length of the dLGA is 144 mm. The effective FoV is 80 mm and the used FoV is 60 mm (the used FoV should be smaller than the half of the dLGA, because only one FFP should stay in the FoV at the same time) [2]. The coil pair for the second encoding direction (x-axis) is oriented orthogonally to the dLGA. It is designed in a saddle-coil configuration to use the space within the receiving coil array more efficiently. The saddle coil is driven at a higher frequency of f_2=16,5 kHz. Therefore the FFPs travel now not only along the z-axis but on a sinusoidal way on a x-z-plane (see fig. 1B). The field strength of 10-15 mT at 200 W is sufficient to move the traveling FFPs about 6 mm out of the symmetry axis. The higher frequency mixes the MPI signal to the sidebands of the higher harmonics of f_2 (frequency mixing [3]). The result is a higher induction in receiver coils but also a wider bandwidth [7].

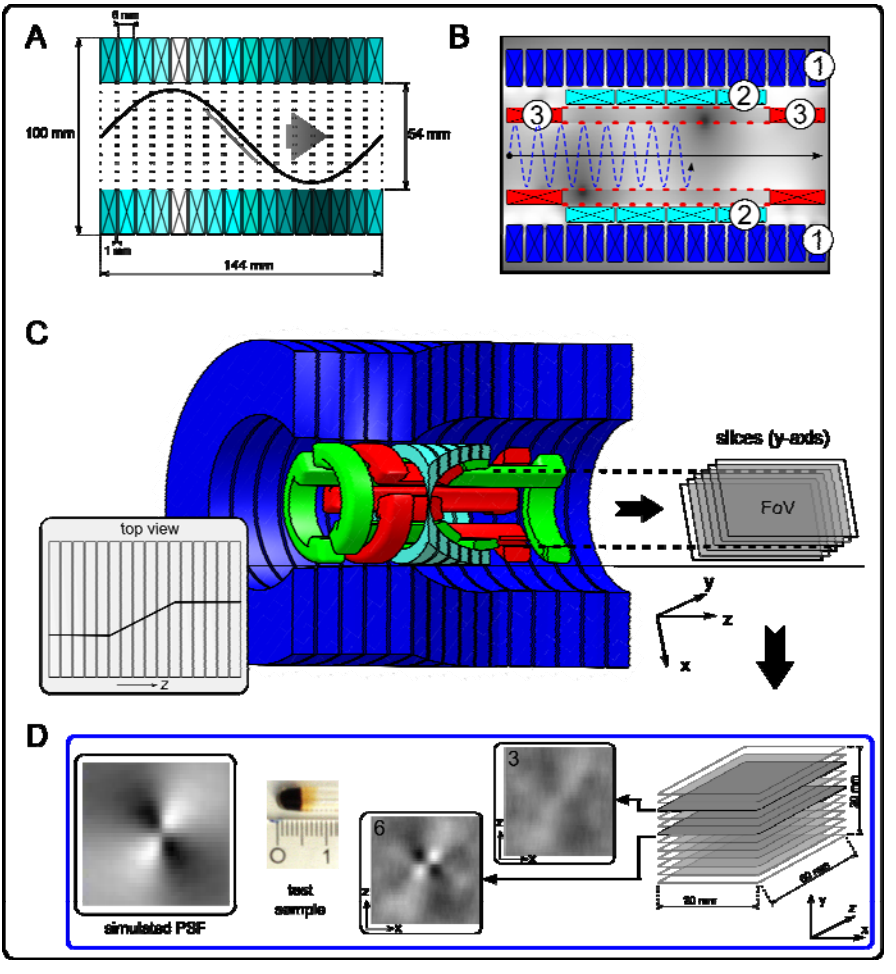

Fig. 1. ***A***: Sketch of the dynamic Linear Gradient Array (dLGA). The 16 elements were driven by a sinusoidal current with an increasing phase shift for consecutive coils (***traveling wave concept***). ***B***: 2D-scanner design: ***blue*** (1): dLGA for generating the two traveling FFPs (1D), ***cyan*** (2): receiving coils array parallel to the dLGA, ***red*** (3): saddle coil for 2D encoding. The two generated FFPs (dark regions) travel along blue dashed path. ***C***: Profile section of the 3D-MPI-scanner. An additional saddle coil (***green***), orthogonal to the first, moves the 2D plane linear along the y-axis and cuts the 3D volume in slices. ***D***: ***left***: simulated PSF, ***right***: a 3D Resovist© test sample shows a different signal in all slices.

A second coil pair oriented orthogonally to the first pair and to the dLGA allows the encoding of the third dimension by shifting the 2D FoV slices step by step. The field strength of the second coil pair is 10–15 mT (200 W) and can move the 2D imaging plane along the y-axis (see fig. 1C).

All coils are driven using common audio amplifiers (TSA4-700 and TA2400 MK-X, t.amp).

The receiving array consists of six separated coils, 140 windings of HF-litz wire (24x0,04 mm) each. The resistance of one coil is about 8 Ω. The resonance frequency of each coil segment is about f=460 kHz. For the first tests all receiving coils were connected in parallel mode. Thereby the eigen resonance frequency of the paralleled receiving array doesn't change. To suppress the excitation frequencies f_1 and f_2 a signal filter (Chebychev high-pass) were used.

Signal processing and image reconstruction:
Prior to reconstruction the signal should be preprocessed. In the first step the characteristics of each receiving channel must be corrected (amplitude and phase correction). In a second step the spectrum is filtered. To obtain a 2D image, the 1D signal is arranged point per point on a two dimensional plane, f_1 in z-axis and f_2 in x-axis each from 0 to 2π. The result is an image with a fourfold signal. The orthogonal frequency mixing provides one type of 2D-PSF [9] (see fig. 1 D). Because of the linearity of the system it is possible to do a 2D deconvolution of the corrected dataset to reconstruct the images.

3 Results

In preliminary tests the simulation results of the 2D point spread function (PSF) were confirmed (see fig. 1D). The measured PSFs were required for the reconstruction of complex samples by a 2D deconvolution. For one slice the acquisition time is 2 ms for the two frequencies f_1=1 kHz and f_2=16,5 kHz (least common multiple is $2xf_2$). That means the FFP travels two times over the sample with a different phase. For a 3D volume there were take 13 slices (see fig. 1D), each with spatial distance of about 1 mm. Thus a whole 3D volume can be imaged in 26 ms. In addition, the spatial resolution for Resovist© was determined to be less than 2 mm in z-direction and less than 3 mm in x- and y-direction.

4 Discussion

The dLGA is a novel type of MPI scanner. With the linear approach the complexity of the MPI signal can be simplified. Instead of the complex 2D/3D lissajous trajectory here exists only a 2D sinusoidal trajectory in one direction. The result is a nearly linear way of the FFPs over the 2D plane. A linear sampling scheme could allow to probe for anisotropic effects and relaxivity effects of the sample and the tracers.

5 Conclusion

The traveling wave approach provides the possibility to increase the FoV along the symmetry axis (z-axis) without increasing the acquisition time while keeping the specific absorption rate constant. The frequency mixing technique for the 2D encoding increases the SNR by reducing the fractional bandwidth and shifting the signal to higher frequencies. The acquisition time for one slice depends on the least common multiple of the two used frequencies (in this case 2 ms per slice). Hence it is possible to acquire a full 3D volume of 13 slices in only 26 ms. The resulting FoV is about 60x20x20 mm^3.

References

1. Gleich, B., Weizenecker, J.: Tomographic imaging using the nonlinear response of magnetic particles. Nature 435, 1214–1217 (2005)
2. Klauer, P., et al.: Magnetic Particle Imaging: Linear Gradient Array for Imaging with a Traveling Wave. In: Proc. ISMRM 2011 Abstract, 3783 (2011)
3. Krause, H.J.: Magnetic particle detection by frequency mixing of immunoassay applications. JMMM 311, 436–444 (2007)
4. Weizenecker, J., et al.: Three-dimensional real-time in vivo magnetic particle imaging. Phys. Med. Biol. 54, L1–L10 (2009)
5. Goodwill, P.W., et al.: Narrowband magnetic particle imaging. IEEE Trans. Med. Imag. 28(8), 1231–1237 (2009)
6. Schmale, I., et al.: First phantom and in vivo MPI images with an extended field of view. SPIE Medical Imaging, Pre-Print Version of Paper 7965-7935 (2011)
7. Goodwill, P.W., Concolly, S.M.: The x-space Formulation of the Magnetic Particle Imaging Process: 1-D Signal, Resolution, Bandwidth, SNR, SAR, and Magnetostimulation. IEEE Trans. Med. Imaging 29, 1851 (2010)
8. Vogel, P., et al.: Frequency Mixed Traveling Wave for 2D Magnetic Particle Imaging. In: Proc. ICMRM 2011 talk (2011)
9. Goodwill, P.W., Conolly, S.M.: Multi-Dimensional X-Space Magnetic Particle Imaging. IEEE Trans. Med. Imaging 30, 1581 (2011)

Magnetic-Particle-Imaging for Sentinel Lymph Node Biopsy in Breast Cancer

Ksenija Gräfe[1], Timo F. Sattel[1], Kerstin Lüdtke-Buzug[1], Dominique Finas[2], Jörn Borgert[3], and Thorsten M. Buzug[1]

[1] Institute of Medical Engineering, University of Lübeck, Ratzeburger Allee 160
Lübeck, 23562, Germany
graefe@imt.uni-luebeck.de, buzug@imt.uni-luebeck.de
[2] Department of Obstetrics and Gynacology, University of Lübeck,
Ratzeburger Allee 160
Lübeck, 235382, Germany
[3] Phillips Technologie GmbH, Innovative Technologies, Research Laboratories,
Röntgenstraße 24-26
Hamburg, 22335, Germany

Abstract. Magnetic Particle Imaging (MPI) is a very recent medical imaging technique providing tomographic data avoiding use of ionizing radiation. The first MPI scanner presented by Gleich and Weizenecker has a closed geometry which has to fit the object of interest [1]. In order to be able to examine larger objects, Sattel et al. developed a new coil configuration, the single-sided MPI scanner geometry [2]. The detection of axillary sentinel lymph nodes is one medical application scenario. MPI improves the surgical procedure by real-time 3D image guidance and may contribute towards reducing cost and the time needs per patient. This contribution presents improvements of various coil topologies. Furthermore, the cooling system is optimized and the send and receive chain will be improved.

1 Introduction

The first MPI scanner had a symmetric assembly and was presented by Gleich and Weizenecker [1] in 2005. The coil arrangement has the drawback that the object of interest has to be small enough to fit inside the assembly. The single-sided MPI scanner presented by Sattel et al. [2] overcomes this limitation. This scanner is composed of two circular coils, which are arranged concentrically. MPI in general is based on super-paramagnetic iron oxide nanoparticles (SPIONs) as tracer material exploiting their nonlinear magnetization behavior in the imaging process.

The sentinel lymph node biopsy (SLNB) is a medical application scenario of MPI. It is a method to find out if the cancer has accumulated

T.M. Buzug and J. Borgert (Eds.): Magnetic Particle Imaging, SPPHY 140, pp. 237–241.
springerlink.com

metastases in lymph nodes. For this it is necessary to dissect the tracer enriched sentinel lymph node for histologic examination. Today, surgical guidance strategies are commonly used based on scintigraphy or blue dye injection. Scintigraphy, which employs a radioactive tracer, achieves a better localization of sentinel lymph nodes than blue dye injection. However, the great disadvantage in the use of radioactive material is that it results in costly disposal and places surgical staff at risk. MPI achieves good localization without the use of radioactivity. MPI provides in situ real-time images that are visible through the position changes. The scintigraphy is a rigid and only two dimensional image of axillary region. The tracer is injected into the breast tumor region and via the lymphatic system the tracer first reaches the sentinel lymph node. A radioactive tracer can be located by using a Geiger-Müller counter. In the MPI scenario the SPIONs, which accumulate in the sentinel lymph node, will be detected and accurately located by the MPI scanner.

The first single-sided MPI scanner has been built at the Institute of Medical Engineering at the University of Lübeck [2]. The following is a presentation of improvements made to coil topologies. It will be outlined how the send and receive chain have been improved and how the cooling system had been optimized.

2 Material and Methods

The geometry of the original 1D single-sided scanner is shown in figure 1a. The two coils are supplied with direct current in opposite direction. In addition, the inner coil is supplied with alternating current to drive the FFP.

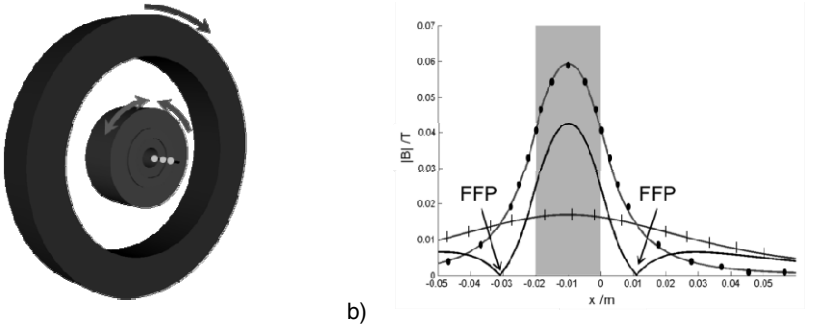

Fig. 1. 1D single-sided scanner (a) and the magnetic fields (b) [2].

The dotted line in figure 1b shows the shape of the magnetic field which is generated by the inner coil and the dashed line shows the magnetic field generated by the outer coil. The gray background illustrates the position of the scanner assembly. The magnetic fields cancel each other out in two points, one in front of the scanner and one in the back. In these field free

points (FFP), the static magnetic field is zero. An FFP is important for the imaging process and can be moved by the alternating current on the inner coil. The nonlinear magnetization curve of the SPIONs causes a responding signal that contains not only the excitation frequency but also its harmonics (figure 2a). The signal is picked up by the receive coil in front of the inner coil and is required for the imaging process. The important point is that only the SPIONs in direct neighborhood to the FFP contribute to the receive signal. The reason is that saturation effects occur even at low field strength. If the SPIONs are in saturation almost no signal is induced (figure 2b).

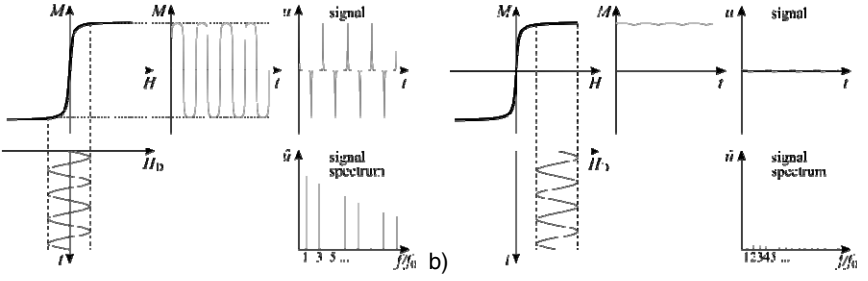

Fig. 2. Particle response to an external magnetic field [1].

For multidimensional imaging, the Lissajous trajectory is applied to scan the field of view (FOV). The trajectory describes the path $\psi(t)$, which the FFP follows. This trajectory is generated from overlaid sinusoidal excitations fields and is defined by

$$H(\psi(t),t) = 0, \qquad t \in [0.T)$$

By changing the excitation frequency, it is possible to determine the period length and the trajectory density. It is necessary to suppress all higher harmonics in the transmit signals to avoid the overlap of the particle response by the sending signal. For this purpose, a third order analog filter is used. For 3D imaging, for every spatial direction a separate excitation frequency is essential and for this reason it is necessary to used three different filters, one for each channel.

3 Results

In figure 3, the simulation results of the trajectories with different coil geometries are shown. In order to achieve a 2D trajectory, the original flat two-coil geometry for 1D imaging is extended by additional coils. In the first case, two circular coils are tilted by 45 degrees from the main scanner axis. The resulting FOV is diamond-shaped. In the next simulation the 1D scanner is extended by one rectangular coil, which in part is located in the inner coil. The diamond-shaped FOV is wider than the first. The third

assembly is extended by one D-shaped coil which is orientated perpendicularly to the gradient coils. The simulation shows a rectangular FOV. Similar results are achieved by the fourth setup. Here, two D-shaped coils are added directly under the circular coils preserving the flat coil design.

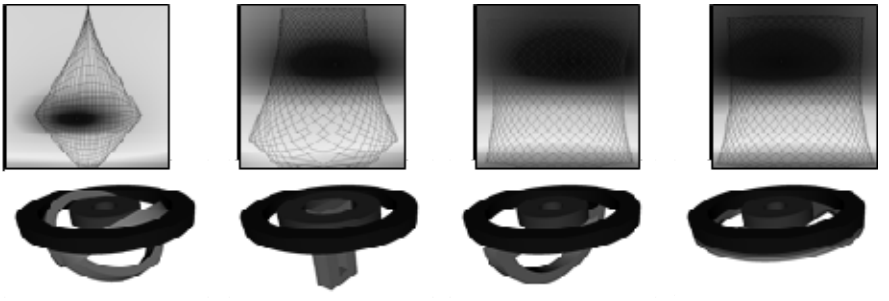

Fig. 3. Simulation results of different coil geometries for a 2D single-sided scanner [3].

To obtain a pure excitation signal, it will be first filtered with a band-pass filter (BPF). In figure 4, the transfer functions of the different BPFs are shown. They differ by the center frequency, which is chosen to be the transmit frequency of the corresponding transmit channel. They are designed to pass the signal at the base frequency but to suppress higher order harmonics. Since the third harmonic distortion is most prominent, it is desirable to achieve a high damping at this particular frequency. Accordingly, BPF 25.252 kHz achieves a damping of 86 dB at a frequency of 74.8 kHz. At 76.5 kHz, BPF 26.042 kHz results in a damping of 86 dB, and the damping of BPF 26.882 kHz at 79.8 kHz is 89 dB. All three filters have the minimal damping of 0.5 dB around 25 kHz.

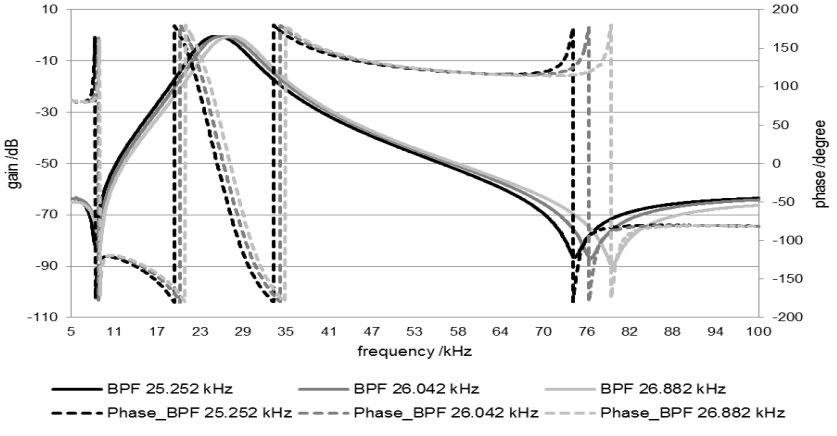

Fig. 4. Transfer function (gain and phase) of the different BPFs.

4 Discussion

The best scanner geometry for 2D and 3D MPI is archived by positioning two pairs of D-shaped coils under the circular coils, which are rotated by 90 degrees. The FOV resembles a rectangle. A further advantage is that the power losses are low [3]. The application scenario puts higher demands on the cooling system as compared to the experimental setup in [2].

The BPF have been refined, so the excitation signal contains only the main frequency. At the excitation frequency - around 25 kHz - the damping is very subtle and especially at the frequency of the third harmonic, near 75 kHz, the signal will be attenuated by 87 dB. The result of these filters is that the harmonics caused by the transmit chain are small and do not overlay the particle response.

5 Outlook

After improving the cooling system and the frequency tuning, functional tests may soon be accomplished. The next steps are the acquisition of a system matrix required for image reconstruction and the performance of phantom measurements.

References

1. Gleich, B., Weizenecker, J.: Tomographic imaging using the nonlinear response of magnetic particles. Nature 435, 1214–1217 (2005)
2. Sattel, T., Knopp, T., Biederer, S., Gleich, B., Weizenecker, J., Borgert, J., Buzug, T.M.: Single-sided device for magnetic particle imaging. Journal of Physics D: Applied Physics 42(2), 1–5 (2009)
3. Sattel, T.F., Biederer, S., Knopp, T., Buzug, T.M.: Magnetic Field Generation for Multi-Dimensional Single-Sided Magentic Particle Imaging. In: Proceedings of the Inetrnetional Society for Magnetic Resonance in Medicine, Mai, Stockholm,18, p. 3297 (2010)

Experimental 3D X-Space Magnetic Particle Imaging Using Projection Reconstruction

Justin Konkle[1], Patrick Goodwill[1], Oscar Carrasco-Zevallos[1], and Steven Conolly[1,2]

[1] Department of Bioengineering & [2] EECS, University of California, Berkeley, 340 Hearst Memorial Mining Building # 1762 Berkeley, CA 94720-1762, USA
jkonkle@berkeley.edu

Abstract. Tomographic imaging using a shifted and rotated field free line (FFL) with filtered backprojection image reconstruction can approach an order of magnitude SNR improvement over a field free point (FFP) given equal scan time. In this paper, we demonstrate a projection reconstruction x-space imager. The imager consists of a 2.4 T/m permanent magnet FFL gradient, a Helmholtz pair of off-the-shelf electromagnets, a solenoidal transmit coil and a gradiometer receive coil. A motor driven rotary table rotates the sample and the system acquires multiple projection images at evenly spaced angles between zero degrees and 180 degrees. Filtered back-projection is used to reconstruct a three-dimensional tomographic image stack. Sample rotation, which is sometimes employed in commercial mouse CT scanners, has been used to test this method. Later systems may rotate the gradient similar to a human-sized CT gantry or may generate an electronically rotated FFL gradient. In previous work, we have shown an MPI capable FFL scanner. Here, we show 3D experimental results of our PR-MPI scanner using acrylic USPIO imaging phantoms and post-mortem mice.

1 Introduction

Three-dimensional tomographic imaging via projection reconstruction will theoretically improve SNR by an order of magnitude over MPI using a field free point (FFP). This increase is due to signal averaging since many projection rotation angles are acquired to reconstruct a 3D volume. Simulation studies using an electronically rotated field free line (FFL) have demonstrated an approximately four-fold to ten-fold SNR gain [1]. Simulation studies have also shown that reconstruction is possible using multiple receive coils with transmit and receive in the radial direction in the x-y plane [2]. Here, we experimentally demonstrate three-dimensional tomographic MPI via projection reconstruction.

T.M. Buzug and J. Borgert (Eds.): Magnetic Particle Imaging, SPPHY 140, pp. 243–247.
springerlink.com

2 Material and Methods

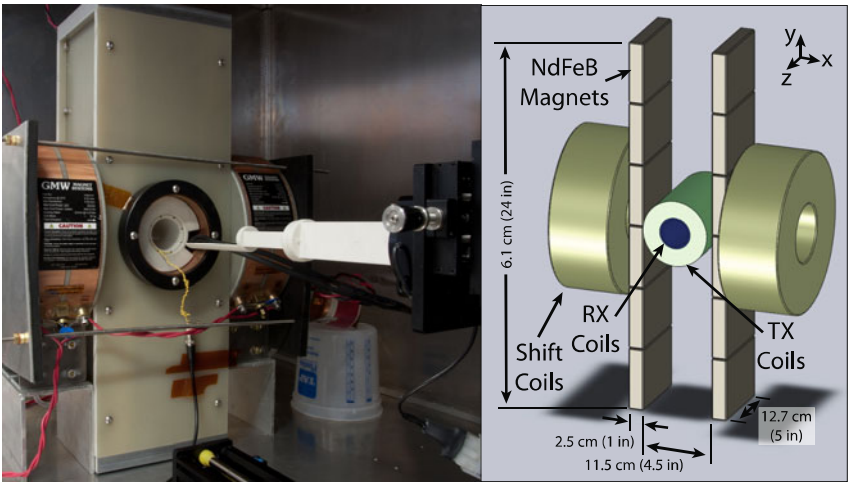

Fig. 1. Left: Image of our Field Free Line scanner. Right: Diagram of the permanent magnets that generate the Field Free Line and associated electromagnets necessary for projection imaging. Current imaging speed is 4 s per image.

Figure 1 shows an image and a diagram of our Field Free Line (FFL) projection MPI scanner [3]. Two NdFeB magnet sections with opposing magnetization create a 2.4 T/m gradient for the FFL. Each of the two magnet sections is composed of six NdFeB permanent magnets assembled with matching magnetization direction. The two sections are then assembled with opposing magnetization to produce the FFL along the y axis. Two GMW Associates electromagnets oriented as a Helmholtz pair are driven by an AE Techron industrial linear amplifier to translate the FFL for a total x axis field of view of 6 cm. Another AE Techron linear amplifier drives a solenoidal transmit coil with a sinusoidal excitation at 20 kHz to produce a z axis partial field of view of 2 cm. The transmit chain includes a 20kHz band-pass filter. A gradiometer receive coil concentric and internal to the transmit coil receives the signal resulting from a tracer excitation while rejecting transmit feed-through. A receive high-pass filter removes most of the remaining transmit feed-through. Custom Matlab software communicates to a NI Daq for signal receive and transmit.

A linear stage is used to translate the sample within the imaging bore. As the sample is translated, multiple partial fields of view are acquired and stitched together to produce a projection image with a maximum z axis field of view of 20 cm.

Figure 2 illustrates the process to obtain a 3D image volume from a 2D projection format MPI scanner. A motor driven rotary stage rotates a sample within the imaging bore at equally spaced angles between zero degrees and 180 degrees. Figure 2 shows an acrylic phantom with a Resovist distribution in the shape of the letters UC at three of the 60 rotation angles. Projection

images are taken at each rotation angle. Row by row in every projection image, a single slice is selected and filtered backprojection is used to reconstruct a 3D imaging volume. The resulting image is shown in Figure 2.

3 Results

Figure 3 illustrates the capability of our projection reconstruction MPI process to produce a 3D imaging volume from 2D projection images. Two acrylic imaging phantoms with distinct distributions of Resovist tracer are shown. The acrylic phantoms were stacked and imaged using the process described in Figure 2 with 60 rotations separated by three degrees. Of the 60 acquired images, one example, shown in Figure 3, illustrates the projection through both phantoms. After filtered backprojection, a 3D image volume is produced. Two slices of this image volume are shown, which resolve the two layers of the 3D volume containing each phantom.

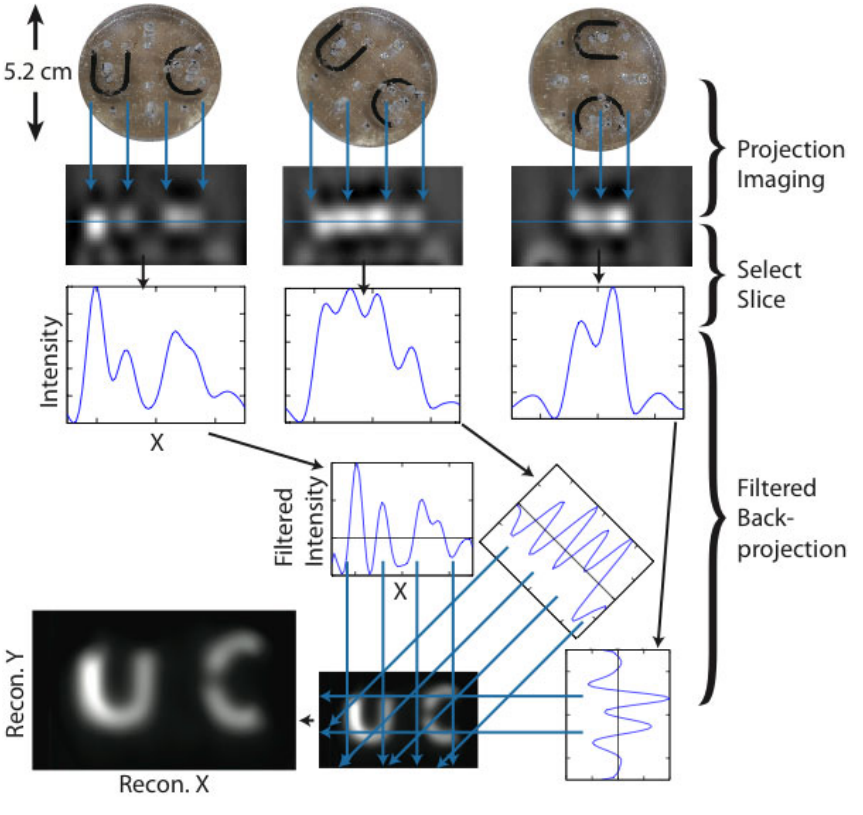

Fig. 2. Diagram of the projection reconstruction imaging process using real data acquired from our Field Free Line Scanner. (top row) Acrylic phantom at three rotation angles. (second row) Projection images at each rotation. (third row) Single slice selected from each projection image. (fourth and fifth rows) Filtered backprojection and a resulting image.

Figure 4 shows a volume rendering of a mouse injected with resovist. The mouse was sacrificed 30 s after the 20 uL injection. Sixty projection images were taken and filtered backprojection was used to reconstruct the image volume. Osirix was then used to volume render the image.

4 Discussion

We have chosen to simplify our hardware configuration by rotating the sample instead of rotating the FFL. In a human sized scanner, patient rotation would not be feasible. Instead, an electronically or mechanically rotated FFL could be used.

Note that the endpoints in the C in Figure 3 are about half the distance of the endpoints in Figure 2 due to overall phantom size and Resovist filling. The distance between the end-points of the C in Figure 3 are less than the resolution of the scanner; thus the C appears as an O.

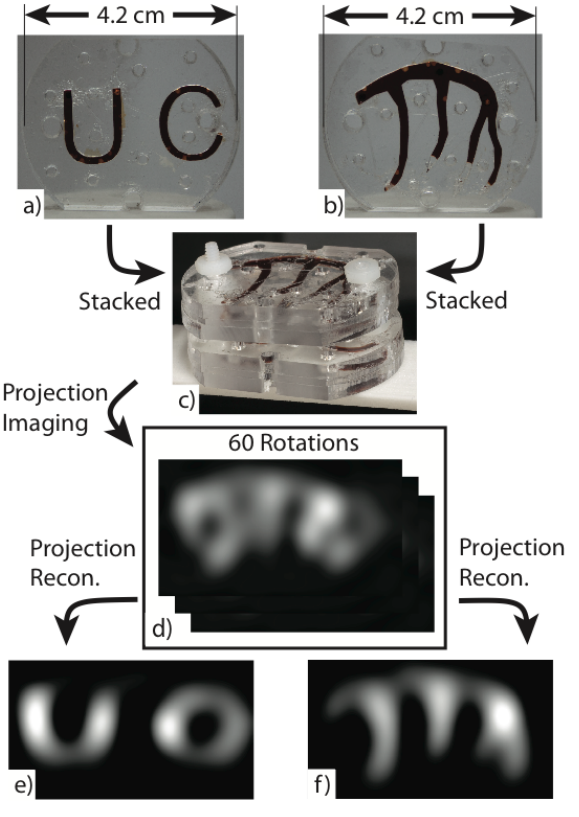

Fig. 3. Imaging results of two overlapping phantoms resolved via projection reconstruction. a) and b) Two acrylic imaging phantoms. c) Stacked acrylic phantoms. d) One of 60 rotation images. e) and f) Two image slices of the 3D image stack acquired via filtered backprojection.

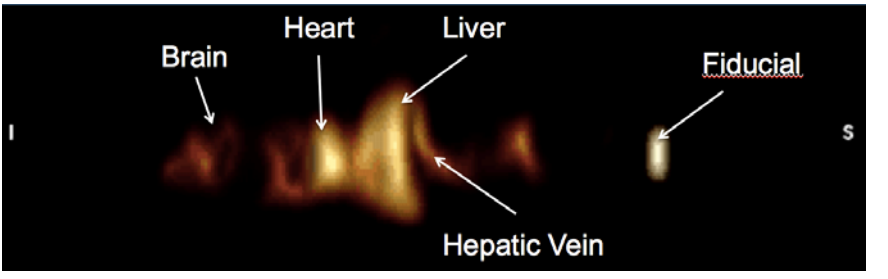

Fig. 4. Volume rendering of a mouse. The mouse was sacrificed 30 s after a 20 uL injection of Resovist. 60 projection images were taken and a volume image was reconstructed via filtered backprojection.

5 Conclusion

We have experimentally demonstrated the world's first 3D tomographic images using a FFL MPI scanner. Filtered backprojection was used to reconstruct the imaging volume from a set of projection images. The images created via this method theoretically have an order of magnitude higher SNR than images created using a FFP. This increase in SNR would be very beneficial in detecting smaller concentrations of a USPIO tracer.

Acknowledgements. We would like to thank our sponsors: the National Science Foundation, the California Institute of Regenerative Medicine, the University of California Discovery Grant, and the National Institute of Health.

This material is based upon work supported by the National Science Foundation Graduate Research Fellowship under Grant No. DGE 1106400.

References

1. Weizenecker, J., Gleich, B., Borgert, J.: Magnetic particle imaging using a field free line. Journal of Physics D: Applied Physics 41(10), 105009 (2008)
2. Knopp, T., Erbe, M., Sattel, T.F., Biederer, S., Buzug, T.M.: A Fourier slice theorem for magnetic particle imaging using a field-free line. Inverse Problems 27(9), 095004 (2011)
3. Konkle, J., Goodwill, P., Conolly, S.: Development of a field free line magnet for projection MPI. In: Proceedings of SPIE, vol. 7965, p. 79650X (2011)

Enlarging the Field of View in Magnetic Particle Imaging – A Comparison

Mandy Grüttner, Timo F. Sattel, Matthias Graeser, Hanne Wojtczyk, Gael Bringout, Wiebke Tenner, and Thorsten M. Buzug

Institute of Medical Engineering, University of Lübeck,
Ratzeburger Allee 160, 23562 Lübeck, Germany
{gruettner,buzug}@imt.uni-luebeck.de

Abstract. Magnetic Particle Imaging evolves rapidly and human scanners are conceivable, already. However, the growing scanner size and therefore the increasing data within the field of view give rise to several unsolved problems. The reconstruction process, solving an inverse problem with the measured signal and the system function, is a storage consuming procedure for high resolution 3D imaging. Additionally, the size of the field of view strongly depends on the used gradient field and field amplitudes. Due to technical as well as medical limitations, such as specific absorption rates and peripheral nerve stimulation, the conventional procedures will not be sufficient to image large regions of interest. This paper compares and discusses approaches enlarging the field of view that might be used to reduce the reconstruction process and/or enlarge the field of view despite limited technical properties.

1 Introduction

Since the introduction of Magnetic Particle Imaging (MPI) in 2005 [1] several generations of scanner topologies have been developed. Recently, a demonstrator with 12 cm bore size was introduced [2]. The conventional imaging process allows only for small field of views (FOV) when high spatial and temporal resolution is required. This is already a challenge for the demonstrator and will be an issue for larger scanners in particular. On the one hand, system functions as well as measured data become larger and therefore the reconstruction process demands more storage. On the other hand, currents, excitation frequencies and the gradient strength are limited by technical properties and patient safety issues, such as specific absorption rates (SAR) and peripheral nerve stimulation (PNS).

In order to overcome the limitations of a small FOV two techniques to enlarge the FOV [3, 4, 5] were introduced. The first idea is to cover the region of interest (ROI) using multiple FOV patches, the second idea uses

T.M. Buzug and J. Borgert (Eds.): Magnetic Particle Imaging, SPPHY 140, pp. 249–253.
springerlink.com

an additional excitation frequency that slowly moves the FOV through the ROI.

This paper compares the two approaches with the conventional procedure of the FOV and discusses advantages and drawbacks concerning image reconstruction and technical prospects. Choosing the power in a technical possible range and limiting the field amplitudes to fulfill medical safety protocols are the main goals of this work. Nonetheless, we will not discuss these values in detail, but only show a proof of concept, i. e. SAR and PNS thresholds are not fully evaluated for MPI yet.

2 Material and Methods

Usually, imaging in MPI is performed by drive fields with slightly different excitation frequencies in each dimension (f_x, f_y, f_z) and a selection field for spatial encoding. The superposition of oscillating fields with these frequencies form a Lissajous pattern, which is up to now the best known trajectory [6]. The size of the FOV is given by

$$[-2\frac{A_x^D}{G}, 2\frac{A_x^D}{G}] \times [-\frac{A_y^D}{G}, \frac{A_y^D}{G}] \times [-2\frac{A_z^D}{G}, 2\frac{A_z^D}{G}], \quad (1)$$

where A_x^D, A_y^D and A_z^D are the amplitudes of the corresponding frequencies and G denotes the gradient of the selection field.

As proposed in [3] the ROI can be subdivided into multiple FOV patches to be measured and reconstructed separately. The possibly overlapping patches may be combined using a fade in/out weighting. The individual FOV size can be described by (1). In our experiments, 10 % of each FOV overlapped with others.

A third approach, already mentioned in [1], is based on a special field called focus field, which additional to the drive fields moves the field-free point with low frequencies (f_x^{moving}, f_y^{moving}, f_z^{moving}) through space. The size of the moving FOV is given by

$$[-2\frac{A_x^{D+M}}{G}, 2\frac{A_x^{D+M}}{G}] \times [-\frac{A_y^{D+M}}{G}, \frac{A_y^{D+M}}{G}] \times [-2\frac{A_z^{D+M}}{G}, 2\frac{A_z^{D+M}}{G}], \quad (2)$$

where $A_x^{D+M} = A_x^D + A_x^{moving}$ is the sum of the drive and focus field amplitudes. Same holds for the other two dimensions.

To achieve an appropriate comparison, the temporal resolution of the independent imaging procedures is chosen similar. Aiming for 3D real-time imaging (i. e. 25 frames per second) the repetition time T_{rep} covering the

complete ROI has to be less than 40 ms. Additionally, the frequencies should be close to 25 kHz. Considering these parameters the frequencies and corresponding repetition times can be calculated as shown in table 1.

Table 1. Specific values for 3 different approaches to cover the ROI. The repetition time T_{rep} is related to 3D imaging. Only the frequencies necessary for 2D imaging are stated.

	T_{rep} in *ms* (for 3D imaging)	f_x in *Hz*	f_y in *Hz*	f_x^{moving} in *Hz*	f_y^{moving} in *Hz*
large FOV	39.28	26041.67	25252.53	-	-
4 static FOVs	4*9.79 = 39.16	28409.09	27173.91	-	-
moving FOV	39.28	26041.67	25252.53	30.55	76.37

The frequencies to move the FOV are chosen preferably small and additionally form a trajectory as dense as possible without increasing the limited repetition time.

The size of the ROI has been chosen to 50 x 50 mm². The static FOV patches therefore have a size of 30 x 30 mm² and the moving FOV is 25 x 25 mm² (when considered as static). The simulation was done with a phantom including dots of size 5 mm, 3 mm, 2 mm and 1 mm assuming undiluted Resovist as tracer material. To solve the system of equations the iterative Kaczmarz's method has been used.

3 Results

The resulting reconstructions, visualized in figure 1, show that both methods, multiple static FOV patches and one moving FOV, are possible procedures to enlarge the field of view. The resolution of all three reconstructions is similar. The resulting reconstruction of the moving FOV has some smeared parts, which might be due to an unsuitable frequency ratio that needs to be investigated in more detail. The images of the static approach show artifacts at the borders and the overlapping regions cause stripes at their edges. Corresponding to the size of the FOV patches the amplitude of each sine wave could be decreased by a factor of nearly two. This, of course, affects the amplitudes of the DC currents, but could be neglected concerning patient safety.

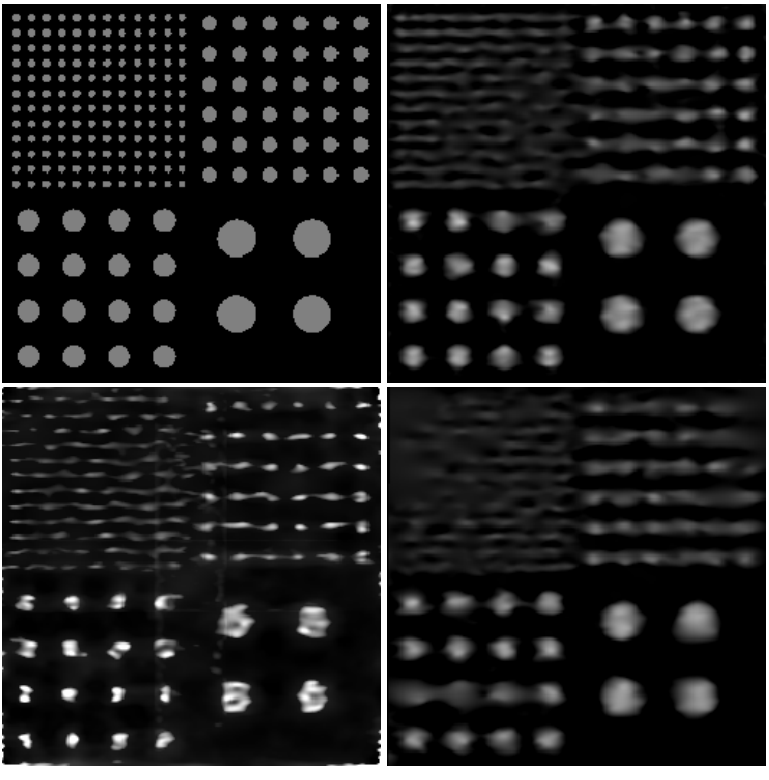

Fig. 1. From left to right: phantom and reconstruction of one large FOV, four static FOVs and one moving FOV (movement in both directions). The applied frequencies correspond to the stated frequencies in table 1. No scaling of intensities has been carried out.

4 Discussion

We showed that both methods enlarging the FOV in MPI are suitable and promising.

Regarding reconstruction the static FOV approach is highly interesting, because due to the increasing number of FOVs the storage needed for an individual reconstruction process decreases. However, this simulation study did not consider the time necessary to switch the gradient for the different FOVs, which is important for temporal resolution. This problem has to be determined more detailed and efficient techniques have to be developed.

The moving FOV is advantageous from a technical point of view. The drive-field coils can be supplemented by additional focus-field coils or by an efficient movement of the gradient field to enlarge the FOV. Unfortunately, the reconstruction effort cannot be reduced by this approach. Furthermore,

an additional filtering will be necessary and analysis concerning the therefore missing signal for reconstruction will be of fundamental importance.

5 Conclusion

In this MPI simulation study two methods have been compared enlarging the conventional FOV. It has been shown that both are suitable regarding image reconstruction. Nonetheless, the approaches strongly depend on scanner properties and technical limitations. From the reconstruction point of view the static approach is highly interesting to decrease the size of the linear system. Experiments including noise and inhomogeneous fields are important to validate the relevance of the presented procedures.

Acknowledgements. We acknowledge the support of the Federal Ministry of Education and Research, Germany (BMBF) (grant numbers 01EZ0912 and 13N11090), the European Union and the State Schleswig-Holstein (Programme for the Future – Economy: 122-10-004) (MGrä, MGrü, HW, GB) and Germanys Excellence Initiative [DFG GSC 235/1] (WT).

References

1. Gleich, B., Weizenecker, J.: Tomographic imaging using the nonlinear response of magnetic particles. Nature 435, 1214–1217 (2005)
2. Gleich, B., et al.: Fast MPI Demonstrator with Enlarged Field of View. In: Proc. Intl. Soc. Mag. Reson. Med., vol. 18, p. 218 (2010)
3. Schmale, I., et al.: First phantom and in vivo MPI images with an extended field of view. SPIE Med. Imag. (2011)
4. Rahmer, J., et al.: Results on Rapid 3D Magnetic Particle Imaging with a Large Field of View. In: Proc. Intl. Soc. Mag. Reson. Med., p. 19 (2011)
5. Rahmer, J., et al.: Rapid 3D in vivo Magnetic Particle Imaging with a Large Field of View. In: Proc. Intl. Soc. Mag. Reson. Med., p. 19 (2011)
6. Knopp, T., et al.: Trajectory Analysis for Magnetic Particle Imaging. Physics in Medicine and Biology 54(2), 385–397 (2009)

Continuous Focus Field Variation for Extending the Imaging Range in 3D MPI

J. Rahmer[1], B. Gleich[1], J. Schmidt[1], C. Bontus[1], I. Schmale[1], J. Kanzenbach[1], J. Borgert[1], O. Woywode[2], A. Halkola[3], and J. Weizenecker[4]

[1] Philips Technologie GmbH Innovative Technologies, Research Laboratories, Röntgenstraße 24-26, 22335 Hamburg, Germany
juergen.rahmer@philips.com
[2] Philips Medical Systems DMC GmbH, Röntgenstraße 24-26, 22335 Hamburg, Germany
[3] Institute of Medical Engineering, University of Lübeck, Ratzeburger Allee 160, 23562 Lübeck, Germany
[4] University of Applied Sciences, Moltkestraße 30, 76133 Karlsruhe, Germany

Abstract. The imaging volume that is rapidly encoded by drive fields in 3D magnetic particle imaging is limited by power dissipation and nerve stimulation thresholds. Additional coils have been implemented to generate so-called focus fields that operate at lower frequencies and extend the accessible imaging range. This contribution presents the possibility of sweeping the rapidly encoded imaging volume along an arbitrary 3D path using continuous focus field variations. This technique can be useful for following a tracer bolus, for tracking devices, or for dynamically moving the image focus to different regions of interest.

1 Introduction

The imaging range or accessible imaging volume in magnetic particle imaging (MPI) is mainly determined by the volume that can be covered by the field free point (FFP) trajectory [1]. The FFP is generated by a selection field, whose gradient strength is inversely related to the achievable spatial resolution [2]. With currently available tracer materials, a field gradient of at least $G = 1\ \mathrm{T/m/\mu_0}$ is necessary to reach a resolution of about 2 mm. Assuming a constant selection field gradient, a homogeneous drive field of strength H_D can displace the FFP by $\Delta x = H_D / G$. However, the drive field is typically applied at frequencies above the audio range, e.g. at 25 kHz, so that its amplitude is limited by power dissipation in the coils and by potential nerve stimulation in the subject to be imaged. The upper limit of achievable drive field amplitudes is expected to be on the order of $H_D = 20\ \mathrm{mT/\mu_0}$, so that in a selection field gradient of $1\ \mathrm{T/m/\mu_0}$, a linear imaging range of $FOV_x = 2\ \Delta x = 40$ mm can be accessed. To circumvent

T.M. Buzug and J. Borgert (Eds.): Magnetic Particle Imaging, SPPHY 140, pp. 255–259.
springerlink.com

this limitation, homogeneous offset fields have been introduced that allow moving the focus of the small imaging volume accessed by the drive fields [3]. These focus fields operate at low frequencies up to 100 Hz and thus are less subject to power dissipation or nerve stimulation issues. Step-wise variation of focus field strengths can be used to enlarge the field of view (FOV) by combining overlapping sub-volumes into one large volume, however at the cost of temporal resolution. An increased imaging volume covering the heart and liver region of a rat has been demonstrated using this multi-station approach with 12 sub-volumes [4]. Here, an alternative approach is presented in which sub-volumes are not combined, but acquired sequentially during a smooth focus field sweep over a region of interest.

2 Material and Methods

Scans have been performed using the pre-clinical demonstrator system sketched in Fig. 1a. The selection field permanent magnets generate gradients of strength $G_x = G_y = 1.25$ T/m/μ_0 and $G_z = 2.5$ T/m/μ_0. The drive field amplitude was $H_D = 13$ mT/μ_0 on all three orthogonal drive coils, which were driven at frequencies $f_x = 24.5$ kHz, $f_y = 26.0$ kHz, and $f_z = 25.3$ kHz to generate a dense 3D FFP trajectory that repeats after 21.5 ms. The volume covered by the FFP trajectory is thus about 2 x 2 x 1 cm³. Since signal is also generated in the vicinity of the FFP, image information can be reconstructed to a slightly larger volume called imaging volume in the following. The system function necessary for reconstruction was determined by measuring a calibration sample containing 1.6 µl of pure Resovist [5] at the 28 x 28 x 20 positions of a 3D grid, which covered a volume of 3.4 x 3.4 x 2.0 cm³. For improved SNR, a set of dedicated receive coils mounted on a hollow cylinder with inner diameter 6.5 cm and length 8.0 cm was inserted into the scanner bore.

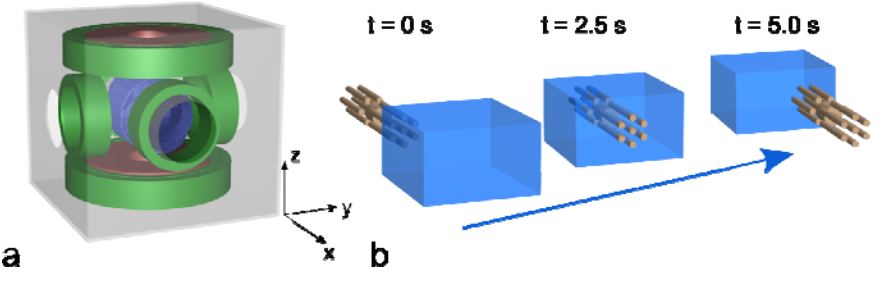

Fig. 1. Sketch of MPI field generating unit and phantom. (a) The scanner bore has a diameter of 12.5 cm and holds a receive coil insert (not shown). Permanent magnets (red) generate the selection field, the three orthogonal sets of coils close to the bore generate the drive fields (blue), and the three outer sets of coils generate the focus fields (green). (b) The phantom consisted of three compartments with several channels filled with diluted Resovist (brown). Starting, center, and end position of the imaging volume during the diagonal focus field sweep are indicated by transparent boxes (blue).

The phantom consisted of three compartments with several channels that were filled with diluted Resovist at a concentration of 25 mM(Fe)/l (cf. Fig. 1b). The two outer compartments each had 7 channels of length 20 mm with a channel diameter and separation of 2 mm. The center compartment had a single channel of length 8 mm and diameter 6 mm. The phantom was placed at the center of the bore, while over a period of 5 s, the focus fields were driven using a linear ramp in *x* and *y* direction, thus moving the imaging volume diagonally over the phantom. Towards the end of the field sweep, the phantom was slightly rotated manually and shifted along *x*. The maximum focus displacements were chosen to be ± 46.4 mm in *x* direction and ± 5.8 mm in *y* direction. During one field sweep, 5 s / 21.5 ms = 232 volumes were acquired, all of which have been reconstructed using the same system function. The reconstruction scheme described in [6] has been applied. It uses regularization to improve image SNR at the cost of resolution.

3 Results

Figure 2 shows orthogonal slices extracted from the reconstructed 3D volumes ("frames") at equally spaced points in time. In *x* direction, the slices were arranged to show the shift of the imaging volume over the static

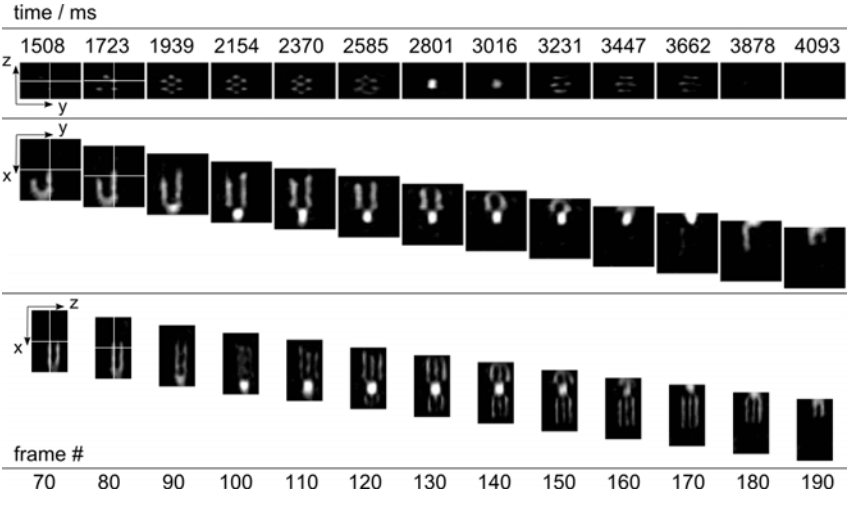

Fig. 2. Selected time frames from a 4D data set acquired during a focus field sweep in *x* and *y* direction. The total sweep duration was 5 s, corresponding to 232 time frames. The diagonal motion of the imaging volume over the phantom can be observed. The anisotropic resolution in the *yz* slices is due to the higher gradient in *z* direction. The cross hairs in the first two columns indicate the respective slice positions in the volume. As the imaging volume sweeps over the phantom, the planes also glide through the object. In the last three columns shown, the phantom has been rotated and moved manually in addition to the focus field sweep.

phantom. In *y* direction, one can observe that the phantom slightly “moves” to the right. The sweep range was large enough to cover the whole phantom, which was 48 mm long.

4 Discussion

Although the focus field changes during acquisition of the drive field sequence, the image quality is comparable to the quality obtained in static imaging. This is due to the slow focus field variation corresponding to shifts of only $\Delta x = 0.40$ mm and $\Delta y = 0.05$ mm per acquired volume. Thus, the shift is clearly below the spatial resolution and no blurring can be observed. The total sweep was about 9.3 cm in *x* and 1.2 cm in *y* direction and the sweep velocities were $v_x = 18.6$ mm/s and $v_y = 2.4$ mm/s. In view of a desired resolution of 1 to 2 mm, one can expect that these velocities can be increased further without inducing relevant blurring. From the data published in [7], the bolus velocity in the vena cava of a mouse was found to be about 6 mm/s after tracer injection into the tail vein. The demonstrated focus field sweep is therefore fast enough to follow a bolus in the blood vessels. While here the field sweep was executed along a line, arbitrary sweep trajectories can be implemented. The approach can also be useful for tracking devices, e.g. by following the tip of a catheter that has been marked with MPI active material. Either automated or manual steering of the focus of the imaging volume can be conceived. This would, however, require real-time image reconstruction and data visualization, which is not available on our experimental system. In view of the fact that multi-station imaging of large volumes using many sub-volumes slows down the imaging rate [4], approaches using only one or few sub-volumes that are moved to the region of interest are very attractive. Furthermore, the combination with a variable selection field gradient, which can be expected from future systems, promises high flexibility in shaping the imaging volume to find a good compromise between imaging speed, spatial coverage, and resolution.

In Fig. 2, one can observe that the phantom image becomes distorted towards the edges of the imaging volumes. This is due to the fact that image resolution drops outside the volume directly covered by the FFP trajectory. However, it seems sensible to include this region in reconstruction in order to properly assign signal coming from these regions. Probably, the best approach would be to remove the edge regions after reconstruction.

Furthermore, Fig. 2 shows that the image quality towards the beginning and the end of the sweep, i.e. close to maximum focus field strengths, is similar to the quality at the center. Since the system function used for reconstruction has been determined only at the center of the setup, field distortions and the drop in receive coil sensitivity towards the end points of the sweep could have had adverse effects on image quality. A more detailed analysis is necessary to estimate the magnitude of this expected effect.

5 Conclusion

The introduction of focus fields to 3D MPI systems offers high versatility in shaping the imaging volume. Previously, stepped focus fields were used to achieve large spatial coverage in multi-station imaging with several sub-volumes. As an alternative, the results presented here demonstrate the possibility of moving the rapidly encoded imaging volume smoothly along an arbitrary 3D trajectory in space.

Acknowledgement. The authors acknowledge funding by the German Federal Ministry of Education and Research (BMBF) under the grant numbers FKZ 13N9079 and 13N11086.

References

1. Gleich, B., Weizenecker, J.: Tomographic imaging using the nonlinear response of magnetic particles. Nature 435, 1214–1217 (2005)
2. Rahmer, J., et al.: Signal encoding in magnetic particle imaging: properties of the system function. BMC Medical Imaging 9, 4 (2009)
3. Gleich, B., et al.: Fast MPI Demonstrator with Enlarged Field of View. In: Proc. ISMRM, vol. 18, p. 218 (2010)
4. Rahmer, J., et al.: Rapid 3D in vivo Magnetic Particle Imaging with a Large Field of View. In: Proc. ISMRM, vol. 19, p. 3285 (2011)
5. Lawaczeck, R., et al.: Magnetic iron oxide particles coated with carboxydextran for parenteral administration and liver contrasting. Pre-clinical profile of SH U555A, Acta Radiologica 38, 584–597 (1997)
6. Weizenecker, J., et al.: A simulation study on the resolution and sensitivity of magnetic particle imaging. Physics in Medicine and Biology 52, 6363–6374 (2007)
7. Weizenecker, J., et al.: Three-dimensional real-time in vivo magnetic particle imaging. Physics in Medicine and Biology 54, L1–L10 (2009)

Third Generation X-Space MPI Mouse and Rat Scanner

Patrick Goodwill, Laura Croft, Justin Konkle, Kuan Lu, Emine Saritas, Bo Zheng, and Steven Conolly

Department of Bioengineering and EECS, University of California, Berkeley
Berkeley, CA 94720-1762, USA
goodwill@berkeley.edu

Abstract. Here we describe the construction of our third generation x-space MPI scanner, the fifth MPI scanner built at UC Berkeley. The scanner has two goals, (1) High-resolution native MPI resolution using x-space reconstruction, and (2) extended FOV suitable for mice and rats. In this paper we describe our design criteria, and we show the initial characterizations of the 7 T/m gradient field.

1 Introduction

Following theoretical work on x-space MPI [2,3,4] we have constructed three generations of x-space MPI scanners. Here, we describe the construction of our third generation x-space imager, the fifth MPI scanner built at UC Berkeley. The third generation x-space scanner has two primary design goals:

1. High resolution native MPI resolution using x-space
2. Extended FOV suitable for mice and rats

The new MPI scanner is optimized more for resolution and sensitivity than for imaging speed. Still, full mouse and rat FOV images (up to 12 cm x 5 cm x 5 cm) will require only approximately 3 seconds per image. The speed limitation is not fundamental to the technique, but is due rather to power supply limitations.

The resolution of the system can be predicted by x-space theory. To achieve a 1.2 mm x 2.4 mm x 2.4 mm resolution, we require an 8 T/m x 4 T/m x 4 T/m gradient [3]. Consequently, we set our design goal for a permanent magnet with an 8 T/m gradient and a linear FOV of 12 cm. We also needed to construct integrated homogeneous FFP shifting magnets to achieve this scanning range.

T.M. Buzug and J. Borgert (Eds.): Magnetic Particle Imaging, SPPHY 140, pp. 261–265.
springerlink.com

2 Material and Methods

The main magnetic field gradient is constructed using two large NdFeB magnet cylinders (16.5 cm OD, 15 cm thickness, 35 kg) wrapped in water-cooled homogeneous electromagnets (40 cm OD, 13 cm thickness, 76 kg, 4 kW). As designed, the NdFeB gradient would generate an 8 T/m static field gradient. The electromagnets are independently driven and enable shifting the FFP in the *x*-axis as well as boosting the gradient strength if driven in opposition. The FFP is shifted in the *y* and *z*-axes using matched pairs of water-cooled electromagnets wound using hollow core magnet wire. The system is driven using high power switch-mode amplifiers that deliver up to 300 A_{rms}.

The magnet has a free bore of 12 cm before addition of transmit and receive coils, and up to a 7 cm imaging free bore following insertion of the coils. The bore is constructed using a seamless piece of high conductivity copper. The transmit and receive coils in the *x* and *z*-axes are bolted into the bore and can be readily changed depending on the type of animal being imaged.

3 Results

Shown in Fig. 1, we see one of the halves of the main magnet assembly. The sub-assembly is constructed using a NdFeB magnet epoxied to an electromagnet. In Fig. 2, we see the completed main magnet assembly. In Fig. 3, we see the transmit and receive coils, which are placed inside the main magnet assembly.

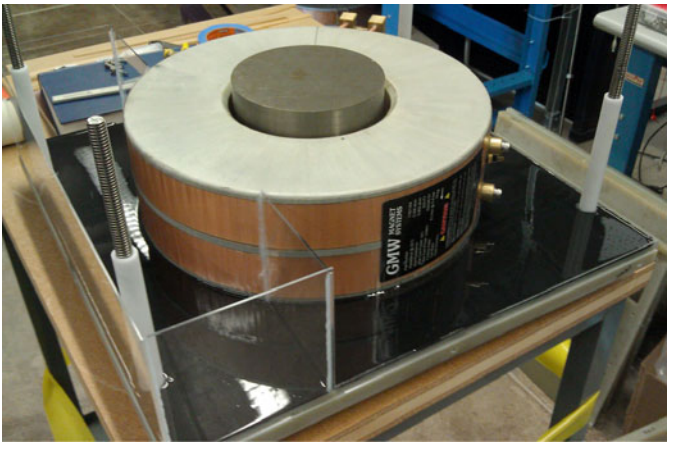

Fig. 1. Half of main field gradient containing NdFeB slug and water cooled electromagnet. The NdFeB magnet is potted in epoxy to accommodate the forces between the permanent magnet gradient and high power electromagnet.

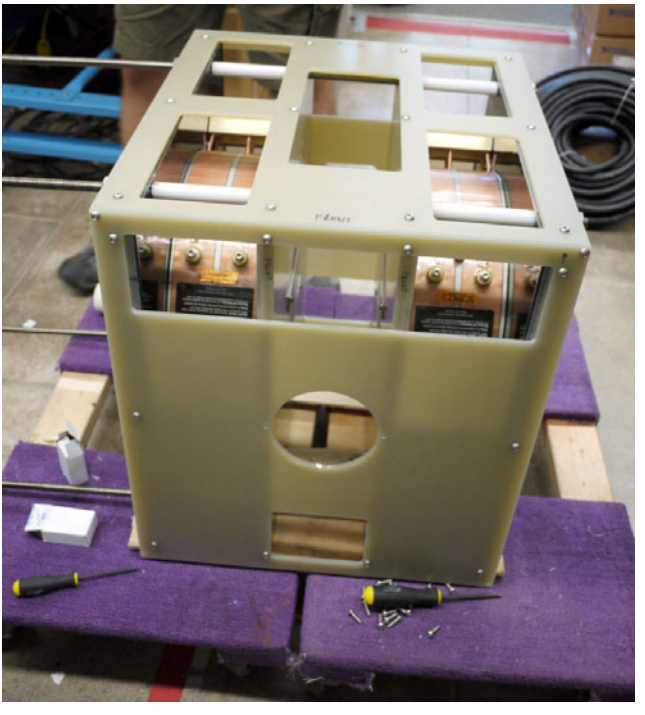

Fig. 2. Assembled main magnet gradient with screwdrivers for scale. The superstructure is constructed using G10 fiberglass composite, which is non-conductive, non-magnetic, and strong. The shown apparatus weighs over 300 kg.

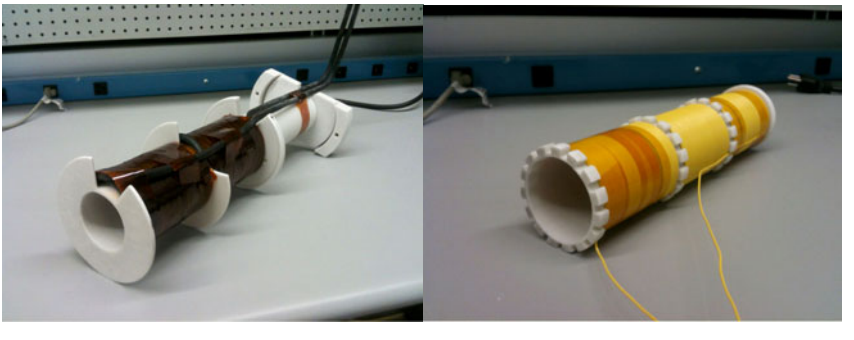

Fig. 3. Mouse transmit and receive coils. [LEFT] High power transmit coil wound with hollow core magnet wire. [RIGHT] receive coil wound with insulated wire.

Shown in Fig. 4, we see the characterization of the main magnet using hall effect probes (Model 475, LakeShore Cryotronics, Westerville, Ohio, USA). We calculate the total field gradient as the maximal field gradient at a given position in the magnet. The field gradients experienced by a mouse and a rat are similar:

Table 1. Mean field gradients in the x, y, and z axes across mouse and rat FOVs.

Animal	*FOV*	*Gx [T/m]*	*Gy [T/m]*	*Gz [T/m]*
Mouse	3 cm x 8 cm	6.7 +/- 0.2	3.4 +/- 0.1	3.3 +/- 0.2
Rat	5 cm x 12 cm	6.4 +/- 0.6	3.3 +/- 0.2	3.1 +/- 0.4

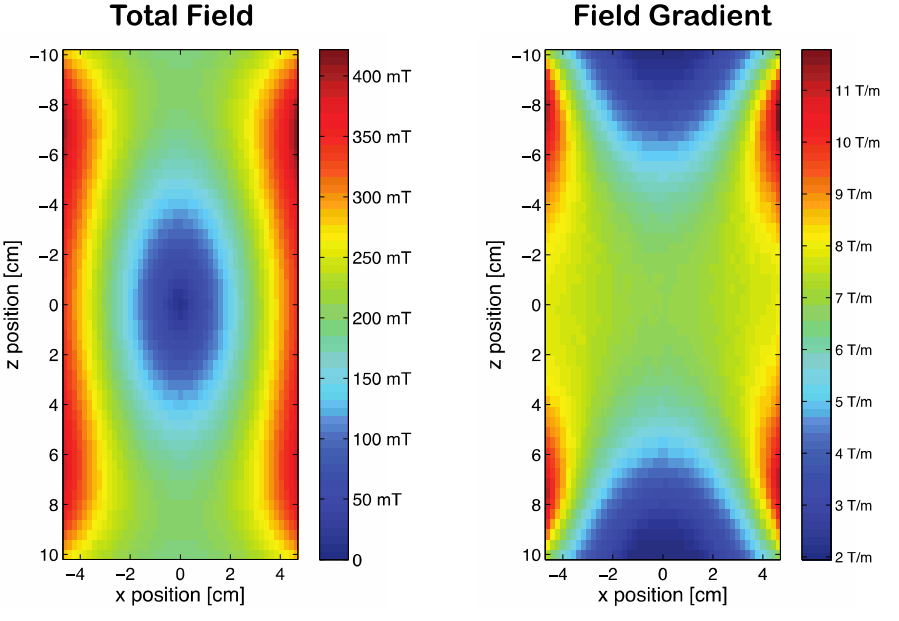

Fig. 4. Main magnet characterization of the completed magnet. [LEFT] The field magnitude approaches 400 mT next to the permanent magnet pole pieces. [RIGHT] Maximal field gradient. The field gradient is approximately 7 T/m in the center of the field of view, and increases to near 11 T/m at the pole pieces.

4 Discussion

The main magnet produces a field gradient of 7 T/m in the isocenter of the magnet, and 6.7 T/m on average across the scan area for a mouse. This is

12.5% weaker gradient strength than the design goal of 8 T/m, most likely due to incomplete saturation of the magnet pole pieces.

We are currently building the supporting systems for the magnet which include high power control systems, the transmit and receive chains, as well as the y and z slow FFP movement magnets. Together, this will enable this third-generation x-space MPI system to image in real-time.

5 Conclusion

We have described the construction of a third generation x-space MPI scanner suitable for mice and rat imaging, the fifth MPI scanner built at UC Berkeley. The scanner has two goals, (1) High resolution native MPI resolution using x-space, and (2) extended FOV suitable for mice and rats. The magnet had a design goal of 8 T/m, and an achieved gradient strength of 7 T/m.

References

1. Gleich, B., Weizenecker, J.: Tomographic imaging using the nonlinear response of magnetic particles. Nature 435, 1214–1217 (2005)
2. Goodwill, P., Conolly, S.: The x-space formulation of the magnetic particle imaging process: 1-D signal, resolution, bandwidth, SNR, SAR, and magnetostimulation. IEEE Transactions on Medical Imaging 29, 1851–1859 (2010)
3. Goodwill, P., Conolly, S.: Multidimensional x-space magnetic particle imaging. IEEE Transactions on Medical Imaging 30, 1581–1590 (2011)
4. Goodwill, P., et al.: Ferrohydrodynamic relaxometry for magnetic particle imaging. Applied Physics Letters 98, 262502–262502-3 (2011)

Projection X-Space MPI Mouse Scanner

Patrick Goodwill, Justin Konkle, Bo Zheng, and Steven Conolly

Department of Bioengineering and EECS, UC-Berkeley,
340 Hearst Memorial Mining
Berkeley, CA 94720-1762, USA
goodwill@berkeley.edu

Abstract. Here we describe the construction and images of the first projection x-space MPI scanner. The scanner is a side-access quadrupole design, and generates a 2.35 T/m main field gradient. The system excites the sample and receives signal in one axis, and reconstructs full-body images using x-space reconstruction. The resulting images are of high quality, and we demonstrate linear and shift invariance of the imaging system by imaging a resolution phantom and mice injected with Resovist.

1 Introduction

Projection Magnetic Particle Imaging (MPI) can improve imaging speed by over 100-fold over traditional 3D MPI. In this paper, we describe the design, construction, and imaging results of a 2D projection x-space MPI scanner for real-time mouse imaging. To date, all experimental MPI scans have been performed with a field free point (FFP) [1], which requires a 2D raster scan of a 3D volume to create an image. Current state-of-the-art MPI is intrinsically three-dimensional due to the design of the main magnet. These scanners form a single point in three-dimensions termed the Field Free Point (FFP), where the magnetic field magnitude is weaker than the saturation magnetization of a magnetic nanoparticle tracer. Stretching the point along one axis converts the FFP into a line, termed a Field Free Line (FFL) by the first publication in this area [2]. Other work has described possible techniques to rotating the FFL electronically [3].

2 Material and Methods

Our FFL gradient design concept was to construct a side-access quadrupole magnet. To achieve the magnetic field gradients necessary for MPI,

T.M. Buzug and J. Borgert (Eds.): Magnetic Particle Imaging, SPPHY 140, pp. 267–271.
springerlink.com

we used NdFeB permanent magnets with no field return. The main magnet generates a 2.35 T/m field gradient, which corresponds to a native resolution of 3.8 mm using Resovist. The magnet free bore is 10 cm, and we have sized the receive coil for mouse imaging (4 cm ID). Transmit and receive coils can be easily changed for imaging larger (or smaller) FOVs. The system images 2.5 cm x 5.0 cm partial FOV images at 10 frames per second. Acquisition of the partial FOVS can be sped up through the use of a larger amplifier or a redesigned shift coil. Full FOVs of 10 cm x 5.0 cm are acquired in 4 seconds and can be sped up through the addition of an additional electromagnet to move the FFP in the z axis rather than the current mechanical translation.

Images are reconstructed using x-space MPI reconstruction theory. X-space MPI is a new theoretical approach to MPI signal processing and reconstruction that enables acquisition of a native MPI image, and does not require a system function, harmonics, or pre-characterization of the nanoparticles or imager. We described the x-space technique in detail in our first two x-space papers [4,5]. All MPI image reconstructions require the recovery of the lost low frequency information filtered out to avoid direct feedthrough [8]. We have experimentally shown that MPI with x-space reconstruction can produce Linear and Shift Invariant images, a property crucial to the reliability and efficacy of MPI in medical imaging.

3 Results

Shown in Fig. 1, is the UC Berkeley FFL scanner. The scanner was constructed in-house, including machining of the G10 fiberglass composite structural plates as well as assembly of the magnets. The magnet configuration is similar to a quadrupole magnet used in a linear acclerator, with two sides removed for access. In Fig. 2, we used the FFL scanner to image a complex resolution phantom constructed using laser-cut acrylic. The resolution phantom enables measurement of the system's native resolution when imaging Resovist tracer. Fig. 3 shows two mice imaged using the system. The mice images show that the x-space MPI image is not affected by tissue, as well as the high contrast that is inherent to the MPI technique.

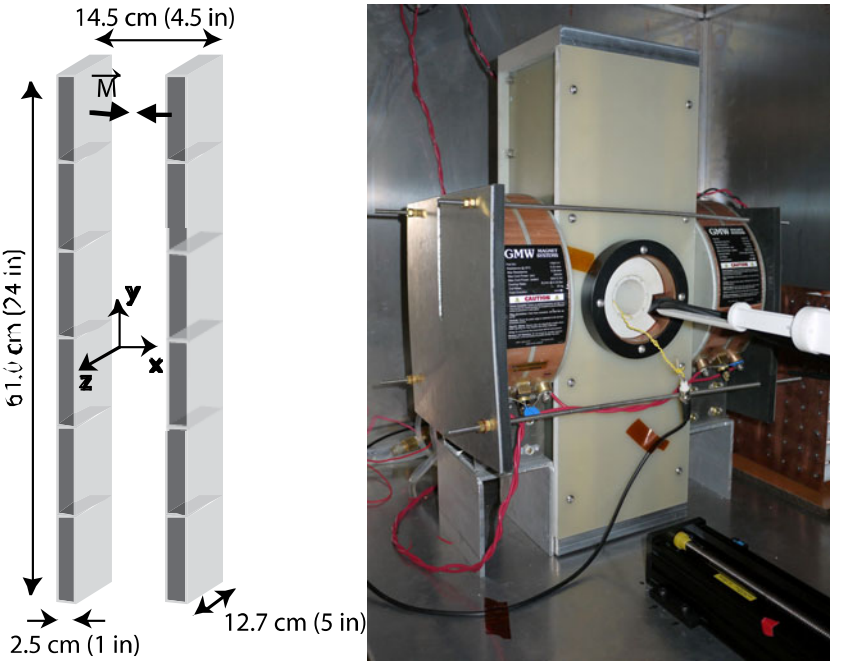

Fig. 1. UC Berkeley Projection X-space MPI Scanner. [LEFT] The 12 rectangular NdFeB magnets that produce the main field gradient are configured as two large magnets in opposition. [RIGHT] The main field gradient produces a 2.35 T/m field gradient. Excitation and signal reception occur in one axis (down the bore in the z axis).

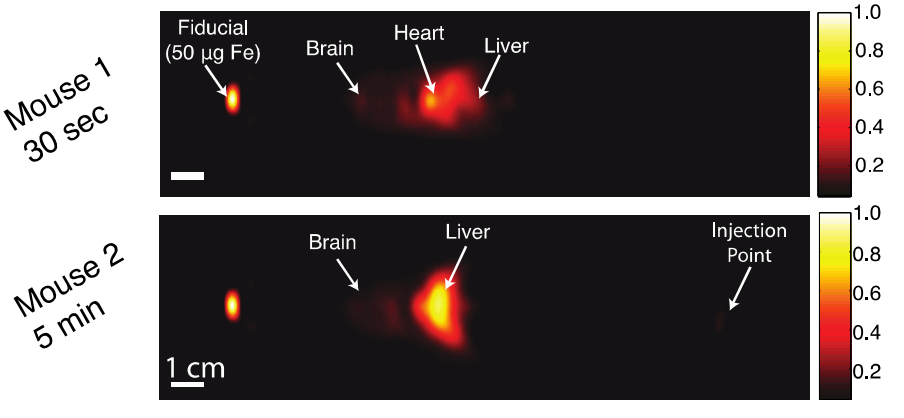

Fig. 2. Mouse Images of two different mice injected to 20 micro-liters undiluted Resovist. The mice were identically prepared, but one was sacrificed 30 seconds after injection, and the other after 5 minutes. The mice were imaged post-sacrifice. Total imaging time: 15 seconds.

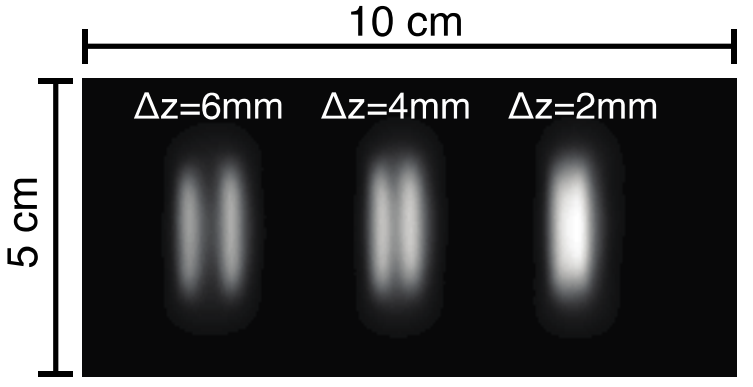

Fig. 3. Resolution Phantom. The phantom is constructed using acrylic and filled with diluted resovist (1 part Resovist, 9 parts water). Total imaging time: 4 seconds.

4 Discussion

The measured native resolution of the system is 3.8 mm, which is consistent with our models and measurements that show that Resovist acts similar to a nanoparticle with a 17 nm magnetic core diameter [5,6]. It is of great importance that we develop tracers that are better optimized for MPI resolution and SNR [7]. This measured resolution is apparent in Fig. 2, as the samples separated by 2 mm are not discernable, 4 mm are just discernable, and 6 mm are easily discernable.

For the proper operation of MPI in a projection format, the field accuracy of the FFL scanner is crucial. The inhomogeneity of the field free line demonstrated here leads to minor signal fading and a depth dependent point spread function; and we have experimentally demonstrated less than 2% fading and widening of the point spread function at the far ends of the FFL scanner (not shown in this paper).

The images of the mice in the scanner shows the high contrast that would provide allow MPI to acquire ideal angiography images. The technique does not see tissue whatsoever, and sees only the nanoparticle tracer. This ideal contrast would enable acquisition of a full projection across the patient and produce an image similar to an x-ray angiogram, but without the dangers of iodine tracer or radiation.

5 Conclusion

We have designed and constructed the first projection MPI scanner, and used the system to image complex phantoms and mice. The projection format could enable imaging up to 100 times faster than a 3D MPI scanner because images are acquired in 2D instead of 3D. The UC Berkeley scanner reconstructs images using x-space reconstruction, which enables the

acquisition of native MPI images with no pre-characterization of the tracer/scanner. The projection scanner produces a 2.35 T/m main field gradient, and has an experimentally measured 3.8 mm resolution down the bore. The system was also used to image whole mice, and the resulting images show the high contrast inherent to MPI.

References

1. Gleich, B., Weizenecker, J.: Tomographic imaging using the nonlinear response of magnetic particles. Nature 435, 1214–1217 (2005)
2. Weizenecker, J., Gleich, B., Borgert, J.: Magnetic particle imaging using a field free line. Journal of Physics D: Applied Physics 41 (2008)
3. Knopp, T., Sattel, T.F., Biederer, S., Buzug, T.M.: Field-free line formation in a magnetic field. Journal of Physics A: Mathematical and Theoretical 43(1), 012002 (2010)
4. Goodwill, P., Conolly, S.: The x-space formulation of the magnetic particle imaging process: 1-D signal, resolution, bandwidth, SNR, SAR, and magnetostimulation. IEEE Transactions on Medical Imaging 29, 1851–1859 (2010)
5. Goodwill, P., Conolly, S.: Multidimensional x-space magnetic particle imaging. IEEE Transactions on Medical Imaging 30, 1581–1590 (2011)
6. Goodwill, P., et al.: Ferrohydrodynamic relaxometry for magnetic particle imaging. Applied Physics Letters 98, 262502–262502-3 (2011)
7. Ferguson, R.M., Minard, K.R., Khandhar, A.P., Krishnan, K.M.: Optimizing magnetite nanoparticles for mass sensitivity in magnetic particle imaging. Medical Physics 38(3), 1619 (2011)
8. Lu, K., Goodwill, P., Zheng, B., Conolly, S.: The impact of filtering direct-feedthrough on the x-space theory of magnetic particle imaging. In: Proceedings of SPIE, vol. 7965, p. 79852 (2011)

Magnetic Particle Theory

Reconstruction of Magnetization Curve Using Magnetic Spectroscopy

Iulian Teliban[1], Steffen Chemnitz[1], Claas Thede[1], Christoph Bechtold[1], Babak Mozooni[1], Eckhard Quandt[1], and Hans-Joachim Krause[2]

[1] Institute for Materials Science, Christian-Albrechts-University, Kaiserstr. 2 Kiel, 24143, Germany
iut@tf.uni-kiel.de
[2] Peter Grünberg Institute (PGI-8), Forschungszentrum Jülich Jülich, 52425, Germany

A new measurement principle based on the frequency mixing technique for investigating the shape of the magnetization curve of soft non-hysteretic magnetic materials is introduced. Based on Taylor expansion of the magnetization curve and spectral investigation of an inductively detected signal, a mathematical model for the reconstruction of M(H) is proposed, [7]. Here, the model is experimentally verified using a nanocrystalline soft magnetic material with defined properties. It is shown that the magnetization curve can be reconstructed very accurately and the influence of an additional parameter, i.e. strain, can be investigated in detail as well.

1 Introduction

Measurement of full magnetization curve is an important prerequisite to achieve a complete characterization of sample's magnetic properties. Up to date several systems have been developed for this purpose, [1, 2]. Standard techniques are vibrating sample/coil magnetometers where mechanical vibration of the sample/coil is required. Measurement of magnetization curve in complex geometries such as inline in production or estimation of local properties are difficult to be realized using these conventional methods. They require huge and robust systems which are difficult to manipulate. More flexible are optical methods such as magneto-optical Kerr measurements [3, 4], but they can measure only the surface properties in nanoscale range.

In this paper, a new sensor technique based on the frequency mixing method is proposed to measure the magnetization curve of soft magnetic materials. The performance of the technique is tested on a magnetic sample with defined properties. Additionally, the sample's strain level is investigated.

T.M. Buzug and J. Borgert (Eds.): Magnetic Particle Imaging, SPPHY 140, pp. 275–279.
springerlink.com

2 Material and Methods

In the frequency mixing method, the magnetic material is exposed to a magnetic field consisting of two components: $H_1(f_1)$ and $H_2(f_2)$ with $f_1 >> f_2$ (blue line in Fig. 1a). The amplitude of the low frequency component of the field is chosen to be high enough ($H_2 >> H_1$) to ensure that the magnetic material is periodically driven in saturation. As a result, additional harmonics and new mixing components can be detected in spectra of the response signal of the material (blue line in Fig. 1d). The appearance of these components is highly specific to the nonlinear magnetization curve of the material (Fig. 1b). With this technique, a very good selectivity can be achieved. Other materials in the interaction volume such as ceramics, metals, etc., will not produce any frequency mixing signals if their magnetic behaviour is linear, i.e., paramagnetic or diamagnetic in the considered range of the magnetic field. Therefore, by measuring the mixing components, information about ferromagnetic material content can be obtained. A detailed description of this principle has been published in [5, 6].

The presence only of the even mixing terms, i.e. f_1+2nf_2 in the spectra is a consequence of the symmetry of the magnetization curve. Any disturbance of the symmetry will give rise to odd terms, too. If a DC field offset H_0 is applied to the material (red line in Fig. 1a), both AC fields, H_1 and H_2, are shifted towards the saturated regime of the magnetization curve. As a result the magnetization answer becomes asymmetric (red line in fig. 1c). The induced asymmetry in the transfer function, M(H), will introduce odd mixing components in the spectra (red line in Fig. 1d), too. Based on this effect and using Taylor expansion of magnetization curve, a mathematical relationship between magnetization M of a material and the amplitude of the induced mixing components in the frequency spectra of $M(t)$ was formulated [7], and can be expressed as:

$$\left.\frac{d^2M}{dH^2}\right|_{H=H_0} = -\frac{2}{H_1H_2}\left[\mathrm{Re}\{f_1+f_2\}+3\,\mathrm{Re}\{f_1+3f_2\}+5\,\mathrm{Re}\{f_1+5f_2\}\right] \quad (1)$$

$$\left.\frac{d^3M}{dH^3}\right|_{H=H_0} = -\frac{8}{H_1H_2^2}\left[\mathrm{Im}\{f_1+2f_2\}+4\,\mathrm{Im}\{f_1+4f_2\}+9\,\mathrm{Im}\{f_1+6f_2\}\right] \quad (2)$$

It should be noted that this model is valid only for magnetic material without hysteresis. If a material is magnetically hysteretic, minor loops that are caused by the application of the AC fields will deviate from the major loop of the magnetization curve. Thus, a misleading smoothing of the hysteresis curve will be observed.

Both Eqs.(1) and (2) depend either on even or odd mixing components and also on the magnitude of applied AC fields. Reducing the AC fields results in an increase of the measurement method's resolution but also in a lower signal amplitude. Therefore, the amplitude of both fields H_1 and H_2 has to be chosen carefully in order to obtain an adequate signal-to-noise ratio (SNR). In order to minimize the influence of field amplitudes and

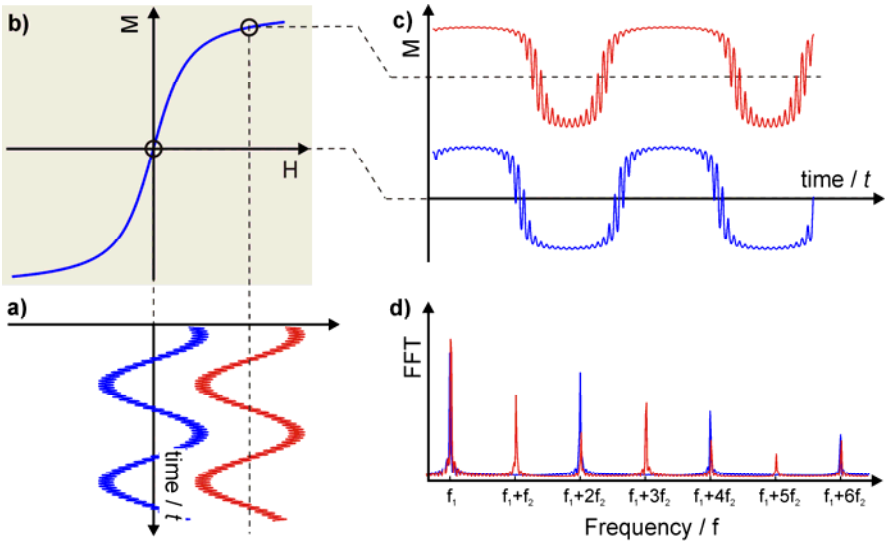

Fig. 1. Frequency mixing principle: a) the applied two-frequency field; blue without, red with an offset field H_0; b) sample's magnetization characteristics; c) resulting magnetization M(t) of the material and d) corresponding frequency spectra at the upper sideband of f_1.

noise amplification by integration, only equation (1) is used for magnetization curve reconstruction.

Numerical simulation of the frequency mixing technique [7] has shown that the magnetization curve can be reconstructed well by numerical integration of Eq.(1).

The sensor system developed for measurement of magnetization curve using the above described frequency mixing technique is described in detail in our previous publications [5-7].

3 Results

To investigate the sensor performance and to prove the above described M(H) reconstruction principle, a ribbon (18μm thickness) of a nanocrystalline soft magnetic material was tested. This alloy consisting of Fe, Cu, Nb and Si (Vitroperm 800) was provided by Vacuumschmelze. In the as quenched state this material has a magnetostriction constant of about 20ppm. Therefore the application of stress induces a magnetically easy axis parallel to the stress direction. With this approach, magnetization curves with different shape are obtained. In addition, the sample's strain level can be investigated.

The data obtained from the frequency mixing sensor are compared to measurements using a standard technique (VSM, Lake-Shore 7300

Series). For VSM investigations, a sample holder was designed that allowed to apply stress to the sample during the measurement. Due to the fact that both space and weight were limited in the VSM, the exact quantity of stress and strain cannot be monitored. In the sensor system, the space in between the pick-up coils can be accessed more easily. Furthermore, the sample is not mechanically vibrated. This allows to implement a more sophisticated tensile testing system. Here, strain is applied via a micrometer screw and stress is monitored using a high sensibility force gauge (Inelta KMM62).

The magnetic properties of the sample under mechanical stress, investigated using VSM are shown in Fig.2(a, b). All measurements were in-plane perpendicular to the stress direction. It can be seen that increasing the strain is followed by a reduction of the slope of the magnetization curve at zero field. This monotonous decrease of μ_r with strain has also been demonstrated by MOKE measurements in previous works [6]. However, as motivated above, the monitoring of the applied strain level is difficult to be realized both in VSM and MOKE, the latter one also being restricted to surface magnetization analysis only.

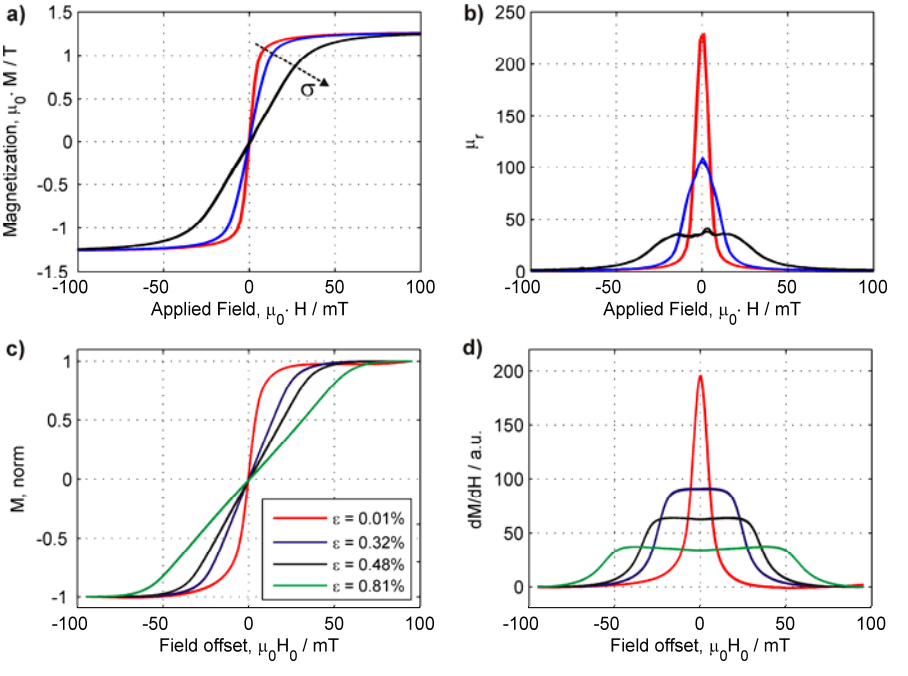

Fig. 2. Magnetic properties of the FeCuBSi foil at different strain levels. (a) Magnetization curve measured using VSM, perpendicular to the applied strain direction. (b) Relative permeability obtained by differentiation of (a). (c, d) Reconstructed magnetization curves using frequency mixing technique.

The magnetization curves and the relative permeability reconstructed using the frequency mixing technique and Eq. (1) for different strain levels are shown in Fig. 2(c, d). Due to different amplification factors within the electronic components and the nescience of the exact sample interaction volume v, only qualitative information, such as the shape of the magnetization curve can be gained by this method. For this reason, all magnetization curves were normalized in Fig. 2(c). However, the influence of strain on the magnetic properties is accurately observable. Furthermore, using appropriate amplification factors for specific materials and specific sample geometries, the reconstructed properties are in the same range, e.g. $\mu_r \in (30-200)$, compared to the data obtained by conventional techniques, Fig. 2(b) vs. Fig. 2(d).

4 Summary and Conclusions

In this paper, a non-contact measurement principle to measure the magnetization curve shape of soft magnetic materials has been introduced. For this purpose, an inductive detection sensor based on frequency mixing technique has been used. The performance of the designed sensor and M(H) reconstruction principle has been shown experimentally using a ferrous, nanocrystalline ribbon with positive magnetostictive properties. After reconstruction, the influence of stress on the shape of the magnetization curves is in good agreement with VSM data and previous investigations [6]. Furthermore, using proper calibration factors and approximations for the interaction volume, the reconstructed magnetic properties are also quantitatively the same as measured by standard techniques. Based on the high adaptability of the measurement setup, such sensors can be designed to suit difficult geometries or to perform locally restricted measurements. The frequency mixing technique is highly selective, making such a sensor also applicable to systems where the magnetic phase is embedded in complex matrix, e.g. multilayer coatings. Otherwise, this technique provides a reliable low cost alternative for M(H) investigations of soft magnetic materials.

References

1. Foner, S.: Review of Scientific Instruments 30, 548 (1959)
2. Fiorillo, F.: Measurement and Characterization of Magnetic Materials. Elsevier Academic Press (2004)
3. Bader, S.D., Moog, E.R., Grunberg, P.: Journal of Magnetism and Magnetic Materials 53, L295–L298 (1986)
4. Teixeira, J.M., et al.: Review of Scientific Instruments 82, 043902 (2011)
5. Teliban, I., Chemnitz, S., Thede, C., Bechtold, C., Quadakkers, W.J., Schütze, M., Quandt, E.: Review of Scientific Instruments 80, 115106 (2009)
6. Bechtold, C., Teliban, I., Thede, C., Chemnitz, S., Quandt, E.: Sensors and Actuators A: Physical 158, 224–230 (2010)
7. Teliban, I., Chemnitz, S., Thede, C., Bechtold, C., Mozooni, B., Krause, H.-J., Quandt, E.: Journal of Magnetism and Magnetic Materials (in Press)

Multiferroic Behavior of BTO-Nanoparticles

Steffen Trimper[1], Safa Golrokh Bahoosh[1], and Julia M. Wesselinowa[2]

[1] Institute of Physics, Martin-Luther-University, Von-Seckendorff-Platz
Halle (Saale), 06120, Germany
steffen.trimper@physik.uni-halle.de
[2] Department of Physics, University Sofia, Blvd.J.Bouchier 5
Sofia 1164, Bulgaria
julia@phys.uni-sofia.bg

Abstract. Using microscopically models and Green's function techniques we demonstrate how one can get information of ferroelectric nanoparticles. The approach can be extended to multiferroic systems which are defined as materials possessing two or more ferroic orders in a single phase. In detail we show that the unexpected ferromagnetic properties of $BaTiO_3$ (BTO) observed recently at room temperatures are due to oxygen vacancies at the surface of the nanocrystalline materials. Such vacancies lead to the appearance of Ti^{3+} or Ti^{2+} ions with nonzero net spin. The resulting different valence offers a nonzero magnetization which decreases with increasing particle size. The system shows a multiferroic behavior below a critical size of the nanoparticles and the related polarization tends to a saturation value when the particle size is enhanced.

1 Introduction

Since ferromagnetism and ferroelectricity in lower dimensions promise a drastic increase of the storage density of RAM, nanoscale materials have attracted extensive attention. The anticipated benefit depends on whether the phase transition and the polarized low temperature state still exist when the system is scaled down up to less than 100 nm. The challenge in low dimensional finite structures concerns the synthesis, the experimental characterization of their size-dependent properties as well as the theoretical description. Nanostructures are observed in a wide variety of realizations such as nanoparticles, nanorods, nanowires, nanocubes and nanotubes. Generally, the size of nanoscale material is assumed to be less than 100 nm, for a recent review on ferroelectric and ferromagnetic nanoparticles see [1, 2]. Another interesting aspect is the recent observation, reported from both experiments and first-principles calculations, that typical ferroelectric material such as $BaTiO_3$ (BTO) and $PbTiO_3$ (PTO) become multiferroic when they are prepared at the nanoscale [3]. Nanocrystalline BTO offers at

T.M. Buzug and J. Borgert (Eds.): Magnetic Particle Imaging, SPPHY 140, pp. 281–285.
springerlink.com

room-temperature magnetic hysteresis as well as temperature-dependent dielectric constant and a polarization. Multiferroics that exhibit magnetoelectric coupling are widely discussed from quite different context [4]. However, apart from a density functional calculation as vacancy-induced magnetism in BTO(001) thin films [5] a well accepted theoretical description of the ferroic properties of nancrystalline BTO is still missing. In a previous paper [6] we have proposed a model for BTO which allows finding out the multiferroic properties.

2 Material and Methods

We are interested in a theoretical description of the unexpected magnetic behavior of BTO. To that aim we use the Ising model in a transverse field is an appropriate tool to describe the properties of ferroelectric nanoparticles [1]:

$$H = - \Omega \Sigma_i S_i^x - \Sigma J_{ij} S_i^z S_i^z .$$

Since the ferroelectricity in BTO is originated from the off-centering of the Ti ions with respect to the cubic perovskite crystal we assume as the simplest model that there are two positions of the Ti atoms in a double-well potential. These two states are mapped on the S^z- component of a pseudo spin-1/2 operator whereas the S^x-component characterizes the tunneling between the wells with the frequency Ω. We define a nanoparticle by fixing the origin at a certain spin in the center of the particle and including all spins within the particles into shells, see Fig. 1. Surface effects or defects are included by different coupling parameters within the surface shell.

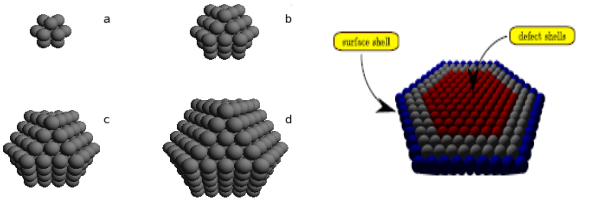

Fig. 1. Ferroelectric nanoparticles of different size composed of shells. Each sphere represents an operator according to the Hamiltonian (a) one central spin plus N=1 shell, (b) N=2 (c) N=3 and (d) N=4. Second part: Surface and defect shells of nanoparticles.

The magnetic properties of BTO are analyzed using the Heisenberg model for the resulting different valence states on the surface composed of Ti^{3+} or Ti^{2+}.The Hamiltonian reads

$$H = - \Sigma A_{ij} B_i B_i .$$

Here B_i is the Heisenberg spin operator at the site i and A_{ij} is the exchange integral between the nearest neighbors of the Ti^{3+}-ions. Different to many

oxides the exchange coupling is positive. In a similar manner like for the ferroelectric system we calculate the magnetization M. The nanoparticles are composed of distinct shells indicating the size, see Fig. 1. Different to the ferroelectric case the surface exchange interaction A_s is assumed to be larger as the related bulk coupling A_b. Therefore only the surface spins yield a significant contribution to M, which is again found by the finite temperature Green's function approach.

3 Results

The thermodynamic Green's function method enables us to calculate the size dependence of the polarization P in BTO-nanoparticles for $J_s < J_b$ [1]. The results confirm that the polarization shrinks with the particle size N is decreasing and is vanishing at a critical value N_c =3. The result for the polarization is shown as curve 1 in Fig. 2. The polarization is enhanced with increasing shell number N and becomes saturated for large size of the nanoparticles.

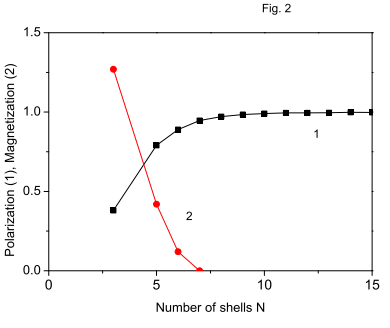

Fig. 2. Size dependence of the polarization (1) and magnetization (2).

To analyze the magnetic properties let us coming back to the structure of conventional perovskite-based ferroelectrics like BTO more specifically. As mentioned before the ferroelectricity arises in that material as the result of the displacement of the so-called B-site cation (Ti^{4+}) with respect to the oxygen octahedral cage. Consequently the transition metal ion (Ti^{4+} in BTO) needs an empty d-shell since the ferroelectric displacement occurs due to the hopping of electrons between the d-state Ti and p-state O atoms. Usually this process excludes the occurrence of any net magnetic moment because magnetism requires partially filled d-shells of the transition metal. Practically, all ferroelectric perovskites contain transition metal ions with an empty d-shell, such as Ti^{4+}, Ta^{5+}, W^{6+}. The ferroelectricity in these systems is caused by the off-center shifts of the transition metal ion, which forms strong covalent bonds with one or three oxygen atoms using their empty d-states. And somehow, the presence of real d electrons in the

d^n configurations of magnetic transition metals is able to suppress this process, preventing ferroelectricity in magnetic perovskites. This effect is well known as the so-called d^0 versus d^n problem. In [7] one finds magnetic measurements of BTO samples with 60 nm, 100 nm and 2 μm. While the sample on the nanometer scale reveals clearly ferromagnetism at room temperature the sample of μm scale shows a diamagnetic behavior as it is also expected for the bulk BTO material. The smaller the particle size is the higher is the saturation magnetization. The effect that larger particles lead to a lower magnetization is consistent with the suggestion that surface defects decrease with increasing particle size.

4 Discussion

As argued in [7] the observed ferromagnetism in such BTO-NP can be correlated with the presence of oxygen vacancies at the surface of the NP. So positron annihilation studies in BTO-NP reveals a lower annihilation rate of positrons with the 2p electrons of oxygen in the sample of 100 nm and 60 nm in comparison to the bulk system. This observation indicates the presence of oxygen vacancies [7]. Each oxygen vacancy is expected to donate two electrons to the empty d-state of a single Ti^{4+} (d^0) ion in order to produce a Ti^{2+} (d^2) ion with spin S = 1. An alternative mechanism is that each oxygen electron goes to different Ti^{4+} ions and generate two Ti^{3+} ions in state d^1 with spin S = ½ [7]. With decreasing particle size the number of oxygen vacancies increases and hence the number of Ti^{2+} or Ti^{3+} ions is also enlarged. This enhancement of Ti ions with nonzero spin gives rise to a weak ferromagnetism. Probably there is also the creation of a mixed valence state composed of a superposition of both states d^2 and d^1. The presence of the mixed valence state of the Ti-ions due to point defects could be also the origin for the observed room-temperature ferromagnetism in TiO_2 nanoparticles.

5 Conclusion

In conclusion, we have shown that the observed ferromagnetic properties in BTO- or PTO nanoparticles at room temperatures could be originated due to the oxygen vacancies at the surface and to the appearance of a different valence state composed of Ti^{3+} or Ti^{2+}. As the result one observes multiferroic properties of the nanoparticles. Whereas the polarization decreases with decreasing particle size, the magnetization increases below a critical particle size N_c which is of the order of 4-8 Å. The critical size should be enhanced by an increasing external magnetic field. BTO is multiferroic in a small size interval below a critical one of the BTO-particle. Let us remark that our approach can be also used to analyze BTO-NP doped with transition metal ions like FE, Mn, Co or Ni.

References

1. Wesselinowa, J.M., Michael, T., Trimper, S.: Ferroelectric nanoparticles. In: Handbook of Nanophysics, vol. 4, p. 3.1–3.29, Taylor & Francis (2010)
2. Reiss, G., Hütten, A.: Magnetic nanoparticles. In: Handbook of Nanophysics, vol. 4, pp.2.1–2.13, Taylor & Francis (2010)
3. Liu, H., Cao, B., O'Connor, C.: Intrinsic magnetism in BTO with magnetic transition element dopants. J. Appl. Phys. 109, 07B516-07B518 (2011)
4. Kimura, T., Tokura, Y.: Magnetoelectric phase control in a magnetic system showing cycloidal spin order. J. Phys.: Condens. Matter 20, 434204–434214 (2008)
5. Cao, D., Cai, M.Q., Hung, W.Y., Yu, P., Huang, H.T.: Vacancy-induced magnetism in BTO (001) thin films based on density functional theory. Phys. Chem. Chem. Phys. 13, 4738–4745 (2011)
6. Bahoosh, S.G., Trimper, S., Wesselinowa, J.M.: Origin of ferromagnetism in $BaTiO_3$ nanoparticles. Phys. Stat. Sol. RRL 5, 382–384 (2011)
7. Mangalam, R.V.K., et al.: Multiferoic properties of nanocrystalline BTO. Solid State Communication 149, 1–5 (2009); Identifying defects in multiferroic nanocrystalline BTO. J. Phys.: Condens. Matter 21, 445902–445907 (2009)

Point Spread Function Analysis of Magnetic Particles

Ingo Schmale[1], Jürgen Rahmer[1], Bernhard Gleich[1], Jörn Borgert[1], and Jürgen Weizenecker[2]

[1] Philips Technologie GmbH Innovative Technologies
Röntgenstraße 24, 22335 Hamburg, Germany
ingo.schmale@philips.com
[2] Hochschule Karlsruhe, Fakultät für Elektro- und Informationstechnik
Moltkestraße 30, 76133 Karlsruhe, Germany
juergen.weizenecker@hs-karlsruhe.de

Abstract. Starting from the basic principles of a Magnetic Particle Spectrometer (MPS), this paper explains the benefits and limitations of conventional spectral representation of the magnetization behavior of magnetic particles. After motivating the advantages of direct $\boldsymbol{m}(\boldsymbol{H})$ representation for particle analysis, it is shown how this curve, or at least its derivative, which is related to the point spread function, can be derived from the measured data. To illustrate, MPS results for Resovist® are presented, that show experimental evidence of hysteresis in dynamically acquired $\boldsymbol{m}(\boldsymbol{H})$ curves.

1 Introduction

Dynamic large-signal magnetization analysis of magnetic particles consists of subjecting them to an externally applied sinusoidal magnetic excitation field $\boldsymbol{H}(\boldsymbol{t})$ [in A/m] and of detecting their change of magnetic moment $\boldsymbol{m}$ [in Am^2] in response to it. The derivative of $\boldsymbol{m}$ manifests itself in the form of a voltage $\boldsymbol{u}$ induced in the receive coil

$$u(t) = -\mu_0 \cdot S \cdot \left(\frac{d}{dt} m(t) \right) \tag{1}$$

with $\boldsymbol{\mu_0} = 4\pi\ 10^{-7}$ Vs/Am and $\boldsymbol{S}$ [in 1/m] being the coil sensitivity.

A magnetic particle spectrometer ("MPS") is the instrument of choice to assess the suitability of magnetic particles for imaging. Different from a 3D-scanner, it excites the particles by a single frequency oscillating field $\boldsymbol{H}(\boldsymbol{t}) = \boldsymbol{H_{pk}} \sin(\boldsymbol{\omega t})$ that points in a fixed spatial direction. Since localization

T.M. Buzug and J. Borgert (Eds.): Magnetic Particle Imaging, SPPHY 140, pp. 287–292.
springerlink.com

is not required, a MPS neither has a selection field; it can thus be considered a “0-dimensional” scanner. The MPS-results are hitherto typically provided in the frequency domain. To this end, eqn. (1) is Fourier-transformed

$$u(\omega) = -j\omega \cdot \mu_0 \cdot S \cdot m(\omega) \tag{2}$$

and solved for $\boldsymbol{m}(\boldsymbol{\omega})$. Several spectra $\boldsymbol{m}(\boldsymbol{\omega})$ are typically acquired for different peak excitation amplitudes $\boldsymbol{H_{pk}}$. Fig.1 shows such a spectrum for Resovist®, today’s “gold standard”.

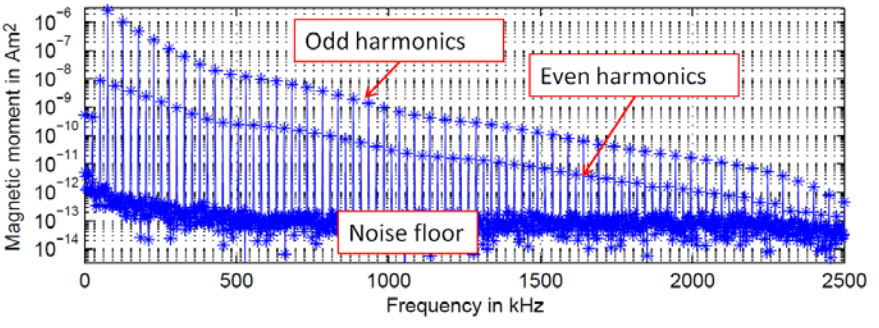

Fig. 1. Spectrum of 10µl undiluted Resovist® (500mM(Fe)) excited with $\boldsymbol{H_{pk}}$ = 25mT/μ_0 at 25kHz, as acquired using Bruker’s commercial MPS [1]. The interesting information is within the odd harmonics; even harmonics are about 2 orders of magnitude lower and due to residual external offset fields. The noise floor is at frequencies which are not harmonics of the excitation frequency. Altogether, 100 harmonics are detected.

2 Motivation

The benefit of a spectral representation is that the suitability of particles can easily be assessed: the stronger the higher order harmonics, the better for imaging. However, in order to understand particle dynamics better, it is more rewarding to look at the dependency $\boldsymbol{m}(\boldsymbol{H})$, or at least its derivative $d\boldsymbol{m}(\boldsymbol{H})/d\boldsymbol{H}$, which are both characteristic for the particles. Fig. 2 shows the Langevin-based $\boldsymbol{m}(\boldsymbol{H})$ curve, together with a hysteresis-affected magnetization curve.

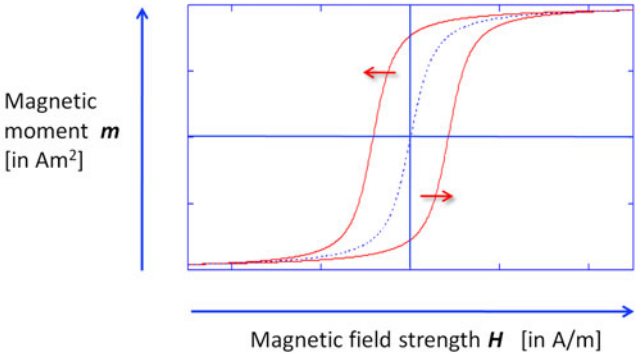

Fig. 2. Sketch of the response of a magnetic particle in terms of magnetic moment $\boldsymbol{m}(\boldsymbol{t})$ as a function of the external magnetic field $\boldsymbol{H}(\boldsymbol{t})$. The blue dotted curve shows a particle following Langevin-theory. The red solid curve deviates from such ideality by introducing hysteresis. The red arrows indicate the direction of the transition.

To study hysteresis, as predicted in [2] for particles affected by anisotropy (shape, crystal etc), looking at the magnitude spectrum alone, however, is insufficient. The information is contained within the (typically ignored) phase spectrum..

3 Method

Due to "jamming" from the far stronger externally applied field $\boldsymbol{H}(\boldsymbol{t})$, traditional spectrometers are unable to provide the response at the excitation frequency. Hence, it is impossible to recover $\boldsymbol{m}(\boldsymbol{t})$ and in consequence $\boldsymbol{m}(\boldsymbol{H})$. Whilst this limitation can only be solved by gradiometer based instruments [4], it is possible to solve for $\mathrm{d}\boldsymbol{m}(\boldsymbol{H})/\mathrm{d}\boldsymbol{t}$. To this end, the initial induction equation (1) is reformulated as

$$u(t) = -\mu_0 \cdot S \cdot \left(\frac{d}{dt} m(t)\right) = -\mu_0 \cdot S \cdot \left(\frac{d}{dH} m(H)\right) \cdot \left(\frac{d}{dt} H(t)\right) \tag{3}$$

such that the derivation is separated into two independent factors: the first $\mathrm{d}\boldsymbol{m}(\boldsymbol{H})/\mathrm{d}\boldsymbol{H}$ solely describes the magnetic particle, the second $\mathrm{d}\boldsymbol{H}(\boldsymbol{t})/\mathrm{d}\boldsymbol{t}$ solely describes the externally applied magnetic field. Since $\boldsymbol{H}(\boldsymbol{t}) = \boldsymbol{H}_{pk} \sin(\boldsymbol{\omega t})$, it follows $\mathrm{d}\boldsymbol{H}(\boldsymbol{t})/\mathrm{d}\boldsymbol{t} = \boldsymbol{\omega}\, \boldsymbol{H}_{pk} \cos(\boldsymbol{\omega t})$, so we solve equation (3) for $\mathrm{d}\boldsymbol{m}(\boldsymbol{H})/\mathrm{d}\boldsymbol{H}$:

$$\frac{d}{dH} m(H) = \frac{-1}{\mu_0 \cdot S \cdot \omega \cdot H_{pk}} \cdot \frac{u(t)}{\cos(\omega t)} \tag{4}$$

The result can be visualized as a parametric plot $\{\boldsymbol{H};\ \mathrm{d}\boldsymbol{m}(\boldsymbol{H})/\mathrm{d}\boldsymbol{H}\}$, with time $\boldsymbol{t}$ being the independent parameter, as suggested in [3]. Fig. 3 shows this for the particles from Fig. 2. The hysteresis now manifests itself in the form of split peaks.

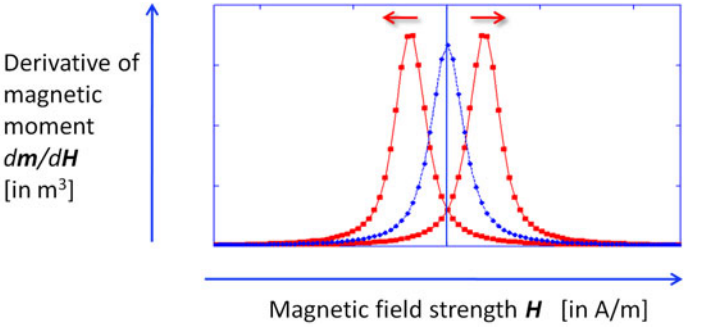

Fig. 3. Sketch of the derivate of the curves shown in fig.1, as a parametric plot. The hysteresis leads to the appearance of two peaks in the red curve, one for either direction.

Since the measured $\boldsymbol{u}(\boldsymbol{t})$ lacks an unknown fundamental frequency term $\boldsymbol{u}_{\boldsymbol{in\_phase}}$*cos($\boldsymbol{\omega t}$) + $\boldsymbol{u}_{\boldsymbol{in\_quadrature}}$*sin($\boldsymbol{\omega t}$), the division (eqn. 4) by cos($\boldsymbol{\omega t}$) leads to two error terms: a constant $\boldsymbol{e}_{\boldsymbol{in\_phase}}$ and a time-dependent $\boldsymbol{e}_{\boldsymbol{in\_quadrature}}$*tan($\boldsymbol{\omega t}$). Whilst the first is just a harmless horizontal offset in the scatter plot of d$\boldsymbol{m}$($\boldsymbol{H}$)/d$\boldsymbol{H}$, as pointed out in [3], the second is a singularity at the field reversal points, which can be expressed as a function of $\boldsymbol{H}(\boldsymbol{t})$:

$$\tan(\omega t) = \frac{\sin(\omega t)}{\cos(\omega t)} = \frac{\sin(\omega t)}{\pm\sqrt{1-\sin(\omega t)^2}} = \frac{H(t)\ /\ H_{pk}}{\pm\sqrt{1-\left(H(t)\ /\ H_{pk}\right)^2}} \qquad (5)$$

Fig. 4 shows the qualitative nature of the difference between true and measured d$\boldsymbol{m}$($\boldsymbol{H}$)/d$\boldsymbol{H}$; quantitatively no values are available.

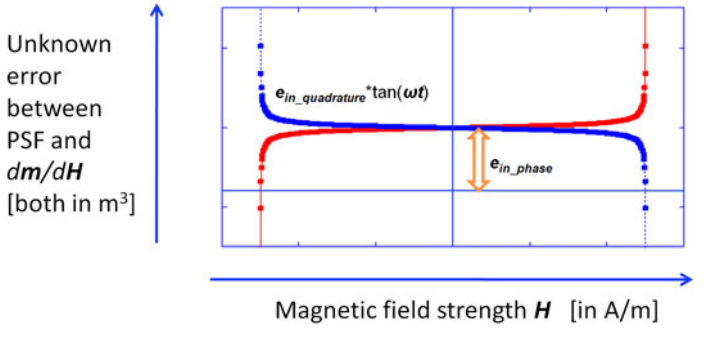

Fig. 4. Sketch of the error between the calculated PSF and the true d$\boldsymbol{m}$/d$\boldsymbol{H}$ curve.

Since the fundamental frequency component is also "jammed" within imaging, the calculated d$\boldsymbol{m}$($\boldsymbol{H}$)/d$\boldsymbol{H}$ this way shall be termed (1-dimensional) "point-spread function" (PSF) within MPI. By definition, we algorithmically suppress any discontinuities of the PSF at the field reversal points, and set the offset such that max(PSF) = 0. We plot PSF with respect to the excitation field strength $\boldsymbol{H}$, which is useful in spectrometry. Alternatively, for a given scanner hardware, PSF can be plotted versus spatial position $\boldsymbol{x}$ of the field-free point [3], which is horizontally scaled by the gradient of the selection field

$$\frac{\mathrm{H(t)}}{\mathrm{x(t)}} = \frac{\mathrm{d}}{\mathrm{dx}}\mathrm{H_{SF}(x)} \quad . \tag{6}$$

4 Results and Discussion

From the PSF of Resovist in Fig. 5, clear evidence of hysteresis can be seen. The two peaks in are set apart by approximately 4mT/$\boldsymbol{\mu_0}$.

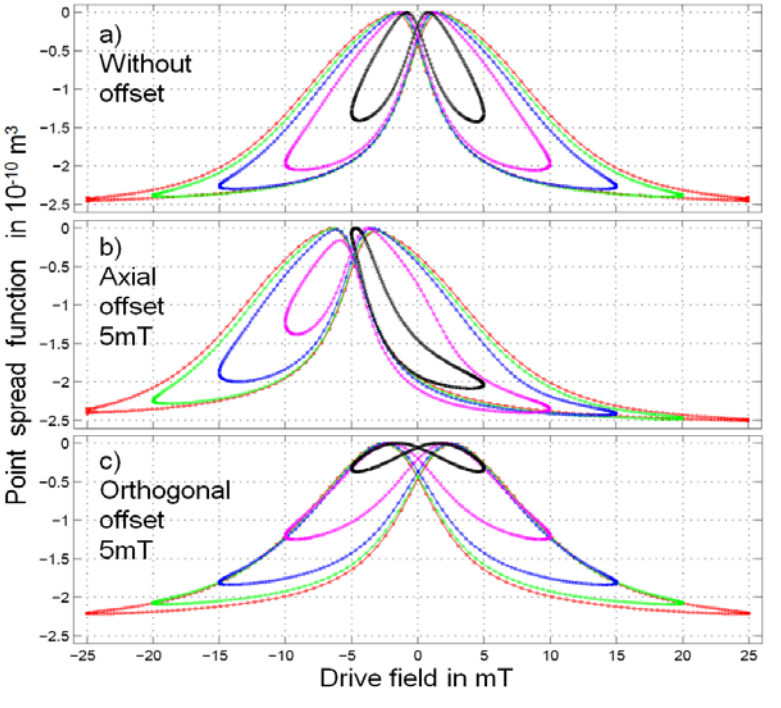

Fig. 5. Measured PSF of diluted Resovist® (1:10, 50mM(Fe)) excited at 5 different magnetic field strengths $\boldsymbol{H_{pk}}$ = 5; 10; 15; 20; 25 mT/$\boldsymbol{\mu_0}$, at 25kHz, a) without or with static magnetic offset fields in b) axial or c) orthonal direction.

To the knowledge of the authors, this is the first direct quantification of hysteresis, a phenomenon not only useful for hyperthermia [5], but also for the simultaneous imaging of distinct particles [6]. In addition to the simple model used for figs. 2 and 3, asymmetry can be observed in the edges. As the rising edge is steeper than the falling one, it seems intuitive to apply relaxation [7], despite leaving the small-signal regime [5]. Detailed particle simulations including anisotropy [2], on the other hand, predict the falling edge to be the steeper one. The observed shape of asymmetry is nevertheless explicable by a distribution of particle diameters and anisotropies.

5 Conclusion

The point-spread function can be derived with little effort from the spectral magnetization response as provided by a magnetic particle spectrometer. It allows investigating hitherto concealed properties of magnetic particles such as hysteresis and asymmetry.

Acknowledgements. The authors gratefully acknowledge funding support from the German Federal Ministry of Education and Research (BMBF) under grant numbers FKZ 13N9079 and FKZ 13N11086.

References

1. Snyder, S.R., Heinen, U.: Characterization of Magnetic Nanoparticles for Therapy and Diagnostics. Bruker BioSpin Application note 04/11 T128513, http://www.bruker-biospin.com/mps-tech.html, and http://mps-apps.html
2. Weizenecker, J., et al.: Particle dynamics of mono-domain particles in MPI. In: First. Int. Workshop on MPI, pp. 3–15. World Scientific Publishing (2010) ISBN 981-4324-67-1
3. Lu, K., et al.: The impact of filtering direct-feedthrough on the x-space theory of magnetic particle imaging. In: Proceedings of SPIE, paper 7965-90 (2011)
4. Biederer, S., et al.: A compensation unit for a magnetic particle spectrometer to measure the full magnetization spectrum of SPIO nanoparticles. In: Proceedings of BMT, Freiburg (September 2011); Biomed. Tech. 56(suppl.1) (2011)
5. Hergt, R., Dutz, S., Zeisberger, M.: Validity limits of the Néel relaxation model of magnetic nanoparticles for hyperthermia. Nanotechnology 21 (2010)
6. Schmale, I., et al.: Particle distinction within MPI. In: Proceedings of BMT, Rostock (September 2010); Biomed. Tech. 55(suppl.1) (2010)
7. Croft, L.R., et al.: The x-space formulation of Magnetic Particle Imaging including non-negligible relaxation effects. In: Proceedings of SPIE, paper 7965-93 (2011)

Magneto-Relaxometry

Spatially Resolved Measurement of Magnetic Nanoparticles Using Inhomogeneous Excitation Fields in the Linear Susceptibility Range (<1mT)

Uwe Steinhoff[1], Maik Liebl[1], Martin Bauer[1], Frank Wiekhorst[1], Lutz Trahms[1], Daniel Baumgarten[2], and Jens Haueisen[2]

[1] Physikalisch-Technische Bundesanstalt
Abbestrasse 2-12
Berlin, D-10587, Germany
uwe.steinhoff@ptb.de
[2] Institute of Biomedical Engineering and Informatics
Ilmenau University of Technology
Ilmenau, D-98684, Germany

Abstract. For small excitation fields in the microtesla (μT) range, the dependency of the magnetic moment of magnetic iron oxide nanoparticles (MNP) on the external field can be regarded as linear. Sensitive superconducting quantum interference devices (SQUIDs) enable the detection of the response of MNP in biological tissue in the pT range. The coregistration of the excitation field is reduced by appropriate geometrical configuration of excitation coil and sensor coil. MNPs in a wide range of mean diameter and distribution parameters can be used for signal generation. The spatial distribution of MNP is reconstructed using data from a parallel multi-sensor and sequential multi-coil arrangement and applying linear estimation techniques. The time delayed response of MNP due to Brownian and Néel relaxation processes represents a specific signal not being influenced by the diamagnetic contribution of water in the tissue. We present the theoretical background and measurement data from different setups that will exemplify the concept.

1 Introduction

The application of magnetic nanoparticles both for diagnostic and therapeutic purposes is an area of intensive research in biomedical science. These developments require a quantitative measurement technique for the noninvasive determination of magnetic nanoparticle distributions in biological tissue. The general approach to solve this problem is to modify established magnetic measurement techniques that have been developed for lab specimens, so that they will also work noninvasively on biological

T.M. Buzug and J. Borgert (Eds.): Magnetic Particle Imaging, SPPHY 140, pp. 295–300.
springerlink.com

objects of larger physical extent. In this paper we investigate the applicability of well-known linear magnetic susceptibility and magnetic relaxation measurements for spatially resolved quantification of magnetic nanoparticles in tissue. The theoretical background is summarized and some initial experimental results are presented.

2 Material and Methods

We assume that nanoparticles of known magnetic susceptibility χ are injected into a biological system and we are interested in the spatial distribution of the concentration c[m^{-3}] of the nanoparticles over the biological object. The volume of interest is partitioned into K voxel volumes V_k with homogeneous particle concentration c_k. For a noninvasive measurement the magnetizing field H_k in voxel V_k is induced by coils outside the biological object constructed of piecewise linear segments i carrying an electrical current I [1].

$$\mathbf{H}_k = \frac{1}{4\pi}\sum_i \left[\frac{s_{1,i}+s_{2,i}}{s_{1,i}\cdot s_{2,i}} \cdot \frac{\mathbf{s}_{2,i}\times\mathbf{s}_{1,i}}{s_{1,i}\cdot s_{2,i}+\mathbf{s}_{1,i}\cdot\mathbf{s}_{2,i}} \cdot I_i \right] \tag{1}$$

The terms $\boldsymbol{s}_1$ and $\boldsymbol{s}_2$ denote the distance vectors from voxel k to the end points of the current filament i. The magnetic moment of the k-th voxel is given by:

$$\mathbf{m}_k(c_k) = \frac{V_k m^2}{3\,\mathrm{k_B} T}\mu_0 \mathbf{H}_k c_k \tag{2}$$

since the Langevin function describing the magnetic behavior of the nanoparticles can be linearized for $| m\mu_0 H / \mathrm{k_B} T | << 1$. Here, m is the magnetic moment of a single nanoparticle in units of the Bohr magneton μ_B, $\mathrm{k_B}$ is the Boltzmann constant and T the temperature. A magnetic field sensor installed outside the biological object will measure the directional magnetic induction B_k from the k-th voxel:

$$B_k(c_k) = \frac{\mu_0}{4\pi}\left(\frac{3\mathbf{n}^{\mathrm{T}}\left(\mathbf{r}_k^{\mathrm{T}}\mathbf{r}_k\right)}{r_k^5} - \frac{\mathbf{n}^{\mathrm{T}}}{\mathrm{r_k^3}} \right)\mathbf{m}_k(c_k) \tag{3}$$

with μ_0 being the magnetic vacuum permeability, $\boldsymbol{r}$ the distance between voxel and sensor, $\boldsymbol{n}$ the sensitive direction of the sensor. The contributions from all voxels have to be summed up to get the total signal sensor in sensor s [2]:

$$B_s(\mathbf{c}) = \sum_k L_k c_k = \mathbf{L}\mathbf{c} \tag{4}$$

with

$$L_k = \frac{\mu_0^2 V_k m^2}{48\pi^2 \mathrm{k_B} T}\left(\frac{3\mathbf{n}^{\mathrm{T}}\left(\mathbf{r}_k^{\mathrm{T}}\mathbf{r}_k\right)}{r_k^5} - \frac{\mathbf{n}^{\mathrm{T}}}{r_{\mathrm{k}}^3} \right)\cdot \sum_i \left(\frac{s_{1,i}+s_{2,i}}{s_{1,i}\cdot s_{2,i}} \frac{\mathbf{s}_{2,i}\times\mathbf{s}_{1,i}}{s_{1,i}\cdot s_{2,i}+\mathbf{s}_{1,i}\cdot\mathbf{s}_{2,i}} I_i \right)$$

where the vector **L** contains the sensitivities of the setup for the voxels and **c** contains the local nanoparticle concentrations. By using AC-susceptometry (ACS) or magnetorelaxometry (MRX), we exploit the time delayed response of the magnetic nanoparticles to external field changes in order to distinguish their signal from the diamagnetic background of the water in the tissue. The characteristic equation of the MNP temporal response in small excitation fields is

$$\tau_{eff}\,\mathrm{d}m_k(t)/\mathrm{d}t + m_k(t) = \chi H(t)\,. \tag{5}$$

Equ. (5) can be solved in principle for any special excitation function leading to a further amplitude factor ξ. For the sinusoidal excitation function in ACS we get $\xi(\omega,\tau_{eff}) = (\mathrm{i}\omega\tau_{eff}+1)^{-1}$ and for the step function in MRX we get $\xi(t,\tau_{eff}) = \exp(-t/\tau_{eff})$ [3]. Variation of coil position or sensor position relative to the biological object by using parallel multi-sensor and sequential multi-coil arrangements results in linearly independent realizations of Equ. (4) [4]. The distribution of nanoparticles is reconstructed by linear estimation techniques applying the Moore-Penrose pseudoinverse of **L** [5,6]:

$$\hat{\mathbf{c}} = \xi^{-1}\left(\mathbf{L}^{\mathrm{T}}\mathbf{L}\right)^{-1}\mathbf{L}^{\mathrm{T}}\mathbf{B}\,. \tag{6}$$

3 Experiments and Results

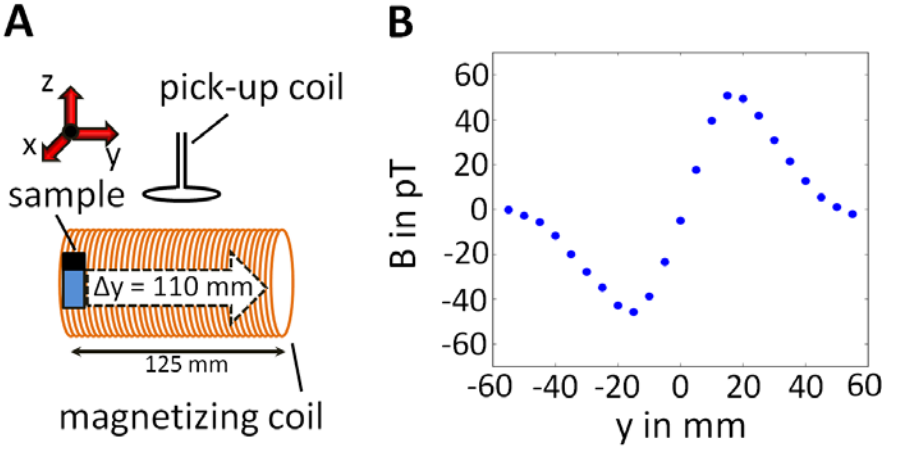

Fig. 1. A) Experimental setup for ACS .The sample is shifted through the coil (d = 25 mm, h = 125 mm, N = 250). **B**) The measured AC-amplitude is clearly modulated by the MNP according to the y-position of the sample.

In a first experiment, we placed a small MNP sample (450 µl suspension, Berlin Heart) inside a long coil (d=25 mm, h=125 mm, N=250) according to

Fig. 1A). An AC excitation current (I=50 µA, f=28.6 Hz) produced an inner field of about 125 nT at the coil centre and a residual field in the pick-up coil of the SQUID of about 1 nT. The sample was shifted for 110 mm along the y-axis in steps of 5 mm. The AC amplitude was measured by the SQUID at each sample position and the residual field was subtracted. The result is depicted in Fig. 1B). In a second experiment a shorter coil (d=37.5 mm, h=28 mm, N=50) was placed close to a multi-SQUID system and the sample was moved over 48 mm through the opening of the coil and at each position magnetized with an MRX step function (Figs. 2A), 2B)). Fig. 2C shows the source distribution reconstructed on a 20 x 50 mm^2 source grid using Equ. (6). In a third experiment, three samples containing different amounts of MNP (3.9 to 39 µgFe absolute iron mass) were distributed over a distance of 80 mm (Fig. 3A). The samples were magnetized (4 A/m - 60 A/m) using three sequentially driven field coils (d = 25 mm, h = 10 mm, N = 25). The distance of the SQUID to the closest sample was about 50 mm. The magnetic moments and the iron mass of the three samples in three different configurations could be reconstructed in the microgram range using Equ. (6) (Fig. 3B). The mean difference between measured and estimated iron mass amounted to 3 µg(Fe).

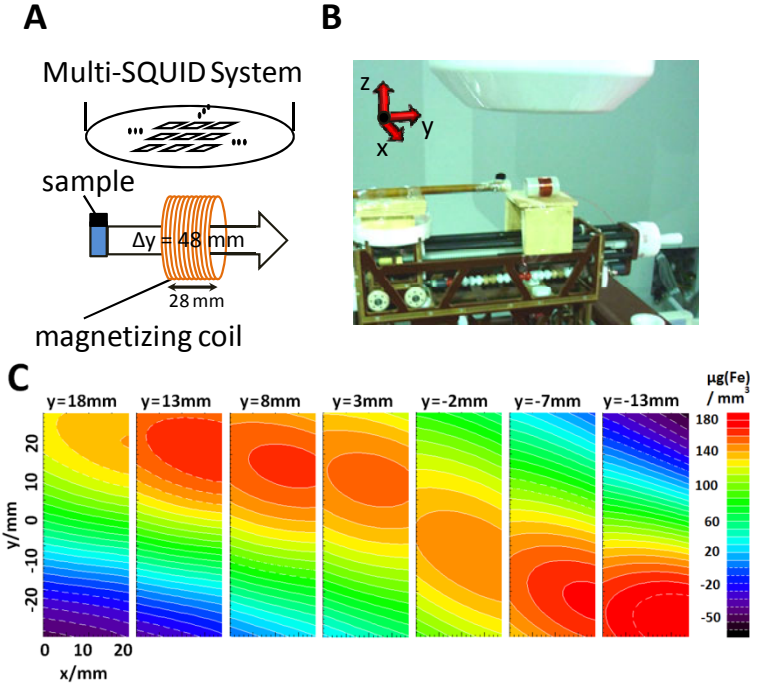

Fig. 2. A) Setup for MRX experiment in an inhomogeneous excitation field. **B**) Experimental realization. On top the multi-SQUID system is visible. **C**) Reconstruction of the iron concentration on a 20 x 50 mm^2 source grid in the x-y plane for different real sample positions y_0.

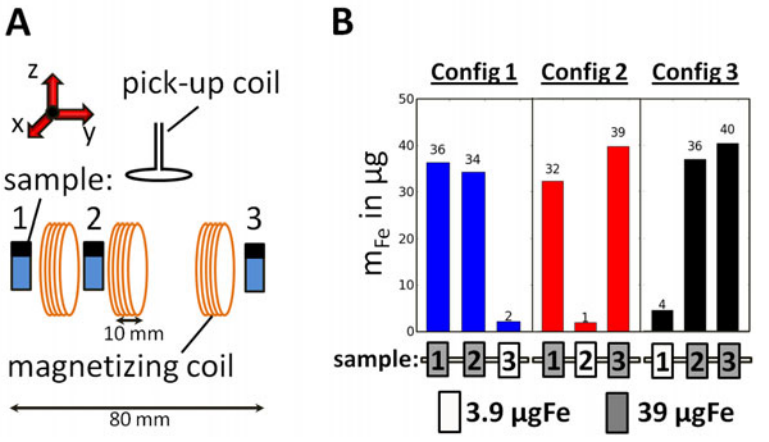

Fig. 3. A) MRX for simultaneous measurement of 3 samples by sequential activation of 3 coils with inhomogeneous excitation field. **B**) Reconstruction of the MNP amount for 3 different configurations according to Equ. (6).

4 Conclusion

It is possible to reconstruct the spatial distribution of magnetic nanoparticles non-invasively from measurements of their magnetic response to time-varying inhomogeneous external magnetization fields below 1 mT. In principle, arbitrary signal shapes can be used for the excitation function. A step function and a sinus function have been experimentally demonstrated. The inverse problem can be solved after a detailed modeling of geometry and environmental parameters of the forward problem. The experimental sensitivity amounted to a few µg Fe over a source extent of several cm. Further research is needed to explore the spatial resolution, the temporal particle response and the practical applicability of the method.

Acknowledgement. This work was financially supported by the DFG research program TR408/5-2.

References

1. Hanson, J.D., Hirshman, S.P.: Compact expressions for the Biot-Savart fields of a filamentary segment. Phys. Plasmas 9, 4410 (2002)
2. Steinhoff, U., Wiekhorst, F., Baumgarten, D., Haueisen, J., Trahms, L.: Imaging of magnetic nanoparticles based on magnetorelaxometry with sequential activation of inhomogeneous magnetization fields. Biomed. Tech. 55(S1(A)), 22–25 (2010)

3. Wiekhorst, F.: Magnetorelaxometry assisting biomedical applications of magnetic nanoparticles. Pharm. Res. (2012), doi:10.1007/s11095-011-0630-3
4. Crevecoeur, G., Baumgarten, D., Steinhoff, U., Haueisen, J., Trahms, L., Dupré, L.: Advancements in magnetic nanoparticle reconstruction using sequential activation of excitation coil arrays using magnetorelaxometry. Accepted in IEEE Trans. Mag. (2011)
5. Sepulveda, N.G., Thomas, I.M., Wikswo Jr., J.P.: Magnetic susceptibility tomography for three-dimensional imaging of diamagnetic and paramagnetic objects. IEEE Trans. Magn. 30, 5062–5069 (1994)
6. Baumgarten, D., Liehr, M., Wiekhorst, F., Steinhoff, U., Münster, P., Miethe, P., Trahms, L., Haueisen, J.: Magnetic nanoparticle imaging by means of minimum norm estimates from remanence measurements. Med. Biol. Eng. Comp. 46, 1177–1185 (2008)

Magnetorelaxometry for In-Vivo Quantification of Magnetic Nanoparticle Distributions after Magnetic Drug Targeting in a Rabbit Carcinoma Model

Frank Wiekhorst[1], Maik Liebl[1], Uwe Steinhoff[1], Lutz Trahms[1], Stefan Lyer[2], Stephan Dürr[2], and Christoph Alexiou[2]

[1] Physikalisch-Technische Bundesanstalt, Abbestraße 2-12
10587 Berlin, Germany
frank.wiekhorst@ptb.de
[2] Department of Oto-Rhino-Laryngology, Head and Neck Surgery,
Section for Experimental Oncology and Nanomedicine,
Else Kröner-Fresenius-Stiftung-Professorship,
University Medical Center Erlangen, Waldstraße 1, 91054 Erlangen, Germany

Abstract. Multi-channel magnetorelaxometry (MRX) is demonstrated to locate and quantify several foci of a magnetic nanoparticle (MNP) distribution after magnetic drug targeting (MDT) in an in-vivo rabbit carcinoma model. By this non-invasively technique MNP accumulations of lateral extensions up to 20 x 30 cm^2 can easily be accessed in biological tissue. The total measurement duration of about 20 min including preparation of the rabbit and measurement of two regions of interests (ROI), tumor and thorax (liver, lung and spleen), enables a high throughput of animals. Modelling the MNP distribution either by magnetic point dipoles (ROI tumor) or by an extended, homogenously magnetized body (ROI thorax) of simple geometry, e.g. cuboid, the total magnetic moment and location of each focus is determined by minimum norm estimation. Simultaneously, vital functions like respiration and heart activity can be monitored directly and non-invasively during the MRX measurements. Thus, our MRX procedure gains valuable information for monitoring of MDT procedures in large scale animal models.

1 Introduction

In Magnetic Drug Targeting (MDT) magnetic nanoparticles (MNP) are used as carriers for chemotherapeutic agents [1]. They are administered into a supplying artery or vein and then accumulated at the tumor region by an external magnetic field gradient. The investigation of the complex interplay

T.M. Buzug and J. Borgert (Eds.): Magnetic Particle Imaging, SPPHY 140, pp. 301–305.
springerlink.com

between physical and physiological parameters during MDT requires a detailed quantitative knowledge about the resulting MNP distribution and is studied in in-vivo carcinoma animal models. Apart from the amount of MNP that can be enriched in the tumor by the force of the targeting magnet, the uptake of MNP by other organs like liver, lung and spleen is of vital importance.

Magnetorelaxometry (MRX) is a non-invasive technique that provides such quantitative and spatially resolved information [2]. The usability of this technique has been proven previously for the in-vitro quantification of MNP accumulations after MDT in an artery model [3] and after MDT of magnetic aerosol in a pig lung model [4]. Here, we present the application of in-vivo MRX on tumor bearing rabbits (VX-2 squamous cell carcinoma) after MDT to quantify the amount and distribution of MNP after intraarterial application.

2 Material and Methods

Magnetic drug targeting application (MDT): The VX2 squamous cell carcinoma were implanted at the hind leg of New Zealand White rabbits and grown for 2-3 weeks. For the MDT application the rabbit was placed with its tumor underneath the pole tip of an electromagnet (Siemens, magnetic field gradient: 72 T/m) and 1-2.5 ml MNP suspension (iron oxide nanoparticles coated by phosphated starch polymers and bound to mitoxantrone as chemotherapeutic agent, c(Fe): 6.3 $mg \cdot ml^{-1}$, hydrodynamic diameter: 100(40) nm) were injected into the supplying femoral artery close to the tumor. The field gradient at the tumor site was maintained for up to 90 min to restrain the drug locally. As a reference we prepared 200 µl of the administered MNP in varying dilution steps (10^0,10^1,10^2) immobilized in plaster and determined their MRX moment amplitude.

All experiments were approved by the regional animal care committee (District Government Mittelfranken 54-2531.31-27/06) and were in accordance with international guidelines on the ethical use of animals.

Magnetorelaxometry (MRX): MRX measurements consist of two parts [2]: First the MNP are exposed to a moderate homogeneous magnetizing field of about 1 mT generated by a Helmholtz coil (*d=84 cm*) to (gradually) align their magnetic moments. Then, the field is rapidly switched off and the magnetic relaxation of the MNP moments is recorded by a magnetic field sensor for some time interval. For spatially resolved MRX we utilized the PTB 304-SQUID system (a multi-channel system detecting the magnetic field vector $\mathbf{B}=B_x,B_y,B_z$ within an area of about 20 cm diameter at different horizontal layers) operated in a magnetically shielded room. For the measurement the anesthetized rabbit is fastened in lateral position on a Perspex support. To determine the body location with respect to the

sensor system two small copper coils are fixed at the tumor (5 turns, m_{ac}/I =26(3) cm^2) and thorax (7 turns, m_{ac}/I =83(4) cm^2) region, additionally. After 60 s magnetizing (field orientation parallel to sensor B_z-direction) outside the shielded room the rabbit is rapidly (within 7 s) transferred and positioned below the sensor system. The relaxation of the magnetic field from an MNP distribution is then recorded for at least 75 s at a sampling rate of 250 Hz. Each MRX measurement is followed by subsequent measurements of the two marker coils driven by an AC current (I: 5-100 mA, f=29 Hz) without changing the position of the rabbit. The coil locations (and moments as a control) are determined by fitting the data to a magnetic point dipole model using a Levenberg-Marquardt algorithm.

To account for the large animal extension of about 50 cm compared to the sensor array diameter of about 20 cm two MRX measurements are performed for each rabbit, one with the sensor array focussed at the tumor position (*ROI tumor*) near the rabbit's hind leg and another measurement with the sensor array above the thoracic region of the animal (*ROI thorax*, with MNP accumulated in liver, lung, spleen).

Each MRX measurement is followed by an automated data preprocessing. First by constructing a software planar gradiometer using a peripheral sensor within each layer as reference the SNR of the data is enhanced. Then timing parameters of the MRX interval are determined (t_{start}=15 s after magnetic field is switched off, $t_{end}=t_{start}+60$ s), from which the measured relaxation field pattern $B(r,t_{start})$-$B(r,t_{end})$ is formed.

These patterns are displayed together with the two marker coil locations enabling a first assessment of the data.

3 Results and Discussion

As an example Fig. 1 shows typical MRX magnetic field patterns. Already by mere visual examination of these maps, two foci, a stronger at *ROI tumor* and a smaller at *ROI thorax* can be distinguished. Since the magnetization direction is determined to be parallel B_z, the lateral centre of gravity is at the (local) extreme value of the magnetic field.

Assuming an extended homogenous MNP distribution (cuboid with edge lengths 2 x 6.5 x 6.5 cm^3) for *ROI thorax* and a point-like accumulation for *ROI tumor* we determined the locations and magnetic moments of both ROIs by an iterative minimum norm estimation scheme. Normalizing to the reference sample moment measured under identical conditions an amount of 1.5(2) mg Fe in *ROI thorax* and 3.4(3) mg Fe in ROI tumor was estimated. The centres of gravity of both ROIs are found within 1 cm from the corresponding marker coil locations.

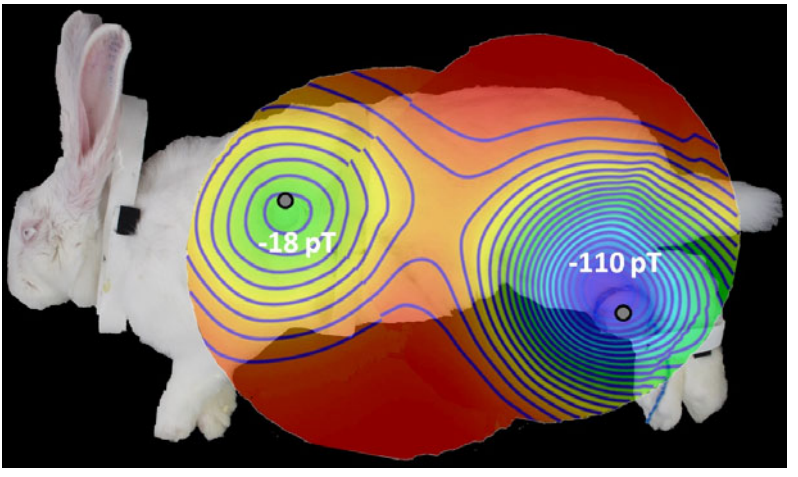

Fig. 1. Combined magnetic field pattern (isocontour plot, field step width 2 pT) of the *ROI thorax* and the *ROI tumor* MRX measurement overlayed a photograph of the rabbit. The grey dots mark the lateral (center) positions of the ROIs with regard to the sensor system in the MRX measurements as determined from the two marker coil field patterns.

Within 2 hours six rabbits could be measured by in-vivo MRX including anesthetizing of the rabbit, fixating and wiring of the marker coils. Additionally to the MRX relaxation, magnetic signal traces of the rabbit's heart activity and breathing are included in the measurement data as shown in Fig. 2.

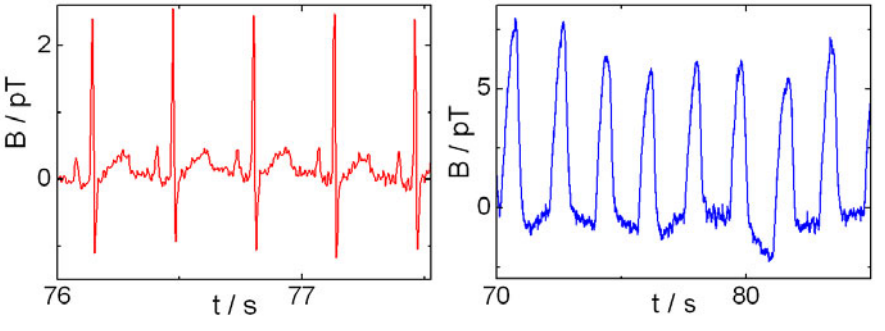

Fig. 2. Monitoring of vital functions during MRX measurements. Left: magnetocardiogram reflecting heart activity measured by a bottom B_z-sensor above the rabbit's heart. Right: Breathing as seen by a B_z-sensor above the abdominal region of the rabbit.

4 Conclusion

The multi-channel MRX allows one to non-invasively locate and quantify several foci of an MNP distribution in-vivo. The total extent of the investigated region amounts up to 20 x 30 cm^2 and may easily be increased by performing additional MRX measurements. Together with a detection limit of 100 µg Fe absolute for this type of MNP and the present MRX setup, valuable information for monitoring of MDT procedures in large scale animal models can be generated. A total measurement duration of about 20 min including preparation enables a high throughput of our method. Simultaneously, vital functions like respirative and heart activity can be monitored directly and non-invasively during the MRX measurements.

Acknowledgements. This work was financially supported by the DFG research programs “Magnetische Nanopartikel für die Krebstherapie” TR408/4-1, AL552/3-1 and “Magnetische Nanopartikel für die Zelluläre und Molekulare MR-Bildgebung” TR408/5-2 and the BMBF project FKZ:01EX1012B.

References

1. Alexiou, C., Jurgons, R., Schmid, R.J., Bergemann, C., Henke, J., Erhardt, W., Huenges, E., Parak, F.: Magnetic drug targeting—biodistribution of the magnetic carrier and the chemotherapeutic agent mitoxantrone after locoregional cancer treatment. J. Drug Target 11, 139–149 (2003)
2. Wiekhorst, F., Steinhoff, U., Eberbeck, D., Trahms, L.: Magnetorelaxometry assisting biomedical applications of magnetic nanoparticles. Pharm. Res (2011) (in press), doi:10.1007/s11095-011-0630-3
3. Seliger, C., Jurgons, R., Wiekhorst, F., Eberbeck, D., Trahms, L., Iro, H., Alexiou, C.: In vitro investigation of the behaviour of magnetic particles by a circulating artery model. J. Magn. Magn. Mater. 311, 358–362 (2007)
4. Wiekhorst, F., Steinhoff, U., Eberbeck, D., Schwarz, K., Richter, H., Renner, R., Roessner, M., Rudolph, C., Trahms, L.: Quantification of Magnetic Nanoparticle Concentration in Pig Lung Tissue after Magnetic Aerosol Drug Targeting by Magnetorelaxometry. In: Vander Sloten, J., Verdonck, P., Nyssen, M., Haueisen, J. (eds.) IFMBE Proceedings ECIFMBE 2008. IFMBE, vol. 22, pp. 2326–2329. Springer, Heidelberg (2008)

Imaging Technology and Safety Aspects

A Control Unit for a Magnetic Particle Spectrometer

R. Marquina-Sanchez[1], S. Kaufmann[1], M. Ryschka[1], T.F. Sattel[2], and T.M. Buzug[2]

[1] Medical Electronics Lab, Stephensonstraße 3,
Lübeck University of Applied Sciences
Lübeck, 23562, Germany
rmarquina@gmail.com,
kaufmann@fh-luebeck.de,
ryschka@fh-luebeck.de
[2] Institute of Medical Engineering,
University of Lübeck, Building 64
Ratzeburger Allee 160, Lübeck, 23562, Germany
sattel@imt.uni-luebeck.de,
buzug@imt-luebeck.de

Abstract. Magnetic Particle Imaging (MPI) is a quite new imaging technique, based on the non-linear magnetization behavior of superparamagnetic iron oxide nanoparticles (SPIOs). These SPIOs are applied to a patient as tracer material. An important key aspect for successful and reliable imaging is tracer development and characterization. Hence, a Magnetic Particle Spectrometer (MPS) is needed to perform extensive studies about the SPIOs dynamic magnetization behavior. The MPS hardware build-up consists mainly of a drive coil, a receive coil, a cooling circuit, amplifiers and a control unit. This paper proposes a new self-contained control unit hardware system based on a System-On-Chip (SoC) Field-Programmable-Gate-Array (FPGA). The control unit controls, collects, and maintains data acquisition, coil excitations and the behavior of the cooling circuit in real-time. The SoC is also able to pre-process measurement data (i.e. filtering, averaging, up- and down-sampling etc.). The generation of the magnetic field in the drive coil is controlled by a 14 bit Digital/Analog Converter (DAC) coupled with an external amplifier. The receive coil signal is amplified and digitalized via a 14 bit Analog/Digital Converter (ADC). To prevent system overheating, also temperature is supervised and kept under certain limits. For that purpose four Resistive Thermal Devices (RTDs) in combination with a cooling unit are utilized. The transmission of measurement data is realized via USB 2.0 with up to 40 MByte/s. The USB link can also be used to setup the control unit and as power supply for the self-containing SoC.

T.M. Buzug and J. Borgert (Eds.): Magnetic Particle Imaging, SPPHY 140, pp. 309–312.
springerlink.com

1 Introduction

Magnetic Particle Imaging (MPI) is a relatively new tomographic real-time imaging technique, based on measurement and reconstruction of the spatial distribution of a magnetic tracer material. The used tracer consists of superparamagnetic iron oxide nanoparticles (SPIOs). For the measurements, oscillating magnetic fields are applied and the SPIO response is measured. This magnetic particle moment is about eight times larger than the proton magnetic moment used in Magnetic Resonance Imaging (MRI), which gives higher sensitivity compared to other medical imaging techniques [1] [5].

To obtain accurate measurements, a reliable characterization of the used tracer material is needed. This characterization can be done with a Magnetic Particle Spectrometer (MPS) [2] [3] [4]. The MPS hardware set-up consists of five main parts: a drive coil, a receive coil, a cooling circuit, an amplification stage and a control unit [6]. The present work presents a cost-sensitive self containing embedded Field Programmable Gate Array (FPGA) based System on Chip (SoC) control unit for an MPS system.

2 Material and Methods

The proposed self-contained control unit hardware system is in charge for data acquisition and signal excitation. Moreover, it also provides the communication to a remote PC and commands the behavior of the cooling circuit in real-time. The control unit is also able to preprocess the acquired data directly (i.e. filtering, averaging, up- and down-sampling etc.). The SoC firmware can be easily adapted for changing requirements or research purposes. A block diagram of the control unit is shown in Figure 1.

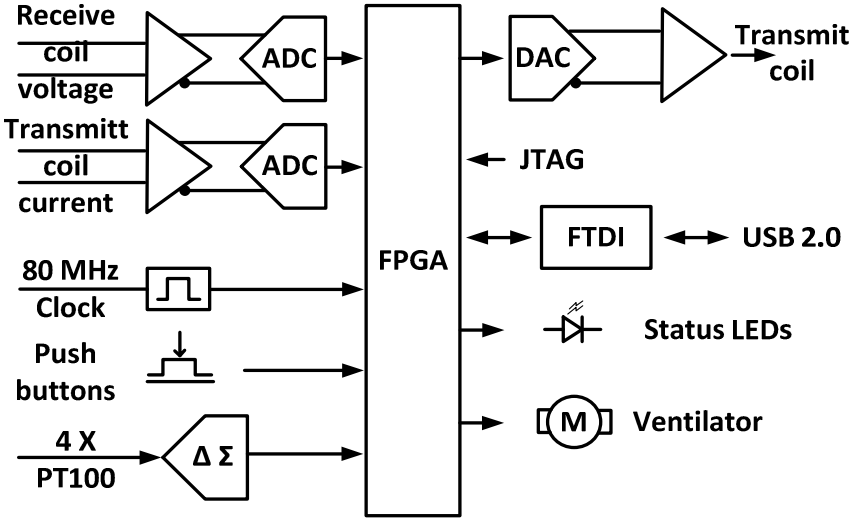

Fig. 1. Control unit block diagram

The central part of the control unit is a Lattice XP2-5E FPGA. The FPGA offers a JTAG interface and persistent on-chip flash to ensure reliable operation and fast boot times. An 80 MHz external low jitter clock is used to ensure reliable measurements. To facilitate easy software development and usage status LEDs, as well as user interface push buttons are attached.

The excitation of the drive coil is controlled by a 14 bit Digital/Analog Converter (DAC) in combination with an external amplification stage. The signal input from the receive coil is externally amplified before arriving to a 14 bit Analog/Digital Converter (ADC), which allows for sampling rates up to 25 MSPS. For accurately acquiring the current in the drive coil a second ADC is used.

The cooling circuit relies on four Remote Temperature Sensors (RTS) equipped with four PT100, allowing for accurate temperature measurements. In case of the detection of overheating, the FPGA activates the cooling ventilator, maintaining a constant cooling of heated parts. The data transmission from the system to a remote computer for the reconstruction of the measurement data is realized via an USB 2.0 interface, which provides up to 40 MByte/s. A FTDI FT2232H chip handles the USB communication by acting as synchronous FIFO interface in USB slave mode.

Once the design was done, a Printed Circuit Board (PCB) has been developed, by following strict development constrains. With these constrains good manufacturability and signal integrity are ensured [7] [8]. The final PCB has only four layers and a board size of approximately 12.5 cm × 7.0 cm.

3 Discussion and Conclusion

This contribution presents a cost-sensitive self containing embedded control unit for an MPS. The proposed design compiles all needs on an MPS and enables great flexibility through a well established FPGA hardware architecture. The system promises very good results, by keeping noise levels low and making data prepossessing directly on the embedded system possible. Once the design is manufactured the performance of the system will be evaluated and reported in details.

References

1. Gleich, B., Weizenecker, J.: Tomographic imaging using the nonlinear response of magnetic particles. Nature 435, 1214–1217 (2005)
2. Biederer, S., Kren, S., Sattel, T.F., Erbe, M., Knopp, T., Lüdtke-Buzug, K., Buzug, T.M.: Ein magnetisches Partikel-Spektrometer zur Messung der Magnetisierung von Nanopartikeln unter der Verwendung von AC- und DC-Feldern, 44. In: Jahrestagung der Deutschen Gesellschaft für Biomedizinische Technik im VDE - BMT 2010, Rostock, Germany, vol. 55, p. 295 (2010)

3. Biederer, S., Sattel, T.F., Kren, S., Erbe, M., Knopp, T., Lüdtke-Buzug, K., Buzug, T.M.: A Spectrometer Using Oscillating and Static Fields to Measure the Suitability of Super-Paramagnetic Nanoparticles for Magnetic Particle Imaging. In: World Molecular Imaging Congress, Kyoto, Japan, p. 96 (2010)
4. Biederer, S., Sattel, T.F., Knopp, T., Erbe, M., Lüdtke-Buzug, K., Vogt, F.M., Barkhausen, J., Buzug, T.M.: A Spectrometer to Measure the Usability of Nanoparticles for Magnetic Particle Imaging, Magnetic Nano-particles: Particle Science, Imaging Technology, and Clinical Applications, vol. 1, pp. 60–65. World Scientific Publishing Company (2010)
5. Biederer, S., Knopp, T., Sattel, T.F., Lüdtke-Buzug, K., Gleich, B., Weizenecker, J., Borgert, J., Buzug, T.M.: Estimation of Magnetic Nanoparticle Diameter with a Magnetic Particle Spectrometer. In: Dössel, O., Schlegel, W.C. (eds.) World Congress on Medical Physics and Biomedical Engineering, WC 2009, September 2009. IFMBE, vol. 25/VIII, pp. 61–64. Springer, Heidelberg (2009)
6. Biederer, S., Sattel, T., Knopp, T., Lüdtke-Buzug, K., Gleich, B., Weizenecker, J., Borgert, J., Buzug, T.M.: A Spectrometer for Magnetic Particle Imaging. In: Vander Sloten, J., Verdonck, P., Nyssen, M., Haueisen, J. (eds.) ECIFMBE 2008. IFMBE, vol. 22, pp. 2313–2316. Springer, Heidelberg (2008)
7. Techreport (High-SpeedPCBDesignConsiderations) Lattice Technical Note TN1033 - High-Speed PCB Design Considerations Lattice Semiconductor Corporation, April 21 (2010)
8. Mitzner, K. (ed.): Complete PCB Design Using OrCad Capture and PCB Editor Newnes. Elsevier (2009)

Optimization of Circular Current Distributions for Magnetic Field Generation in MPI: A Comparison of the Selection Field Coil and the Drive Field Coil Geometry

Timo F. Sattel, Marlitt Erbe, and Thorsten M. Buzug

Institute of Medical Engineering, University of Lübeck, Ratzeburger Allee 160
23562 Lübeck, Germany
{sattel,buzug}@imt.uni-luebeck.de

Abstract. Magnetic Particle Imaging in general applies two different types of magnetic field geometries in order to obtain information about the spatial distribution of magnetic nanoparticles. First, a static gradient field called selection field is used for spatial encoding. It either provides a field free point or a field free line. Second, additional uniform drive fields are superimposed to steer the field free region through the field of view. Most efficiently, the latter fields are orientated perpendicularly to each other. For field generation, current carrying coils are used, while the static field generation may be supported by strong permanent magnets. In this contribution, discs carrying circular current distributions are investigated for generating both types of field geometries. These distributions are optimized with respect to the achieved field quality as well as to the total power loss.

1 Introduction

Up to now, most of the presented magnetic particle imaging (MPI) devices apply symmetric sets of circular coils carrying direct or alternating currents for magnetic field generation [1, 2, 3]. In theory, these geometries are well known as Helmholtz coil configuration carrying identical currents on each coil and as Maxwell coil configuration carrying currents in opposite directions.

According to the theory, the generated fields are either homogenous or have a linear gradient at the center point. The drawbacks of these coil geometries, however, are that they assume infinitely or at least sufficiently thin wires, a given ratio of coil radius to the distance to the center plane and the restriction to the center point concerning the declaration about field geometry. In other words, these coil geometries are not suited for MPI since acceptable power losses are an issue and the constraints about field

T.M. Buzug and J. Borgert (Eds.): Magnetic Particle Imaging, SPPHY 140, pp. 313–318.
springerlink.com

quality have to be fulfilled within a given field of view (FOV). It is expected that the demands on field quality will further increase to apply new, fast reconstruction methods [4, 5].

In some MPI scanner setups, the same coil pair is used for generation of uniform as well as gradient fields by applying appropriate current directions. This may be efficient in terms of space usage and total power loss but may not lead to optimal field geometries.

2 Material and Methods

The problem of appropriate field generation will be formulated as minimization problem, which results in current values, which yield good field quality within a given FOV and low total power losses at the same time. This method is then applied to both considered field geometries.

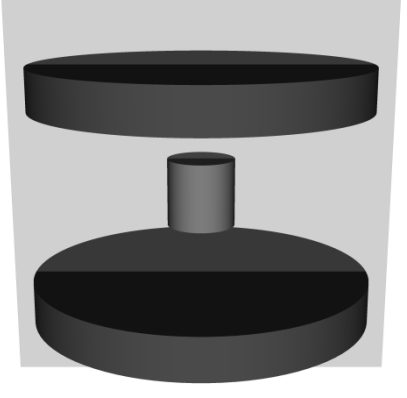

Fig. 1. Setup of two conducting discs (dark gray) with a cylindrical FOV (light gray) in-between. The x/z-plane is illustrated as semi-transparent rectangle.

First, the geometry of the current paths is defined. As shown in Fig. 1, two circular discs of conducting material are positioned at opposite sides of the FOV. In consonance with the Maxwell and the Helmholtz coil geometries, the current paths are defined to be circular and concentrically within the conducting material. In this way, only the current density distribution has to be determined. To perform numerical evaluations, the conducting material is discretized into single rings with rectangular cross-section, in which the current density is constant. The field profiles $\mathbf{h}_i$ are obtained by evaluation of the Biot-Savart law, such that $\mathbf{H}_i = I_i \mathbf{h}_i$ is the magnetic field generated by the current I_i on the conducting ring i.

Second, a measure is needed, which evaluates the quality of the generated magnetic field $\mathbf{H}$. It is the root-mean-square deviation

$$\epsilon_H = \|\mathbf{H} - \mathbf{H}_{\text{ideal}}\|_2 = \sqrt{\frac{\sum_{j=1}^{N_{\text{FOV}}} \sum_{k=x,y,z} \left(H_k(r_j) - H_{\text{ideal},k}(r_j)\right)^2}{N_{\text{FOV}}}}$$

to the ideal field $\mathbf{H}_{\text{ideal}}$, which here is either the uniform field $\mathbf{H}_{\text{uni}}$ or the gradient field $\mathbf{H}_{\text{grad}}$ with

$$\mathbf{H}_{\text{uni}} = h_{\text{uni}} \begin{pmatrix} 0 \\ 0 \\ 1 \end{pmatrix}, \qquad \mathbf{H}_{\text{grad}} = h_{\text{grad}} \begin{pmatrix} -0.5 \\ -0.5 \\ 1 \end{pmatrix}.$$

In this way, each component (x, y, z) of the field vector is taken into account in each considered point in space r_j within the FOV.

As measure of the power loss, which in general limits the achievable field strengths, the resistive losses within each conducting ring are evaluated by $P_i = I_i^2 R_i$ considering the resistances R_i. They contribute equally to the total power loss $P_{\text{tot}} = \sum_i P_i$.

Finally, the inverse problem can be formulated as follows:

$$\arg\min_{\mathbf{I}} \ \epsilon_H^2 + \lambda P_{\text{tot}}^2 = \arg\min_{\mathbf{I}} \ \|\mathbf{H} - \mathbf{H}_{\text{ideal}}\|_2^2 + \lambda \left\|\sqrt{\mathbf{R}}\mathbf{I}\right\|_2^2$$

Both measures are weighted against each other by the regularization parameter λ. This gives the possibility to obtain low power systems by allowing higher field deviations. In contrast, high precision fields can be generated at the cost of higher power losses. The solution of the inverse problem can be calculated with standard methods.

3 Results

Here, an example case is considered for generation of both types of magnetic field geometries. The considered FOV is cylindrical with a radius of 40 mm and a length of 80 mm. The conducting discs are 400 mm in diameter and have a length of 50 mm. They are separated by a gap of 200 mm. The discretization is 6 by 24 rings.

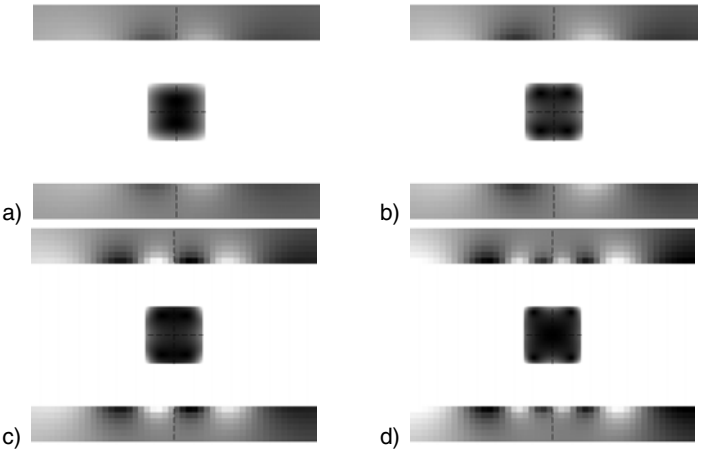

Fig. 2. Uniform field generation: resulting current density distribution and corresponding field deviation as x/z-plane cross section plot. Current color coding is black for negative values and white for positive values. Field deviation color coding is white for high value and black for zero. **a)** $\epsilon_H = 2.20\,\mathrm{mT}/\mu_0,\ P_{\mathrm{tot}} = 1.44\,\mathrm{kW}$ **b)** $\epsilon_H = 0.48\,\mathrm{mT}/\mu_0,\ P_{\mathrm{tot}} = 2.7\,\mathrm{kW}$ **c)** $\epsilon_H = 0.11\,\mathrm{mT}/\mu_0,\ P_{\mathrm{tot}} = 4.0\,\mathrm{kW}$ **d)** $\epsilon_H = 0.03\,\mathrm{mT}/\mu_0,\ P_{\mathrm{tot}} = 5.7\,\mathrm{kW}$

Since the FOV is chosen to be circular and the setup is symmetric, it is sufficient to consider only the center 2D plane and applying weights depending on the radial distance to the center axis.

In the first case, it is aimed for generating a uniform magnetic field with $h_{\mathrm{uni}} = 50\frac{\mathrm{mT}}{\mu_0}$. Different regularization parameters are investigated. Fig. 2 shows the according current distributions as well as the deviation to the ideal field. Numbers on ϵ_H and P_{tot} are given below the figures.

In the second case, the generation of a gradient field is considered. The gradient strength is $h_{\mathrm{grad}} = 2\frac{\mathrm{T}}{\mathrm{m}\mu_0}$. The results are illustrated in Fig. 3.

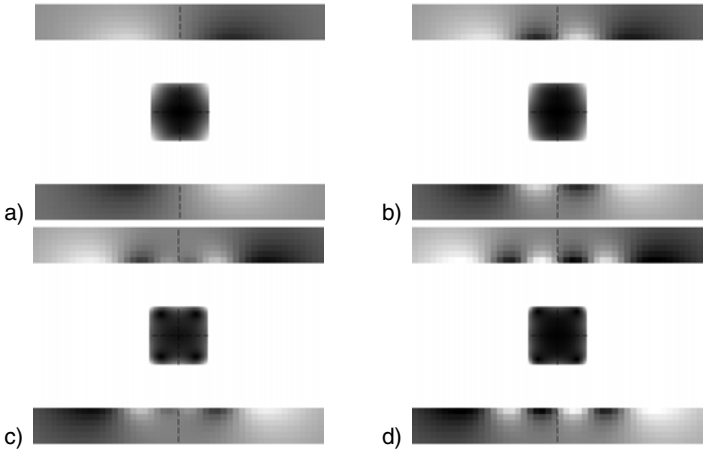

Fig. 3. Gradient field generation: resulting current density distribution and corresponding field deviation as x/z-plane cross section plot. Current color coding is black for negative values and white for positive values. Field deviation color coding is white for high value and black for zero. a) $\epsilon_H = 4.6\,\mathrm{mT},\ P_{\mathrm{tot}} = 11.9\,\mathrm{kW}$ b) $\epsilon_H = 1.1\,\mathrm{mT},\ P_{\mathrm{tot}} = 20.4\,\mathrm{kW}$ c) $\epsilon_H = 0.28\,\mathrm{mT},\ P_{\mathrm{tot}} = 27.4\,\mathrm{kW}$d) $\epsilon_H = 0.05\,\mathrm{mT},\ P_{\mathrm{tot}} = 37.9\,\mathrm{kW}$

4 Discussion

By choosing the regularization parameter λ, different current density distributions are obtained. Allowing for higher power losses, more current sections with alternating current directions occur. This results in partly cancellation of the generated field contributions but in lower resulting field deviations.

When realizing a simulated coil setup in hardware, often only discrete current density distributions can be achieved. Thus, each conducting ring needs its own controlled current source. Another possibility is using wire material with different cross sections. Different current densities can be obtained by connecting those in series and feeding the system with a single current source.

5 Conclusion

In general, determining current density distributions from a given magnetic field geometry is a non-trivial task. This problem could be reduced by choosing appropriate current paths and discretization of the conducting material. This led to a system of linear equations, which can be solved with standard methods. The trade-off between power loss and field quality is accounted for by a single regularization parameter. When comparing the resulting current density distributions of the considered cases, one may

conclude that different coil setups should be applied for selection field and for drive field generation when high precision in field geometry is required.

We acknowledge the financial support by the BMBF (grant number 01EZ0912) and the BMWi (grant number 03EFT6SH12).

References

1. Gleich, B., Weizenecker, J.: Tomographic imaging using the nonlinear response of magnetic particles. Nature 435, 1214–1217 (2005)
2. Knopp, T., Erbe, M., Biederer, S., Sattel, T.F., Buzug, T.M.: Efficient generation of a magnetic field-free line. Medical Physics 37(7), 3538–3540 (2010)
3. Goodwill, P.W., Scott, G.C., Stang, P.P., Conolly, S.M.: Narrowband Magnetic Particle Imaging. IEEE Trans. Med. Imag. 28(8), 1231–1237 (2009)
4. Rahmer, J., Weizenecker, J., Gleich, B., Borgert, J.: Signal encoding in magnetic particle imaging: properties of the system function. BMC Medical Imaging 9(4) (2009)
5. Schomberg, H.: Magnetic Particle Imaging: Model and Reconstruction. In: IEEE International Symposium on Biomedical Imaging From Nano to Macro, pp. 992–995 (2010)

Capacitor Distortion in Magnetic Particle Imaging

Bo Zheng, Patrick Goodwill, Wisely Yang, and Steven Conolly

Department of Bioengineering, UC Berkeley, 340 Hearst Memorial Mining Building
Berkeley, CA 94720, USA
bozheng@berkeley.edu

Abstract. The signal-to-noise ratio in magnetic particle imaging can be limited by distortion interference arising in the imaging system. In this work, we investigate the contribution of resonant transmit capacitors to system interference. Feedthrough interference spectra obtained using four capacitors with varying voltage ratings in a custom MPI interference testbed show a 20dB reduction in distortion interference with higher-rated capacitors. Finally, we discuss the applicability of the interference testbed to treat other interference mechanisms in magnetic particle imaging.

1 Introduction

Magnetic Particle Imaging (MPI) is an emerging modality that images superparamagnetic iron oxide (SPIO) tracers [1]. In MPI, a parallel resonant LC circuit is typically employed to reduce the current requirements of the transmit power supply. The transmit coil creates a sinusoidal magnetic field, which induces a rich spectrum of signals in any SPIO particles that are located within the field free region of the transmit coil (Fig. 1). A detector (or receive) coil simultaneously detects the particle signal as well as an undesired direct feedthrough signal. In real MPI systems, this feedthrough signal comprises of signals at both f_0, the excitation frequency, and distorted interfering signals at harmonics of f_0. Unfortunately, this direct feedthrough interference remains significant and therefore limits the signal-noise ratio (SNR) of the MPI scanner (Fig. 2). Measurements on the latest Berkeley MPI imager show higher-order distortion interference to be 40-fold above our noise floor. Removal of this distortion interference would dramatically improve SNR and enable more accurate disease diagnosis.

T.M. Buzug and J. Borgert (Eds.): Magnetic Particle Imaging, SPPHY 140, pp. 319–324.
springerlink.com

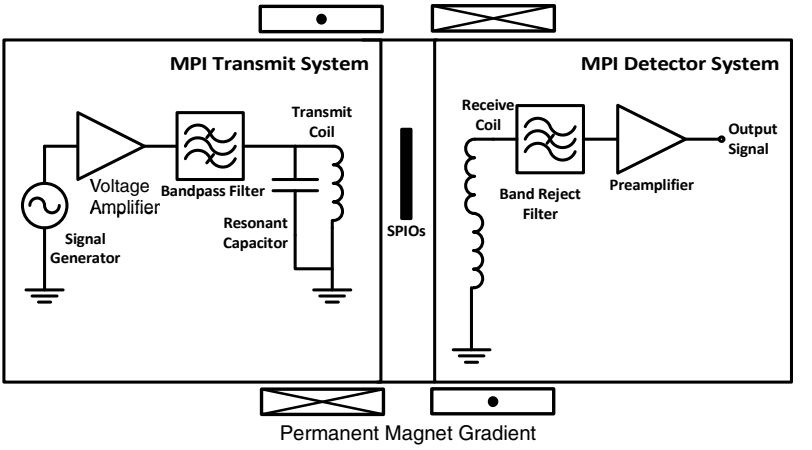

Fig. 1. MPI system diagram. Here we are focusing on nonlinearities in the parallel resonant capacitor, which can induce significant interference in any MPI scanner.

Previously, efforts to address the distortion interference problem have focused on filtering distortion at the output of the power amplifier (Fig. 1) [2-3]. However, significant filtering [4] did not decrease the total amount of distortion interference present in the received signal spectrum, suggesting that distortion interference may arise elsewhere in the system.

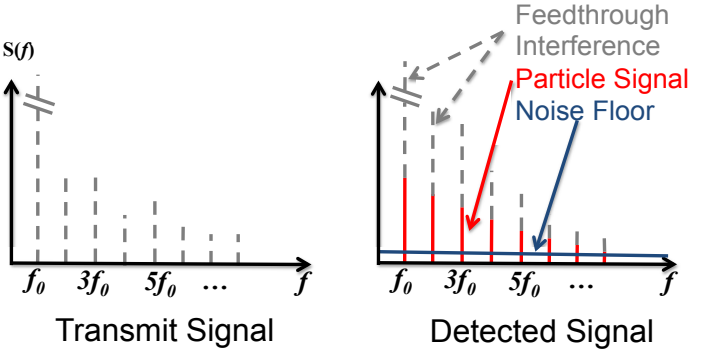

Fig. 2. Broadband distortion interference from the transmitted signal can feed through to the detected signal and limit the SNR of the MPI detector.

To investigate possible distortion mechanisms in MPI, we have constructed a non-imaging testbed with a complete transmit/receive system (Fig. 3). Here, we investigate the contribution of the resonant transmit

capacitor (Fig. 1) as a distortion mechanism in MPI. Several models for capacitor nonlinear distortion have been proposed in audio literature, including dielectric memory [5] and capacitance changes from applied voltage [6]. Here, we measure system interference using resonant capacitors with four operating voltage ratings to investigate the contribution of capacitor distortion in MPI.

2 Materials and Methods

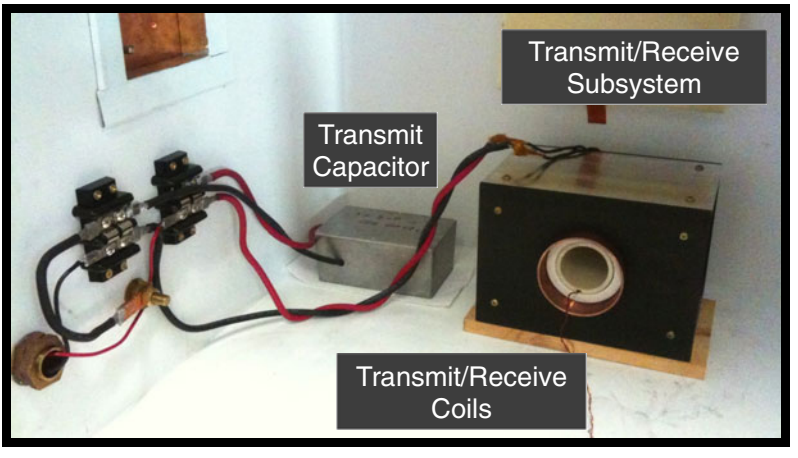

Fig. 3. Berkeley MPI interference testbed. In the transmit/receive subsystem, the receive coil is concentrically inside the transmit coil. Not shown: Audio analyzer, transmit filter, receive filter, preamplifier, RF enclosure.

A non-imaging system for interference testing was constructed (Fig. 3). A low-distortion sinusoidal signal was generated using a SR1 Audio Analyzer (Stanford Research Systems, Sunnyvale, CA), amplified with a LVC5050 Linear Amplifier (AE Techron, Elkhart, IN), bandpass filtered at f_0, and transmitted in a resonant coil to create a time-varying magnetic field. Feedthrough and particle signals are detected with a pickup coil, notch filtered at f_0, preamplified (SR560, Stanford Research Systems, Sunnyvale, CA), and digitized using a SR1 Audio Analyzer. For suppression of environmental noise, the transmit/receive subsystem was enclosed in a RF shielded chamber (ETS-Lindgren, St. Louis, MO).

Four high-power polypropylene film capacitors (Fig. 4) were tested as resonant transmit capacitors with AC operating voltage ratings of 75 Vrms

(CDE940C, Cornell Dubilier, Liberty, SC), 500 Vrms (CDE942C, Cornell Dubilier), 700 Vrms (Celem, Jerusalem, Israel), and 1050 Vrms (105FPA, Illinois Capacitor, Chicago, IL). Feedthrough interference spectra from DC to the 4th harmonic were obtained on the SR1 Audio Analyzer with a fixed capacitor voltage at 200 Vrms.

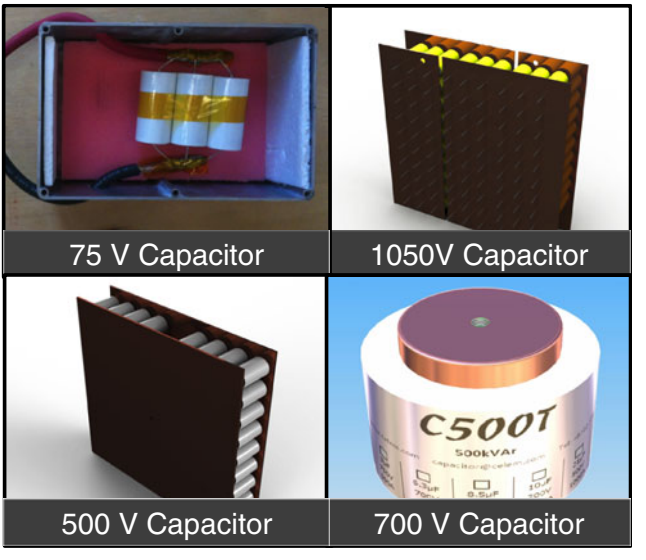

Fig. 4. Capacitors tested for contributions to feedthrough interference, all with identical capacitance. The 500 V and 1050 V-rated capacitors were custom assembled for voltage/current derating.

3 Results

The amount of total feedthrough interference in the system is plotted in Fig. 5 (left). The fundamental feedthrough signal at f_0 remains constant for all capacitors tested and suggests that the same AC excitation magnetic field was created in all cases, as we hoped. However, distortion interference drops significantly with increasing capacitor voltage rating. The 1050 Vrms-rated capacitors generated 15x less interference at $3f_0$ than 75 Vrms-rated capacitors. Fig. 5 (right) shows that interference at $3f_0$ in dB decreases linearly ($R^2 = 0.95$) for varying capacitor voltage ratings.

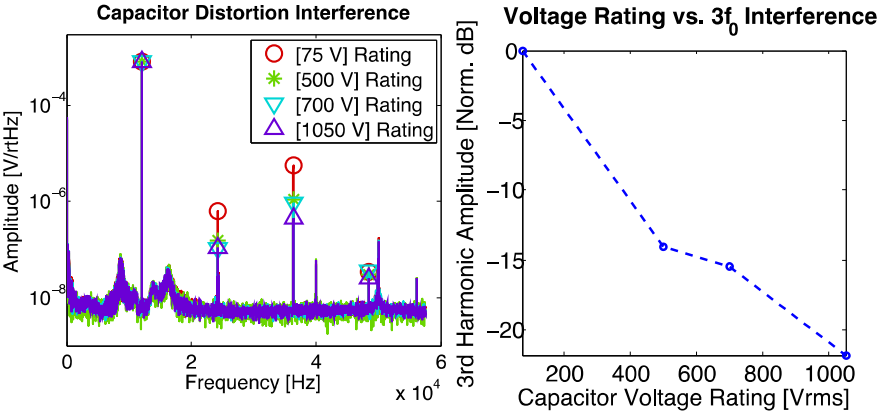

Fig. 5. (Left) Feedthrough distortion interference spectra for the four capacitors under test from DC to 52 kHz, with f_0 at 12 kHz. Noise spikes at 40, 50, and 58 kHz are from the audio analyzer power supply and environmental interference. (Right) Feedthrough distortion interference amplitude (plotted in normalized dB) at $3f_0$ for various capacitor ratings.

4 Discussion

Here we demonstrated experimentally that transmit capacitor distortion can be dramatically reduced by simply using over-rated capacitors. This is an important finding as it may translate to more than a 20 dB improvement in SNR in MPI.

Our data is consistent with a nonlinear capacitor model where the capacitance value changes instantaneously with applied voltage [6]. Here, we may model changes in capacitance using dielectric strain from capacitor plate forces and predict the effectiveness of further increasing capacitor ratings to reduce feedthrough interference.

We have also established the usefulness of a feedthrough interference testbed to achieving coil-noise dominance in MPI. Using this system, additional distortion interference mechanisms in MPI may be investigated, including interactions between the generated AC magnetic field in the transmit coil and the magnetic gradient, nonlinear power amplifiers, and filter component nonlinearities.

5 Conclusion

In this work, we show that resonant capacitors can be a significant source of system interference in Magnetic Particle Imaging. Using a customized non-imaging feedthrough testbed, we tested four capacitor types with varying voltage ratings and found distortion interference to decrease with higher capacitor rating. We conclude that an analytical investigation into the

capacitor distortion mechanism and further exploration on other system distortion mechanisms is necessary to achieving coil-noise dominance in MPI.

Acknowledgments. The authors would like to acknowledge: California Institute for Regenerative Medicine, UC Discovery Grant, and National Institutes of Health. This material is based upon work supported by the National Science Foundation Graduate Research Fellowship.

References

1. Gleich, B., Weizenecker, J.: Tomographic imaging using the nonlinear response of magnetic particles. Nature 435, 1214–1217 (2005)
2. Schmale, I., Gleich, B., Kanzenbach, J., et al.: An Introduction to the Hardware of Magnetic Particle Imaging. In: IFMBE Proceedings. IFMBE, vol. 25, pp. 450–453. Springer, Heidelberg (2009)
3. Goodwill, P.W., Conolly, S.M.: The X-Space Formulation of the Magnetic Particle Imaging Process: 1-D Signal, Resolution, Bandwidth, SNR, SAR, and Magnetostimulation. IEEE Trans. Med. Imaging 29, 1851 (2010)
4. Zheng, B., Goodwill, P., Conolly, S.: Transmit filter design methods for magnetic particle imaging. In: Proc. SPIE Medical Imaging, vol. 7965, pp. 79652H–79652H-6 (2011)
5. Bateman, C.: Capacitor Sounds 3: Capacitances of 10nF and smaller (March 2003), http://diycore.com/patrick/files/electronics/capacitor/capsound3.pdf
6. Van der Veen, M., Van Maanen, H.: Non-linear distortions in capacitors, AES Convention Paper, Amsterdam (2008)

Safety Limits for Human-Size Magnetic Particle Imaging Systems

Emine U. Saritas, Patrick W. Goodwill, George Z. Zhang, Wenxiao Yu, and Steven M. Conolly

Department of Bioengineering, University of California, Berkeley, 340 HMMB Bldg. Berkeley, CA 94720, U.S.A.
saritas@berkeley.edu

Abstract. Current small-animal-sized MPI scanners operate at 1-25 kHz frequency range with 0.1-20 mT peak amplitude, neither of which is optimized. SAR and especially dB/dt safety limits will determine the optimum excitation field, and will impact the optimum scanning speed, field-of-view (FOV) and signal-to-noise ratio (SNR). In this work, we describe the first human-subject safety limit experiments for MPI. Our results indicate that the magnetostimulation threshold monotonically decreases with increasing frequency and is inversely correlated to the body-part size.

1 Introduction

In order to scan across the image field-of-view (FOV) in magnetic particle imaging (MPI), we must shift the origin (called the field-free point or FFP) of a strong (6 T/m) gradient or move the animal. The most common method is to apply a time-varying but spatially homogeneous magnetic field in addition to a static gradient field. The addition of the two fields effectively shifts the origin of the gradient field in space. The homogeneous magnet is driven with a sinusoidal magnetic field in the very low frequency (VLF) range (i.e., below 30 kHz) [1]. Understanding potential safety hazards of this field will be critical for translating MPI to human subjects. The safety limits will impact the optimum scanning speed, field-of-view (FOV) and SNR [2-3].

Time-varying magnetic fields have two known health effects on the human body: peripheral nerve stimulation (PNS) [4-5], and tissue heating, known as specific absorption rate (SAR) [6]. Previous studies have focused on reducing the SAR in MPI [7], but the magnetostimulation effect has not been investigated. Prior studies in VLF electromagnetic safety indicate that the dominant safety constraint for MPI will actually be PNS [4-5].

T.M. Buzug and J. Borgert (Eds.): Magnetic Particle Imaging, SPPHY 140, pp. 325–330.
springerlink.com

Numerous safety limit studies have been conducted for the 1 kHz-range magnetic field gradients and MHz range radiofrequency (RF) magnetic fields of magnetic resonance imaging (MRI) [4-6,8-10]. However, human safety limits in the VLF regime remain relatively under-investigated. When compared to the gradient field in MRI, the excitation field in MPI operates at a wider range of frequencies and is homogeneous in space. In conductive tissue, this homogeneous field can generate dramatically different electric field patterns than an MRI field gradient does. Furthermore, as opposed to MRI, MPI does not require the whole body to be exposed to the magnetic field. However, body-part-specific safety limits have not yet been investigated in the literature. The knowledge of these limits may dramatically improve the performance of MPI scans. In this work, we describe the first human-subject magnetostimulation threshold experiments for MPI.

2 Material and Methods

To determine the magnetostimulation thresholds in the human arm and leg, we built two solenoidal resonant coils (shown in Fig. 1) with the following specifications:

- The arm solenoid (Fig. 1a) had a free bore of 11 cm in diameter and 17 cm in length, with two layers of 36 turns wound using a Litz-wire of 4.6 mm diameter. The resulting inductance was 376 μH, with a DC resistance of 0.08 Ω. The magnetic field amplitude was 410 μT/A at the center, with a measured homogeneity of 5% in a 7 cm–long region down the bore of the coil.
- The leg solenoid (Fig. 1b) had a free bore of 19 cm in diameter and 24 cm in length, with a single layer of 54 turns. The resulting inductance was 380 μH, with a DC resistance of 0.12 Ω. The magnetic field amplitude was 214 μT/A at the center, with a measured homogeneity of 8% in an 11 cm–long region down the bore of the coil.

Because static magnetic fields do not induce stimulation or heating, the static gradient field of the MPI scanner was not incorporated [11]. The solenoids were made resonant at 10 different frequencies with a multiple-switch mechanism, and the resonant circuit at every frequency was impedance-matched to the 0.5 Ω output impedance of AE Techron 7782 power amplifier. At the maximum power limit of the amplifier, the resulting peak-to-peak magnetic fields at the center of the coils were 320 mT and 160 mT for the arm solenoid and the leg solenoid, respectively.

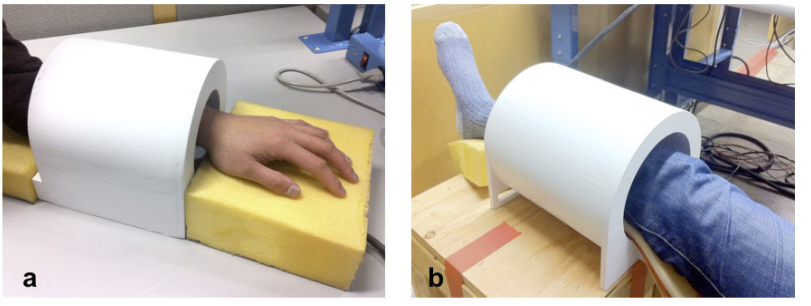

Fig. 1. The solenoidal resonant coils for testing the magnetostimulation thresholds in the human arm and leg. **(a)** Arm coil has a diameter of 11 cm and magnetic field amplitude of 410 μT/A at the center, with a measured homogeneity of 5% in a 7 cm–long region down the bore of the coil. **(b)** Leg coil has a diameter of 19 cm and magnetic field amplitude of 214 μT/A at the center, with 8% homogeneity in an 11 cm–long region.

The human subjects experiments were approved by the Committee for Protection of Human Subjects at University of California, Berkeley. A total of 20 subjects were recruited from healthy adult volunteers, screened for safety considerations. Excluding criteria were any subjects with metal in their body (e.g., pacemakers, aneurysm clips, metallic implants, etc.), or pregnancy.

The magnetostimulation thresholds were tested at 10 different frequencies from 1-25 kHz. At each frequency, the magnetic field amplitude was increased until the subject reported a twitching/tingling sensation (i.e., PNS). During the experiment, the current running through the solenoids were measured in real-time using a Rogowski AC current probe (PEM Ltd., Nottingham, UK). For each subject, the data points were fitted to a hyperbolic peak-to-peak amplitude vs. frequency curve, which can be written as:

$$B_{pp} = \Delta B_{\min}\left(1+\frac{1}{2\tau_c f}\right) \tag{1}$$

This relation is called the fundamental law of magnetostimulation [10], where ΔB_{min} is the horizontal asymptote for B_{pp}, and τ_c is the chronaxie time as defined in [4]. Any field greater than B_{pp} will induce a PNS sensation. According to this theory, no stimulation occurs if the change in B-field is less than ΔB_{min}, no matter what the frequency is.

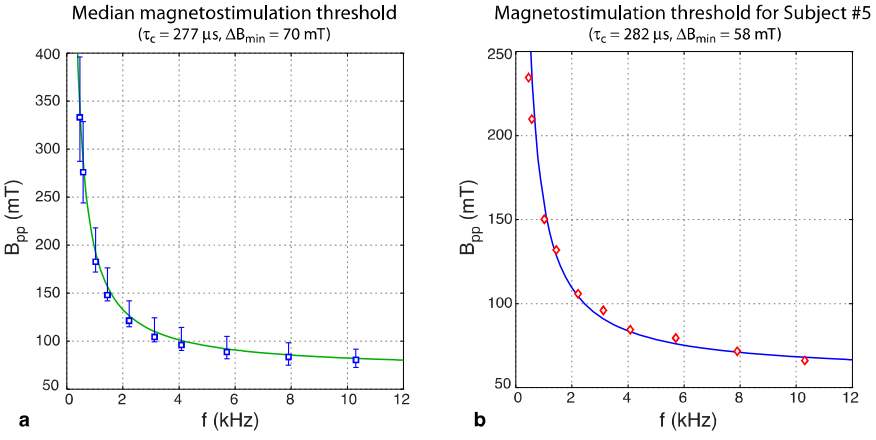

Fig. 2. Magnetostimulation experiments in the arm. The threshold magnetic field amplitudes (peak-to-peak) as a function of frequency along with the fitted hyperbolic threshold curves. **(a)** Median stimulation threshold of all 20 subjects and the 25th-75th percentile. τ_c = 277 µs and ΔB_{min} = 70 mT. **(b)** Data points for one of the subjects and the fitted threshold curve. τ_c = 282 µs and ΔB_{min} = 58 mT. Note that there is excellent agreement between subjects. It is also apparent that the data trends are well-modeled by the hyperbolic fundamental law of magnetostimulation given in Eq. 1.

3 Results and Discussion

The results of the human subject experiments in the arm and leg are given in Figs. 2 and 3, respectively. The median magnetostimulation threshold in the arm had a chronaxie time of τ_c = 277 µs and an asymptote of ΔB_{min} = 70 mT. In the leg, median τ_c = 296 µs with median ΔB_{min} = 44 mT. Also shown in these figures are data points for a single subject, which closely fit the theoretical hyperbolic threshold relation given in Eq. 1.

Our results indicate that the magnetostimulation threshold monotonically decreases with increasing frequency and is inversely correlated to the body-part size. As seen in Figs. 2-3, the variation in threshold magnetic fields decreases with increasing frequency. Furthermore, perhaps because there was a bigger variation in the thickness of our subjects' arms when compared to their legs, the arm stimulation thresholds demonstrated a bigger variation as well.

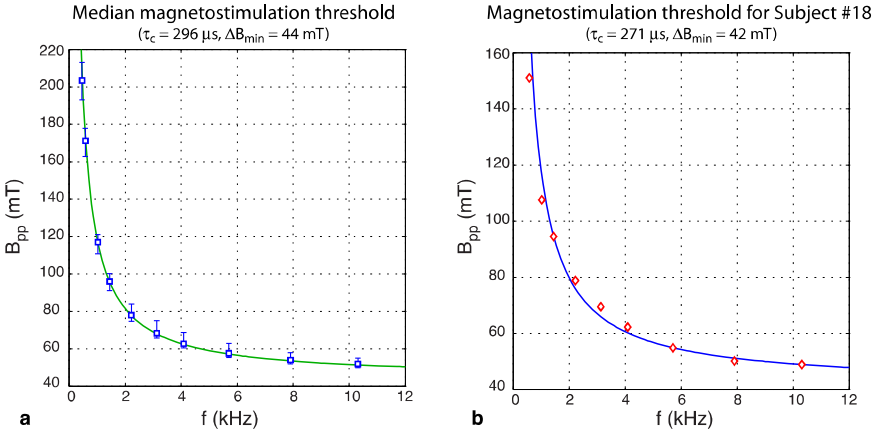

Fig. 3. Magnetostimulation experiments in the leg. The threshold magnetic field amplitudes (peak-to-peak) as a function of frequency along with the fitted hyperbolic threshold curves. **(a)** Median stimulation threshold of all 20 subjects and the 25th-75th percentile. τ_c = 296 µs and ΔB_{min} = 44 mT. **(b)** Data points for one of the subjects and the fitted threshold curve. τ_c = 271 µs and ΔB_{min} = 42 mT. Again, note how uniform the PNS parameters were across our 20 volunteers and how well the trend is modeled by the hyperbolic fundamental law of magnetostimulation.

4 Conclusion

We have successfully implemented the first safety limit experiment for MPI. The results of this experiment closely match the theoretically calculated threshold vs. frequency curve. These findings will have a great impact on the optimization of MPI parameters, especially in determining the number of partial FOVs required to cover a region of interest.

Acknowledgments. This work was supported by Siebel Stem Cell Institute Postdoctoral Fellowship, the National Institute of Health (NIH), the California Institute for Regenerative Medicine (CIRM) and UC Discovery Grant.

References

1. Gleich, B., Weizenecker, J.: Tomographic imaging using the nonlinear response of magnetic particles. Nature 435, 1214–1217 (2005)
2. Goodwill, P.W., Conolly, S.M.: The X-Space Formulation of the Magnetic Particle Imaging Process: 1-D Signal, Resolution, Bandwidth, SNR, SAR, and Magnetostimulation. IEEE TMI 29, 1851–1859 (2010)
3. Goodwill, P.W., Conolly, S.M.: Multidimensional X-Space Magnetic Particle Imaging. IEEE TMI 30, 1581–1590 (2011)
4. Reilly, J.P.: Peripheral nerve stimulation by induced electric currents: exposure to time-varying magnetic fields. Med. Biol. Eng. Comput. 27, 101–110 (1989)

5. Reilly, J.P.: Maximum pulsed electromagnetic field limits based on peripheral nerve stimulation: application to IEEE/ANSI C95.1 electromagnetic field standards. IEEE Trans. Biomed. Eng. 45, 137–141 (1998)
6. Bottomley, P.A., Edelstein, W.A.: Power deposition in whole-body NMR imaging. Med. Phys. 8, 510–512 (1981)
7. Bohnert, J., Gleich, B., Weizenecker, J., Birgert, J., Dossel, O.: Optimizing Coil Currents for reduced SAR in Magnetic Particle Imaging. In: Dössel, O., Schlegel, W.C. (eds.) IFMBE Proceedings, WC 2009. IFMBE, vol. 25/IV, pp. 249–252. Springer, Heidelberg (2009)
8. Schaefer, D.J., Bourland, J.D., Nyenhuis, J.A.: Review of patient safety in time-varying gradient fields. JMRI 12, 20–29 (2000)
9. Zhang, B., Yen, Y.-F., Chronik, B.A., McKinnon, G.C., Schaefer, D.J., Rutt, B.K.: Peripheral nerve stimulation properties of head and body gradient coils of various sizes. MRM 50, 50–58 (2003)
10. Irnich, W., Schmitt, F.: Magnetostimulation in MRI. MRM 33, 619–623 (1995)
11. Schenck, J.F.: Safety of strong, static magnetic fields. JMRI 12, 2–19 (2000)

Mouse Bed Optimized for MPI

Matthias Weber, Patrick Goodwill, and Steven Conolly

[1] Institute of Medical Engineering, University of Luebeck, Ratzeburger Allee 160
Luebeck, 23562, Germany
Matthias.weber@miw.uni-luebeck.de
[2] Department of Bioengineering and EECS,
University of California Berkeley, 340 HMMB
Berkeley, CA 94720-1762, USA
goodwill@berkeley.edu, sconolly@berkeley.edu

Abstract. Magnetic particle imaging (MPI) is a new imaging modality, which allows for the determination of the distribution of super paramagnetic nanoparticles in vivo with excellent contrast, penetration and high temporal resolution. So far, real-time imaging in a mouse has been realized using a scanning-system with a field free point (FFP). Recently, an alternative encoding scheme has been developed promising faster scanning times and a higher sensitivity. This can be handled by extending the FFP to a field free line (FFL). Preliminary scans of phantoms showed the feasibility of the FFL in practice, based on projection x-space MPI. To ensure the safety of imaging switching from phantom to *in vivo* scans, a specific protocol has to be provided for scanning live animals. This paper describes the construction and testing of a mouse bed for heating as well as delivery and recovery of anesthesia gases. The mouse bed is constructed with non-magnetic materials and sized to the specific scanner. The size of the bed is limited by the diameter of the bore, and a larger bed (and bore) would be required for larger animals.

We designed a mouse bed fulfilling all mentioned requirements by engineering a specialized water warming system and a modified connection for the anesthesia system. The whole bed is moveable and rotatable in and around the longitudinal axis of the bore by jointing it to a robot. Rotation is critical for performing volumetric 3D MPI with projection reconstruction (or Radon) computerized tomography.

1 Introduction

Magnetic Particle Imaging (MPI) is a new imaging modality that determines the spatial distribution of super-paramagnetic nanoparticles [1]. This method uses a specific configuration of magnetic coils to implement spatial encoding with a field free point (FFP). In 2009, the first three-dimensional

T.M. Buzug and J. Borgert (Eds.): Magnetic Particle Imaging, SPPHY 140, pp. 331–335.
springerlink.com

and real-time images of a mouse were presented using a FFP [2]. A projection format for MPI was first proposed by Philips using a field free line (FFL) magnet concept. The first FFL imaging scanner was recently constructed by the Berkeley Imaging Systems Laboratory. Images are reconstructed with an x-space image reconstruction algorithm in real-time [3]. Preliminary scans of phantoms showed the feasibility of the FFL in practice. To ensure the safety of imaging switching from phantom to *in vivo* scans, a specific protocol has to be provided for scanning live animals. To avoid artifacts as a result of movement, the animal should be sedated. In addition, anesthesia reduces the body temperature and requires further patient heating. Finally, to allow for 3D projection-reconstruction tomographic imaging, the bed must allow for rotation. This paper describes the engineering of a customized mouse bed for the FFL system that maintains mouse temperature homeostasis and stable anesthesia.

2 Material and Methods

To engineer a customized mouse bed for MPI and, in this case, the mentioned FFL-scanner, certain requirements have to be determined. Figure 1 shows an overview of the relations between the mouse bed and the anesthesia system, water warming device and FFL scanner.

The mouse bed was designed with a CAD program (Solidworks, Dassault Systèmes SolidWorks Corp.) and printed using a three-dimensional printer (ZPrinter 150, Z Corporation). In the last step of procedure, the final structured rigidity was assured by applying an epoxy composite (Z-Max 90, Z Corporation) to the model. All materials are MPI compatible and non-magnetic (i.e. not ferromagnetic/paramagnetic).

Functional capability was tested with a warming pump (T/Pump Classic - TP650, Gaymar) and an anesthesia system (Table Top Laboratory Animal Anesthesia System, VetEquip).

Routing of the water warming system was implemented with two different approaches: internal and external water routing (Figure 2). When using internal routing, the water has direct contact with the model. Here, a structure has to be designed that is able to resist the water pressure and feature a compact design. Hence, a specific honeycomb structure [4] was implemented. On the other side the external routing uses external water pipes that are integrated in the model. Consequently, this removes the water pressure on the mouse bed.

In addition to the water warming system, a customized anesthesia mask was designed in the mouse bed (Figure 3). Here, a non-rebreathing-system served as the template (CX-SP Non-Rebreathing System, VetEquip).

Overall, the bore size of the system (44 mm ≈ 1.73 in) limited the size of the mouse bed. Hence, a diameter of 42 mm (≈ 1.65 in) was chosen to ensure a required clearance between mouse bed/bore and to compensate possible imprecisions.

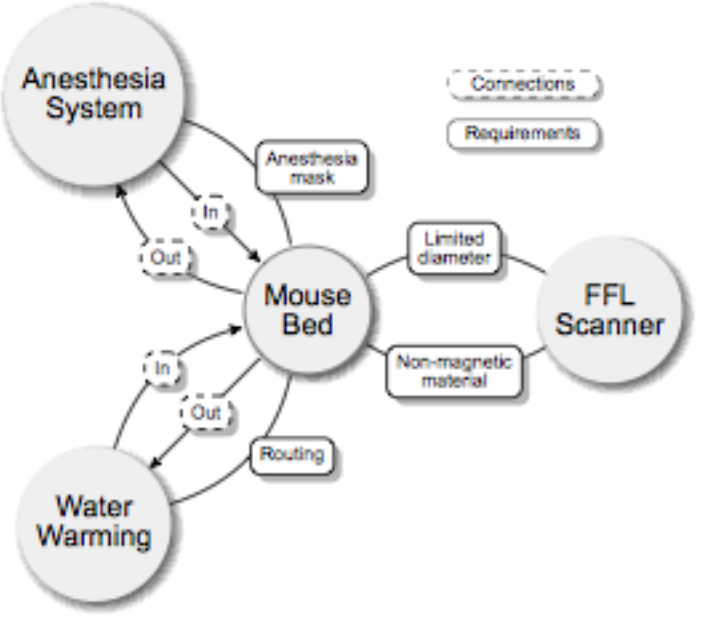

Fig. 1. Requirements (solid line) and Connections (dashed line) for designing the mouse bed.

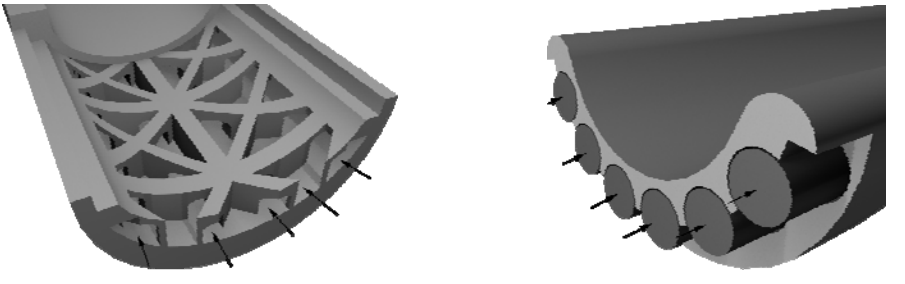

Fig. 2. Two approaches for the water warming (section through the models). Left: Implementation with internal routing using a honeycomb structure. Right: Implementation with external pipe routing. The arrows illustrate the water flow.

3 Results

Figure 3 shows the final mouse bed design with a customized anesthesia mask at the front including the required connections to the anesthesia system. For mouse heating the water warming was implemented at the bottom. Water warming and anesthesia system could be tested with live mice within an imaging cycle. During this time period (~ 10 minutes) the mouse bed could guarantee water warming and animal sedation.

Though, after a couple of days the internal routing exhibited slight bending and expanding. The external routing showed especially more stability and easier manufacturing.

4 Discussion

It has been shown that a working mouse bed for MPI could be engineered that features a specific external water warming routing as well as an anesthesia supply. A fully operational internal routing could be partially realized using the mentioned materials and size limitations, since direct contact between water/material and high water pressure lowers stability after multiple use. Hence, a permanent application needs further improvements.

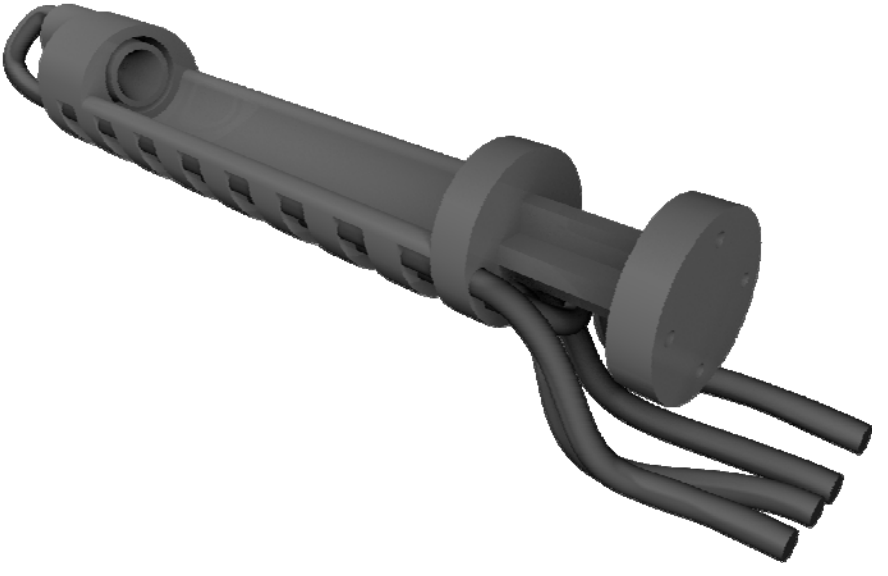

Fig. 3. Final design of the mouse bed: an external pipe routing is used to warm the patient. The anesthesia mask is implemented at the front. The whole mouse bed can be connected to a robot using the extension.

A non-water-interacting epoxy and a water warming pump with lower pressure might improve stability. Despite this, when implementing a mouse bed for a smaller bore, the internal routing could offer a more compact design. However, when scaling this mouse bed to different dimensions, external routing should always be the first choice based on easier design and engineering.

5 Conclusion

In this paper the engineering of a fully operable mouse bed for MPI was carried out. MPI requires non-magnetic materials and no mice movement during scans. Hence, anesthesia supply and mice warming was implemented. The final design fulfills all these properties and requirements.

Further work could be done especially, when scaling the bed to smaller bore sizes.

References

1. Gleich, B., Weizenecker, J.: Tomographic imaging using the nonlinear response of magnetic particles. Nature 435, 1214–1217 (2005)
2. Weizenecker, J., Gleich, B., Rahmer, J., Dahnke, H., Borgert, J.: Three-dimensional real-time in vivo magnetic particle imaging. Phys. Med. Biol. 54, L1–L10 (2009)
3. Goodwill, P.W., Conolly, S.M.: The x-space formulation of the magnetic particle imaging process: One-dimensional signal, resolution, bandwidth, SNR, SAR, and magnetostimulation. IEEE Trans. Med. Imaging 29(11), 1851–1859 (2010)
4. Blitzer, T.: Honeycomb Technology: Materials, Design, Manufacturing, Applications and Testing, Hexcel Corporation, pp. 193–199 (1997)
5. Weizenecker, J., Gleich, B., Borgert, J.: Magnetic particle imaging using a field free line. J. Phys. D: Appl. Phys. 41(10), 105009 (2008)

Transmembrane Voltages Caused by Magnetic Fields – Numerical Study of Schematic Cell Models

Alexander Kramlich, Julia Bohnert, and Olaf Dössel

Institute of Biomedical Engineering, Karlsruhe Institute of Technology (KIT)
Kaiserstraße 12, 76131 Karlsruhe, Germany
Julia.bohnert@kit.edu

Due to forthcoming use of MPI on humans there is an urgent need for a thorough research on possible adverse effects of this technique on patients' health. However, the health impact of exposure to time-varying magnetic fields in a frequency range between 10 kHz and 100 MHz, such as the MPI drive field, are still poorly investigated.

The current paper intends to give an overview on an in-silico approach to investigation of stimulating effects that could be caused by the MPI drive field. For this purpose, cell models of myocardiocyte, myocyte and neurocyte, as well as a suitable setup for the simulation of the exposure to time-varying magnetic fields have been developed. The evaluation of performed simulations was carried out on the basis of transmembrane voltage elevation and induced current densities.

1 Introduction

During an MPI examination, the patient will be exposed to a time-varying magnetic field with a frequency of about 25 kHz and a magnetic flux density of 20 mT [1]. The drive field generates an electric field according to Faraday's Law:

$$\nabla \times \vec{E} = -\frac{d\vec{B}}{dt} \tag{1}$$

In an excitable cell, the induced electric field is able to trigger an action potential, if the resting transmembrane voltage of about –90 mV is raised by approximately 25 mV. The effect of an induced action potential can range from unpleasant sensations to life endangering ventricular fibrillation, depending on the location where the action potential is initiated and the number of excited cells.

T.M. Buzug and J. Borgert (Eds.): Magnetic Particle Imaging, SPPHY 140, pp. 337–342.
springerlink.com

2 Material and Methods

In our simulations cells are modeled as bricks, consisting of the intracellular fluid (ICF) and a shell representing the cell membrane. Assembled to a cell patch model, those cells are surrounded by the extracellular fluid (ECF). The dimensions of the myocardiocyte model are 50 µm × 10 µm × 10 µm. The myocyte model and the neurocyte model are of identical cross section, but differ in length: the myocyte is twice as long as the myocardiocyte, whereas the neurocyte fills out the entire length of the cell patch. The spacing between the cells as well as the thickness of the cell membrane are set to 1 µm. This increase of the real cell membrane size by a factor of about 100 was necessary to enable numerical calculation with sufficient precision within a reasonable calculation time.

Table 1. Dielectric properties of the cell compartments used for the cell models.

	ECF		ICF		Membrane	
	σ in S/m	ε_r	σ in S/m	ε_r	σ in S/m	ε_r
Myocardiocyte	0.129	74.3	0.612	74.3	$1.08\ 10^{-10}$	2260
Myocyte	0.643	74.3	0.612	74.3	$1.08\ 10^{-10}$	2260
Neurocyte	–	74.3	0.245	74.3	$1.08\ 10^{-10}$	2260

The ICF and the ECF as well as the cell membrane are dielectric media, each having a distinct set of dielectric properties, such as electric conductivity σ and relative permittivity ε_r. The values of the above parameters were adjusted for all three cell compartments, as shown in Table 1, so that the electrical behavior of the cell patch model matched that of biological excitable tissues, described by Gabriel et al [2].

The cell patches used for the simulations consisted of 5 × 25 × 3 and 3 × 25 × 3 single cells with a total volume of 273 × 284 × 42 µm^3 and 318 × 284 × 42 µm^3 for the myocardial tissue and the muscle tissue, respectively. The cells in the myocardial cell patch were connected with each other by some randomly placed gap junctions. For the simulation of the nervous tissue, a row of myocytes in the muscle tissue cell patch was replaced by a single neurocyte.

For the generation of a widely homogeneous time-varying magnetic field, a Helmholtz coil pair with a radius of 70 µm was used. With a current flow of 1.56 A through each loop, a magnetic flux density in the center of the arrangement reached 20 mT.

Fig. 1 shows an example of a cell patch model used for the simulations and the position of the upper coil relative to the cell patch.

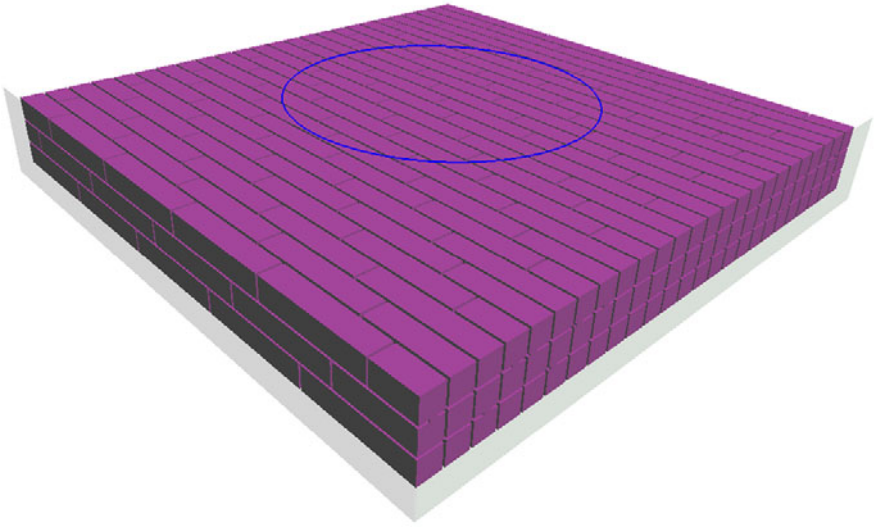

Fig. 1. Cell patch model of myocardial tissue and the position of the coil relative to the cell patch

All simulations were performed using SEMCAD X (SPEAG, Switzerland), which is a software package for computational electrodynamics [3]. For the particular experimental setup, a magneto quasi-static solving algorithm, based on the finite element method, was chosen. The calculations are of sufficient accuracy as long as the wavelength of the simulated electromagnetic fields is large compared to the size of the cell patch model.

3 Results

The distribution of the electric field inside the myocardial cell patch is shown in Fig.2.

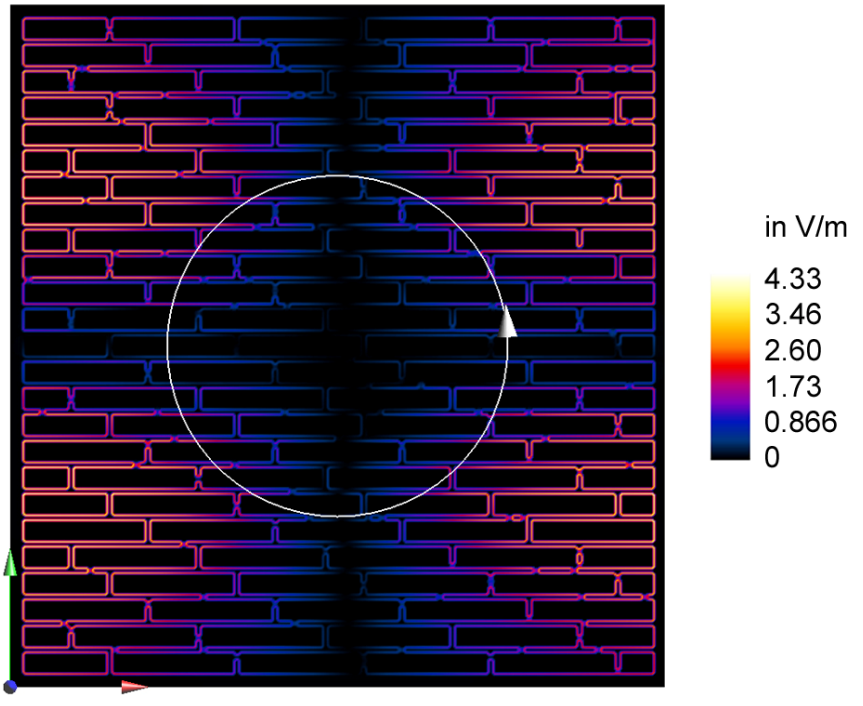

Fig. 2. Root mean square value of the electric field vector inside the myocardial cell patch

The transmembrane voltage (TMV) is defined here as the line integral of the electric field through the cell membrane. The following investigation applies only to induced transmembrane voltages. The resting potential is not taken into account.

$$V_m = \int \vec{E} \cdot d\vec{s} \tag{2}$$

It can be assumed that there is only insignificant variation in the electric field inside the cell membrane along the direct path between the ICF and ECF. Hence the electric field inside the cell membrane was calculated only at a single location half way through the membrane. The integral in (2) can be approximated by the product of the membrane thickness and the component of computed electric field vector that is oriented perpendicular to the membrane.

$$V_m = E_n \cdot \Delta s \tag{3}$$

The following results refer to the area of the cell patch enclosed by the coils where the magnetic field can be assumed to be homogeneous. The

strength of the electric field in this area increases from the center of the arrangement towards its edge. Hence the largest values of the TMV, summarized in the middle column of Table 2, were generated nearby the current loops.

Table 2. Maximum values of the TMV generated in the simulation with a 70 µm coil and anticipated maximum TMV values inside a human MPI scanner with a likely coil radius of 30 cm.

	TMV (R=70 µm)	TMV (R=30 cm)
Myocardial tissue	3.32 µV	14.2 mV
Muscle tissue	3.92 µV	16.8 mV
Nervous tissue	3.83 µV	16.4 mV

Since the strength of the electric field increases with the radius of the coil, the anticipated TMV in a human size MPI scanner can be estimated by multiplication of the simulated TMV value with the ratio between the likely radius of the coil in the MPI scanner and the radius of the coil used for the simulations. The expected maximum values of the TMV are summarized in the right column of Table 2.

4 Discussion

If the magnetic flux density and the frequency of the magnetic field remain fixed, the threshold for initiating an action potential is not likely to be exceeded inside Helmholtz coils with radii less then 30 cm. Thereby the maximum amplitude of the electric field within the coil could reach values around 300 V/m, which is a transgression of the reference level for occupational exposure to time-varying electric field in a frequency range between 3 kHz and 1 MHz, proposed in [4], by over 50 times. The ICNIRP[1] guidelines are based on the assumption that electric fields of 30 V/m already lead to nerve stimulation, whereas the present study suggests threshold electric fields of about 300 V/m.

5 Conclusion

All performed simulations show realistic results despite the simplicity of the cell models. It could be proven that the stimulation of excitable tissues by the MPI drive field is conceivable yet very unlikely, unless the parameters of the drive field such as frequency and/or magnetic flux density are going

[1] International Commission on Non-Ionizing Radiation Protection.

to be increased. Furthermore the stimulation is expected mainly on the periphery of the human body, whereas the tissues of the heart will experience smaller excitation.

References

1. Gleich, B., Weizenecker, J.: Tomographic imaging using the nonlinear response of magnetic particles. Nature 435, 1214–1217 (2005)
2. Gabriel, S., Lau, R., Gabriel, C.: The dielectric properties of biological tissues: III. parametric models for the dielectric spectrum of tissues. Physics in Medicine and Biology 41, 2271–2293 (1996)
3. SEMCAD X, Version 14.6 Aletsch, http://www.semcad.com
4. ICNIRP: Guidelines for limiting exposure to time-varying electric, magnetic and electromagnetic fields (1 Hz to 100 kHz). Health Physics 99, 818–836 (2010)

Concept for a Modular Class-D Amplifier for MPI Drive Field Coils

Jonas Jockram[1], Oliver Woywode[1], Bernhard Gleich[2], and Klaus Hoffmann[3]

[1] Philips Healthcare, GTC Development, Philips Medical Systems DMC GmbH
Röntgenstrasse 24, 22335 Hamburg, Germany
Jonas.Jockram@philips.com, Oliver.Woywode@Philips.com
[2] Philips Technologie GmbH Innovativ Technologies, Research Laborarories,
Röntgenstrasse 24, 22335 Hamburg, Germany
Bernhard.Gleich@philips.com
[3] Helmut-Schmidt-University,
Department of Electrical Engineering, Power Electronics
Holstenhofweg 85, 22043 Hamburg, Germany
Klaus.Hoffmann@hsu-hh.de

Abstract. This paper studies the performance of a modular class-D switching amplifier to supply the drive field coils of a magnetic particle imaging scanner with a high quality sinusoidal voltage. While a class-A or class-AB amplifier is capable of delivering such a sinusoidal voltage, its low efficiency does not qualify for an economic solution. Therefore, a class-D amplifier has been used. The modular amplifier consists of commercially available class-D amplifier chips, which are connected in parallel, to achieve the required output power. This paper describes the simulation model and a hardware setup of the modular amplifier which consists of 10 chips connected in parallel.

1 Introduction

Magnetic particle imaging (MPI) is a new method to acquire images of the interior of living bodies after administration of magnetic nano-particles. The particles are driven by an external magnetic field (drive field) to bring the particles in and out of saturation and the change of the particles' magnetization is recorded by extremely sensitive receive coils. This magnetic field is produced by an exciting coil, which can be treated electrically as an inductance with low parasitic resistance. The coil is connected with a capacitance as a parallel resonator and tuned to a resonance frequency. Thus in resonance, the amplifier is loaded by a purely resistive behavior of the

T.M. Buzug and J. Borgert (Eds.): Magnetic Particle Imaging, SPPHY 140, pp. 343–347.
springerlink.com

resonator and only needs to generate a low output power. If the operating frequency is changed to a lower or higher frequency, the amplifier will be also loaded by a reactive load, which requires a higher output power. Because of that, the required output power depends on the frequency bandwidth requirements of the MPI-System.

The basic idea was a scalable (modular) amplifier concept to obtain high flexibility and redundancy. Such an amplifier concept may consist of many individual modules made of commercial class-D amplifier chips connected in parallel. Theoretically one may connect as many chips/modules in parallel as practically feasible. This paper describes the simulation and a hardware setup of one module of the amplifier which consists of 10 chips connected in parallel and produces an output power of approximately 4kW with efficiency slightly above 90%.

2 Class-D Amplifier Chip (TDA8954)

The selected commercial chip is the TDA8954 [1] from NXP. This chip is a stereo high efficient audio chip with two class-D amplifier stages and delivers an output power of 2x210W@4Ω. The two channels can also be tied together to run in a bridge tied load (BTL) mode with an output power of 420W@8Ω. A symmetrical DC voltage of ±41V is needed to supply the amplifier chip. In addition, only few external parts are needed to get the amplifier to work.

An important feature of the chip is that it has a separate Pin for an external clock. This pin allows the user to set the PWM frequency of the chip, an essential part for this parallel concept. Because of this, a setup of many chips connected in parallel can be operated in an interleaved switching mode to reduce the input ripple current.

3 Simulation Model of the Class-D Amplifier

A simulation model of the modular class-D amplifier was built in Matlab/Simulink/Plecs. Fig. 1 shows a simplified schematic of the simulation model of the class-D amplifier. Due to space constraints just two class-D amplifier chips (full bridge inverter) are shown in Fig. 1. The actual simulation model contains ten class-D amplifier chips.

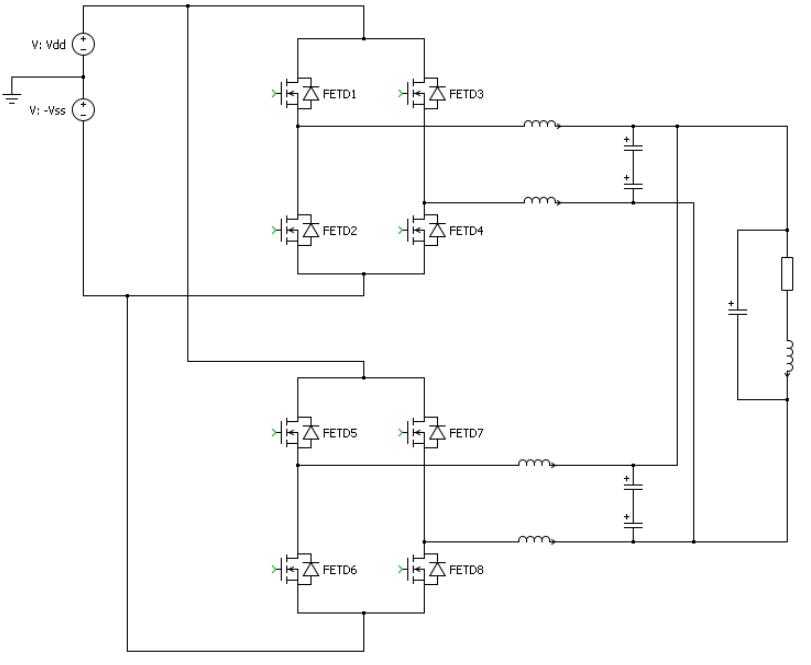

Fig. 1. A simplified schematic of the class-D amplifier with two chips connected in parallel. Chip 1 is represented by FETD1 – FETD4 and Chip 2 is represented by FETD5 – FETD8

An interleaved PWM algorithm has been build in Simulink to drive the entire modular amplifier. The simulation model also contains basic models of the output filter and the load. Furthermore it was made for designing and testing the laboratory setup.

4 Hardware Setup of the Class-D Amplifier

Based on the simulation model of 10 TDA8954 connected in parallel, a hardware setup were developed to confirm the simulation. The hardware setup consists of:

- 10 x TDA8954TH (SMD-Package)
- Special build, high quality coils for the output filter
- A fairly large quantity of DC-Link capacitors
- A water cooling concept to cool the amplifier module

Fig. 2 presents the developed hardware setup in top and bottom view.

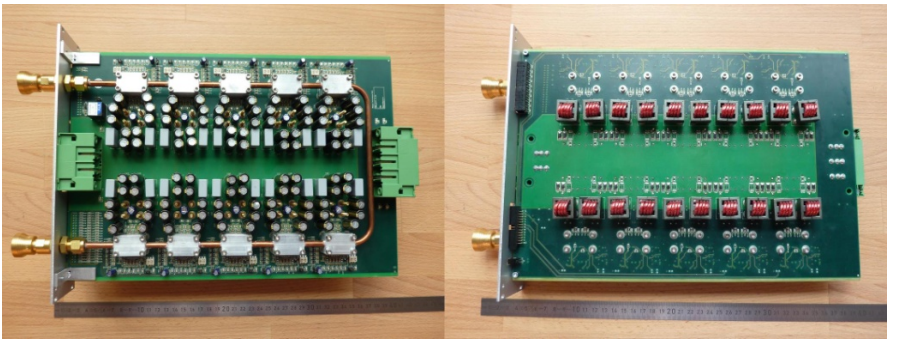

Fig. 2. Two pictures of the hardware setup. Top view (left) with the water cooling and DC-Link capacitors and bottom view (right) with the output filter coils.

The needed interleaved switching is externally generated by a controller for the amplifier module. This controller also deliverers the input signal to the amplifier and recognizes errors generated by the amplifier chips. If an error occurs, the controller will deactivate the complete amplifier module. Fig. 3 shows the controller card which is able to monitor up to six of these amplifier modules.

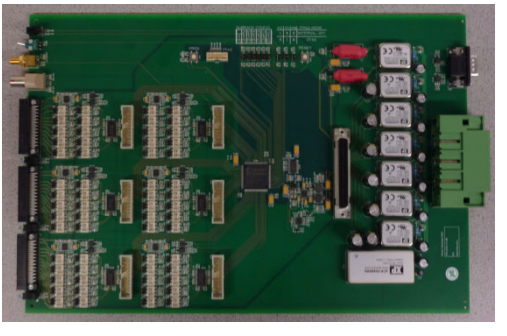

Fig. 3. Controller for up to six class-D amplifier modules

5 Results and Conclusion

The measured output voltage, output current and output power of the amplifier module is shown in Fig. 4. Thereby the DC input voltage was $V = \pm 40V$, input current was $I \approx 48A$ and the load had a value of $Z = 0.8\Omega@25kHz$.

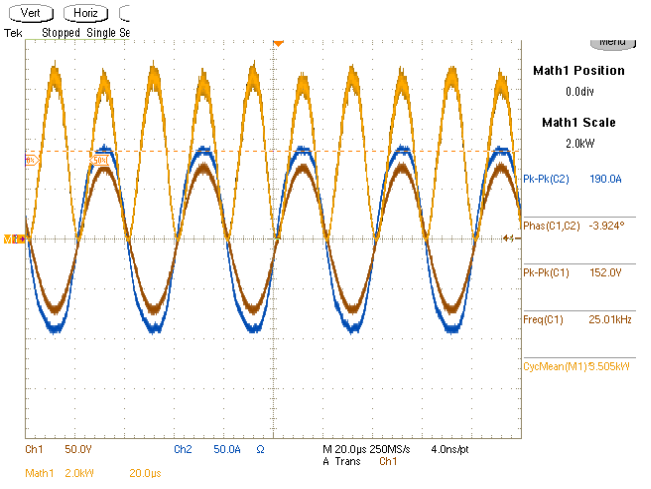

Fig. 4. Output parameters of the amplifier module; output voltage (brown), output current (blue) and output power (yellow)

Given by Fig. 4 the amplifier module generated a measured output power of $P \approx 3.5$kW with a calculated efficiency of round about 91%. A low THD value is also achieved by the amplifier module at this output power. It is possible to increase the output power of the amplifier module to measured 4kW, with respect to a higher THD value.

Moreover, the collected data of the measurements and the achieved experiences result in an improvement of the simulation model. The developed hardware setup of the amplifier module shows the success of the proposed parallel concept. Testing of two or more amplifier modules connected in parallel is the next step. If this test is successful it will be possible to build the needed scalable class-D amplifier for an MPI-System.

Reference

1. NXP Semiconductors: Datasheet TDA8954 2 × 210 W class-D power amplifier, Rev. 01, December 24 (2009)

A Hybrid Filter Topology for a Reduction of High Frequency Harmonics

J. Bergmann[1], K.F. Hoffmann[1], B. Gleich[2], and O. Woywode[3]

[1] Department of Power Electronics, University of the Federal Armed Forces, Helmut Schmidt University, Holstenhofweg 85 Hamburg, 22043, Germany
joern.bergmann@hsu-hh.de
[2] Philips Technologie GmbH Innovative Technologies, Research Laboratories, Röntgenstraße 24-26, 22335 Hamburg, Germany
[3] Philips Medical Systems DMC GmbH, Röntgenstraße 24-26, 22335 Hamburg, Germany

Abstract. In this paper a hybrid filter topology for the reduction of the total harmonic distortion in AC sources is introduced. The hybrid filter contains active and passive components. The structure of the digital filter influencing the signals gain and phase will be explained. Furthermore an analytical consideration of optimal filter coefficients is shown. For the validation of the concept a matlab/plecs simulation is presented.

1 Introduction

In medical applications it is often necessary to produce voltages or signals with low total harmonic distortions (THD). There are different opportunities for achieving this. Passive filter networks are a simple approach and are used in a wide range of power applications [1], [2]. On the one hand they are easy to design but on the other hand passive filters, containing inductors, can be very expensive and large in size. More and more active concepts are used in high power applications [3]. Researchers have studied different control and coupling strategies [4-6]. This paper presents a new analytical based FIR filter concept eliminating harmonics in high frequency applications.

T.M. Buzug and J. Borgert (Eds.): Magnetic Particle Imaging, SPPHY 140, pp. 349–354.
springerlink.com

2 Operation Principle

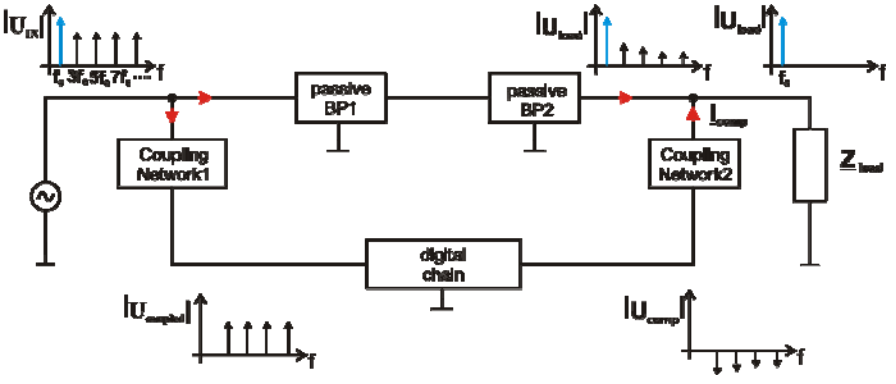

Fig. 1. Operation Principle

Fig. 1 shows the operation principle of an AC source with harmonic compensation. Furthermore it displays an AC source with a fundamental oscillation frequency f_0 and harmonic components. To achieve very low total harmonic distortions in Z_{Load}, bandpass filters BP1 and BP2 are introduced. In addition to that normal build up, a parallel leg containing coupling filter networks and a digital chain is added. The coupling network1 is designed as a bandstop filter for f_0 and is supposed to decouple the harmonics and transfer them to the digital chain. The digital chain changes the phase angle and the gain of each harmonic. The phase angle will be changed in that way, that after coupling network2 the harmonics of the source and the changed harmonics from the digital chain interfere with each other to zero. The main challenge is to design a digital chain that alters the gain and phase of the harmonic signal in a way, which leads to destructive interference after combining the signals of both legs. One topology, which fulfills these requirements, is a FIR filter.

3 FIR-Filter

Digital filters can be classified into finite impulse- (FIR) and infinite impulse response filters (IIR). One advantage of FIR filters is, that they are always stable, because they do not have feedbacks in there structure. The general structure of a digital FIR filter is shown in Fig. 2.

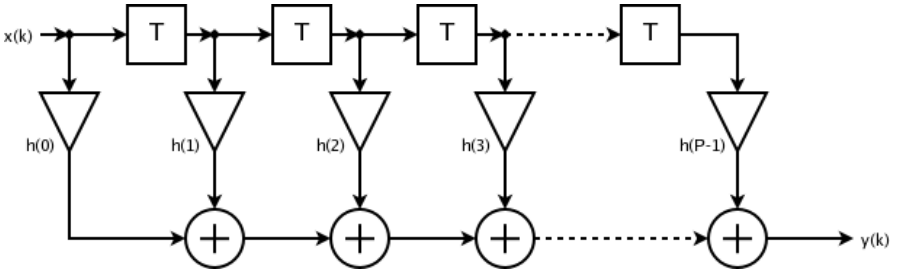

Fig. 2. FIR Filter

A FIR filter consists of an array of delay elements T, adders and multipliers h(0)-h(N-1). The characteristic of the filter belongs to the filter coefficients h(0)-h(P-1). There are three design methods for calculating the filter coefficients [7].

- Windowing Method
- Optimal Filter Design Method
- Frequency Sampling Method

The exact knowledge of the gain and phase values are very important in this application. The disadvantage of the windowing method is a lack of precise control of the critical frequencies.

The basic idea of the optimal filter design method is to design the filter coefficients by a recursive function until a particular error is minimized.

The only way for a total control of exact parameters is the frequency sampling method. Certainly all these techniques are used for the design of prototype lowpass, highpass or bandpass filters.

In this paper an analytical design method based on the frequency sampling method for irregular shape of the frequency response is introduced.

Equation 1 shows the difference equation of an FIR-filter.

$$y[n] = \sum_{k=0}^{N-1} b_k x[n-k] \tag{1}$$

$x[n]$ are the input and $y[n]$ are the output samples in the time domain. N is the order of the filter. The frequency response $H(\Omega)$ of such a system is given by:

$$H(\Omega) = \sum_{k=0}^{N-1} b_k e^{-j\Omega k} \qquad \text{with} \qquad \Omega = \frac{2\pi f}{f_{sample}} \tag{2}$$

f_{sample} is the sampling frequency of the digital system. With the introduction of desired gains G_M and phase angles Φ_M by a single frequency f equation 2 can be modified to:

$$G_M e^{-j\phi_M} = \sum_{k=0}^{N-1} b_k e^{-j\Omega_M k} \tag{3}$$

For multiple frequency points (e.g. $N = 4$) equation 3 can be expanded to

$$\begin{bmatrix} G_0 e^{-j\phi_0} \\ . \\ . \\ G_3 e^{-j\phi_3} \end{bmatrix} = \begin{bmatrix} 1 & e^{-j\Omega_0} & \dots & e^{-j\Omega_0(N-1)} \\ . & e^{j\Omega_0} & \dots & . \\ . & e^{-j\Omega_1} & \dots & . \\ 1 & e^{j\Omega_1} & \dots & e^{j\Omega_1(N-1)} \end{bmatrix} * \begin{bmatrix} b_0 \\ b_1 \\ b_2 \\ b_3 \end{bmatrix}. \tag{4}$$

Formula 4 is a system of linear complex equations, which can easily be solved. Now it is possible to calculate exactly an arbitrary frequency response with a nonlinear phase. The calculated filter coefficients b_0-b_3 are real numbers.

In fig. 3 a set of calculated filter parameters for a FIR filter with a nonlinear phase response is shown.

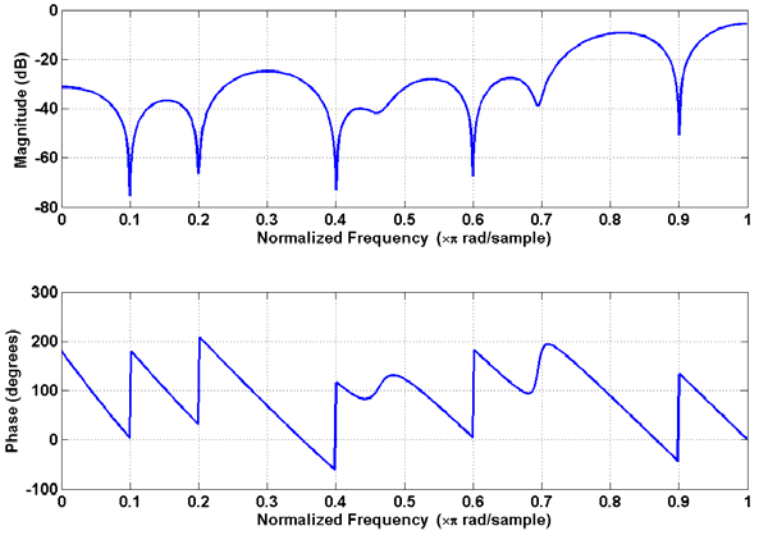

Fig. 3. Bode Chart of the calculated filter

The Bode Chart is plotted with a sample frequency $f_{sample} = 500$ kHz. The order N of the filter is 16.

4 Simulation Results

As a proof of concept a Matlab/Plecs model has been built up. The circuit is stimulated by an AC source with a voltage U_{IN} = 282.5 V and a frequency f = 25 kHz. The source voltage has only odd values of harmonics. In this simulation the source signal contains mainly three harmonics. The frequency response of the used FIR filter is shown in fig. 3. The load Z_{load} is purely ohmic. Fig. 4 shows the simulated spectrum of the system already presented in fig.1.

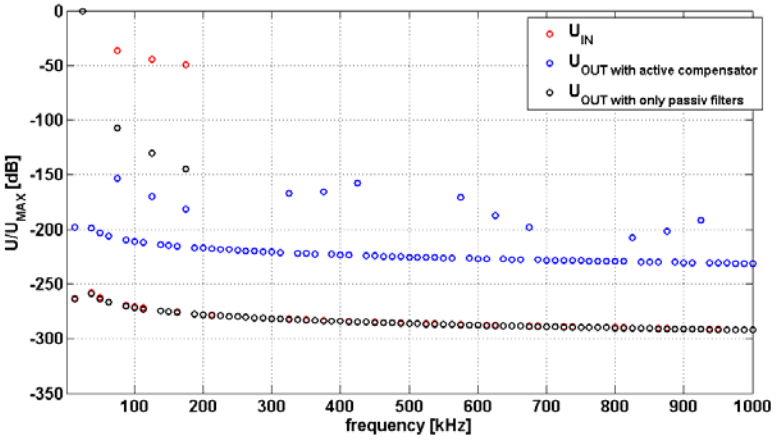

Fig. 4. Simulated spectrum of Z_{LOAD}

The spectrum values below -200 dB can be assumed as system noise. With the introduction of the active compensator an additional damping by 40 dB of each harmonic can be realized. The additional frequency components above 300 kHz are image frequencies of the FIR filter. They can be reduced by increasing the order of the reconstruction lowpass. A simple way to get rid of the image frequencies is to push them to higher frequencies by increasing the sampling frequency. This will increase the order of the filter. Another way to reduce them is the increase of the passive reconstruction filter.

5 Conclusion

In this paper an active compensator for the reduction of the total harmonic distortion in AC sources is introduced. Furthermore an analytical consideration of optimal filter coefficients is shown. Based on the difference equation of linear time discrete systems, a linear system of complex equations is calculated. Using this formula arbitrary FIR filters can be designed. For a

proof of concept a matlab/plecs simulation is presented showing good agreement with the analytical FIR filter calculation. The active compensator can introduce an additional damping of 40 dB per harmonic component compared to normal passive filter networks.

References

1. Osttroznik, S., Bajec, P., Zajec, P.: A Study of a Hybrid Filter, vol. 57. IEEE (2010)
2. Rivas, D., Moran, L., Dixon, J.W., Espinoza, J.R.: Improving Passive Filter Compensation Performance with Active Techniques. IEEE Transaction on Industrial Electronics 50 (2003)
3. Uceda, J., Aldana, F., Martinez, P.: Active filters for static power converters, vol. 130. IEEE (1983)
4. Lu, J., Huang, J., Gao, C.: Design and Application of a harmonic Detection Algorithm. In: ICICTA, vol. 2 (2011)
5. Zhang, L., He, C., Wang, P.: Harmonic Elimination using Independent Component Analysis. In: Automation Congress, pp. 1–4 (2008)
6. Akagi, H.: Active Harmonic Filters, vol. 93. IEEE (2005)
7. Proakis, J.G., Manolakis, D.G.: Digital Signal Processing. Prentice Hall (2000)

Safety Aspects for a Pre-clinical Magnetic Particle Imaging Scanner

Gael Bringout[1], Hanne Wojtczyk[1], Mandy Grüttner[1], Matthias Graeser[1], Wiebke Tenner[1], Julian Hägele[2], Florian M. Vogt[2], Jörg Barkhausen[2], and Thorsten M. Buzug[1]

[1] Institute of Medical Engineering, University of Lübeck,
Ratzeburger Allee 160, Lübeck, Schleswig-Holstein, 23562, Germany
bringout@imt.uni-luebeck.de, buzug@imt.uni-luebeck.de
[2] Clinic for Radiology and Nuclear Medicine,
University Hospital Schleswig-Holstein,
Ratzeburger Allee 160, Lübeck, Schleswig-Holstein, 23562, Germany

Abstract. Magnetic Particle Imaging is a promising new imaging technique using magnetic fields to image magnetic tracer material in the body. As with MRI systems, time varying magnetic fields raise some safety issues. The stimulation of peripheral nerves and tissues is one of them. In the paper, the stimulation thresholds are explained and an evaluation of the stimulation generated by a pre-clinical scanner is calculated. It appears clearly that, even if driving fields of high amplitude are used, cardiac arrhythmias are unlikely to be induced. However, it is yet unclear whether some peripheral nerve stimulation may be induced.

1 Introduction

Imaging devices using non-ionizing energy offer safer imaging acquisition procedures for patients and medical staff. Although Magnetic Particle Imaging (MPI) belongs to this category, some safety criteria are still to be evaluated to ensure a safe routine use of such technologies, similar to what has been done for MRI [1].

A conventional 3D MPI device is based on two different magnetic fields [2]: one static gradient field, which aims to saturate the tracer magnetization everywhere in the imaging volume, except for one point, the field free point (FFP); and three different time varying fields, which are applied in order to move the FFP through the space. By varying in time, those three magnetic fields will induce currents in the object, i.e. the patient, which may be sufficiently high to trigger tissue stimulation. Two different levels of stimulation are commonly defined [3, 4], based on the tissues which are stimulated. The first level is the stimulation of the peripheral nerves (called the Peripheral Nerve Stimulation - PNS - threshold), going from the onset of

T.M. Buzug and J. Borgert (Eds.): Magnetic Particle Imaging, SPPHY 140, pp. 355–359.
springerlink.com

sensation to intolerable or painful stimulation [1] for the patient, and the second level comes from the stimulation of myocardial muscles, which leads to cardiac stimulation. As in MRI, it may be possible to operate the scanner beyond the painful PNS threshold, but this has only to be done in very rare cases and requires a specific ethical approval. For normal daily use, the scanner has to be operated below the painful PNS threshold, and thus, below the cardiac stimulation threshold.

Unfortunately, those thresholds are not well defined, and may considerably vary from one patient to another [1, 3, 4]. Moreover, the relation between the field output of a scanner in the imaging volume and the PNS threshold greatly vary according to patient size and coil design. The Maxwell-Faraday law defines the relationship between the patient geometry and the magnetic and electrical field properties through the equation:

$$\oint_{\partial S} \boldsymbol{E} d\boldsymbol{l} = \int_{S} \frac{\partial}{\partial t} \boldsymbol{B} d\boldsymbol{A}. \quad (1)$$

With $\boldsymbol{B}$ being the magnetic field over the surface $\boldsymbol{S}$ bounded by the closed contour $\partial \boldsymbol{S}$ and $\boldsymbol{E}$ being the electrical field on the contour of that area. The Biot-Savart law can be used to calculate the magnetic field according to the coil geometry with the following equation:

$$\boldsymbol{B} = \frac{\mu_0}{4\pi} \int \frac{I\, d\boldsymbol{l} \times \boldsymbol{r}}{r^3}.$$

With μ_0 being the permeability of free space, I the current in the coil, $\boldsymbol{dl}$ a vector element with a length equal to that of the wire carrying the current and $\boldsymbol{r}$ is the displacement vector between the wire and the point at which the field is calculated. From those two equations, we can say that the induced current in the tissue will depend on the surface perpendicular to the vector of the absolute magnetic field, and that the magnitude of the magnetic field decreases according to the distance to the current-carrying wire.

Thus, we can conclude that for two scanners with the same driving field amplitude, if the PNS threshold is exceeded for a human sized system with a human patient, it may not be exceeded for a small animal sized system with a small animal inside. In other words, the safety aspect regarding PNS is not solely related to the driving field amplitude, but it depends also of the scanner geometry.

2 Material and Methods

The scanner we want to evaluate is an open scanner for interventional Magnetic Particle Imaging. Driving fields in the x, y and z direction are designed to have a center value of around 40, 17 and 23 mT, respectively. The maximum magnetic field values are reported on table 1 for each coil and field direction.

Table 1. Maximum field values of the driving coils in the mid plane of the scanner.

	B_x / mT	B_y / mT	B_z / mT	B_{abs} / mT
x driving coil	40	0	0	
y driving coil	0	17	7	
z driving coil	0	10	23	
Sum of fields	40	27	30	57

Each coil is fed with sinusoidal current at a slightly different frequency: 24.51 kHz, 25.25 kHz and 26.04 kHz [5]. The maximum value, the time and the perpendicular surface of the peak d$\boldsymbol{B}$/dt value will thus depend on the frequency applied to the different coils. In order to simplify the calculation, the animal will be approximated as a sphere with a radius r of 10 cm. The maximum d$\boldsymbol{B}$/dt value is then numerically calculated assuming a uniform magnetic field distribution, and the induced electrical field E_i (in V/m) is calculated according to equation (1) as

$$E_i = \frac{r}{2} \max\left(\frac{d|\boldsymbol{B}|}{dt}\right).$$

As threshold for PNS, two standards will be considered. The first one is the ICNIRP guideline [6], which considers the safety of general exposure to electro-magnetic fields from 1 Hz to 100 kHz, the second one is the PNS and cardiac stimulation thresholds from J.P. Reilly [4], which are also used as reference for MRI safety criteria [1].

The ICNIRP takes, for field frequencies between 3 kHz and 10 MHz, a limit of 170 V/m whereas Reilly proposes the following equation for our frequency range:

$$E_t = E_0 \left(\frac{f}{f_e}\right)^{0.9}.$$

Where E_t is the electric field threshold (in V/m), E_0 is the minimum threshold at the optimum frequency (in V/m), which is equal to 7.2 V/m in our case [4], f is the considered frequency (in Hz) and f_e is an empirically determined frequency. There are two values for the f_e frequency regarding PNS, namely 500 Hz and 5400 Hz. The first one has been determined based on a literature review done by Reilly [4], and the other one stems from simulations carried out by Reilly [4]. For cardiac stimulation, a third value, f_e = 120 Hz, has been determined by Reilly [4], based on a literature review. For our calculations, we will consider the heart of the animal as a sphere of 4 cm in radius.

3 Results

The maximum value for E_i has been calculated for different frequency configurations. When the x, y and z drive fields are used with frequencies of 24.51 kHz, 26.04 kHz and 25.25 kHz respectively, we induce a

maximum electrical field of 447 V/m for the whole body, and 179 V/m for the heart. When we use other configurations, we may induce a field up to 2% higher. Those induced fields are above the two Reilly PNS and the ICNIRP thresholds, but still below the Reilly threshold for cardiac stimulation. Those data are summarized in table 2.

Table 2. E values calculated for the different thresholds and for the configuration which produces the smaller E_i value

	Reilly 5400 Hz (body)	ICNIRP (body)	Reilly 500 Hz (body)	This scanner (body)	This scanner (heart)	Reilly 120 Hz (heart)
E / V/m	29	170	247	447	179	2230

4 Discussion

To consider the magnetic field to be constant over the whole volume with an amplitude equal to the maximum value of the magnetic field in the mid plane seems to be conservative, but we have to keep in mind that the higher field value will be generated near the coils, i.e. near the animal skin, and thus, a higher electrical field may be induced. However, considering the electrical field induction as a sinusoidal signal with a constant amplitude equivalent to the peak value of the field induction is conservative [7]. Moreover, PNS thresholds seem to be higher for inductive excitation than for direct electrical excitation [8]. As Reilly's thresholds are based on direct electrical excitations, the use of those thresholds for inductive excitation is also a conservative assumption. Moreover, ICNIRP thresholds are calculated using high a factor to compensate for dosimetric uncertainties [9]. Nevertheless, those preliminary numbers show that the induced electrical field with our scanner is below the threshold of cardiac stimulation, thus allowing us to perform animal experiments in good condition. We still have to perform calculations with more precise models, in terms of magnetic field representation and animal model geometries. Finally, heating of the animal tissue still has to be examined according to Specific Absorption Rate (SAR) standards and actual work on MPI related application [10].

5 Conclusion

Through this paper, we showed that our animal scanner should not cause any cardiac arrhythmias on the animal, even if we use high driving field amplitudes. But the threshold for PNS is still too vague to conclude on peripheral nerve stimulation, and further experiments have to be carried on.

Acknowledgments. The authors gratefully acknowledge the financial support of the German Federal Ministry of Education and Research (BMBF) under grant number 13N11090, of the European Union and the State Schleswig-Holstein (Programme for the Future – Economy) under grant number 122-10-004 and of Germany's Excellence Initiative [DFG GSC 235/1].

References

1. IEC: Medical electrical equipment. Part 2. Particular requirements for the safety of magnetic resonance equipment for medical diagnosis. ISO 60601-2-33 (2008)
2. Gleich, B., Weizenecker, J.: Tomographic imaging using the nonlinear response of magnetic particles. Nature 435, 1214–1217 (2005)
3. Irnich, W., Schmitt, F.: Magnetostimulation in MRI. Magn. Reson. Med. 33(5), 619–623 (2005)
4. Reilly, J.: Magnetic field excitation of peripheral nerves and the heart: a comparison of thresholds. Med. Biol. Eng. Comput. 29(6), 571–579 (1991)
5. Weizenecker, J., Gleich, B., Rahmer, J., Dahnke, H., Borgert, J.: Three-dimensional real-time in vivo magnetic particle imaging. Phys. Med. Biol. 9, 4 (2009)
6. International Commission of Non-Ionizing Radiation Protection: Guidelines for limiting exposure to time-varying electric and magnetic fields (1 Hz to 100 kHz). Health Phys. (2010)
7. Reilly, J.: Peripheral nerve stimulation by induced electric currents: exposure to time-varying magnetic fields. Med. Biol. Eng. Comput. 27, 101–110 (1989)
8. Recoskie, B.J., Scholl, T.J., Zinke-Allmang, M., Chronik, B.A.: Sensory and Motor Stimulation Thresholds of the Ulnar Nerve from Electric and Magnetic Field Stimuli: Implications to Gradient Coil Operation. Magn. Reson. Med. (2010)
9. International Commission of Non-Ionizing Radiation Protection: General approach to protection against non-ionizing radiation. Health Phys. (2002)
10. Bohnert, J., Gleich, B., Weizenecker, J., Borgert, J., Dössel, O.: Simulations of Current Densities and Specific Absorption Rates in Realistic Magnetic Particle Imaging Drive-Field Coils. Biomed. Tech. 55 (2010)

Short Contributions

Citrate-Coated Magnetite Nanoparticles Are Highly Efficient Agents for Magnetic Labeling of Human Mesenchymal Stem Cells

Kristin Andreas[1], Jochen Ringe[1], Michael Sittinger[1], and Norbert Buske[2]

[1] Tissue Engineering Laboratory and Berlin-Brandenburg Center for Regenerative Therapies, Department of Rheumatology and Clinical Immunology, Charité-Universitätsmedizin Berlin, Charitéplatz 1, 10117 Berlin, Germany
kristin.andreas@charite.de
[2] Magnetic Fluids, Köpenicker Landstrasse 203, 12437 Berlin, Germany

Motivation: Systemic transplantation of human mesenchymal stem- and progenitor cells (MSC) is a promising approach in regenerative medicine. Magnetic resonance imaging (MRI) of transplanted MSC labeled with superparamagnetic iron oxide nanoparticles (SPION) is an excellent tool for *in vivo* cell tracking because it offers a high spatio-temporal, sensitive and non-invasive cell detection. However, cell labeling with commercial SPION is still inefficient and requires the use of potentially toxic transfection agents. New results are reported here about magnetite@citrate ferrofluids that allow highly efficient magnetic MSC labeling without transfection agents.

Methods: Magnetic labeling of human MSC was performed dose-dependently with experimental Citrate SPION and commercially available dextran-coated Endorem and carboxydextran-coated Resovist SPION without using transfection agents. Cell labeling was investigated by intracellular iron quantification with inductively coupled plasma optical emission spectrometry, Prussian Blue staining and *in vitro* MRI of cell phantoms. Standard proliferation, differentiation and chemotaxis assays were performed to analyze the impact of intracellular SPION on MSC function. Furthermore, FACS analysis was conducted to determine alterations in the exposition of typical cell surface markers. SPION-labeled MSC were transplanted into rat muscle and *in vivo* visualization was conducted using 7T MRI. Transplanted cells were detected *ex vivo* by Prussian Blue and immunohistochemical stainings with anti-CD44 and anti-mitochondria MCT02.

Results: Efficient magnetic labeling of human MSC was only achieved with Citrate SPION that was more than one order of magnitude increased compared to labeling with commercial SPION as shown by high intracellular

T.M. Buzug and J. Borgert (Eds.): Magnetic Particle Imaging, SPPHY 140, pp. 363–364.
springerlink.com

iron content and decrease in MR signal intensity. Magnetic labeling of human MSC did not affect cell proliferation, cell surface marker antigen presentation and differentiation into the adipogenic and osteogenic lineages. However, chondrogenic differentiation and chemotaxis were significantly impaired with increasing SPION uptake, potentially hampered by internalized SPION that interfere with the cytoskeleton. The detection limit of Citrate SPION-labeled MSC amounted to 31.3 cells/mm^3 to be significantly retrieved by 7T MRI. Transplanted SPION-labeled MSC were visualized *in vivo* after intramuscular injection in rats by MRI and were retrieved *ex vivo* by Prussian Blue staining and were confirmed by specific immunohistochemical stainings.

Conclusion: Magnetite@citrate SPION are attractive candidates as efficient intracellular magnetic labels for *in vivo* stem cell tracking by MRI. However, a careful titration of SPION incorporation, cellular function and MRI visualization is essential.

This study was supported by the Berlin-Brandenburg Center for Regenerative Therapies (BMBF-Grant No: 0313911).

Dendronized Iron Oxides as Smart Nano-objects for Multimodal Imaging

B. Basly[1], G. Popa[1], A. Garofalo[1], D. Felder-Flesch[1], S. Begin-Colin[1], and C. Billotey[2]

[1] Institut of Physic and Chemistry of Materials, UMR CNRS-Unistra 7504, 23, rue du Loess Strasbourg, F-67204, France
Sylvie.Begin@ipcms.unistra.fr, delphine.felder@ipcms.unistra.fr
[2] Laboratoire de Physico-chimie des Matériaux Luminescents LPCML-UCBL UMR 5620 5 place d'Arsonval F-69437 Lyon, France

Superparamagnetic iron oxide nanoparticles (NPs) with appropriate surface coating are widely used for numerous *in vivo* applications and in particular for MRI contrast enhancement. To improve the contrast enhancement and targeting properties as well as the biodistribution of functionalized iron oxide NPs, challenges have to be overcome such as: *(i)* the design of an organic coating favouring ideal biodistribution, ensuring multifunctionalization (targeting, optical imaging…) and preserving a small size distribution of coated NPs in physiological media (<50 nm), *(ii)* the synthesis of iron oxide NPs with good magnetic properties and *(iii)* the development of strong anchors at the NPs surface avoiding desorption of molecules in blood. Indeed, the coating design as well as the interaction nature between the organic shell and the nanocrystal surface are more and more key points to address.

We thus propose a concept based on dendritic and phosphonate approaches. Indeed, phosphonate groups ensure a strong anchoring at the NPs surface while preserving their magnetic properties[1], and dendritic architectures, in addition to their small size, are very promising as the diversity of functionalization brought by the arborescent structure simultaneously may solve the problems of biocompatibility, low toxicity, large *in vivo* stability and specificity.

Iron oxide NPs synthesized by co-precipitation and thermal decomposition were coated with functional oligoethyleneglycol (OEG) dendrons (bearing only PEG chains or with, among PEG chains, a PEG chain bearing either a carboxylate or an ammonium group) to improve colloidal stability, graft fluorescent molecules and investigate cell interactions.[2, 3, 4] Different grafting strategies were optimized as a function of the NPs synthesis and dendron nature. The size distribution, colloidal stability in isoosmolar

T.M. Buzug and J. Borgert (Eds.): Magnetic Particle Imaging, SPPHY 140, pp. 365–366.
springerlink.com

media, nature of surface complex, biodistribution and contrast enhancement properties evaluated through *in vitro* and *in vivo* MRI experiments were compared as a function of the nature of both dendrons and nanoparticles. All functionalized nanoparticles (whatever the synthesis method) display good colloidal stability in water but, in isoosmolar media, best results were observed with functional dendronized NPs bearing carboxylates at their periphery. The grafting rates are similar whatever the NPs synthesis method but depend on the nature of dendrons. Furthermore the surface complex was found to vary according to the method what should affect the magnetic properties. The contrast enhancement properties of all dendronized nanoparticles were found higher than the one of commercial products (polymer-decorated) and the best values were recorded for the nanoparticles synthesized by coprecipitation due to their higher saturation magnetization. Cell viability tests, relaxivity measurements, biodistribution studies through optical imaging and *in vivo* MRI experiments demonstrated the low toxicity of these dendronized nanoparticles and their interest as multimodal contrast agent.[4, 5]

1. Daou, T.J., Greneche, J.-M., Pourroy, G., Begin-Colin, S., et al.: Chem. Mater. 20(18), 5869–5875 (2008)
2. Basly, B., Felder-Flesch, D., Perriat, P., Pourroy, G., Bégin-Colin, S.: Contrast Med. and Mol. Imaging 6, 132–138 (2011)
3. Basly, B., Felder-Flesch, D., Perriat, P., Billotey, C., Taleb, J., Pourroy, G., Begin-Colin, S.: Chem. Comm. 46, 985–987 (2010)
4. Lamanna, G., Kueny-Stotz, M., Mamlouk-Chaouachi, H., Basly, B., Ghobril, C., Billotey, C., Berniard, A., Pourroy, G., Begin-Colin, S., Felder-Flesch, D.: Biomaterials 32, 8562–8573 (2011)
5. Basly, B., Popa, G., Fleutot, S., Pichon, B., Garofalo, A., Ghobril, C., Billotey, C., Berniard, A., Martinez, H., Perriat, P., Felder-Flesch, D., Begin-Colin, S.: Chem. Mater. (submitted)

Superparamagnetic Dextran Coated Iron Oxide Nanoparticles (SPIO) as Potential Markers for Tumor Cell Detection

R. Pries[1], K. Lüdtke-Buzug[2], A. Lindemann[1], B. Hüsing[1], T.M. Buzug[2], and B. Wollenberg[1]

[1] Klinik für HNO, UKSH Lübeck, Ratzeburger Allee 160
Lübeck, 23538, Germany
rallepries@yahoo.de
[2] Institute of Medical Engineering, University of Luebeck, Ratzeburger Allee 160
Lübeck, 23562, Germany
luedtke-buzug@imt.uni-luebeck.de

Head and neck cancer includes the squamous cell carcinomas of the oral cavity, pharynx and larynx and is one of the most common solid neoplasms worldwide. The malignancy is an important public health problem worldwide with more than 500000 new cases diagnosed each year. The change in survival over the last 20 years remains minimal and despite recent attention, the mortality rates are still high due to local tumor invasion and to a high predilection for the development of relapses and metastases. The cellular and molecular mechanisms responsible for tumor aggressiveness and its response to chemo- and radiation therapies remain mostly unknown.

Fur5hermore, it has been shown in recent studies that tumor progression and metastasis are assumed to be stem cell driven processes and that these 'tumor initiating cells' provide a future outlook for innovative cancer therapy and diagnostic approaches. To monitor and characterize these tumor stem cell populations in head and neck squamous cell carcinoma (HNSCC) we focus on the visualization of their migration activity and tumor initiating potential. Therefore, HNSCC cells were labelled with newly developed superparamagnetic dextran coated iron oxide nanoparticles (SPIO) in order to make them detectable via magnetic particle imaging (MPI). Nanoparticle uptake and cytotoxicity of SPIOs were determined and no influence on cell death or proliferation of the HNSCC cells was examined.

The aim of this study is to identify and characterize tumor subpopulations in head and neck squamous cell carcinoma (HNSCC) and to analyze and visualize their migration activity and their tumor inducing potential. Therefore, cells were labelled with superparamagnetic dextran coated iron oxide nanoparticles (SPIO) in order to make them detectable via 'magnetic particle

T.M. Buzug and J. Borgert (Eds.): Magnetic Particle Imaging, SPPHY 140, pp. 367–368.
springerlink.com

imaging' (MPI), which is a new quantitative imaging technique capable of determining the spatial distribution of superparamagnetic nanoparticles at high temporal and spatial resolution. Tumor cells' nanoparticel uptake was corroborated and to ensure the nanoparticle applicability the cytotoxicity of the SPIOs was determined. In addition, initial experiments with the MPI Spectrometer showed that the dextran coated iron oxide nanoparticles uptaken by HNSCC cells are detectable with MPI.

The newly developed dextran-coated magnetic nanoparticles are very promising for the MPI and a future cancer therapy application and further modifications for instance the surface could specify the uptake or binding. Based on these results further investigation will in deatail analyze the behavior, migration and tumor initiating potential of SPIO coated HNSCC tumor cells.

Low Field NMR as a Tool for Neuronal Current Detection: A Feasibility Study in a Phantom

Rainer Körber[1], Nora Höfner[1], Martin Burghoff[1], Lutz Trahms[1], Jens Haueisen[2], Sven Martens[2], and Gabriel Curio[3]

[1] Physikalisch-Technische Bundesanstalt, Berlin
Abbestrasse 2-12, 10587 Berlin, Germany
rainer.koerber@ptb.de
[2] Institut of Biomedical Engineering and Informatics,
Ilmenau University of Technology
Gustav-Kirchhoff-Straße 2, 98693 Ilmenau, Germany
jens.haueisen@tu-ilmenau.de
[3] Department of Neurology, Campus Benjamin Franklin,
Charité-Universitätsmedizin Berlin
Hindenburgdamm 30, 12203 Berlin, Germany
gabriel.curio@charite.de

The detection of neuronal currents (NC) may foster the understanding of the flow of information in the brain. Existing methods of NC detection like electro- and magnetoencephalography (EEG/MEG) are limited by the ambiguity of the inverse problem, while imaging methods like fMRI monitor secondary effects (e.g., blood oxygenation changes). On the other hand, attempts to directly detect NC in high field NMR techniques by a local shift of the ^{1}H resonance frequency have yielded controversial results. In magnetic fields around 1 microTesla, the relative contribution of the biomagnetic field generated by neuronal currents is orders of magnitude higher than in conventional high fields. This may make the situation much more favourable.

We propose two different approaches to detect NC at low magnetic fields. The resonant mechanism aims at observing the influence of the locally induced neuronal field on the spin dynamics. In this case, the neuronal field can be viewed as a tipping pulse in resonance with the Larmor frequency of the surrounding protons, leading to a detectable deflection of the nuclear magnetisation in brain matter. This mechanism is exclusively accessible to low field NMR, where the Larmor frequency of the cerebral ^{1}H protons matches the spectral content of local cerebral electrical activities. The DC mechanism is based on local neuromagnetic fields generated by long-lasting neurocurrents that superimpose the applied field. Such fields may induce local frequency and line-width changes during the complete NMR cycle.

T.M. Buzug and J. Borgert (Eds.): Magnetic Particle Imaging, SPPHY 140, pp. 369–370.
springerlink.com

Their spatio-temporal pattern strongly depends on the structure of the underlying NC and leads to different local effects on the T_2^* of the NMR signal. A neuronal field that may be suitable for the demonstration of the two mechanisms is the brain activity generated by repetitive electrostimulation of the nervus medianus. This evokes both fast activity and, depending on the stimulation procedure, sustained activity. We characterised both neuronal activations with MEG measurements showing that such activities can be modelled by an equivalent current dipole with a typical strength of around 15 nAm.

In order to prove the principal feasibility of NC detection by low field NMR, we simulated the two mechanisms by emulating neuronal activity using a single dipolar source in a physical phantom. The phantom setup consists of a hollow sphere made of PVC, which is filled with a conducting aqueous saline solution. Inside the sphere we mounted an electric current dipole, which was made from two insulated twisted copper wires with non-insulated platinum endings. We investigated the influence of the dipole moment in the phantom on the NMR signal. We found that, to make the two mechanisms observable, we need dipole strengths by two orders of magnitude higher than those we had observed in our MEG study of evoked fields. Alternatively, an increase of the polarizing field and a reduction of system noise should also improve the signal-to-noise-ratio sufficiently to make the observation of NC by low field NMR possible under real physiologic conditions. We will demonstrate that this can be done by realistic improvements of the experimental set-up.

Low Field Nuclear Magnetic Relaxation of Water and Brain Tissue

Stefan Hartwig, Hans-Helge Albrecht, Nora Höfner, Ingo Hilschenz, Rainer Körber, Hans-Jürgen Scheer, Jens Voigt, Martin Burghoff, and Lutz Trahms

Physikalisch-Technische Bundesanstalt
Abbestraße 2-12
10587 Berlin, Germany
Stefan.Hartwig@PTB.de

In the endeavor to perform in vivo magnetic resonance imaging in very low fields, we developed a dedicated SQUID based NMR/MRI measurement system. The low noise performance of < 30 fT/√Hz above 1 Hz enables the measurement of nuclear magnetic precession at magnetic fields well below 50 μT down to 100 nT. The system is operated inside a heavily magnetically shielding - the Berlin Magnetically Shielded Room BMSR-2.

Each measurement starts with a prepolarization of the sample in a field of up to 5 mT. After this preparation, the free precession decay in the much weaker detection field is measured by the SQUID.

Because ^{1}H of water is the most important nucleus for MRI, we first investigated the nuclear magnetic relaxation of water at very low magnetic fields. We observed a decrease of the relaxation time constant by about 25% at Larmor frequencies below 1 kHz, which is known from earlier studies. Surprisingly, we also found a strong variation of both longitudinal and transversal relaxation time around Larmor frequencies of 100 Hz that has not been observed before, and that is not in line with the standard NMR relaxation theory.

With the knowledge of waters behavior and systems spectral resolution we recorded the ^{1}H line of the human brain tissue. Here we found line widths of about 3 Hz corresponding to T_1 relaxation times of 100 mT. The aim behind these investigations is the measurement of the influence of neuronal currents to this NMR lines. This might open the possibility of a direct recording of neuronal currents by low field NMR. To this end we proposed two possible mechanisms: a DC-mechanism and a resonant mechanism. To localize the source of such neuronal currents one has to combine neuronal current detection with low field magnetic resonance imaging. In this spirit we actually develop low-field MRI below 1 kHz as the prerequisite to fulfill the requirements of the resonant mechanism for neuronal current detection.

T.M. Buzug and J. Borgert (Eds.): Magnetic Particle Imaging, SPPHY 140, p. 371.
springerlink.com

In Vivo Biodistribution and Pharmacokinetics of Optimized Magnetic Particle Imaging Tracers

Amit P. Khandhar[1], R. Matthew Ferguson[2], and Kannan M. Krishnan[1]

[1] LodeSpin Labs LLC, PO Box 95632
Seattle, WA 98145-2632, USA
amit.khandhar@gmail.com
[2] Materials Science & Engineering, University of Washington, 302 Roberts Hall
Seattle, WA 98195, USA
mferg47@uw.edu, kannanmk@uw.edu

Magnetic particle imaging (MPI) is an emerging magnetic nanoparticle detection technique that has great potential as a novel biomedical imaging procedure. Particularly, MPI offers a safer real-time option over conventional x-ray angiography procedures since it uses safe magnetic fields (no ionizing radiation) and biocompatible superparamagnetic magnetite (Fe_3O_4) nanoparticle tracers, which are the source of the signal and play a significant role in spatial resolution. Current tracer formulations such as Resovist® offer poor spatial resolution, and thus, inadequate performance for high-quality angiographies. Alternatively, our superparamagnetic magnetite (SuperMag) tracers show 30% improvement in spatial resolution compared to Resovist®. However, an ideal MPI tracer consists of a balance between an optimized magnetic core and a biocompatible shell that enhances circulation times combined with appropriate functionalization necessary to enhance the tracer's bioavailability. For angiographies, tracer availability in the vasculature is of utmost importance to determine the most effective method of administration and ensure sufficient time for the imaging procedure. In this preliminary study we report pharmacokinetics and biodistribution characteristics of SuperMag tracers in an animal model. SuperMag tracers were formulated with variations in the polymeric shell and subsequently tested in CD-1 mice. Dose-dependent biodistribution was studied using MR-imaging and post-mortem histology analysis. Implications of *in vivo* circulation characteristics on MPI angiography procedures are discussed.

T.M. Buzug and J. Borgert (Eds.): Magnetic Particle Imaging, SPPHY 140, p. 373.
springerlink.com

Imaging with Optimized Magnetite MPI Tracers

R. Matthew Ferguson[1], Amit P. Khandhar[2], Patrick W. Goodwill[3], Steven M. Conolly[3], and Kannan M. Krishnan[1]

[1] Materials Science & Engineering, University of Washington, Box 352120 Seattle, WA 98195-2120, USA
mferg47@uw.edu, kannanmk@uw.edu
[2] LodeSpin Labs LLC, PO Box 95632 Seattle, WA 98145-2632, USA
amit.khandhar@gmail.com
[3] Bioengineering, University of California, Berkeley Berkeley, CA 94720-1762
goodwill@berkeley.edu, sconolly@berkeley.edu

Magnetite nanoparticle (MNP) tracers can be optimized for Magnetic Particle Imaging (MPI) by tuning their magnetic core size and size distribution. In previous work, our group showed that ~15 nm MNPs were optimal at 250 khz by synthesizing a series of tracers with tuned size and narrow size distributions. This optimization approach is general, and here we present experimental results that demonstrate that the same principles apply at 25 khz excitation. The key result of this work is that MPI spatial resolution can be improved by the appropriate selection of MNPs.

We synthesized MNP tracers in our labs with median diameters of 20-25 nm and narrow size distributions. Each tracer consisted of magnetite cores that were synthesized in organic solvents to ensure uniform size and subsequently coated with an amphiphilic polymer and dispersed in water. Tracer performance was characterized using a home-built MPI magnetometer that excites tracer magnetization with a field of up to 36 $mT\mu_0^{-1}$ (peak to peak) and measures the signal induced in a receive coil by the derivative of tracer magnetization, *M'(H(t))*. In preliminary results, our tuned tracers showed 30% better spatial resolution compared to Resovist, determined from the point-spread function: the full-width-half-maximum of *M'(H(t))*. The tuned tracers also yield harmonic spectra with greater intensity than Resovist, when normalized by iron concentration, for all of the 40 harmonics measured by our device.

In addition to measurements of the point spread function we present preliminary results of phantom imaging experiments using the tuned tracers. These results highlight the improved performance of our tracers compared with Resovist, the current standard tracer for MPI.

T.M. Buzug and J. Borgert (Eds.): Magnetic Particle Imaging, SPPHY 140, p. 375.
springerlink.com

A Magnetometer Cooled with Liquid Nitrogen for the Characterization and Quantification of Magnetic Nanoparticles in Biological Samples at Room Temperature

Martijn Visscher, Matthias Holling, Joost Pouw, and Bennie Ten Haken

MIRA-Institute for Biomedical Engineering and Technical Medicine, Neuro-Imaging Group, University of Twente, Enschede, P.O. Box 217, 7500 AE, The Netherlands
m.visscher@utwente.nl

For several medical applications of magnetic nanoparticles (MNP) it is desired to know the quantity and characteristics of the particles in the tissue of interest. That can either be necessary to determine how successful a procedure was of how it will be. Therefore a system is built, that is suitable to analyze small intact biological samples at room temperature. The magnetometer is used for the analysis and selection of sentinel lymph nodes in colorectal cancer. In this clinical procedure MNPs are administered in the resected part of the colon to determine the sentinel lymph node. The magnetometer is based on copper wound coils and comprises of two detection coils in series opposition, enclosed by two separately driven excitation coils. The detection coils are wound on a vacuum insulated sample tube with 11 mm inner diameter. To increase sensitivity and both mechanical and electrical stability of the system, the excitation and detection coils are cooled in liquid nitrogen at 77 K. By stabilization of the thermal expansion in the coil set, drift and offset components in the detection signal are reduced [1]. The systems output drift over a few hours of operation was less than 20 μV h^{-1}. Furthermore, thermal noise in the passive detection coils is reduced, theoretically with a factor 5.4, which improves the detection limit of MNPs. To keep the sample at room temperature, the sample tube is built as an anti-cryostat using an internal heater and vacuum insulation. The magnetometer provides both simple AC-magnetometry with frequency sweeps, as well as frequency mixing detection using excitation fields with two different frequencies. Earlier experiments with sentinel lymph nodes in a vibrating sample magnetometer (VSM) revealed that iron content in the order of 1-100 μg can be significantly dominated by linear diamagnetic contributions from (fat) tissue. The frequency mixing approach enables specific quantification of the MNP content in a sample, since the linear magnetic contributions of

T.M. Buzug and J. Borgert (Eds.): Magnetic Particle Imaging, SPPHY 140, pp. 377–378.
springerlink.com

tissue and sample holder are not contributing to the mixing component in the detection signal [2]. As a specific frequency mixing detection algorithm, one of the excitation fields is applied as a DC-field (B ~ 17 mT) that is switched on and off. Caused by the non-linear response of MNPs to the excitation field, the detected response to the AC-field is different for both situations. This sample response modulation with the switch of the DC-field is used as a measure of the content of MNPs. To conclude, this magnetometer provides accurate measurement of MNPs in intact biological samples with a high stability and specificity. Because additional sample processing is not required, the measurements do not interfere with possible other (clinical) analyses. Furthermore the measurement time of less than 1 minute per sample makes the system already suitable for clinical selection of the sentinel lymph node from a series of harvested lymph nodes.

[1] Rabbers, J.J., ten Haken, B., et al.: Advanced ac loss measurement methods for high-temperature superconducting tapes. Review of Scientific Instruments 72(5), 2365–2373 (2001)

[2] Krause, H.J., Wolters, N., et al.: Magnetic particle detection by frequency mixing for immunoassay applications. Journal of Magnetism and Magnetic Materials 311(1 SPEC. ISS.), 436–444 (2007)

Uniform Magnetite Nanoparticles Larger Than 20 nm Synthesized by an Aqueous Route

Sabino Veintemillas-Verdaguer[1], María del Puerto Morales[1], Carlos J. Serna[1], Manuel Andrés-Vergés[2], Jesús Ruiz-Cabello[3], and Fernando Herranz[3]

[1] Instituto de Ciencia de Materiales de Madrid (CSIC), Sor Juana Inés de la Cruz 3, 28049 Madrid, Spain
sabino@icmm.csic.es

[2] Departamento de Química Orgánica e Inorgánica, Universidad de Extremadura, Avda Elvas s/n, 06071 Badajoz, Spain
manver@unex.es

[3] Unidad de Imagen Avanzada, Centro Nacional de Investigaciones Cardiovasculares (CNIC), C/Melchor Fernandez Almagro 3 28029 Madrid, Spain
fernando.herranz@cnic.es

Here we present an aqueous route for the synthesis of uniform magnetite nanoparticles with sizes around the monodomain diameter (20-100 nm). The method is based on the precipitation of an Fe(II) salt in a mild oxidant in hydroalcoholic solutions, and leads to highly uniform and crystalline magnetic nanoparticles in a single step. Colloidal suspensions of these particles were directly obtained by simple ultrasonic treatment of the powders thanks to the presence of sulphate anions at the particle surface. All magnetisation curves saturate at much lower magnetic fields and show larger saturation magnetization than samples prepared by coprecipitation. Saturation magnetisation values vary between 83 and 92 emu g−1, close to the theoretical values reported for bulk magnetite at room temperature. Those magnetic particles have shown the maximum heat efficiency for magnetic hyperthermia and they could show great potential in MPI imaging.

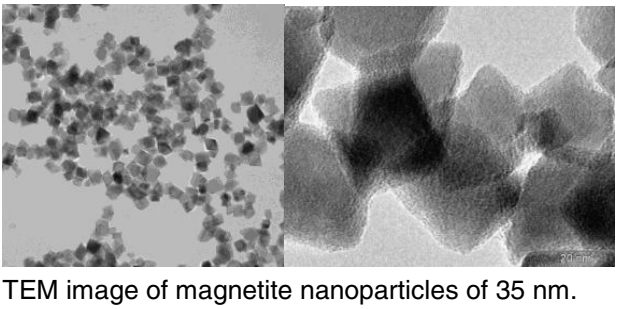

TEM image of magnetite nanoparticles of 35 nm.

T.M. Buzug and J. Borgert (Eds.): Magnetic Particle Imaging, SPPHY 140, p. 379.
springerlink.com

Author Index